DISSERTATION

submitted to the
Combined Faculties for the Natural Sciences and Mathematics
of the Ruperto-Carola-University of Heidelberg, Germany
for the degree of

Doctor of Natural Sciences

put forward by

M.Sc. Dominik Mitzel

born in Baden-Baden

Oral examination: December 19th, 2018

Search for new physics in rare four-body charm decays at LHCb

Referees:
Prof. Dr. Ulrich Uwer
Prof. Dr. Klaus Reygers

For Stefanie Herr.

Abstract

This dissertation presents a search for physics beyond the Standard Model in $D^0 \to \pi^+\pi^-\mu^+\mu^-$ and $D^0 \to K^+K^-\mu^+\mu^-$ decays at the LHCb experiment. These rare four-body decays of neutral charm mesons receive contributions from electroweak flavour-changing neutral current $c \to u\ell^+\ell^-$ transitions and are unique probes for potential new heavy degrees of freedom and for additional sources of CP violation in the up-type quark sector. Using a sample of proton-proton collisions corresponding to an integrated luminosity of $2\,\text{fb}^{-1}$ recorded at a center-of-mass energy of 8 TeV in 2012, the first observation of $D^0 \to \pi^+\pi^-\mu^+\mu^-$ and $D^0 \to K^+K^-\mu^+\mu^-$ decays is reported. Furthermore, their branching fractions are measured. With an increased data set, corresponding to an integrated luminosity of $5\,\text{fb}^{-1}$ and recorded at center-of-mass energies of $7, 8$ and 13 TeV in the years 2011-2016, the first measurement of the CP asymmetry A_{CP}, the forward-backward asymmetry in the lepton system A_{FB} and the triple-product asymmetry $A_{2\phi}$ in these decays is presented. All observables are also investigated as functions of the dimuon mass. The results are consistent with Standard Model predictions.

Zusammenfassung

In dieser Dissertation wird die Suche nach Physik jenseits des Standardmodells in den Zerfällen $D^0 \to \pi^+\pi^-\mu^+\mu^-$ und $D^0 \to K^+K^-\mu^+\mu^-$ beim LHCb Experiment vorgestellt. Diese seltene Vierkörperzerfälle neutraler Charm-Mesonen sind sensitiv auf Beiträge von flavouründernden $c \to u\ell^+\ell^-$ Übergängen, die durch elektroschwache neutrale Ströme vermittelt werden. Sie stellen die einzigartige Möglichkeit dar, nach neuen schweren Freiheitsgraden und zusätzlichen Quellen der CP-Verletzung im up-type Quarksektor zu suchen. Mit Hilfe von Proton-Proton Kollisionsdaten, die einer integrierten Luminosität von $2\,\text{fb}^{-1}$ entsprechen und bei einer Schwerpunktsenergie von 8 TeV im Jahre 2012 aufgezeichnet wurden, können die seltenen Zerfällen $D^0 \to \pi^+\pi^-\mu^+\mu^-$ und $D^0 \to K^+K^-\mu^+\mu^-$ zum ersten mal nachgewiesen werden. Außerdem werden ihre Verzweigungsverhältnisse gemessen. Unter Verwendung eines erweiterten Datensatzes, der einer integrierten Luminosität von $5\,\text{fb}^{-1}$ entspricht und in den Jahren 2011-2016 bei Schwerpunktsenergien von $7, 8$ und 13 TeV aufgezeichnet wurde, wird die erste Messung der CP-Asymmetrie A_{CP}, der vorwärts-rückwärts Asymmetrie im Leptonensystem A_{FB} und der Spatproduktasymmetie $A_{2\phi}$ in diesen Zerfallskanälen vorgestellt. Alle Observablen werden auch als Funktion der invarianten Masse des Zwei-Myonsystems untersucht. Die Ergebnisse bestätigen die Vorhersagen des Standardmodells.

Preface

The measurements presented here have been published in peer-reviewed journals:

- "Observation of D^0 meson decays to $\pi^+\pi^-\mu^+\mu^-$ and $K^+K^-\mu^+\mu^-$ final states", published in Phys. Rev. Lett. 119 (2017) 181805 [1].
- "Measurement of angular and CP asymmetries in $D^0 \to \pi^+\pi^-\mu^+\mu^-$ and $D^0 \to K^+K^-\mu^+\mu^-$ decays", published in Phys. Rev. Lett. 121 (2018) 091801 [2].

The author of this thesis is the main author of the above publications and the main person responsible of the analysis work from which they originate. This work has been carried out by the author within the LHCb collaboration, which is an international association of more than 1200 scientists and engineers from 77 institutes in 17 countries. This implies the usage of common software to analyse the data collected by the LHCb experiment. Both the collection of the data and the development of common software used to analyse them result from the effort of many current and former collaboration members. The author presented the results of the above publications for the first time to a public audience at the *European Physical Society Conference on High Energy Physics 2017* in Venice and the *9th International Workshop on Charm Physics 2018* in Novosibirsk, respectively. Supplemental material has been made public in Refs. [3, 4]. A more technical and detailed description of the analyses is available internally to the LHCb collaboration in Refs. [5, 6].

Physikalisches Institut Heidelberg, October 2018

Contents

Introduction

For a long time, precision measurements of the parameters of the Standard Model (SM) of particle physics have been the primary goal of experimental high energy particle physics. The SM is the theory describing the fundamental particles and their interactions in the frame of a relativistic quantum field theory. The complete formulation of the SM has been finally confirmed only in 2012 with the observation of the Higgs boson, the quantum field responsible for electroweak symmetry breaking. Based on a very limited number of parameters that need to be determined experimentally, the SM is able to describe with great accuracy a large body of experimental high-energy-physics data. However, it is widely recognized that there are many phenomena that the SM cannot account for, pointing to the idea that a more fundamental theory must exist. Examples are the origin of the masses of the neutrinos; the existence of dark matter and dark energy, which are experimentally well motivated by astronomical observations; the necessity for additional sources of CP violation that can explain the observed matter-antimatter asymmetry of the universe. For these (and many other) reasons, instead of measuring the SM parameters with increasing precision, today, the effort is rather aimed at finding hints for its breakdown.

Situated at the *European Organization for Nuclear Research* (CERN), a circular collider called the *Large Hadron Collider* (LHC) has been in operation since 2009. Four large detectors are built around the crossing points of two oppositely circulating hadron beams, where proton-proton interactions at center-of-mass energies up to $\sqrt{s}$=13 TeV are recorded. This high collision energy allows to search for physics beyond the SM that has never been accessible in a laboratory before.

At the LHC, there are two main approaches to search for SM extensions. The first one is to search for heavy new particles in the *direct* production at the energy frontier as for example done by the ATLAS and CMS collaborations. The second approach is followed by the LHCb collaboration, whose primary goal is to study decays of heavy flavoured hadrons containing c- and b-quarks. At LHCb, physics beyond the SM is searched for indirectly via the investigation of processes involving higher order quantum loops, where heavy and yet unobserved particles

can contribute. New particles can both enhance the rate of such a process, but also change the angular distributions of the final state particles, or introduce additional sources of CP violation.

In this respect, a promising field of research is the study of rare decay processes mediated by flavour-changing neutral currents (FCNC), as they can *only* occur via electroweak quantum loop amplitudes and are therefore highly sensitive to potential contributions of unknown particles and interactions. In the past decades, most of the experimental effort has focussed on studying FCNC processes in the kaon and beauty sectors, while the investigation of charm transitions has just started.

In this thesis, the rare charm decays[2] $D^0 \to \pi^+\pi^-\mu^+\mu^-$ and $D^0 \to K^+K^-\mu^+\mu^-$, collectively referred to as $D^0 \to h^+h^-\mu^+\mu^-$ ($h = \pi, K$), are studied. These decays may proceed at *short distances* (SD) via FCNC $c \to u\ell^+\ell^-$ transitions that would account for a branching fraction of $\mathcal{O}(10^{-9})$. However, *long-distance* (LD) contributions due to tree-level decays via intermediate resonances V of the form $D^0 \to h^+h^-V(\to \mu^+\mu^-)$ are also possible and increase the branching fraction to $\mathcal{O}(10^{-6})$. These decays have been below the experimental sensitivity for many years and are accessible only today at LHCb, where, thanks to the huge $c\bar{c}$ production cross-section available, $\mathcal{O}(10^{12})$ neutral charm mesons have been produced during the years 2011-2016.

Experimentally, access to the SD physics can be gained by measuring the branching fraction in regions of dimuon mass where the influence of the resonances is minimal. This approach is, however, limited because the long tails of the resonances populate the whole dimuon-mass spectrum and can only lead to hints of physics beyond the SM if their contributions are large. A more promising strategy is to exploit the rich angular structure of four-body decays and to investigate kinematical correlations of the final state particles. CP asymmetries and some angular asymmetries are expected to be null in the SM, but can be as large as $\mathcal{O}(10^{-2})$ in new physics scenarios.

This thesis presents the first observation of $D^0 \to \pi^+\pi^-\mu^+\mu^-$ and $D^0 \to K^+K^-\mu^+\mu^-$ decays, the measurement of their branching fractions and a number of angular and CP asymmetries.

The structure is as follows: in chapter 1, the theoretical background is presented, focussing on the limitations of the SM, the phenomenology of rare charm decays and how these can be used to search for physics beyond the SM. The LHC accelerator and LHCb experiment, which are the experimental environment relevant for this thesis, are described in chapter 2. Then, chapter 3 briefly discusses the signal decay

[2]Charge-conjugated decays are implied unless stated otherwise.

topology and how the rare signal processes are searched for in the proton-proton collision samples collected by the LHCb detector. Signal yields are determined on a statistical basis using a maximum likelihood fit, whose details are presented in chapter 4. The first observation and measurement of the branching fraction is presented in detail in chapter 5. The description of the measurement of the CP asymmetry and angular asymmetries follows in chapter 6, before final concluding remarks are given in the end.

1 Charm physics in the Standard Model and beyond

The theoretical background of the thesis is set in this chapter. Starting from a general description of the Standard Model, its limitation and possible extensions are discussed. Special focus is given on rare charm decays and how they can be used to search for hints of physics beyond the Standard Model. This is followed by a more detailed description of the phenomenology of $D^0 \to h^+h^-\mu^+\mu^-$ decays, where all the observables that are measured in the context of this thesis are discussed.

1.1 The Standard Model of particle physics

The Standard Model (SM) of particle physics was developed over the years by many scientists around the world with its current formulation dating back to the mid-1970's [7–9]. In this section, a short summary of the SM is given. The aim is not to depict the SM in full details but to give an overview of the fundamental particles and forces that it describes. For a more detailed review see for example Ref. [10].

The SM is a renormalizable quantum field theory, combining the principles of Lorentz invariance and quantum theory. Building a field theory starts with postulating a symmetry group and the particle[1] content. The dynamics and kinematics of the theory are then derived from the *Lagrangian* which contains all possible and renormalizable terms that are invariant under transformations of the symmetry group. Interactions mediated by the exchange of gauge bosons with integer spin naturally arise as a consequence of the gauge invariance. The (unbroken) symmetry group of the SM is

$$G_{SM} = SU(2)_L \times U(1)_Y \times SU(3)_C,$$

[1] In a quantum field theory, particle *fields* are the fundamental objects, where the *particles* are created by excitations of the fields. For simplicity, in this chapter the terms are used synonymously.

Generation	fermions					
	leptons			quarks		
	flavour	el. charge	mass	flavour	el. charge	mass
1	ν_e	0	$<0.2\,\mathrm{eV}/c^2$	u	+2/3	$2.2\,\mathrm{MeV}/c^2$
	e	-1	$0.51\,\mathrm{MeV}/c^2$	d	-1/3	$4.7\,\mathrm{MeV}/c^2$
2	ν_μ	0	$<0.2\,\mathrm{eV}/c^2$	c	+2/3	$1.28\,\mathrm{GeV}/c^2$
	μ	-1	$105.66\,\mathrm{MeV}/c^2$	s	-1/3	$95\,\mathrm{MeV}/c^2$
3	ν_τ	0	$<0.2\,\mathrm{eV}/c^2$	t	+2/3	$4.2\,\mathrm{GeV}/c^2$
	τ	-1	$1776.86\,\mathrm{MeV}/c^2$	b	-1/3	$173\,\mathrm{GeV}/c^2$

Interaction	bosons			
	particle	el. charge	spin	mass
electromagnetic	photon (γ)	0	1	0
weak	W^+	1	1	$80.4\,\mathrm{GeV}/c^2$
	W^-	-1	1	$80.4\,\mathrm{GeV}/c^2$
	Z^0	0	1	$91.2\,\mathrm{GeV}/c^2$
strong	gluon (g)	0	1	0
	Higgs	0	0	$125.18\,\mathrm{GeV}/c^2$

Table 1.1: The fermionic (top) and bosonic (bottom) particle content of the spontaneously broken SM. Masses taken from [12].

where invariance under $SU(2)_L \times U(1)_Y$ is responsible for the *electroweak*, *i.e.* the combined *electromagnetic* and *weak* interactions and $SU(3)_C$ leads to the *strong interaction*. Gravity is not included in the SM. According to Noether's theorem [11], each continuous symmetry of the system leads to a conserved charge. The gauge bosons couple only to the particles that carry charge under the underlying symmetry transformation.

The particle content of the SM is summarised in Table 1.1. Note that the masses of the particles are based on experimental measurements. No fundamental reason for the observed hierarchy of masses spanning several order of magnitudes can be given within the SM. The same is true for the coupling strengths of the fundamental interactions.

The fundamental matter particles consist of 12 fermions with half-integer spin. These are further classified in quarks and leptons. The quarks are ordered in three generations, each consisting of an up-type quark (u, c, t) with fractional electric charge[2] of 2/3 and a down-type quark (d, s, b) with electric charge of $-1/3$. Also the leptons are grouped in three generations, where each generation consists of an electrically charged lepton (e^-, μ^-, τ^-) with negative unit charge and an associated uncharged neutrino (ν_e, ν_μ, ν_τ). For each particle, an antiparticle with

[2]Electric charges are in units the proton's charge $e \approx 1.6 \times 10^{-19} C$ [12].

all charges inverted exists.

The *electroweak* force is the combination of the electromagnetic and the weak forces. Their unification can only be understood in the context of spontaneous symmetry breaking [13–15], which is realised by the Higgs mechanism in the SM. An additional scalar field, the Higgs field, whose ground state does not obey the gauge symmetry of the SM, leads to a mixing of the three $SU(2)_L$ gauge bosons W^1, W^2, W^3 and the single $U(1)_Y$ gauge boson B^0 into the two electrically charged W^+ and W^-, the neutral Z^0 and the photon (γ). While the $W^\pm$ and Z^0 become massive mediators of the weak force, the photon remains the massless carrier of the electromagnetic force. The large masses [12] of the $W^\pm$ ($\sim 80\,\mathrm{GeV}/c^2$) and Z^0 ($\sim 91\,\mathrm{GeV}/c^2$) set a limit on the range of the weak interaction of $\sim 10^{-18}\,\mathrm{m}$, while there is no limit for the electromagnetic force.

Within the SM, flavour changing processes can only occur via the weak *charged current* interactions mediated by the exchange of a $W^\pm$ of the form $q \to W^+ q'$ ($q \to W^- q'$), where q and q' are up- and down-type quarks, respectively. The transition probabilities are modified by a corresponding matrix element $V_{qq'}$ ($V^*_{qq'}$) of the Cabibbo–Kobayashi–Maskawa (CKM) matrix [16,17]. The CKM matrix is a complex and unitary 3×3 matrix and has four physical degrees of freedom, which are three real angles and one phase. The SM does not provide any prediction for the magnitude of these parameters. Based on experimental measurements [12], it is convenient to write the CKM matrix in terms of the Wolfenstein parameters [18] $\lambda \approx 0.23$, $A \approx 0.83$, $\bar{\rho} \approx 0.16$ and $\bar{\eta} \approx 0.35$, reflecting its hierarchical nature [19]:

$$V_{CKM} = \begin{pmatrix} V_{ud} & V_{us} & V_{ub} \\ V_{cd} & V_{cs} & V_{cb} \\ V_{td} & V_{ts} & V_{tb} \end{pmatrix} = \begin{pmatrix} 1-\lambda^2/2 & \lambda & A\lambda^3(\rho - i\eta) \\ -\lambda & 1-\lambda^2/2 & A\lambda^2 \\ A\lambda^3(1-\rho-i\eta) & A\lambda^2 & 1 \end{pmatrix} + \mathcal{O}(\lambda^4).$$

The CKM matrix is almost diagonal and symmetric. The diagonal elements (V_{ud}, V_{cs}, V_{tb}) describe transitions within a generation and are of $\mathcal{O}(1)$, while transitions between two different generations are suppressed by powers of λ. The unitarity condition $\sum_i V_{ij} V^*_{ik} = \delta_{jk}$ imposes nine equations, six of them can be represented as triangles in the complex plane. Within the SM, the CKM matrix is the dominant source of *CP* violation (CPV)[3], where *CP* transformations are simultaneous charge conjugation (C) and parity (P) transformations. Charge conjugations change the sign of all charges of a particle, while the parity transformation is the flip of signs of all spatial coordinates of a system ($\vec{x} \to -\vec{x}$).

[3] Another possible source of CP violation may be present in the Lagrangian describing the strong interactions through the θ_{QCD} parameter [20] that is experimentally found to be negligibly small (this fact is known as the strong CP problem).

The weak interactions only act on the left handed chiral components of the fermions, while the electromagnetic interaction couples to left and right handed particles with the same strength. Left handed neutrinos only interact weakly, while right handed neutrinos do not exist in the SM. The weak interaction is the only interaction that can cause C, P, T and CP violation[4], making it a particularly attractive field to study.

The *strong force* binds the quarks into composite objects and it is the reason why no isolated "free" quarks can be observed. The interactions are mediated via the exchange of eight massless bosons, the *gluons*. Similar to photons that only couple to objects that carry electric charge, gluons only couple to objects carrying *colour charge*, which are quarks and gluons by themselves. The fact that gluons are also coloured results in gluon-gluon interactions. Because of the gluon self-interactions, the coupling strength of the strong force (α_s) increases at large distances (or equivalently at small momentum transfer) leading to the *confinement*, meaning that freely propagating quarks cannot exist. Quarks form bound states, called hadrons, which are net-colourless. A colourless state can be reached in different configurations. Either a quark-antiquark pair (meson) or a combination of three quarks (baryon). Also more complicated objects consisting of four and five quarks are possible and have been confirmed experimentally very recently [22–24]. On the other hand, at small distances (high energies), α_s is decreasing and quarks become asymptotically quasi-free at a length scale smaller than the extension of hadrons $\lesssim 1\,\text{fm}$.

The mathematical framework describing the strong force is called *quantum chromodynamics* (QCD). As long as α_s is not too large, theoretical predictions can be made with help of perturbation theory. One defines an energy scale Λ_{QCD}, above which perturbative methods can be applied, while for energies below Λ_{QCD} the coupling becomes too large and alternative, non-perturbative methods that often do not give analytical solutions, such as lattice QCD, must be used. Since the mass of the c-quark is only slightly above Λ_{QCD}, in charm physics, QCD effects lead to large uncertainties on theoretical predictions from perturbation theory. On the other hand, the c-quark is too heavy to reliably use chiral perturbation theory.

[4] T transformations reverse the time direction ($t \to -t$). While the individual symmetries C, P, T and CP may be violated, the combined CPT symmetry must be conserved in any local field theory with Lorentz invariance [21].

1.2 The need for physics beyond the Standard Model

A widely discussed open question in the SM is the *hierarchy problem*. Since, in contrast to the leptons and gauge bosons of the SM, no symmetry protects the mass of the Higgs boson, radiative corrections can lead to a very high mass. If the theory is claimed to be valid up to the Planck scale ($10^{19}\,\mathrm{GeV}/c^2$), where all the fundamental interactions (including gravity) are expected to be unified, corrections to the Higgs mass of the same order of magnitude would be expected. The experimentally observed mass of the Higgs boson of $125\,\mathrm{GeV}/c^2$ [12] can only be explained if the parameters of the SM are *fine tuned* such that these corrections are cancelled. One possibility to solve this fine tuning is to extend the SM gauge symmetry and introduce additional particles. In *supersymmetric* (SUSY) models (see for example Ref. [25]), a supersymmetric partner with opposite statistics is postulated for each SM particle, *i.e.* an additional fermion for each boson and vice versa. Alternative theories are represented by little Higgs models [26], where the Higgs particle is a pseudo-Nambu-Goldstone boson of a spontaneously broken higher global symmetry. It has also been suggested to enlarge the space-time dimensionality as done for example in Randall-Sundrum models [27, 28]. They explain the weakness of gravity by the postulation of *warped extra dimensions* and find more natural solutions to the hierarchy problem by lowering the Planck scale. If the SM is tried to be embedded into a more fundamental *grand unified theory* (GUT), often, a new particle species called *leptoquarks* [29, 30] arises. Leptoquarks carry both lepton and baryon numbers and can lead to transitions from quarks to leptons and act as a unification of the fermions. Leptoquarks have recently been of special interest, as they can explain hints for SM deviations in the flavour sector, see *e.g.* Ref. [31].

From experimental observations such as the modification of galactic rotation curves [32, 33] or weak gravitational lensing [34], the fraction of the energy density of the universe that can be described by the SM is estimated to be only 5%. The remaining 27% and 68% are made of *dark energy* and *dark matter*, respectively. Dark matter and dark energy are called *dark*, as no direct detection has been successful so far, although gravitational influences at large distances are evident. The existence of dark matter and dark energy are not described within the SM and extensions of the SM, often referred to as *new physics*, must include suitable candidates that are stable on cosmological time scales and participate in gravitational interactions to explain experimental observations. As their coupling

to the SM particles can only be very small, a popular class of dark matter candidates are *weakly interacting massive particles* (WIMPS). For example, the lightest stable particles in supersymmetric models are well motivated dark matter candidates [35].

The observation of neutrino oscillations [36, 37] unambiguously indicates that neutrinos are massive particles. While the oscillations can be described by introducing a rotation matrix called *Pontecorvo–Maki–Nakagawa–Sakata* (PMNS) matrix [38, 39] which is similar to the CKM matrix of the quark sector, the origin of the neutrino masses remains unclear. Heavy, right-handed *sterile neutrinos* that do not participate in any SM interaction have been postulated and could also be possible dark matter candidates [40].

Another striking puzzle is the observed very small density of antimatter compared to that of matter, quantified by[5] $\eta_s \sim 10^{-11}$ [41]. As already pointed out by Sakharov [42], besides the violation of baryon number and interactions out of thermal equilibrium, the emergence of the observed baryon asymmetry requires the presence of CP and C violation. However, the amount of CPV as present in the SM can only account for a tiny fraction [43–45] of the observed asymmetry and new physics must carry additional sources thereof. These could in principle be generated in the lepton sector as the PMNS matrix carries at least one additional phase with respect to the SM[6], however no experimental evidence exists to date. Most models extending the SM imply new sources of CPV, making their searches a powerful tool to look for new physics.

1.3 Direct and indirect searches for new physics

To search for physics beyond the SM, two different approaches exist. In *direct searches*, the interaction of new particles such as dark matter candidates with ordinary baryonic matter or their direct production at the energy frontier of particle colliders are searched for. For example, large volume detectors such as XENON1T [46, 47] are build far below the surface and try to detect the very rare interaction of dark matter candidates with the nuclei of a target material such as liquid xenon. At the Large Hadron Collider [48], ATLAS [49] and CMS [50] are looking for signatures of the production of heavy stable new particles in high energetic proton-proton collisions. The approch of direct searches at colliders has been successful in the past and has lead to the observation of the Higgs boson

[5] Defined as $\eta_s = \frac{n_B - n_{\bar{B}}}{s}$, $n_B(n_{\bar{B}})$ being the densitiy of baryons (antibaryons) and s the entropy of the universe.

[6] Another two additional phases are possible if neutrinos are Majorana particles.

in 2012 [51, 52]. However, the sensitivity of this method is strictly limited by the available center-of-mass energy in the collisions.

A complementary approach which is followed by the LHCb collaboration is to perform *indirect searches*, which are based on precision tests of processes involving quantum loops. According to Heisenberg's uncertainty principle, in quantum loops, heavy and potentially yet unobserved particles can participate in the quantum mechanical process even if the energy is not sufficient for a direct production. This can either lead to processes which are forbidden in the SM or to the modifications of existing SM processes via the interference with SM contributions.

An example for higher order transitions in the SM are decays involving *flavour-changing neutral currents* (FCNC). In contrast to charged currents, weak *neutral currents* of the form $q \to Z^0 q$ ($q^{'} \to Z^0 q^{'}$), mediated by the exchange of a neutral Z^0, can only lead to interactions of a quark or lepton pair of the the same generation. No CKM factors enter and FCNC transitions between two generations cannot happen at lowest order. Example of FCNC transitions at loop level are processes of the form $b \to s\ell^+\ell^-$, $b \to d\ell^+\ell^-$ in B-decays, $s \to d\ell^+\ell^-$ in the kaon sector and $c \to u\ell^+\ell^-$ in the charm system, where $\ell^+\ell^-$ is a pair of oppositely charged leptons. Loop processes with at least two flavour changing weak interaction vertices can lead to effective FCNC processes as schematically shown in Figure 1.1 (left), where a $c \to W^+ d$ transition is followed by the reabsorption of the W^+ of the form $d W^+ \to u$. The lepton pair arising from a radiated Z^0/γ ensures energy and momentum conservation. Higher order interactions of this kind are often referred to as *penguin* contributions. Also possible are similar so-called *box diagrams* (right in Figure 1.1).

Assigning a *flavour* quantum number F to mesons containing a heavy quark, FCNC can lead to processes changing the flavour quantum number of one or two units ($\Delta F = 1$ and $\Delta F = 2$). $\Delta F = 1$ FCNCs describe *rare decays* such as $D^0 \to \mu^+\mu^-$, $B_s^0 \to \mu^+\mu^-$ or $K^0 \to \mu^+\mu^-$, which are heavily suppressed in the SM. The experimental observation of the low branching fraction of $K^0 \to \mu^+\mu^-$ decays is a famous example of how indirect searches can lead to the prediction of new physics, as its suppression [53, 54] led to the prediction of a new quark (the charm quark) in 1970 [55] *before* its experimental confirmation in 1974 [56, 57].

Instead, $\Delta F = 2$ processes such as meson anti-meson transitions $D^0 \to \overline{D}^0$, $B^0 \to \overline{B}^0$, $B_s^0 \to \overline{B}_s^0$ or $K^0 \to \overline{K}^0$, may lead to periodical oscillations between a neutral meson P^0 and its antiparticle $\overline{P}$ and vice versa, caused by flavour *mixing*. The time evolution of the system can be described by the following effective

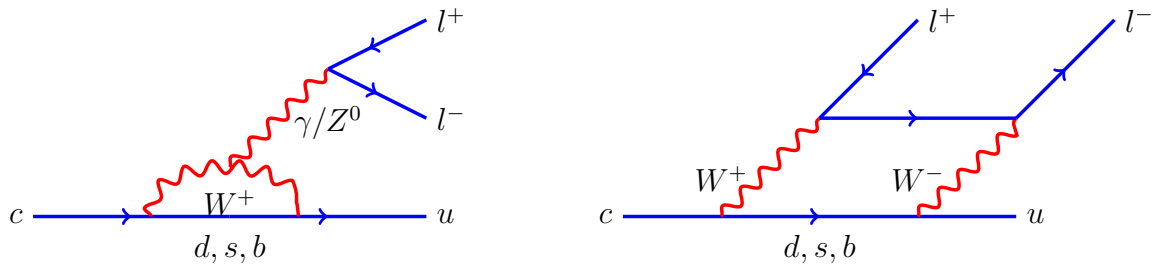

Figure 1.1: Example for generic FCNC $c \to u\ell^+\ell^-$ transitions, electroweak penguin (left) and box-digagram (right).

Schrödinger equation [58]:

$$i\frac{\partial}{\partial t}\begin{pmatrix}|P^0(t)\rangle\\|\overline{P}^0(t)\rangle\end{pmatrix} = \left[\mathbf{M} - \frac{i}{2}\mathbf{\Gamma}\right]\begin{pmatrix}|P^0(t)\rangle\\|\overline{P}^0(t)\rangle\end{pmatrix},$$

where $\mathbf{M}$ and $\mathbf{\Gamma}$ are 2×2 Hermitian matrices. The diagonal elements of $\mathbf{M}$ and $\mathbf{\Gamma}$ correspond to flavour conserving transitions, while the off-diagonal elements are responsible for the mixing of the flavour states. The physical eigenstates of the system are then two states $P_{1,2}$ which are superpositions of the flavour states with the complex coefficients p and q, satisfying $|p^2| + |q^2| = 1$:

$$|P_{1,2}\rangle = p|P^0\rangle \pm q|\overline{P}^0\rangle.$$

The two eigenstates of the system $|P_{1,2}\rangle$ may have distinct decay widths and masses $\Gamma_{1,2}$ and $m_{1,2}$, respectively. For convenience, one defines the two dimensionless parameters x and y as:

$$x = \frac{m_1 - m_2}{\Gamma}, \qquad y = \frac{\Gamma_1 - \Gamma_2}{2\Gamma},$$

with the average decay width $\Gamma = (\Gamma_1 + \Gamma_2)/2$, such that the probabilities for initially produced pure flavour state to oscillate or not as a function of time is given by:

$$\begin{aligned}\left|\langle P^0(t)|P^0(0)\rangle\right|^2 = \left|\langle \overline{P}^0(t)|\overline{P}^0(0)\rangle\right|^2 &\propto e^{-\Gamma t}[\cosh(y\Gamma t) + \cos(x\Gamma t)],\\ \left|\langle \overline{P}^0(t)|P^0(0)\rangle\right|^2 &\propto \left|\frac{q}{p}\right|^2 e^{-\Gamma t}[\cosh(y\Gamma t) - \cos(x\Gamma t)],\\ \left|\langle P^0(t)|\overline{P}^0(0)\rangle\right|^2 &\propto \left|\frac{p}{q}\right|^2 e^{-\Gamma t}[\cosh(y\Gamma t) - \cos(x\Gamma t)]. \quad (1.1)\end{aligned}$$

Mixing occurs if either x or y are non-zero. Periodical transitions of the two

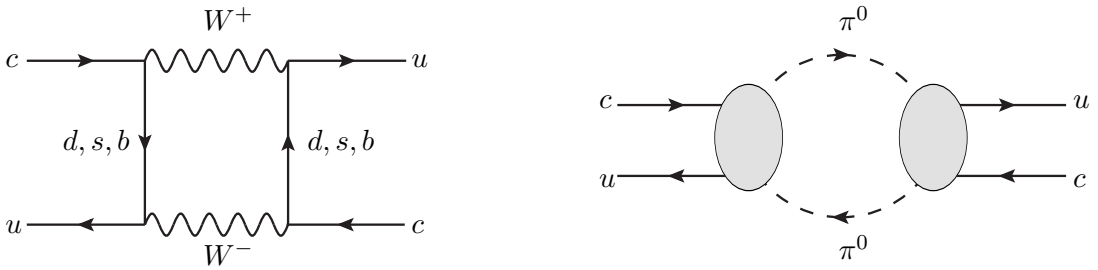

Figure 1.2: Possible contributions to charm mixing. Short-distance box diagram (left) and schematic view of a long-distance contribution via an intermediate two pion state (right) [59].

flavour states are driven by an oscillation term with frequency x, while y appears as argument of a hyperbolic cosine term modifying the exponential decay law. While in the neutral beauty systems oscillations are mainly driven by FCNC transitions at short distances (left in Figure 1.2), these are heavily suppressed in charm and so called long-distance contributions in form of rescattering of intermediate meson states (such as a pair of pions shown in Figure 1.2) become dominant. The dominance of non-perturbative processes make theoretical predictions of the mixing parameters challenging, which can span over several orders of magnitudes [60–64]. For neutral kaons, $|x|$ and $|y|$ are both $\mathcal{O}(1)$ and experimental confirmation of koan mixing was already found in 1956 [65]. Mixing in the B^0-system, where $|x| \sim \mathcal{O}(1)$ and $|y| \sim \mathcal{O}(10^{-3})$ was observed in 1987 [66]. The very fast oscillations as measured in 2006 [67] for neutral B_s^0 ($|x| \sim 20$, $|y| \sim \mathcal{O}(10^{-2})$) required the development of detectors with very good decay time resolutions. In charm, both x and y are very small. The current world averages are $x = (0.35^{+0.21}_{-0.16})\%$ and $y = (0.67^{+0.06}_{-0.13})\%$ [68]. The smallness of the mixing parameters complicates experimental investigations as huge data samples are needed. Charm mixing has only been observed in 2012 from a single experiment [69].

Studying processes involving quantum loops is also a way to measure CPV, as it is a quantum mechanical effect that needs at least two interfering amplitudes to produce a measurable asymmetry. This can be shown by comparing the decay amplitude of a meson P to final state f defined as $\mathcal{A}_f = \langle f|H|P\rangle$ with its CP conjugated process $\bar{\mathcal{A}}_{\bar{f}} = \langle \bar{f}|H|\bar{P}\rangle$. In the presence of CP-odd phases that change sign under CP transformations, the phases of the amplitudes $\mathcal{A}_f$ and $\bar{\mathcal{A}}_{\bar{f}}$ are rotated by 180°. The CP-odd phases are usually referred to as weak phases, because, as already explained, in the SM they only appear in weak transitions. As all measurable quantities are proportional to the amplitude squared, such a phase shift does not play any role as long as only a single amplitude contributes, since $|\mathcal{A}_f|^2 = |\bar{\mathcal{A}}_{\bar{f}}|^2$. In addition to CP-odd phases, CP-even phases that do not change sign under CP transformations can occur from final state interactions or

hadronisation of the quarks to hadrons, which are processes of the *CP* conserving strong interaction (and therefore called *strong phases*). If at least two processes interfere, the total amplitude must be written as their coherent sum:

$$\mathcal{A}_f = |A_1|e^{i(\delta_1+\phi_1)} + |A_2|e^{i(\delta_2+\phi_2)}, \quad \bar{\mathcal{A}}_{\bar{f}} = |A_1|e^{i(\delta_1-\phi_1)} + |A_2|e^{i(\delta_2-\phi_2)},$$

with weak and strong phases ϕ_1, ϕ_2 and δ_1, δ_2, respectively. Then it follows for the asymmetry a_{CP}^{dir} [70]:

$$a_{CP}^{dir} = \frac{|A_f|^2 - |\bar{\mathcal{A}}_{\bar{f}}|^2}{|A_f|^2 + |\bar{\mathcal{A}}_{\bar{f}}|^2} \propto r_f \sin(\delta_1 - \delta_2) \sin(\phi_1 - \phi_2),$$

where r_f is the ratio of the magnitude of the involved amplitudes $|A_2|$ and $|A_1|$. Thus, a_{CP} can only be non-zero if at least two amplitudes with different weak *and* strong phases contribute. This kind of CPV is referred to as CPV in the decay, accessible to both neutral and charged mesons.

Also neutral meson mixing can lead to CPV if the probabilities $P^0 \to \overline{P}^0$ and $\overline{P}^0 \to P^0$ are not equal, equivalent to $|q/p| \neq 1$ as can be seen from Equation 1.1. This type of CPV is called CPV *in mixing*, only relevant for decays of neutral mesons and independent of the final state.

If the $P^0(\overline{P}^0)$ decays into a state f which is accessible to both flavour states, a third type of CPV is possible, arising from the interference of mixing followed by the decay and the direct decay. A non trivial phase between the decay amplitude and mixing might occur. If one defines:

$$\lambda_f = \frac{q}{p}\frac{\bar{\mathcal{A}}_f}{\mathcal{A}_f}$$

CPV in the *interference of mixing and decay* happens if $\mathrm{Im}(\lambda_f) \neq 0$. CPV effects caused by mixing and the interference of mixing and decays are also collectively referred to as *indirect* CPV.

The first observation of (indirect) *CP* violation was found in kaon decays already in 1964 [71]. In 1999, the first observation of direct CPV in kaon decays was reported, followed by observations of indirect CPV in neutral B^0 decays [72, 73] in 2001. More recently, also direct CPV in neutral B^0 [74, 75](2004), charged B^+ [76–78] (2010) as well as in B_s^0-system [79] (2013) have been measured. In charm, no significant sign of CPV has been found so far.

1.4 Rare charm decays in the Standard Model and beyond

Among the flavoured hadron systems, the role of charm is special, as it is the only bound system to test dynamics of the up-type quarks. A simple estimation of the rate for FCNC $c \to u$ transitions can be done with help of Figure 1.1. The total amplitude is the coherent sum of all possible contributions, *i.e.* processes where down-type quarks are exchanged in the loop. Exploiting the unitarity condition, this reads as [80]:

$$\begin{aligned}\mathcal{A}(c \to u) &= V_{cd}^* V_{ud} f(m_d^2/m_w^2) + V_{cs}^* V_{us} f(m_s^2/m_w^2) + V_{cb}^* V_{ub} f(m_b^2/m_w^2) \quad (1.2)\\ &= V_{cs}^* V_{us}[f(m_s^2/m_w^2) - f(m_d^2/m_w^2)]\\ &+ V_{cb}^* V_{ub}[f(m_b^2/m_w^2) - f(m_d^2/m_w^2)],\end{aligned}$$

where $f(m_q^2/m_w^2)$ are kinematical functions of the $W^\pm$ boson and quark masses of the form $f(m_q^2/m_w^2) \sim 1/(16\pi^2) \cdot m_q^2/m_w^2$. The term in the second line of Equation 1.2 of is small due to the similar masses of the light d- and s-quarks, historically known as the Glashow–Iliopoulos–Maiani (GIM) mechanism [55]. The term in the third line is suppressed by the small CKM factor $V_{cb}V_{ub}^* \sim \lambda^5$. Even though the total amplitude is enhanced by QCD effects [80], processes involving $c \to u$ transitions are expectionally rare. The SM branching fraction for inclusive $\mathcal{B}(D^0 \to X_u \ell^+ \ell^-)$ decays, where X_u is any final state containing a u-quark, is estimated to be $\lesssim \mathcal{O}(10^{-9})$ [81]. This is approximately three orders of magnitudes lower than comparable processes in the $b-$quark system involving $b \to s\ell^+\ell^-$ transitions, where the contribution of the heavy t-quark dominates the intermediate loop. Rare charm decays are therefore by far more suppressed than similar processes in beauty (or kaon) decays.

To create CPV, at least three generations need to be involved [82]. The charm system is almost decoupled from the third generation [58], such that processes involving weak phases are suppressed by $r \propto |V_{cb}V_{ub}^*|/|V_{cd}V_{ud}^*| \sim \lambda^4 \sim 0.002$ with respect to CKM favoured first order transitions. Naive estimations should not allow for CPV effects larger than this, even if the involved phases would be sizeable.

To compare measurements with theoretical predictions, usually a model independent *effective field theory* [83] is defined based on the *operator product expansion* (OPE). In this approach, an effective Lagrangian is constructed as sum over all possible operators $\mathcal{O}_i$ that may contribute to the decay and their coupling

strengths C_i (called *Wilson coefficients* [84]):

$$\mathcal{L}_{eff} \sim \sum_i C_i \cdot \mathcal{O}_i.$$

The theory is constructed at a given high energy scale $\tilde{\mu}$, such that all heavy degrees of freedom ($m > \tilde{\mu}$) are integrated out and absorbed in the Wilson coefficients while only light ($m < \tilde{\mu}$) quark fields contribute to the operators and are considered as massless. SM values for the Wilson coefficients are obtained by comparing the effective theory and the SM at a mass scale where both theories are valid (usually the mass of the $W^{\pm}$ boson), and the renormalization group equation (RGE) [85] is used to evaluate the Wilson coefficients at the relevant energy scale (m_c for charm physics). The full set of SM operators up to dimension six describing $\Delta C = 1$ charm decays are the following [86–90]:

$$\begin{aligned}
\mathcal{O}_1^{(q)} &\sim (\bar{u}_L \gamma_\mu T^a q_L)(\bar{q}_L \gamma^\mu T^a c_L)\,, \\
\mathcal{O}_2^{(q)} &\sim (\bar{u}_L \gamma_\mu q_L)(\bar{q}_L \gamma^\mu c_L)\,, \\
\mathcal{O}_3 &\sim (\bar{u}_L \gamma_\mu c_L) \sum_{\{q:m_q<\tilde{\mu}\}} (\bar{q}\gamma^\mu q)\,, \\
\mathcal{O}_4 &\sim (\bar{u}_L \gamma_\mu T^a c_L) \sum_{\{q:m_q<\tilde{\mu}\}} (\bar{q}\gamma^\mu T^a q)\,, \\
\mathcal{O}_5 &\sim (\bar{u}_L \gamma_\mu \gamma_\nu \gamma_\alpha c_L) \sum_{\{q:m_q<\tilde{\mu}\}} (\bar{q}\gamma^\mu \gamma^\nu \gamma^\alpha q)\,, \\
\mathcal{O}_6 &\sim (\bar{u}_L \gamma_\mu \gamma_\nu \gamma_\alpha T^a c_L) \sum_{\{q:m_q<\tilde{\mu}\}} (\bar{q}\gamma^\mu \gamma^\nu \gamma^\alpha T^a q)\,, \\
\mathcal{O}_7 &\sim m_c (\bar{u}_L \sigma^{\mu\nu} c_R) F_{\mu\nu}\,, \\
\mathcal{O}_8 &\sim m_c\, (\bar{u}_L \sigma^{\mu\nu} T^a c_R)\, G^a_{\mu\nu}\,, \\
\mathcal{O}_9 &\sim (\bar{u}_L \gamma_\mu c_L)(\bar{\ell}\gamma^\mu \ell)\,, \\
\mathcal{O}_{10} &\sim (\bar{u}_L \gamma_\mu c_L)(\bar{\ell}\gamma^\mu \gamma_5 \ell)
\end{aligned}$$

where $q = d, s, b$ and γ^μ are the Dirac matrices. Furthermore, $q_{L,R} = P_{L,R}\, q$ with the chirality operator $P_{L,R} = 1/2(1 \mp \gamma^5)$, $F_{\mu\nu}$ is the electromagnetic field strength tensor and T^a are the Gell-Mann matrices. The current-current operators $\mathcal{O}_1$ and $\mathcal{O}_2$ are dominant in charm decays and the only non-vanishing operators at the scale m_W, since the unitarity of the CKM matrix leads to an exact cancellation of loop processes as long as the light fields are massless. Especially the non-existence of the semileptonic operator $\mathcal{O}_{10}$ (axial vector couplings) has crucial impact on the phenomenology of charm decays and is unique among heavy quark systems.

At the beauty scale, the heavy b-quark is integrated out and the operator $\mathcal{O}_9$ (vector couplings) receives contributions from $\mathcal{O}_1$ and $\mathcal{O}_2$, as they can also lead to $c \to u\ell^+\ell^-$ final states if the light quarks are contracted to a loop and couple via a virtual photon to a dilepton pair, while no mixing into $\mathcal{O}_{10}$ occurs and axial vector couplings remain suppressed at all scales.

The effective weak Langrangian at the charm scale reads as:

$$\mathcal{L}_{eff}^{weak} \sim \sum_{q \in d,s} V_{cq}^* V_{uq} \left(C_1(m_c)\mathcal{O}_1^{(q)} + C_2(m_c)\mathcal{O}_2^{(q)} + \sum_{i=3}^{10} C_i(m_c)\mathcal{O}_i \right).$$

The QCD penguin operators $\mathcal{O}_3 - \mathcal{O}_6$ are also heavily suppressed and do not play any significant role.

Contributions from new physics can modify loop induced processes by significantly enhancing the couplings of semiliptonic operators $\mathcal{O}_9$ and $\mathcal{O}_{10}$ or even contribute to scalar or tensor operators which are not existing in the SM. All new physics models mentioned in section 1.2 (SUSY [91–95], leptoquarks [96–99], little Higgs [100–103], Randall-Sundrum [104, 105]) may modify $c \to u\ell^+\ell^-$ processes by loop contributions or even lead to first order $c \to u\ell^+\ell^-$ transitions. Also implications of models with generic Z' [95, 99], two Higgs doublet [106, 107] and an additional up-vector like quark singlet [94, 102] are discussed in literature. Experimentally, this can lead to enhanced rates, modified angular distributions and additional sources of CPV. Although similar arguments hold for dielectron and dimuon modes, the following discussion will be focused on the muonic decays as most experimental effort has been put into their investigation so far.

Theoretically and experimentally, the cleanest rare charm decay is the two-body decay $D^0 \to \mu^+\mu^-$ with a purely leptonic final state, as theoretical hadronic uncertainties are minimal and the experimental detection is rather simple. However, due to the additional helicity suppression, the SM branching fraction of this decay is expected to be $\mathcal{O}(10^{-13})$ [91,92,96,97,108,109], but in some new physics scenario can reach today's experimental limit of $6.2 \cdot 10^{-9}$ at a 90% confidence level [110].

In rare multibody decays of the form $D^{+(0)} \to h^+(h^-)\mu^+\mu^-$ ($h = K, \pi$), the helicity suppression is weakend, but non-perturbative hadronic contributions become dominant due to intermediate resonant states of the form $D^{0,+} \to h^+(h^-)V(\to \mu^+\mu^-)$. These *long-distance* (LD) processes can enhance the total branching fraction up to $\mathcal{O}(10^{-6})$ [95,96,111]. Sensitivity to the *short-distance* (SD) FCNC processes can be gained by investigating the branching fractions as a function of dimuon mass, since the FCNC processes lead to a non-resonant production of the dimuon system, while the dimuon-mass dependence of the resonances can be approximated by Breit-Wigner distributions, characterised by

model	A_{CP}	A_{FB}
Leptoquark models	$\gtrsim A_{CP}^{\text{SM}}$	$\lesssim 8 \cdot 10^{-1}$
Little Higgs model	$\lesssim \mathcal{O}(10^{-3})$	$\lesssim \mathcal{O}(5 \cdot 10^{-3})$
Minimal SUSY SM	$\lesssim \mathcal{O}(10^{-3})$	$\lesssim \mathcal{O}(10^{-1})$
Up vector-like quark singlet	–	$\lesssim 10^{-3}$
Warped extra dimensions	$\lesssim \mathcal{O}(10^{-2})$	$\lesssim \mathcal{O}(5 \cdot 10^{-2})$
SM	$< \mathcal{O}(10^{-3})$	~ 0

Table 1.2: CP asymmetry A_{CP} and forward-backward asymmetry A_{FB} within new physics models. The table is modified from [113] and is a summary of the results presented in [91–93, 95–102, 104, 105, 107, 109, 111, 114].

its width and mass. Often, new physics models predict enhancements of the SD physics, but in general their contributions should not be larger than $\lesssim \mathcal{O}(10^{-8})$. As the long tails of the resonances populate the entire dimuon-mass spectra, only large beyond SM effects can be seen in extreme regions of dimuon mass and the prospects to discover new physics effects in measuring the branching fraction are somewhat limited. In this respect, three-body decays are favoured due to their larger decay phase space compared to four-body decays.

In addition to the branching fraction, multibody decays allow the study of the dimuon-mass spectrum and angular distributions, such that additional experimental observables can be constructed where the influence of hadronic uncertainties is small and sensitivity to the SD physics is gained. Theoretically and experimentally clean observables are asymmetries, as they are defined as differences and ratios and many uncertainties cancel. As weak phases and axial vector currents are practically absent, observables sensitive to their presence such as the forward-backward (FB) asymmetry in the dimuon system and CP asymmetries are SM null test. As summarised in Table 1.2, contributions from physics beyond the SM can enhance the FB and CP asymmetry up to the percent level in rare charm mulitbody decays. As the asymmetries are driven by the interference of SM and beyond SM dynamics, they are enhanced in the vicinity of resonances. This effect is known as *resonances catalysed asymmetries* [96, 112] in literature. As an example, Figure 1.3 shows the possible CP violating effects in $D^+ \to \pi^+\mu^+\mu^-$ decays around the ϕ resonance in dimuon mass in a model with scalar leptoquarks. Different relative strong phase differences of the resonances and new physics contributions are assumed, which might lead to symmetric or antisymmetric asymmetries with respect to the resonance peak.

Experimentally, the LHCb collaboration has set an upper limit of $7.3(41.0) \cdot 10^{-8}$ at 90% confidence level. [115] on the branching fraction of non-resonant

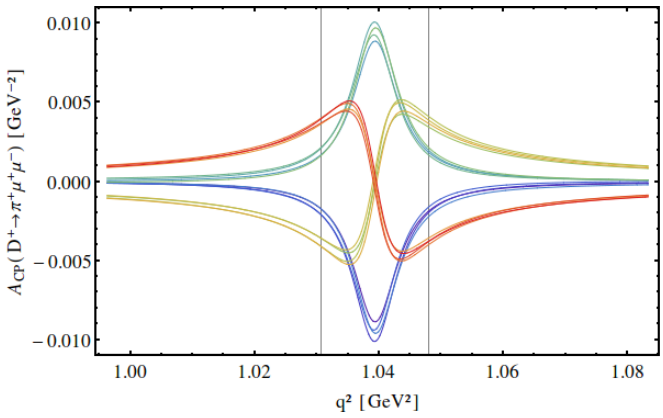

Figure 1.3: Direct CP asymmetry in a scalar leptoquark model in the ϕ region of dimuon mass, shown exemplarily for $D^+ \to \pi^+\mu^+\mu^-$ decays [96]. Different strong phase differences of the involved contributions ($\delta_\phi = 0[\text{yellow}], \pi/2[\text{green}], \pi[\text{blue}], 3/2\pi[\text{red}]$) are assumed.

$D^+(D_s^+) \to \pi^+\mu^+\mu^-$ decays in dimuon-mass regions where the influence of the resonances is minimal. No measurement of angular asymmetries exists. Four-body decays of the form $D^0 \to h^+h^-\mu^+\mu^-$ have received the least experimental attention due to their further suppression. In 2001, the E791 collaboration [116] has set upper limits on the branching fractions of $D^0 \to h^+h^{(\prime)-}\mu^+\mu^-$ decays in the order of $\mathcal{O}(10^{-5})$ [117]. A single search for $D^0 \to \pi^+\pi^-\mu^+\mu^-$ exists at LHCb, which sets an upper limit on the branching fraction in the non-resonant region (extrapolated to the full dimuon-mass region) of $5.5 \cdot 10^{-8}$ at 90% confidence level [118]. With the first observation and measurement of the branching fraction of Cabbibo-favoured $D^0 \to K^-\pi^+[\mu^+\mu^-]_{\rho^0/\omega}$ decays, where the muons are consistent with coming from an intermediate ρ^0/ω resonance made by LHCb [119] in 2015, consistent with theoretical predictions [95], the possibility to measure a significant signal in $D^0 \to h^+h^-\mu^+\mu^-$ decays for the first time has opened at LHCb. In the system of b-flavoured hadrons, corresponding decays involving $b \to s\ell^+\ell^-$ transitions have triggered many theoretical discussions, as consistent hints of physics beyond the SM emerge, see for example Ref. [31] for a detailed discussion.

1.5 Rare $D^0 \to h^+h^-\mu^+\mu^-$ decays

This thesis focusses on the study of rare charm four-body decays of the form $D^0 \to h^+h^-\mu^+\mu^-$. With respect to three body decays, a variety of further angular observables is accessible. However, the decay phase space is more complicated and the resonant structure is more challenging as also the dihadron pair may arise from intermediate resonances. The total branching fraction of these decays has

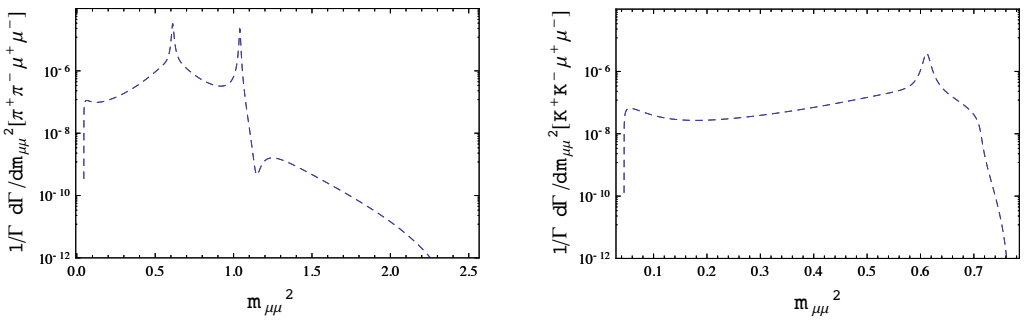

Figure 1.4: Standard Model predictions for the differential branching fractions as a function of the dimuon mass for $D^0 \to \pi^+\pi^-\mu^+\mu^-$ (left) and $D^0 \to K^+K^-\mu^+\mu^-$ (right) (modified from [95]). The long tails over the intermediate resonances populate the entire dimuon-mass range.

been estimated [95] to be

$$\mathcal{B}(D^0 \to \pi^+\pi^-\mu^+\mu^-)^{theo} \sim 1.3 \cdot 10^{-6},$$
$$\mathcal{B}(D^0 \to K^+K^-\mu^+\mu^-)^{theo} \sim 1.1 \cdot 10^{-7}$$

and therefore below the sensitivity of any previous experiment. The two pions in $D^0 \to \pi^+\pi^-\mu^+\mu^-$ are expected to come mainly from intermediate ρ^0 and ω mesons, where the contribution of the ρ^0 is dominant due to the small coupling of the ω to pions. In dimuon mass, the decays are dominated by intermediate vector particles ρ^0, ω and ϕ. Contributions from pseudo scalar $\eta^{(\prime)}$ resonances are sub leading [120]. The expected differential branching fraction as a function of the squared dimuon mass $m^2(\mu^+\mu^-)$ is shown in Figure 1.4 (left). The non-resonant contribution is estimated to be $10^{-10} - 10^{-9}$ [95, 120]. Mainly at low dimuon masses, the branching fraction is slightly enhanced by contributions from bremsstrahlung ($\sim 5.6 \cdot 10^{-9}$ [95]), where a photon is radiated from the weak interaction vertex which converts into a dimuon pair. A region in dimuon mass with minimal influence of the resonances is identified above the ϕ resonance.

The decay phase space of $D^0 \to K^+K^-\mu^+\mu^-$ decays is substantially smaller. These decays mainly proceed via an intermediate ϕ meson which subsequently decays into two kaons. In the dimuon-mass spectrum, contributions from intermediate ρ^0 and ω resonances are dominant. No higher dimuon-mass resonances are kinematically allowed. The contribution of bremsstrahlung is $\sim 5.6 \cdot 10^{-9}$, while the non-resonant contribution is estimated to be as low as $\mathcal{O}(10^{-10})$ [95, 120]. In Figure 1.4 (right), the projection of the differential branching fraction in dimuon mass is shown. Two example Feynman graphs of LD contributions (via an intermediate neutral vector meson) and SD (via an electromagnetic penguin) to the

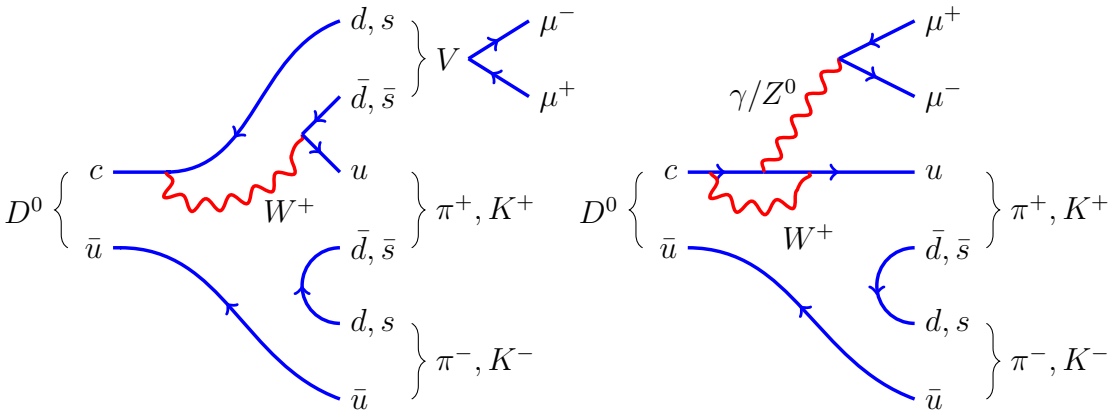

Figure 1.5: A long-distance contribution via the decay of an intermediate light meson (such as ω, ρ^0, ϕ) (left) and a higher order electroweak penguin as example for a short-distance contribution to $D^0 \to h^+h^-\mu^+\mu^-$ decays (right) (modified from [1]).

decay processes are shown in Figure 1.5.

To fully describe a four-body decay, five independent variables are needed. Following Ref. [95,120], the three angles $\cos\theta_\mu$, $\cos\theta_h$, ϕ and two invariant masses of the dimuon and dihadron systems, $m^2(\mu^+\mu^-)$ and $m^2(h^+h^-)$, are used to parametrise the decay topology. The angle ϕ is the angle between the two decay planes of the dimuon and dihadron system (see Figure 1.6), while $\cos\theta_\mu(\cos\theta_h)$ is the cosine of the angle between the momentum of the positive muon (hadron) in the rest frame of the dimuon (dihadron) system with respect to the dimuon (dihadron) flight direction as seen from the rest frame of the D^0. For $\overline{D}^0$, the angles are defined with respect to the negative muon and hadron[7]. The total decay rate can then be expressed as follows and factorises in angular terms c_{1-9} depending on kinematical variables ($\cos\theta_\mu$, ϕ) and the angular coefficients I_{1-9} depending on the dynamical variables ($m^2(\mu^+\mu^-), m^2(h^+h^-), \cos\theta_h$) [120]:

$$\begin{aligned} d^5\Gamma =& \frac{1}{2\pi}\left[\sum c_i(\theta_\mu,\phi) I_i(m^2(\mu^+\mu^-), m^2(h^+h^-), \cos\theta_h)\right] \\ & \cdot dm^2(\mu^+\mu^-) dm^2(h^+h^-) d\cos\theta_h d\cos\theta_\mu d\phi\,, \end{aligned}$$

with:

$$\begin{aligned} & c_1 = 1\,,\ c_2 = \cos 2\theta_\mu\,,\ c_3 = \sin^2\theta_\mu \cos 2\phi\,,\ c_4 = \sin 2\theta_\mu \cos\phi\,,\ c_5 = \sin\theta_\mu \cos\phi\,, \\ & c_6 = \cos\theta_\mu\,,\ c_7 = \sin\theta_\mu \sin\phi\,,\ c_8 = \sin 2\theta_\mu \sin\phi\,,\ c_9 = \sin^2\theta_\mu \sin 2\phi\,. \end{aligned}$$

[7] In particular, this means that the sign of $\cos\theta_\mu$ and $\cos\theta_h$ swaps when transforming from a D^0 to $\overline{D}^0$ meson (and vice versa).

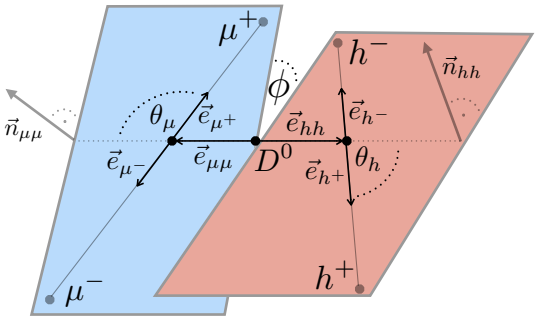

Figure 1.6: The vector $\vec{e}_{ii}$ $(i = \mu, h)$ is the unit vector along the momentum of the dihadron or the dimuon system in the rest frame of the D^0 meson. The vector $\vec{n}_{ii} = \vec{e}_{ii} \times \vec{e}_{i^-}$ is defined as the unit vector perpendicular to the decay plane spanned by the two hadrons (or the two muons). Accordingly, $\vec{e}_{i^-}$ is the unit vector along the momentum of the negatively charged hadron (muon) in the dihadron (dimuon) rest frame. With these vectors one defines $\cos\theta_i = \vec{e}_{ii} \cdot \vec{e}_{i^+}$ and $\sin 2\phi = 2(\vec{n}_{hh} \cdot \vec{n}_{\mu\mu})(\vec{n}_{hh} \times \vec{n}_{\mu\mu}) \cdot \vec{e}_{hh}$ [2].

Although being most desirable, a full angular analysis requires a large signal statistics and is therefore beyond the scope of this thesis. However, individual angular coefficients can already be determined with a limited amount of signal decays, integrating over the other four dimensions. The coefficient I_6 requires contributions of axial vectors, scalar or tensor couplings to be non-zero, while I_9 needs the presence of weak phases. They can therefore be used to construct SM null tests by defining the forward-backward (A_{FB}) and triple product asymmetry ($A_{2\phi}$) as follows:

$$\begin{aligned} A_{FB} &= \frac{1}{\Gamma}\left[\int_0^1 \frac{d\Gamma}{d\cos\theta_\mu} d\cos\theta_\mu - \int_{-1}^0 \frac{d\Gamma}{d\cos\theta_\mu} d\cos\theta_\mu\right] \\ &= \frac{\Gamma(\cos\theta_\mu > 0) - \Gamma(\cos\theta_\mu < 0)}{\Gamma(\cos\theta_\mu > 0) + \Gamma(\cos\theta_\mu < 0)}, \\ A_{2\phi} &= \frac{1}{\Gamma}\left[\int_0^{\pi/2} \frac{d\Gamma}{d\phi} d\phi + \int_\pi^{3/2\pi} \frac{d\Gamma}{d\phi} d\phi - \int_{\pi/2}^{\pi} \frac{d\Gamma}{d\phi} d\phi - \int_{3/2\pi}^{2\pi} \frac{d\Gamma}{d\phi} d\phi\right] \\ &= \frac{\Gamma(\sin 2\phi > 0) - \Gamma(\sin 2\phi < 0)}{\Gamma(\sin 2\phi > 0) + \Gamma(\sin 2\phi < 0)}. \end{aligned}$$

To illustrate the effect of beyond SM physics, Figure 1.7 shows A_{FB} in new physics scenarios assuming generic (and experimentally not yet excluded) additional real and imaginary contributions to the Wilson coefficients ($C_9^{(\prime)} = C_{10}^{(\prime)} = 0.5, 0.5i$)[8]. See also Table 1.2 which refers to specific new physics models. As already seen,

[8]The primed Wilson operators are obtained by inverting the chirality of the operators.

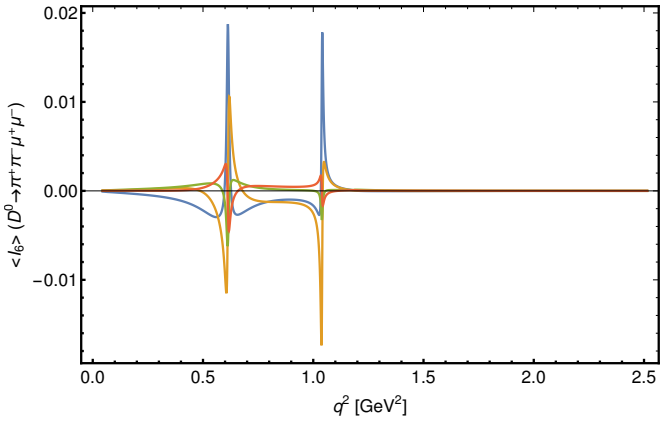

Figure 1.7: The angular observable $\langle I_6 \rangle = A_{FB}/2$ for $D^0 \to \pi^+\pi^-\mu^+\mu^-$ decays as a function q^2 which is the dimuon mass squared. Several generic new physics contributions ($C_9 = -C_{10} = 0.5$[blue], $0.5i$[yellow] and $C_9' = -C_{10}' = 0.5$[green], $0.5i$[red]), which have not yet been excluded experimentally are shown. A relative strong phase between the ρ^0 and ω of $\delta_{\rho^0} - \delta_\omega = \pi$ is assumed [120].

especially in the proximity of resonances, values for A_{FB} of the percent level are possible and not yet excluded by experimental constraints.

$A_{2\phi}$ can also be understood as triple-product asymmetry of the final state particles' momenta (see caption of Figure 1.6). Triple-product asymmetries have been widely used in searches for CP violation in multibody kaon [121, 122], beauty [123, 124] and charm [125–128] decays. The advantage with respect to a measurement of direct CPV is that no flavour tagging and no large strong phase differences are needed, as $A_{2\phi} \propto \sin(\Delta\phi)\cos(\Delta\delta)$, while $a_{cp} \propto \sin(\Delta\phi)\sin(\Delta\delta)$ requires the presence of large strong phase differences to create significant signal. As in general no information about the strong phases is available, a measurement of both observables is beneficial[9]. Assuming new physics contributions in form of C_9 and C_{10} to be $\mathcal{O}(1)$ and generic weak phases $\Delta\phi \sim \pi/4$, Ref. [95] finds values for $A_{2\phi}$ of 8%(6%) for $D^0 \to \pi^+\pi^-\mu^+\mu^-$ ($D^0 \to K^+K^-\mu^+\mu^-$), which is within the expected sensitivity of the measurement presented in this thesis.

In addition to the angular asymmetries, the time integrated CP asymmetry is measured:

$$A_{CP}(f) = \frac{\Gamma(D^0 \to f) - \Gamma(\overline{D}^0 \to f)}{\Gamma(D^0 \to f) + \Gamma(\overline{D}^0 \to f)}.$$

As neutral D^0 mesons are subject to mixing, the measured CP asymmetry contains contributions from direct and indirect CPV, which can in general be separated in a

[9] The phase differences do not need to be necessarily the same depending on which amplitudes interfere and the position in phase space.

time-dependent measurement. Assuming $|x|, |y \ll 1$, the following approximation can be made [129]:

$$\begin{aligned} A_{CP}(f) &= a_{CP}^{dir}(f) + a_{CP}^{ind} \cdot \int \frac{t}{\tau_{D^0}} e^{-t/\tau_{D^0}} \epsilon(t) dt \\ &= a_{CP}^{dir}(f) + a_{CP}^{ind} \cdot \frac{\langle t \rangle}{\tau_{D^0}} \end{aligned}$$

with $\epsilon(t)$ being the decay-time acceptance of the experiment. Depending on the experimental environment, A_{CP} has a different sensitivity to direct and indirect CPV (at LHCb $\langle t \rangle \approx 2\tau_{D^0}$ [130]).

The first part of this thesis describes the first observation and the measurement of the differential branching fraction of $D^0 \to h^+h^-\mu^+\mu^-$ decays. As explained, the prospects to discover new physics in the branching fractions of multibody decays is limited. In contrast to previous analyses in the field, the measurement will not be limited to the non-resonant region in dimuon mass, but the branching fraction will be measured as a function thereof. Limited sensitivity to the SD is still given in the dimuon-mass regions away from the resonances (where no significant signal is expected). The second part of the thesis focusses on studying asymmetries A_{CP}, A_{FB} and $A_{2\phi}$ in these decays, where the vicinity of resonances is beneficial for new physics searches and helps to optimally exploit the available statistics.

The two presented analyses are based on independent publications and have been performed consecutively. This is also the reason why the branching fraction measurement is based on data recorded in 2012 and therefore only a subset of the nowadays available statistics. The measurement of asymmetries includes additionally data recorded during the years 2011, 2015 and 2016, leading to a gain in statistics of approximately a factor two. As the two analyses deal with the same final state, many analysis techniques such as reconstruction and parts of the selection, as well as the strategy to fit the data samples are in common. In the following, the description of the two analyses is done in a parallel way as long as their similarities outweigh the differences, before the specific details of the analyses are reported in dedicated chapters.

2 Experimental Apparatus

Starting from a short description of the accelerator complex, this chapter discusses the LHCb experiment and those detector components that are relevant for the analysis presented in this thesis. The used data and simulated samples are briefly introduced at the end.

2.1 The Large Hadron Collider at CERN

Since its founding in 1952, the *European Organisation for Nuclear Research* (CERN), situated close to Geneva, Switzerland, has been a huge international association of scientists, trying to understand the fundamental structure of matter. Many particle accelerators had been built with increasing energies to probe increasingly smaller structures.

With a circumference of 27 km, the *Large Hadron Collider* (LHC) [48] is the most powerful accelerator that has been built so far. The LHC consists of two circular storage rings where protons or heavy ions are accelerated in opposite directions to energies up to 7 GeV. The LHC is only the end of a complex accelerator system that successively increases the energy of the beams to 450 GeV[1] before they are injected to the LHC rings. The beams are kept on a circular trajectory with the help of strong super-conductive dipole magnets and brought to collision at four interacting points, where large detectors are built to investigate the collisions at rates up to 40 MHz.

In its main operation mode, the LHC collides proton-proton (pp) beams. In 2010 and 2011, the maximum energy per proton beam was set to 3.5 TeV and it was slightly increased in 2012 to 4 TeV. The run period between 2010-2012 is referred to as *Run 1*, which was followed by a long shut down period (LS1) of two years in which modifications of the dipoles have been performed with the goal to increase the center-of-mass energy of the LHC. Since the beginning of *Run 2*, which refers

[1] In its main proton-proton operation mode

to the second period of data taking during 2015-2018, a center-of-mass energy of 13 TeV has been reached. Data taking will continue until the end of 2018, before another shut down period will be used to prepare the LHC and detectors to run at higher luminosities and reach the maximum design energy of the LHC of 14 TeV.

Besides its main operation mode, also proton-lead and lead-lead collisions have been successfully realized with the LHC under a variety of specific operating conditions.

2.2 The LHCb experiment

Among the four large detectors at the LHC, the *Large Hadron Collider beauty* (LHCb) detector [131, 132] has a special role. It is the only one designed to study decay properties of heavy hadrons containing $c-$ or $b-$quarks. As heavy quarks are mainly produced as $q\bar{q}$ pairs in the forward region at the LHC, the LHCb detector is built as a forward spectrometer. Especially in the forward region, heavy hadrons are largely boosted and fly a measurable distance before they decay. A large dipole magnet is used to deflect charged particle trajectories to allow for momentum measurements. The main requirements to accurately investigate decays of heavy flavoured hadrons are the capability to precisely measure the position of the primary pp interaction point and the decay vertex of unstable heavy particles; excellent resolution on the momenta of the final state particles; the ability to identify the species of the particles by means of particle identification. The technical implementations to meet these requirements are briefly discussed in this chapter. The angular coverage of the LHCb detector is 10 to 300 (250) mrad in the bending (non-bending) plane of the magnet. In Figure 2.1, an overview of the LHCb spectrometer with its various sub-detectors is shown. A right-handed cartesian coordinate system is used with the z-axis pointing towards the beam line, while the y-axis is pointing vertically upwards. From this, one defines the azimuthal and spherical angles ϕ and θ, respectively, as well as the pseudo-rapidity $\eta = -\ln\tan\theta/2$.

The physics core program of the LHCb experiment is to precisely measure decay properties of $b-$ and $c-$flavoured hadrons, in particular matter-antimatter asymmetries and transition rates of very rare decays. Beyond that, LHCb has started to extent and broaden its physics program. For instance, LHCb performed a measurement of the production of electroweak gauge bosons in the forward region [133–135], the study of newly discovered exotic particles [23, 24], the production of heavy quarkonia in proton-lead collisions [136–140] and recently even operated in fixed target proton-argon and proton-helium configurations [141, 142].

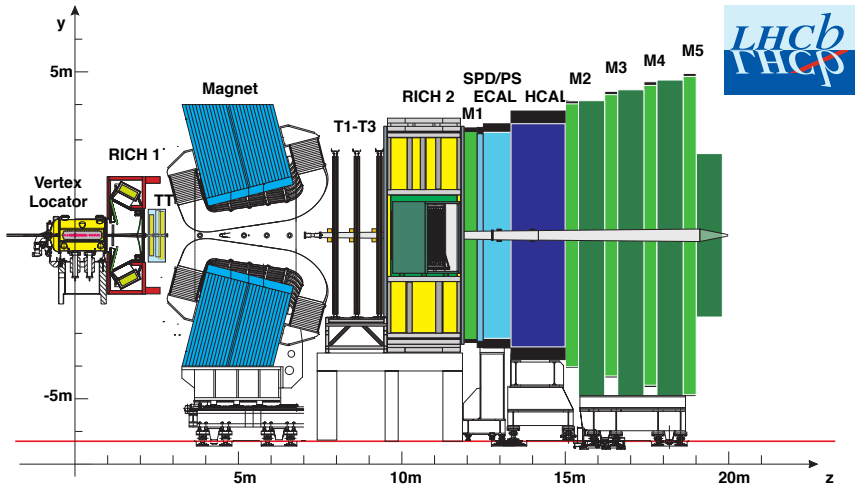

Figure 2.1: The LHCb detector (modified from [131]) and its various sub-systems. Details on each component can be found in the text.

As the word's largest samples of charm and beauty decays have been collected, the LHCb collaboration has made significant contributions to the field of flavour physics and holds many records such as the first significant measurement of the rarest B-meson decay in a single experiment [143].

Vertexing and tracking

Vertexing refers to the reconstruction of the primary interaction points and the reconstruction of secondary decay vertices of the particles, while *tracking* is the measurement of charged particle trajectories (a.k.a. *tracks*). The tracking system consists of the *VErtex LOcator* (VELO) [144, 145], two tracking stations in front of (*upstream*) the magnet [146], and three tracking stations behind (*downstream*) it. The magnetic field is oriented along the y-axis, such that charged particles are deflected in positive or negative x direction, depending on their charge. To cancel detector induced left-right asymmetries, the polarity of the magnet is periodically switched.

With a radial distance of $\sim 7\,\text{mm}$, the VELO is the detector component closest to the beam at the LHC. Inside the VELO, the LHC beam pipe has been removed and only a thin aluminum wall separates the detector from the ultra-high vacuum of the LHC. The VELO consists of 21 stations, each made of two semi-circular shaped halves. The halves are movable and reach their position closest to the interaction point only when the beam is in stable conditions to protect the sensible electronics. Each half is equipped with two different types of silicon strip detectors (on opposite sides) as shown in Figure 2.2. One of these types measures radial

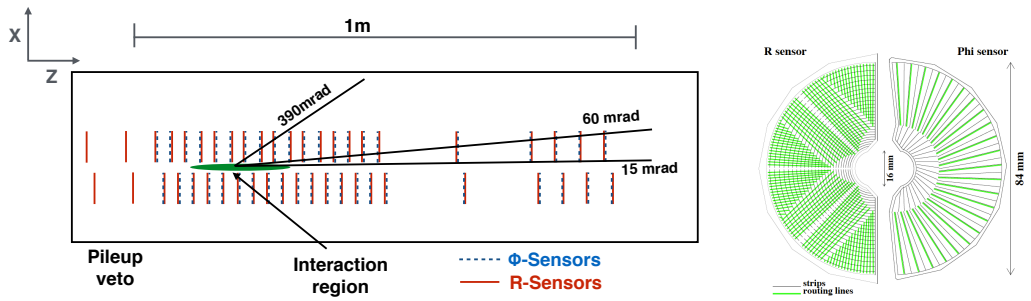

Figure 2.2: Schematic view of the arrangement of the semi circled detector halves of the Velo (modified from [131]) in the $x-z$ plane at a cross section at $y = 0$ (left) and a sketch of the equipment of the sensors in the modules (right) [145].

distances (*r-sensors*), while the other measures the azimuthal angles (ϕ-*sensors*). Charged particles passing through semi-conductive silicon create electron-hole pairs, which travel to the electrodes and cause a measurable pulse. The strip pitch is not constant but varies between 38 and 102 µm, while the spacing decreases in the region closest to the beam. Information in z-direction is obtained from the position of the sensors along the beam line. Four additional r-sensors are positioned in negative z-direction which are used to veto events with a very high number of produced tracks already at trigger level. The performance of the VELO is depending on the number of reconstructed tracks and their momenta, but for a vertex with 25 reconstructed tracks, it is able to reconstruct the point of the primary pp interaction, the *primary vertex* (PV), with a resolution of approximately 13(70) µm in the transverse plane (along the z-axis). The minimal distance of a charged track with respect to the PV, referred to as *impact parameter* (IP), a powerful variable to select tracks of particles coming from a secondary decay vertex (SV), can be reconstructed with a resolution of 35 µm for tracks with momentum larger than 1 GeV/c. The angular acceptance is given by the solid angle in which at least three sensors are hit ($1.6 < |\eta| < 4.9$).

The *Tracker Turicensis* (TT) consists of four layers of silicon micro strip detectors ordered in two stations (TTa and TTb) and placed directly in front of the magnet, about 2.5 m downstream of the interaction region. As shown in Figure 2.3 (left), the strips of the outer layers are aligned with the y-axis, while the inner layers are rotated by an angle of $\pm 5°$ to infer also information on the y-dimension. The strip pitch of 183 µm leads to a spatial resolution in x of ~ 50 µm. With a height of 130 cm and a width of 160 cm, the full angular acceptance of the VELO is covered. The TT can be used to measure tracks of very low momentum particles (~ 2 GeV/c) which are bent out of the detector by the magnetic field, or tracks of unstable particles that decay outside the VELO (such as K^0_S, Λ^0).

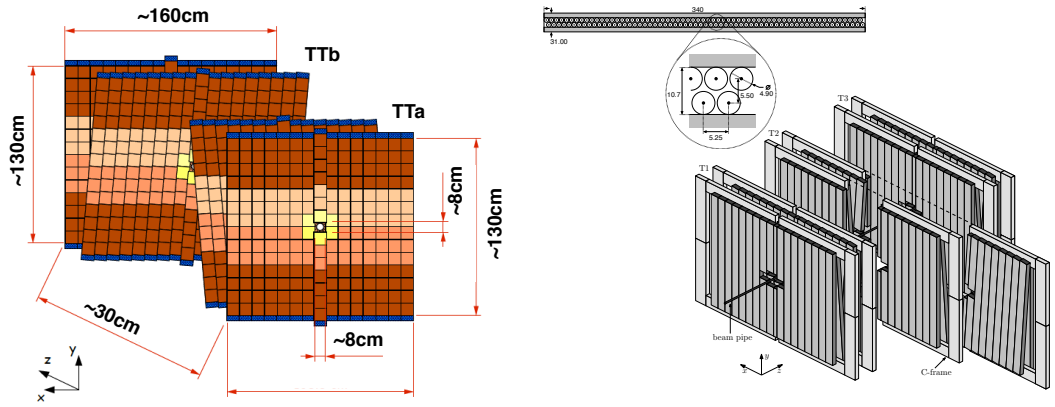

Figure 2.3: Schematic view of the four layers of the TT (left) [131](left) and the OT detector (right) [147]. Also shown is the arrangement of the drift tubes inside the OT (top tight) [131].

The three main tracking stations T1-T3 are installed directly after the magnet at $z = 9\,\text{m}$. Each individual station is made of four layers, where each layer is a hybrid detector made of two distinct technologies. The innermost area of $120 \times 40\,\text{cm}$, subject to the highest particle flux, is covered with the *Inner Tracker* (IT) [148], which is also a silicon micro strip detector. As the technology is similar to the TT, the same spatial resolution of $50\,\mu\text{m}$ is reached in the x-dimension. The outer region is covered by the *Outer Tracker* (OT) [147, 149, 150], which is a gaseous detector constituted of thin drift tubes with a diameter of 4.9 mm operated as proportional counters. Two layers of drift tubes with a relative displacement as shown in Figure 2.3 (right) form one tracking layer. The tubes are mainly oriented in y-direction, however, the inner two layers per stations are arranged as stereo layers rotated by relative angles of $\pm 5°$. When charged particles are passing through the OT, they ionize the gas within the tube and the resulting electrons drift to the anode where they cause a measurable signal. The spatial resolution can be improved by additionally measuring the drift time of the created electrons with respect to the beam crossing signal. The gas mixture is chosen such that the drift time is reasonably fast ($< 50\,\text{ns}$) to cope with the high bunch crossing rate of the LHC. A spatial resolution of $200\,\mu\text{m}$ has been measured, which is worse compared to the IT, however, a substantially larger area of approximately $6 \times 5\,\text{m}^2$ is covered.

Hits from all tracking sub-detectors are combined to form tracks using several algorithms. Most relevant are *long tracks* which are based on hits in the VELO and T-stations (and optionally in the TT). Traversing the whole tracking system, these tracks have the best relative momentum resolution of 0.4% at low momentum and 0.6% at 100 GeV/c. For long-lived particles which decay outside the VELO,

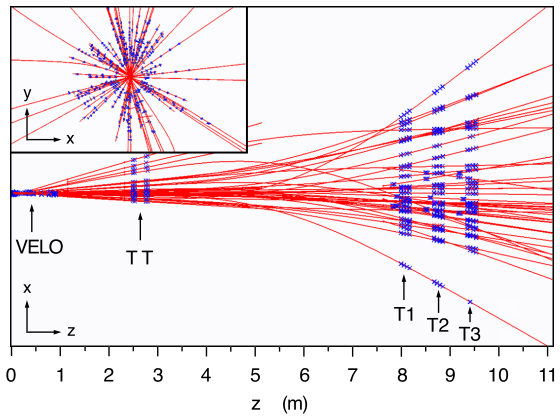

Figure 2.4: Projection of the reconstructed tracks in the tracking system of the LHCb detector in a pp collision event in the $x-z$ and $x-y$ planes [132].

hits from the TT and the T-stations are combined to *downstream tracks* which suffer from a significantly worse resolution. A more detailed description of tracking algorithms can be found for example in Ref. [131,151]. The projections in the $x-y$ and $x-z$ planes of the reconstructed tracks for an exemplary pp collision event at LHCb is shown in Figure 2.4. As the influence of the magnetic field is very small at the position of the tracking detectors, the tracks appear mostly as straight lines and get distracted mainly in the region where the magnet sits ($z = 3-8\,\mathrm{m}$). The average number of reconstructed tracks depends on the run conditions, but is in the order of ~ 100 tracks per event, while on average approximately $\sim 1-3$ PVs are reconstructed per proton bunch crossing. Reconstruction artefacts may lead to *ghost* tracks if unrelated hits are combined; or *clones* if two tracks share more than 70% of their hits. Information from the tracking system is combined to compute a per-track ghost probability (`TrackGhostProb`), which is available in the offline analysis, together with the track fit χ^2 per degrees of freedom (χ^2/dof), allowing for the selection of good-quality tracks.

Particle identification

Identifying the particle species is a crucial ingredient for flavour physics, where the quark content of the final state particles is needed to study the underlying interactions. For rare leptonic decays, a suppression of kinematically and topologically very similar hadronic decays is needed to select the signal decays.

At LHCb, information of several detector components is used for particle identification (PID). Two *Ring-Imaging-CHerenkov detectors* (RICH1 and RICH2) [152, 153] are used for PID of charged particles. They feature a similar setup, consisting of a suitable radiator material, a mirror system and a photo sensitive

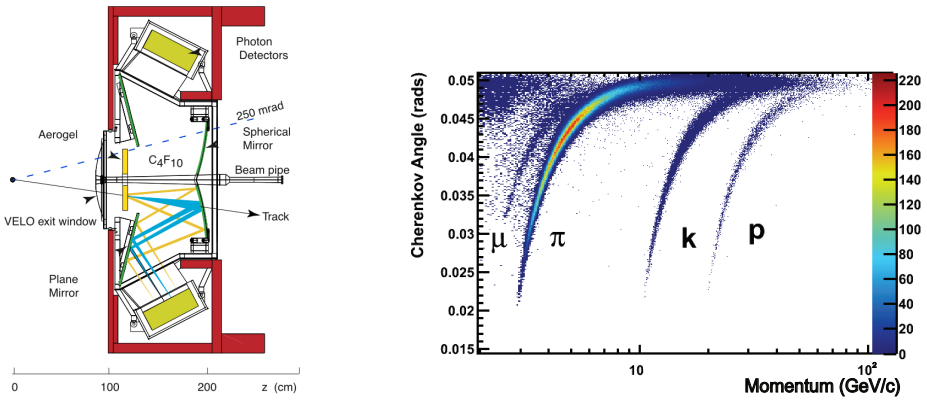

Figure 2.5: Schematic view of the RICH1 detector (left) [131] and the measured Cherenkov θ_c angle as function of the particle momenta (right) [152].

detector component. As example, RICH1 is sketched in Figure 2.5, which is placed between the VELO and TT ($z = 1.5\,\text{m}$), while RICH2 is situated at $z = 11\,\text{m}$ (behind T3). If a charged particle exceeds the speed of light in the radiator, Cherenkov light is emitted in form of a cone, where the opening angle θ_c is purely a function of the particle's velocity: $\theta_c = 1/(n\beta)$, with n the refraction index of the radiator and $\beta = v/c$ the velocity in units of the speed of light. The emitted light cone is then guided by the mirror system to the photo detectors which are placed outside the acceptance of the detector. If the momentum of a particle is known from an independent measurement, the mass can be inferred form the measured angle θ_c. In Figure 2.5, the Cherenkov angle as a function of the momentum is shown, where different particle species appear as shifted bands. To cover a large momentum range, two RICH detectors with different radiators are used. RICH1 uses aerogel and C_4F_4 and can be used for particles in the momentum range $2 - 60\,\text{GeV}/c$, while RICH2 uses CF_4 and covers the momentum range $50 - 150\,\text{GeV}/c$.

A dedicated muon system [154, 155] consisting of five stations (M1-M5) is used for PID of muons and is shown in Figure 2.6 (left). At typical energies of the LHC, muons act as minimum ionizing particles and are the only particle species that travels through the whole detector. The muon stations are therefore mainly placed furthest away from the interaction point ($z > 15\,\text{m}$), where the majority of particles has already been stopped by interactions with the detector material. The muon stations are mainly made of *multi-wire proportional chambers*, where the traversing muons ionise gas in chambers, followed by an amplification and collection of the produced electrons at anode wires. The gas is chosen such that a very short drift time can be reached. Together with the fast readout and high

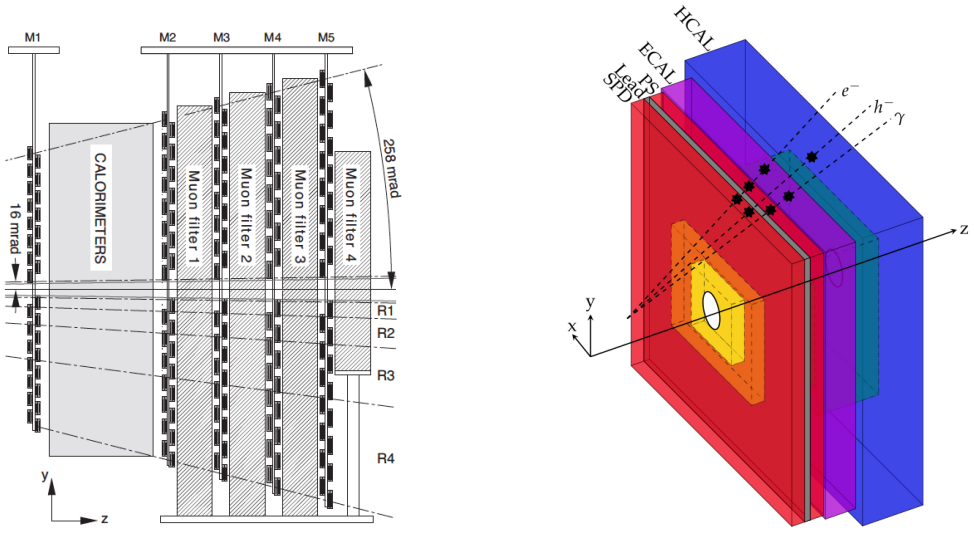

Figure 2.6: Sketch of the muon system (left) [131] and the calorimeter system (right) [156].

efficiency, the muon chambers play a crucial role in the trigger system of LHCb. Between the muon stations, 80 cm thick blocks of iron are added to stop high energetic hadrons that might have reached the muon system. One chamber (M1) is placed in front of the calorimeter system, whose details are given in the following section, and has to cope with a much higher particle rate than the others four stations. However, this layer is helpful in the extrapolation of trajectories from the muon chambers back to the PV as it is done in the trigger.

The main task of the calorimetry system is to measure the particle's energy. At LHCb, the calorimetry system [157, 158] comprises four sub-systems as schematically shown in Figure 2.6 (right). The calorimeters are constructed as sampling calorimeters, meaning that alternating layers of absorber and scintillation material are arrayed in a row. The absorber material is used to induce electromagnetic or hadronic showers, while scintillators detect the particles created in the shower. As the number of produced shower particles is proportional to the primary particle's energy, sampling calorimeters can be used for an energy measurement with a resolution of $\Delta E/E \propto 1/\sqrt{E}$. Two calorimeters are installed. The *Electromagnetic CALorimeter* (ECAL) comprises alternating layers of lead (2 mm) and scintillating tiles (4 mm). Its main purpose is to measure the energy of electrons and photons, which predominantly loose their energy in electromagnetic showers. Furthermore, it plays a crucial role in the reconstruction of neutral pions. Behind the ECAL, the *Hadronic CALorimeter* (HCAL) is located with similar structure, but iron is used as absorber material. The HCAL is used to measure the energy of hadrons, which induce hadronic showers while passing through the iron plates. A *Scintillating*

Pad Detector (SPD) and *PreShower* (PS) are located in front of the ECAL with a layer of lead between them. As only charged particles produce scintillating light, the SPD helps to separate electrons and photons, which do not produce a signal. The PS helps to discriminate charged $\pi^{\pm}$ and electrons, as the energy deposition in the layer of lead will be different for hadrons and leptons. As the calorimeters can be read out at the maximum LHC collision rate of 40 MHz, they are crucial ingredients of the LHCb trigger system and used to select final states containing high energetic hadrons, electrons or photons.

Particle identification algorithms [132, 159] combine the information from these sub-detectors to provide optimal discrimination between the particle species. There are two main sets of observables available. The so-called delta log-likelihood (`DLL`) variables translate the information of the sub-detectors into a likelihood and compute the change of the logarithm of the likelihood when assigning a certain hypothesis to a particle with respect to the charged pion mass hypothesis. The pion hypothesis is chosen as reference, as pions are the most abundant particles in pp collisions. Based on recent developments in machine learning tools, the `ANNPID` variables result from the output of an artificial neural network (`ANN`). Information from all sub-detectors are used in the training and combined into a single response. In the following, these variables are referred to as `ProbNN` variables, *i.e.* `ProbNNk` to select kaons. The `ProbNN` variables also comprise `ProbNNghost` [160] to reject *ghost tracks*, which is based on information from the tracking system only. As muons are the only particles which are likely to reach the muon stations, an additional simple algorithm to identify muons is used. If reconstructed tracks in the tracking stations can be matched to hits in the muon stations, a binary flag called `isMuon` [161] is set, which is already a powerful discriminant to select muons.

Online and offline reconstruction and selection

Over the last years, LHCb has continuously improved the trigger strategy with major changes during LS1. The following section explains the LHCb trigger system and also explains the differences between Run 1 and Run 2, before the offline data flow is briefly discussed.

Online reconstruction and selection

The trigger system [162–165] of the LHCb detector is made of three successively executed steps. Each step iteratively decreases the output rate while the used information from the sub-detectors is increased. This allows for more sophisticated

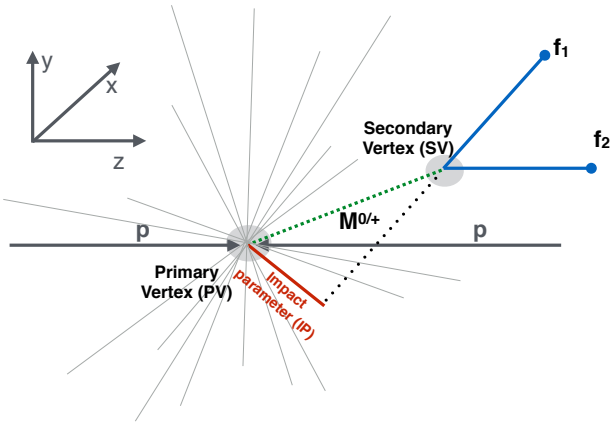

Figure 2.7: Generic topology of a decay of a hadron $M^{0/+}$ containing a heavy quark which furthers decays into two stable final state particles f_1 and f_2. The impact parameter (IP) refers to the IP of the f_1 with respect to the PV.

selection criteria in each step. While there are many different single trigger classification algorithms realised and run in parallel, called *lines* in the following, the general signatures for weakly decaying heavy mesons feature similar topologies as schematically shown in Figure 2.7. Due to their finite lifetime, heavy flavoured beauty and charm mesons travel distances in the order of a centimeter in the detector before they decay, leading to a well separated SV. An experimentally easy, fast and widely used method to find displaced SV is to search for tracks with large IP (see Figure 2.7 for an illustration). Tracks coming from a displaced SV will show will show larger IPs compared to tracks that are produced in the primary pp interaction.

The first trigger level, also called level-zero or L0, is based on dedicated hardware that uses information from the calorimeter and muon systems, as they can be read out at the full bunch crossing rate provided by the LHC. Signatures triggering L0 can either be a large transverse component of the energy dispositions (E_T) in the calorimeters, or high p_T signatures in the muon stations, where p_T is the component of the momentum in the plane perpendicular to the beam axis. The thresholds have been adjusted during operation, but typical values for the minimal energy deposition of hadrons is $E_T > 3.5\,\mathrm{GeV}/c^2$, while for photons and electrons the threshold has been typically a bit lower at $E_T > 3.0\,\mathrm{GeV}/c^2$. The corresponding trigger lines are called `L0Hadron`, `L0Electron` and `L0Photon`. For a single muon, the transverse p_T thresholds is set typically to be $p_T > 1.7\,\mathrm{GeV}/c$, while for two muons the product of their momenta is set to $\sqrt{(p_T^1 \cdot p_T^2)} > 1.6(\,\mathrm{GeV}/c)^2$. These two trigger lines are called `L0Muon` and `L0DiMuon`. The output rate of L0 is limited

to 1 MHz at which the whole detector can be read out. Typically, the hadronic (450 kHz) and muonic (400 kHz) lines fill a large portion of the total rate, while only 150 kHz are allocated to the electron and photon lines. Events passing L0 are sent to the second trigger stage, called high level-level trigger (Hlt), which is fully software based and by itself consists of two stages.

The first stage, called Hlt1, performs a simplified tracking and vertexing algorithm based on information of the VELO and the tracking stations. The main selection concepts are to look for either VELO track segments with high (transverse) momentum which are either significantly displaced from the PV or which can be matched to hits in the muon stations. The aim is to reduce the rate to 80 kHz. Also in Hlt1, the actual selection requirements have been adjusted during the operation time to control the rate. During Run 1, the main Hlt1 trigger line for purely hadronic final states, `Hlt1TrackAllL0`, has selected single well displaced tracks with typical IP of 1 mm with respect to any PV and transverse momenta of $p_T > 1.6 - 1.7\,\text{GeV}/c$. Taking approximately 70% of the total allocated bandwidth, this line dominated the total Hlt1 rate by far. Another selection sequence, called `Hlt1TrackMuon`, tried to match the hits in the muon stations with a track satisfying $p_T > 1\,\text{GeV}/c$. The lower momentum threshold was possible due to the lower rate, as `Hlt1TrackMuon` was only executed if `L0Muon` has returned a positive decision for the event, while `Hlt1TrackAllL0` ran independently of the L0 decision. During LS1, a revision of the Hlt1 selections has been made. Instead of rigid requirements on momenta and IP, simple selection based on *multivariate analysis* (MVA) techniques searching for single (`Hlt1TrackMVA`) and two-track (`Hlt1TwoTrackMVA`) combinations are implemented to increase the selection efficiencies and replace `Hlt1TrackAllL0`. Also for muon candidates a new MVA line has been additionally implemented, called `Hlt1TrackMuonMVA`.

The second stage of the high level trigger, Hlt2, is able to perform a full event reconstruction based on information of all sub-detectors at the rate of 80 kHz. At LHCb, there are two main categories of Hlt2 lines. *Inclusive* lines are selection sequences looking for more generic topological properties of two-, three- and four-body decays coming from displaced B-hadron decays. The selection is mainly based on requirements on the IP of the tracks and sufficient displacement of a secondary vertex with decent quality. Also, loose requirements on the individual and combined momenta and masses are put. *Exclusive* lines on the other hand are designed to fully reconstruct and select a specific final state. Especially for charm decays a lot of exclusive lines exist as the total production cross section of charm mesons at the LHC is huge. To control the rate, an inclusive charm line needs to impose very tight selection requirements. However, this would lead

to insufficient efficiencies for rare processes such as the one investigated in this thesis. This is the reason why a dedicated exclusive trigger line for the investigated $D^0 \to h^+h^-\mu^+\mu^-$ decays is implemented.

Due to several improvements in the software and substantial increase in computing resources, the Hlt2 output rate could be increased from 3.5 kHz in 2011 to 5 kHz in 2012 and 12.5 kHz in 2015. Since the beginning of 2012, Hlt1 has been running asynchronously with the *pp* collisions to make optimal use of the available resources. During data taking in 2012, 20% of the L0 output was temporarily buffered to disc and could be processed by the Hlt1 when the LHC was not providing stable beam, what happened in approximately 70% of the time in 2011. During LS1, the available computing resources were doubled and the Hlt software architecture has been completely revised. Since then, Hlt1 and Hlt2 have been separated and processed completely independent of each other. Instead of deferring the L0 output, this upgrade allows to buffer the entire output of Hlt1 and perform an online calibration and alignment of the detector before the Hlt2 is executed [166]. Together with additional processing time per event, the new strategy has lead to an equal quality of the online and offline reconstruction, while during Run 1, the quality of the reconstructed observables could not reach the level of the offline reconstruction. All events passing Hlt2 are sent to offline storage.

Offline reconstruction and data flow

For the selected events two different data streams exist. In the first stream, which is the only option for Run 1 data, all information from the sub-detectors is saved and a separate offline reconstruction [167] has to be executed prior to offline data analysis. In the offline reconstruction, measured hits of the tracking stations are used to reconstruct tracks and information from the PID systems is added. In a second step, standardised selection sequences [168] combine reconstructed tracks to fit secondary vertices and construct combined objects such as $D-$ or B-hadron candidates. Based on geometric and kinematic variables, specific decay topologies are searched for. As these two processes are very computing intensive, they are run centrally and the analysts are provided with preselected data sets.

The second data stream (called *turbo stream* [169]) has became available with the start of Run 2 and does not require any further offline reconstruction. As the online and offline reconstruction qualities have been equalised, the trigger output is directly made available for data analysis. While during Run 2 both data streams are existing in parallel, the turbo stream is foreseen to be the standard procedure

in the future. As only the relevant information of an event are saved, the event size gets reduced by an order of magnitude.

Recorded data samples and simulation

The LHCb detector has collected pp collision data corresponding to $1\,\text{fb}^{-1}(2\,\text{fb}^{-1})$ of integrated luminosity in 2011(2012), leading to a total of $3\,\text{fb}^{-1}$ recorded during Run 1. The combined data sets recorded in 2015 and 2016 correspond to another $2\,\text{fb}^{-1}$, while the target integrated luminosity of the total Run 2 sample at the end of 2018 is estimated to be $9\,\text{fb}^{-1}$. Throughout this thesis, only data taken in 2015 and 2016 are referred to as Run 2 data, as the data taken in 2017 and 2018 were not available when the analyses of this thesis were performed.

For each year of data taking, simulated samples of the decay channels $D^0 \to h^+h^{(\prime)-}\mu^+\mu^-$ are generated under the corresponding run conditions and processed in exactly the same way as the data. Simulated events are generated with Pythia [170, 171] within the LHCb simulation software framework Gauss [172]. The decay of the generated particles is simulated using the EvtGen [173] package, where an sum of non-interfering resonant and non-resonant contributions is assumed (Table 2.1). The interaction of the particles with the detector is simulated with the Geant4 package [174, 175] and the digitalization of the detector response and the trigger emulation are done using the Boole [176] and Moore packages [177] as implemented in the LHCb software. Simulated samples are needed to estimate reconstruction and selection efficiencies and determine line shapes of mass distributions when fitting the data, as detailed later in this thesis. In total, more than 10^5 simulated candidates are available for each decay channel, which is exceeding the data statistics by at least two orders of magnitude.

Channel	Component	Fraction
$D^0 \to K^-\pi^+\mu^+\mu^-$	$K^{*0}(892)(\to K^-\pi^+)\rho^0(\to \mu^+\mu^-)$	0.16
	$K^{*0}(892)(\to K^-\pi^+)\omega(\to \mu^+\mu^-)$	0.16
	$K^{*0}(892)(\to K^-\pi^+)\mu^+\mu^-$	0.16
	$K^-\pi^+\rho^0(770)(\to \mu^+\mu^-)$	0.16
	$K^-\pi^+\omega(782)(\to \mu^+\mu^-)$	0.16
	$K^-\pi^+\mu^+\mu^-$	0.16
$D^0 \to K^-K^+\mu^+\mu^-$	$\phi(1020)(\to K^-K^+)\rho^0(770)(\to \mu^+\mu^-)$	0.25
	$\phi(1020)(\to K^-K^+)\mu^+\mu^-$	0.25
	$K^-K^+\rho^0(770)(\to \mu^+\mu^-)$	0.25
	$K^-K^+\mu^+\mu^-$	0.25
$D^0 \to \pi^-\pi^+\mu^+\mu^-$	$\rho^0(770)(\to \pi^-\pi^+)\rho^0(770)(\to \mu^+\mu^-)$	0.125
	$\rho(770)(\to \pi^-\pi^+)\omega(782)(\to \mu^+\mu^-)$	0.125
	$\rho(770)(\to \pi^-\pi^+)\phi(1020)(\to \mu^+\mu^-)$	0.125
	$\rho^0(770)(\to \pi^-\pi^+)\mu^+\mu^-$	0.125
	$\pi^-\pi^+\rho^0(770)(\to \mu^+\mu^-)$	0.125
	$\pi^-\pi^+\omega(782)(\to \mu^+\mu^-)$	0.125
	$\pi^-\pi^+\phi(1020)(\to \mu^+\mu^-)$	0.125
	$\pi^-\pi^+\mu^+\mu^-$	0.125

Table 2.1: Simulated composition of the signal samples in terms of dimuon and dihadron intermediate resonances (modified from [5]). For technical reasons, which will be explained later in the thesis, also simulated samples of $D^0 \to K^-\pi^+\mu^+\mu^-$ decays are needed. The following abbreviations will be used throughout this thesis: $\rho^0(770) = \rho^0$, $\omega(782) = \omega$ and $\phi(1020) = \phi$.

3 Reconstruction and selection of signal candidates

On average, less than a single signal decay is expected for every ten million produced D^0 candidates. This chapter explains how the rare signal processes are searched for in the pp collisions samples collected by the LHCb detector.

3.1 Signal decay topology

Unless explicitly indicated, throughout this thesis, all selected D^0 candidates are required to arise from the decay chain $D^{*+}(2010)^1 \to D^0(\to h^+h^-\mu^+\mu^-)\pi^+$, where the D^{*+} meson is produced in the primary pp interaction. Figure 3.1 schematically shows the resulting decay topology. Selecting neutral D^0 mesons from decays of charged D^{*+} helps to greatly reduce background contaminations compared to D^0 mesons which are *promptly* produced in the primary interaction. As the D^{*+} meson decays via the strong interaction into a D^0 meson and a charged pion, it decays instantaneously in the PV. Since the flavour of the c-quark in the decay is conserved, the charge of the pion unambiguously identifies (*tags*) the flavour of the neutral D meson at the time of its production. Due to the small mass difference of the D^{*+} meson and the decay products, the pion has a much smaller momentum than the D^0 meson (on average $5\,\mathrm{GeV}/c$ compared to $100\,\mathrm{GeV}/c$) and is in the following referred to as *soft* pion π_s^+ to avoid confusion with pions coming from the D^0 decay. The D^0 meson decay weakly with a lifetime of about 0.41ps [12], so it flies a few millimetres in the laboratory frame before it decays into the pairs of oppositely charged muons and hadrons. Such a flight distance is sufficient to precisely resolve the position of the secondary D^0 decay vertex from that of the PV.

[1] In the following referred to as D^{*+}.

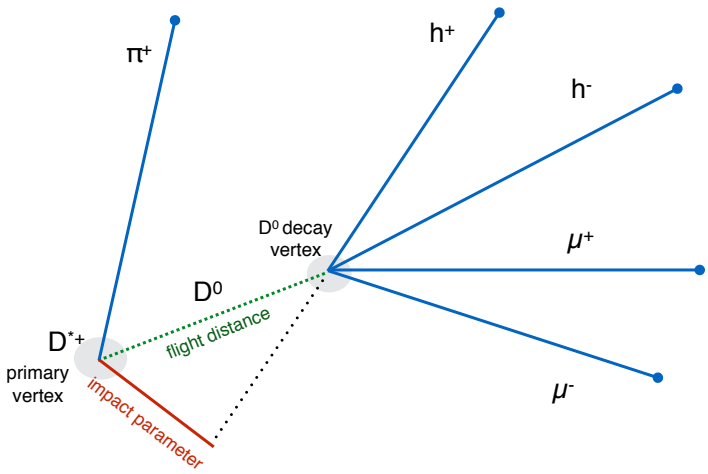

Figure 3.1: Schematic view of the decay topology in the y-z plane of $D^0 \to h^+h^-\mu^+\mu^-$ decays. The relative scale is arbitrary and not realistic. The flight distance (typically a few millimetres) of the D^0 meson is also indicated, as well as the impact parameter of the h^+ meson with respect to the primary vertex (also typically in the order of millimetres).

3.2 Expected backgrounds

There are two main categories of background contributions that can mimic the signal decays. Randomly associated tracks that accidentally pass the final selection requirements and physical backgrounds, where either parts of the decay chain are not reconstructed or particles are misidentified. Also a mixture of these two categories is possible. Processes leading to a wrong flavour tag of the D^0 meson are mainly relevant for the measurement of asymmetries, where the knowledge of the D^0 favour is required (*cf.* section 1.5).

- *Hadronic four-body decays:* Purely hadronic four-body D^0 decays of the form $D^{*+} \to D^0(\to h^+h^-\pi^+\pi^-)\pi_s^+$, where the two final state muons are replaced by a pair of oppositely charged pions, can mimic the signal if the two pions are misidentified as muons. Although the misidentification probability is only $\mathcal{O}(10^{-5})$, these decays have branching fractions that are several orders of magnitude larger than the signal decays (e.g., the ratio of $D^0 \to \pi^+\pi^-\pi^+\pi^-$ to $D^0 \to \pi^+\pi^-\mu^+\mu^-$ is expected to be $\mathcal{O}(10^4)$ [12, 95]).

- *Combinatorial background:* These candidates are entirely made of randomly associated tracks. As the decay topology is imposing tight constraints on the kinematics, their fraction is expected to be greatly suppressed, however

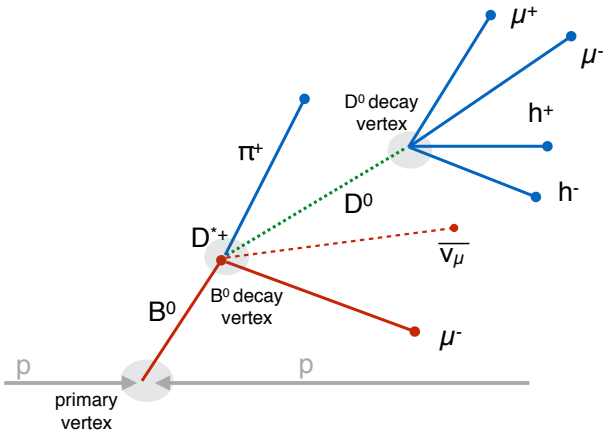

Figure 3.2: Schematic view of the decay topology of secondary decays, where the D^{*+} mesons arise from decays of intermediate b-flavoured hadrons.

cannot be reduced to a negligible level. As these decays feature different kinematic properties, a statistical separation is also possible as explained in chapter 4.

- *Random pion background:* As pions are the most abundant particle species produced by pp collisions, it can happen that a real D^0 candidate is combined with a random low momentum pion to form a D^{*+} candidate that accidentally falls within the considered mass range. When the accompanying soft pion is used to tag the flavour of the D^0, the flavour decision will be based on a random decision if the D^0 meson and π_s are produced independently. The fraction of random pion background can also be estimated statistically, as these decays feature different kinematic properties as far as the D^{*+} candidates are considered.

- *Secondary D^{*+} decays:* D^{*+} mesons not arising from the primary pp interaction, but from the decay of a secondary decay of a B-hadron, such as for example the decay chain $\overline{B}^0 \to D^{*+}\mu^-\overline{\nu}_\mu$, are called *secondary decays*. As secondary decays exhibit a different production mechanism, their presence introduces additional systematic effects compared to promptly produced D^{*+} mesons as discussed in more detail later in this thesis. Due to the relatively long lifetime of B-hadrons, the D^{*+} production vertex is likely to be separated from the PV, as schematically shown in Figure 3.2. This information helps to estimate the fraction of secondary decays.

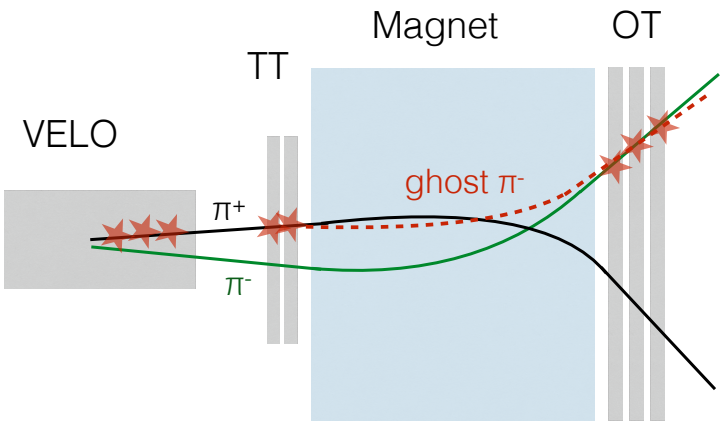

Figure 3.3: Schematic view of a ghost pion background candidate in the x-z plane. The red stars indicate the hits in the tracking system used to reconstruct the ghost pion (red dotted line). Hits in the downstream tracker caused by an unrelated π^- (green solid line) are accidentally combined with the VELO track of the π_s^+ (black solid line) from a signal decay. The charges of the ghost and original signal pion are of opposite sign.

- *Ghost pion background:* Tracks of low momentum pions reconstructed in the VELO can be associated with unrelated hits in the downstream tracking stations and form a *ghost slow pion* as schematically shown in Figure 3.3. Especially for particles with very low momentum, the magnitude of the reconstructed momentum and masses might stay almost unchanged, while the curvature of the trajectory, used to infer the charge of the pion, might change sign and lead to a wrong flavour tag. This background can be suppressed to a negligible level by tight requirements on the ghost probability of the π_s^+ track.

3.3 Building offline signal candidates

Following a standardised basic selection sequence, the offline reconstructed final state particles are combined to build signal candidates for the decay chain $D^{*+} \to D^0(\to h^+h^-\mu^+\mu^-)\pi_s^+$. Except for PID requirements on the hadrons, the sequence is similar for $D^0 \to \pi^+\pi^-\mu^+\mu^-$ and $D^0 \to K^+K^-\mu^+\mu^-$ candidates. The selection is mainly aimed at removing obvious backgrounds and badly reconstructed candidates. Furthermore, loose requirements on (transverse) momenta of the final state tracks and combined objects are imposed to get rid of a large amount

Particle	Variable	Requirement
K,π,μ	p	$> 3\,\text{GeV}/c$
	p_T	$> 300\,\text{MeV}/c$
	Impact-parameter χ^2	> 3
	Track χ^2/dof	< 3
	`ProbNNghost`	< 0.5
K	`ProbNNk`	> 0.2
π	`ProbNNpi`	> 0.2
μ	`isMuon`	True
	`nSharedMuon`	0
D^0	p	$> 3\,\text{GeV}/c$
	p_T	$> 2\,\text{GeV}/c$
	m(DTF)	$> 1810\,\text{MeV}/c^2$
		$< 1940\,\text{MeV}/c^2$
	Vertex χ^2/dof	< 20
	Flight-distance χ^2	> 30
	Impact-parameter χ^2	< 36
	Cosine of the direction angle (a.k.a. DIRA)	> 0.9998
	Largest distance of closest approach of daughters (a.k.a. MAXDOCA)	$< 0.3\,\text{mm}$
	Impact-parameter χ^2 of at least one of the daughters	> 9
D^*	p_T	$> 2\,\text{GeV}/c$
	Vertex χ^2/dof	< 20
	Distance of closest approach of daughters (a.k.a. DOCA)	$< 0.3\,\text{mm}$
	Δm(DTF)	$> 144.5\,\text{MeV}/c^2$
		$< 146.5\,\text{MeV}/c^2$
π_s	p_T	$> 120\,\text{MeV}/c$
	Track χ^2/dof	< 3
	Number of primary vertices	≥ 1

Table 3.1: Preselection requirements for $D^0 \to \pi^+\pi^-\mu^+\mu^-$ and $D^0 \to K^+K^-\mu^+\mu^-$ candidates (modified from [5]).

of combinatorial background, which on average tends to have lower momenta than signals.

In a first step, only events with at least one reconstructed PV are considered. Then, four charged particles satisfying very loose criteria on track quality (χ^2/dof < 3) and being inconsistent with coming from the PV (IP$\chi^2 > 3$) are searched for to form a D^0 candidate, where the IPχ^2 for a particle is defined as the difference between the χ^2 obtained when fitting the PV with and without the considered particle. The IPχ^2 measures whether a particle is consistent with coming from the PV by using also information on the uncertainties in track parameters and PV position. Candidate pions and kaons are required to satisfy loose PID requirements based on the `ANN` PID variables (`ProbNNpi` > 0.2 and `ProbNNK` > 0.2, respectively), while the PID requirements on the muons will be chosen in a later optimisation process separately for both analyses. However, as a basic criterion, a positive `isMuon` flag is required to be set for both muon tracks to suppress a large portion of misidentified hadronic decays. As the L0 trigger decision is mainly based on hits in the muon stations, only pairs of muons are selected

that do not share any hits to ensure that the trigger efficiency can be factorised into product of single-particle efficiencies. The actual requirements are listed in Table 3.1. The amount of artificial ghost tracks created by the reconstruction software is reduced by selecting tracks satisfying criteria on the ghost probability (`ProbNNghost` < 0.5).

If these four tracks pass all the requirements mentioned above and are consistent with coming from a common SV defined by a maximal distance of closest approach (DOCA) of all four tracks of smaller than 0.3 mm, a D^0 decay vertex is fitted and has to satisfy vertex χ^2/dof< 20. The so-formed D^0 candidate has to fulfill further requirements such as significant displacement from the PV ($FD\chi^2 > 30$). From the flight distance (FD), defined as the length of the distance between the PV and SV, a more sophisticated variable, the $FD\chi^2$, relates the information of the FD to the uncertainties of the fits of the vertices, such that a small FD is more significant for well measured vertices than for those having large uncertainties. For the combined D^0 candidate, the cosine of the direction angle (DIRA) is required to be > 0.9998, which is defined as the angle between the momentum vector $\vec{p}$ of the reconstructed intermediate particle with respect to the vector connecting the primary and secondary vertices ($\overrightarrow{FD}$). For signal decays, the $\overrightarrow{FD}$ and $\vec{p}$ have to agree within resolution, *i.e.* the cosine of their enclosed angle will be close to unity, while for background candidates this relation does not necessarily hold true. Furthermore, as the signal D^0 comes from the PV, a requirement on IP$\chi^2 < 36$ is chosen to suppress background from secondary decays, as well as a requirement on the (transverse) momentum of (2)3 GeV/c to further suppress combinatorial background.

In the next step, a low momentum pion with $p > 120\,\text{MeV}/c$ and sufficient track quality (track χ^2/dof< 3) is combined with the D^0 candidate to form a D^{*+} meson. As a consistency check, the DOCA of the D^{*+} daughter particles are required to be less than 3 mm before the decay vertex of the D^{*+} candidate is fitted. Also, the vertex has to satisfy minimal requirements on the fit quality (vertex χ^2/dof < 20) and the momentum of the D^{*+} candidates has to exceed $2\,\text{GeV}/c$.

In the selection sequence described above, the candidates are built following a bottom-up approach, meaning that first the stable final state particles are combined into an intermediate D^0, which then subsequentaly forms the parent D^{*+} meson together with the accompanying pion. If the full sequence is processed successfully, the whole decay chain is refitted using a `DecayTreeFitter` (DTF), which simultaneously fits the full decay chain using a Kalman filter [178] under the constraint that the D^0 and π_s^+ originate from the same point, the PV. This

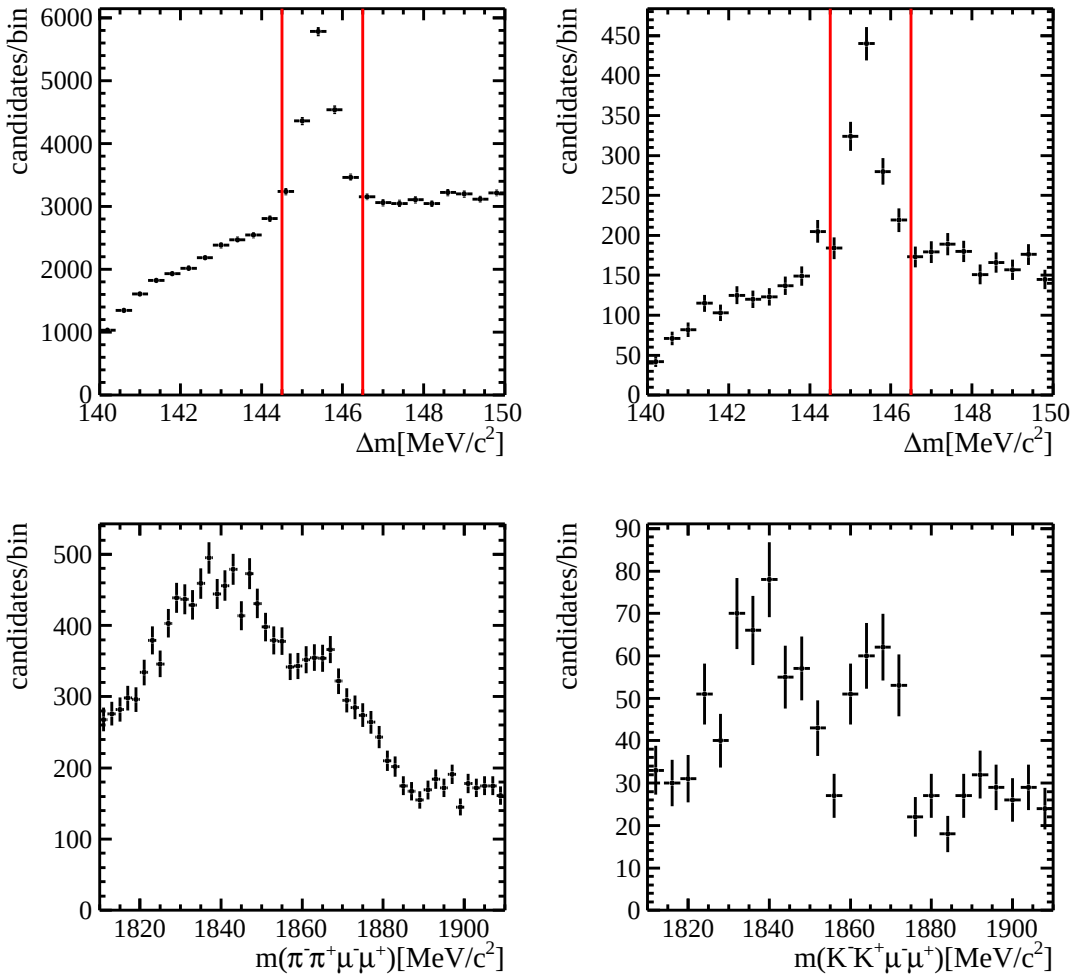

Figure 3.4: Distribution of Δm for (left) $D^0 \to \pi^+\pi\mu^+\mu^-$ and (right) $D^0 \to K^+K^-\mu^+\mu^-$ candidates after the trigger and preselection requirements (except for the Δm requirement, and summing Run 1 and Run 2 data together). The red vertical lines indicate the mass range that is considered after the preselection. The bottom row shows the D^0 mass distributions for (left) $D^0 \to \pi^+\pi^-\mu^+\mu^-$ and (right) $D^0 \to K^+K^-\mu^+\mu^-$ candidates after the trigger and preselection [6].

constraint improves the momentum (and mass) resolution. Finally, two mass windows are defined. The mass difference of the D^{*+} and the D^0 mesons, Δm, is required to be in the range of $144.5 - 146.5\,\mathrm{MeV}/c^2$, corresponding to roughly 3σ of mass resolution around the peak maximum as visible in Figure 3.4. The D^0 mass is limited to the range $1810 - 1940\,\mathrm{MeV}/c^2$. Masses of combined objects are computed from the sum of the four momenta $p^\mu = (E, p_x, p_y, p_z)$ of the final state particles, where the energy is computed from the particle's measured momentum under a given mass hypothesis, i.e. $E = \sqrt{m_{PDG}^2 + p^2}$ with m_{PDG} being the known value of the assumed particle [12]. This means, no energy deposition measured

in the calorimeter system but only the momentum components p_x, p_y and p_z as measured in the tracking system enter the computation. A summary of all preselection cuts is given in Table 3.1.

As explained in more detail in chapter 2, at LHCb, all events that pass the three trigger stages are saved to tape. However, not all recorded events are considered in the following. A well defined restriction to certain trigger lines allows for a precise determination of trigger efficiencies, as needed later to measure the branching fraction. At L0, any of the two muons in the final state are required to be consistent with the object that triggered `L0Muon`. This decision is based on an offline algorithm, that tries to match the (offline) reconstructed particles with the trigger objects that have been responsible for the positive decision. For the measurement of the asymmetries, such a precise knowledge of the hardware trigger efficiencies is not needed. In this case, also events which have been recorded due to any positive L0 trigger decision independent of the final state particles of the signal candidate are accepted.

At Hlt1, Run 1 candidate muons (D^0 daughter particles) must be matched to the trigger objects responsible for a positive decision of `Hlt1TrackAllMuon` (`Hlt1TrackAllL0`), while the requirement for Run 2 candidates is a positive matching of the muons (D^0 candidate) to objects that triggered `Hlt1TrackMuonMVA` (`Hlt1TrackMVA` or `Hlt1TwoTrackMVA`).

Finally, only candidates consisitent with a positive decision of the exclusive Hlt2 line are considered. The Hlt2 selection sequence is very similar to the offline building of signal candidates with the difference that no online D^{*+} candidate is reconstructed in the trigger. As the selection requirements on the offline candidates are tighter than in the online trigger selection, no detailed description of the Hlt2 selection sequence is given in this thesis, but can be found in Ref. [165].

The finally selected signal samples for $D^0 \to \pi^+\pi^-\mu^+\mu^-$ and $D^0 \to K^+K^-\mu^+\mu^-$ candidates are shown in Figure 3.4 (combined Run1 and Run 2 data). Clearly, a small peak at the nominal D^0 of $1865\,\mathrm{MeV}/c^2$ [12] mass is visible together with a very large peaking structure shifted by $\sim 20\,\mathrm{MeV}/c^2$ towards lower masses due to the hadronic $D^0 \to h^+h^-\pi^+\pi^-$ decays, where the two pions are misidentified as muons. The shift in the D^0 mass distribution allows for a statistical separation of this background component as explained later in this thesis. Furthermore, the level of combinatorial background is still sizable. To further suppress the combinatorial background, the following section defines a selection based on a multivariate classifier. The misidentified hadronic decays will later be reduced by means of tight requirements on particle identification on the muons.

3.4 Suppression of combinatorial background

A further suppression of combinatorial background is achieved by means of a *multivariate analysis*. For given signal and background proxies (a.k.a the *training samples*), a multivariate classifier learns to find the multi-dimensional differences between the two samples in a training phase and combines the information into a single variable, the *classifier output*, which is then used in a following *classification phase* to distinguish signal and background in a sample of unknown composition.

In this thesis, a *Boosted Decision Tree* (BDT) [179,180] with gradient boosting as implemented in the *Toolkit for Multivariate Analysis* (TMVA) [181] is trained using simulated signal candidates as signal proxy and data from a control sideband region defined by $m(D^0) > 1890\,\mathrm{MeV}/c^2$ for the background. This region is sufficiently separated from the signal and misidentified physical decays and therefore it is expected to consist of combinatorial background only. A multivariate classifier might be more efficient on samples that have been used in the training phase. To get an unbiased estimation of its performance, the total data and simulated samples are split into disjoint subsamples according to *even* and *odd* event numbers. The choice of this particular splitting is motivated by the fact that the subsamples are by construction of similar size, while no experimental bias on any selection variable caused by this splitting can be thought of. Two BDTs with the same set of *input variables* and configurations are trained on the *even* and *odd* subsamples and then used to classify the other subsample. By doing so, reliable estimations of the true efficiency for a given requirement on the classifier output, referred to as `BDT` value, are expected from simulation.

As the conditions between Run 1 and Run 2 have changed (*e.g.* different center-of-mass energy and track multiplicity, improved tracking and PV reconstruction algorithms), separate classifiers are trained for the two data-taking periods. Due to kinematic differences between $D^0 \to \pi^+\pi^-\mu^+\mu^-$ and $D^0 \to K^+K^-\mu^+\mu^-$ decays, the training is also done separately for both signal decay modes[2].

The BDT is trained with the following discriminating variables as inputs:

- logarithm of the D^0 flight-distance χ^2, $\log(\mathrm{FD}\chi^2)$;
- logarithm of the cosine of the D^0 direction angle, $\log(\mathrm{DIRA})$;
- largest distance of closest approach of the D^0 daughters, $\max(\mathrm{DOCA})$;

[2]The BDTs have been trained separately for the measurement of the branching fraction [1] and the asymmetries [2] (considering the marginal differences in the preselection). However, for the sake of simplicity, in the following, only the performance of the BDT trained for the asymmetry measurement is shown, as no significant differences are observed anyhow.

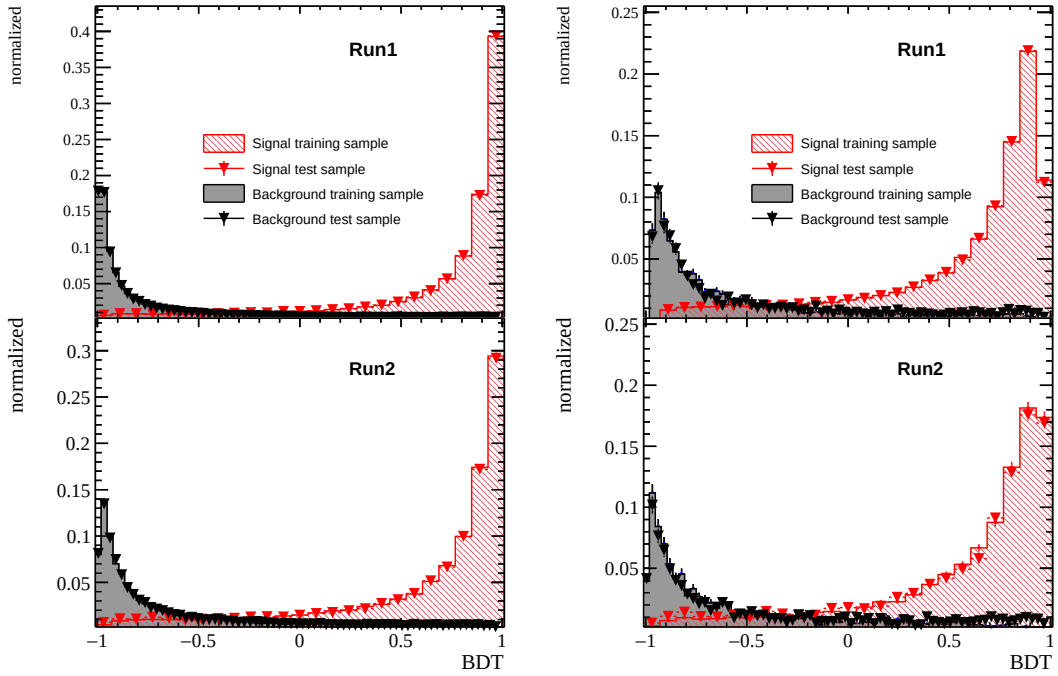

Figure 3.5: Signal and background BDT output distributions, separately for training and test samples and for (left) $D^0 \to \pi^+\pi^-\mu^+\mu^-$ and (right) $D^0 \to K^+K^-\mu^+\mu^-$ decays. The top plots show the samples trained on Run 1 data, while the bottom plots show the distributions trained on Run 2 data (modified from [6]).

- smallest impact-parameter χ^2 of the D^0 daughters, min(IPχ^2);
- D^0 vertex χ^2;
- momentum of the soft pion;
- transverse momentum of the soft pion;
- D^*-cone p_T asymmetry A_{p_T}, defined as $A_{p_T} = \frac{p_T(D^{*+}) - \sum_{tracks} p_T}{p_T(D^{*+}) + \sum_{tracks} p_T}$, where the sum runs over reconstructed tracks which are not part of the signal candidate within a cone of radius $R = \sqrt{(\Delta\eta)^2 + (\Delta\phi)^2} = 1.5$ around the D^* candidate. If no further tracks are found within the cone, $A_{p_T} = 1$. Background candidates are likely to be accompanied by additional charged tracks, leading to $A_{p_T} < 1$.

The distributions of the input variables for $D^0 \to \pi^+\pi^-\mu^+\mu^-$ signal and background candidates are shown in Figure 3.7. Corresponding plots for $D^0 \to K^+K^-\mu^+\mu^-$ decays can be found in Appendix A. The input variables have been chosen with the aim to increase signal and background separation but also to obtain an efficiency that is as much as possible independent of the masses $m(\mu^+\mu^-)$

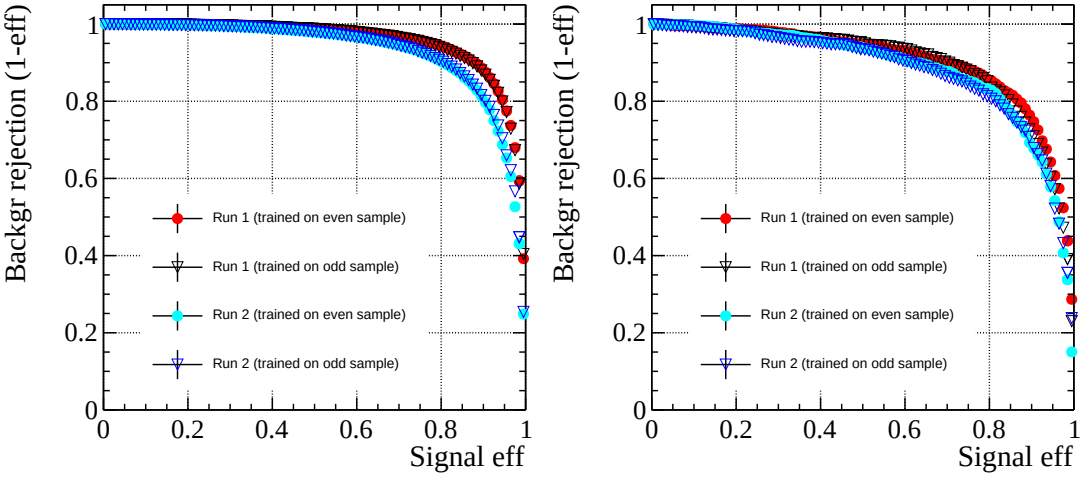

Figure 3.6: Signal efficiency versus background rejection for the BDT trained on (left) $D^0 \to \pi^+\pi^-\mu^+\mu^-$ and (right) $D^0 \to K^+K^-\mu^+\mu^-$ decays and separately for the (filled dots) *even* and (open triangles) *odd* samples and (red-black) Run 1 (cyan-blue) Run 2 data (modified from [6]).

and $\mathrm{m}(h^+h^-)$ of the dimuon and dihadron systems. An efficiency independent of the dimuon and dihadron masses helps to reduce systematic uncertainties due to the assumed decay model in simulated samples. The BDT classifier output distributions for signal and background candidates are shown in Figure 3.5. To use the BDT output in the selection, a minimum requirement, say for example $\texttt{BDT} > 0$, is chosen to reject of a large fraction of background, while the signal efficiency is kept high. The output distribution in Figure 3.5 is shown for the training and a statistically independent *test* sample, which was classified using the trained BDT. The comparison is shown to check if the BDT accidentally learned to distinguish signal and background based on statistical fluctuations of the training samples rather than statistically significant differences in the underlying distribution of the input variables. If this was true, deviation of the BDT distributions as obtained on the training and testing samples would be expected, which is not the case. Furthermore, Figure 3.6 shows the comparison between the receiver operating characteristic (a.k.a. ROC) curves, which is the signal efficiency versus the background for any given requirement on the BDT output. The ROC curves are shown separately for the BDT trained on *even* and *odd* samples, where no significant differences are observed. As the statistical separation of some selection variables has decreased under Run 2 conditions (see Figure 3.7), a slightly better performance of the Run 1 BDT is found.

The BDT selection is designed to suppress combinatorial background, while the background from doubly misidentified hadronic four-body decays will be

suppressed by requirements on particle identification. To account for possible correlations, the optimal PID and BDT requirement are determined simultaneously. As the optimal working point of the selection depends on the specific use case, the optimisation is different for the branching fraction measurement and the asymmetries measurements. The optimisation procedures will be explained in the corresponding dedicated analysis chapters.

If there is more than one signal candidate reconstructed in a single event, these are referred to *multiple candidates*. It is hardly probable that they are coming from two independent true signal decays and more likely to be artefacts of the reconstruction software. If, after the full selection, two candidates are found in the same event, one is chosen at random. This requirement removes less than a percent of the finally selected candidates.

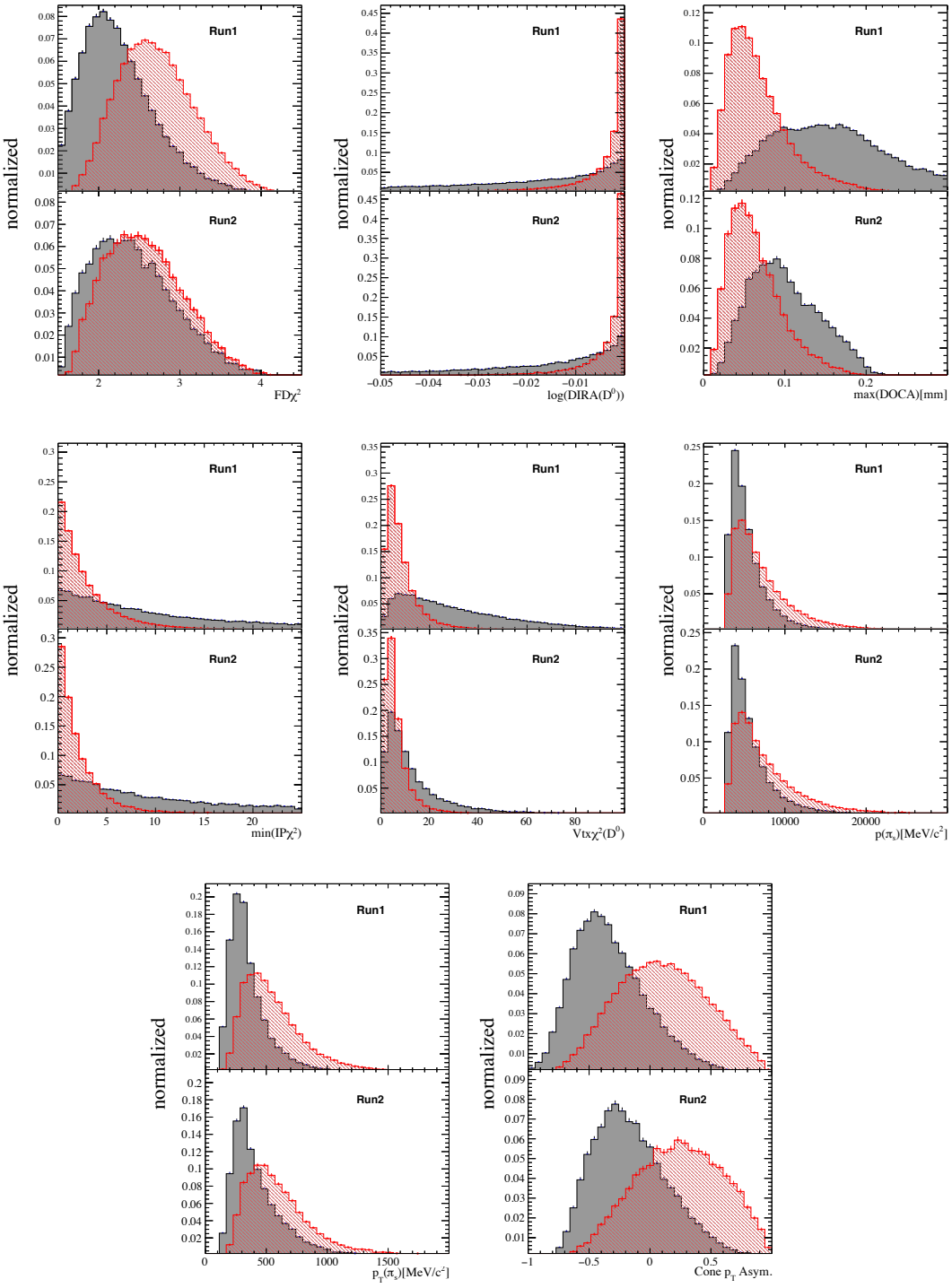

Figure 3.7: Distributions of the BDT input variables for (red) $D^0 \to \pi^+\pi^-\mu^+\mu^-$ signal and (grey) background candidates, and separately for (top panel) Run 1 and Run 2 (bottom panel) data. From top-left to bottom-right: $\log(\text{FD}\chi^2)$, $\log(\text{DIRA})$, $\max(\text{DOCA})$, $\min(\text{IP}\chi^2)$, D^0 vertex χ^2, $\log(\text{IP}\chi^2)$ of the soft pion, momentum of the soft pion, transverse momentum of the soft pion, D^*-cone p_T asymmetry (modified from [6]). Corresponding plots for $D^0 \to K^+K^-\mu^+\mu^-$ candidates can be found in Appendix A.

4 Determining signal and background yields

Determining signal yields are crucial parts of the analyses presented in this thesis. This chapter describes the procedure to separate the various components of the selected samples on a statistical basis. First, it discusses the different features of the components that allow for a discrimination. Then, the fit model is defined and the analytic parametrisation of the mass shapes is outlined.

4.1 Discriminating signal and background

The selected data samples are a mixture of signal and background candidates of unknown composition. The background is mainly composed of misidentified hadronic four-body decays and random combinations of five charged particles (pure combinatorial). Only small contaminations of real D^0 associated with unrelated soft pions and secondary D^{*+} are present after the selection.

Signal, misidentified hadronic decays and combinatorial background can be separated using the reconstructed D^0 meson mass $m(D^0)$, as these components have different kinematic properties. As random pion and secondary D^{*+} background contain of true D^0 mesons, they cannot be distinguished in this dimension. However, random pions (together with purely combinatorial) can be separated in Δm, as they do not come from a true D^{*+} candidate and therefore cannot form a peak in the reconstructed mass of the D^{*+} candidate. Finally, secondary D^{*+} can be separated in the IP distribution of the D^0, as their origin is a displaced SV, causing a larger IP with respect to promptly produced D^0. Figure 4.1 schematically shows the mass projection m(D^0) and Δm, as well as the (logarithm of the) IP distribution for signal and different background candidates. Since the fractions of random pions and secondary decays can be suppressed to the low percent level after the selection, in the following, the signal is separated from the main backgrounds consisting of misidentified four-body decays and combinatorial background using a fit to the $m(D^0)$ distribution. The small neglected contaminations of random

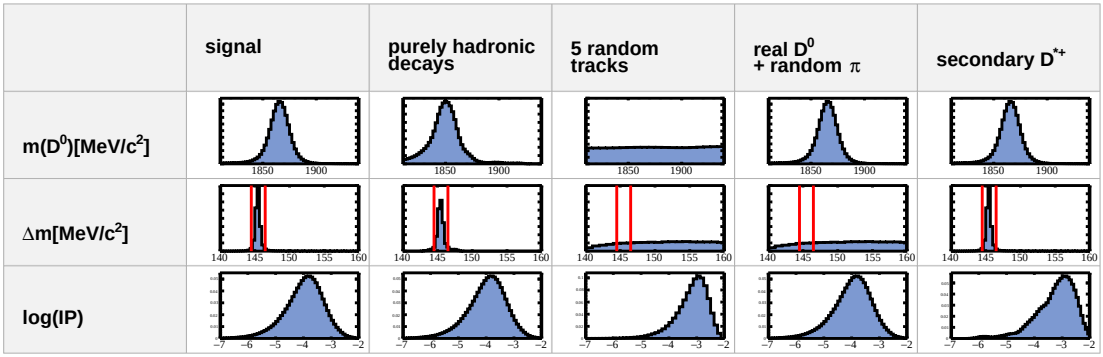

Figure 4.1: Sketches of the the mass ($m(D^0)$, Δm) and $log(IP)(D^0)$ distributions for signal and background candidates. The red vertical lines in Δm show the mass window which has been chosen in the selection to suppress combinatorial background and random pions (see chapter 3 for details of the selection).

pions and secondary decays are treated as sources of systematic uncertainties. The fit model consists of the following three components:

- the signal, *i.e.* $D^0 \to K^-K^+\mu^+\mu^-$ or $D^0 \to \pi^-\pi^-\mu^+\mu^-$ decays[1];
- peaking background from four-body hadronic $D^0 \to h^+h^-\pi^+\pi^-$ decays;
- combinatorial background.

The *probability density functions* (PDFs) that describe the individual components are determined using either simulation or data control samples. As no significant dependency of the PDFs on the data taking period is observed, Run 1 and Run 2 data samples are merged after the final selection. For the sake of simplicity, the dimuon-mass integrated fits for the $D^0 \to h^+h^-\mu^+\mu^-$ decays, *i.e.* with no restriction to a specific dimuon-mass region, are shown in the following sections. However, the mass shapes are determined individually for each considered region of dimuon mass to account for the different kinematical properties of the muons, which are reflected in particular in slightly different background mass shapes. All fits to determine the signal shapes as well as the final fits to determine the branching fractions and asymmetries are *extended unbinned maximum likelihood*[2] fits. Unless stated otherwise, the shape parameters are all fixed to the values as obtained in simulation/control samples when the final fits to the data are performed.

[1] When measuring the branching fraction, an analogous model for $D^0 \to K^-\pi^+\mu^+\mu^-$ decays is defined as explained in more detail in chapter 5.

[2] The maximum likelihood fit technique is a method of parameter estimation given a statistical model and a set of measured observables. A detailed description can be found *e.g.* in Ref. [182].

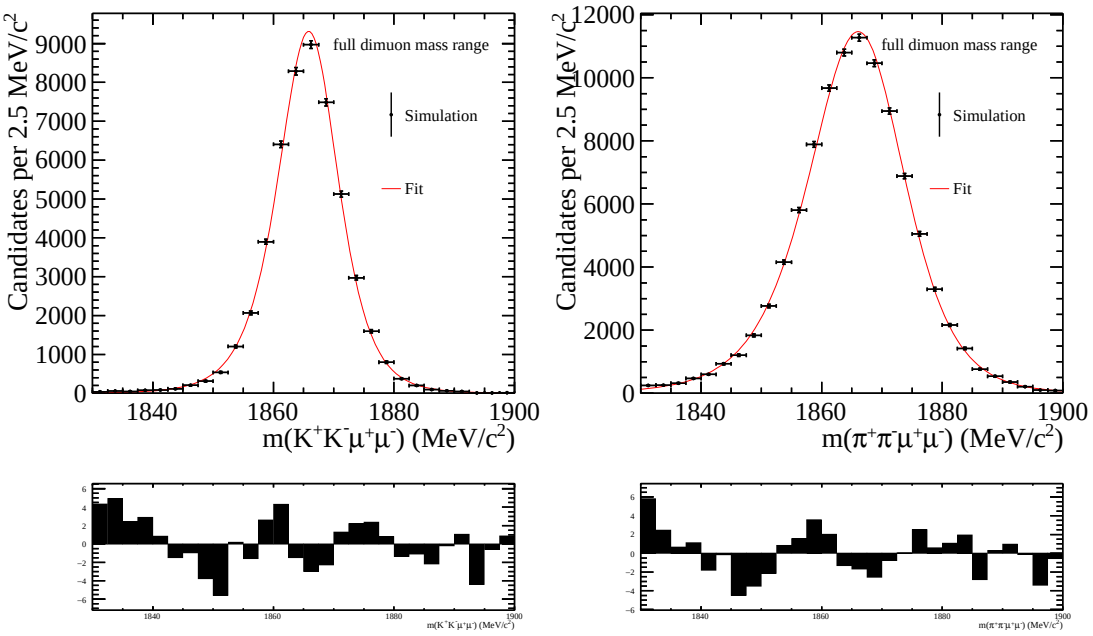

Figure 4.2: Fit to the D^0 mass distribution of simulated (left) $D^0 \to K^+K^-\mu^+\mu^-$ and (right) $D^0 \to \pi^+\pi^-\mu^+\mu^-$ candidates (modified from [6]).

4.2 Parametrisation of the fit components

The signal mass shape is obtained by using simulated samples, which are filtered with exactly the same selection as applied to the data. The Gaussian-like structure shown in Figure 4.2 with a slightly asymmetric left tail, caused by energy loss due to Bremsstahlung effects, is parameterised by a Johnson's S_U distribution [183]. The Johnson's S_U is a four-parameter function resulting from a variable transformation of a normal distribution to allow for asymmetric tails which is well suited to describe the observed D^0-meson mass distribution of signal candidates. The functional form is as follow:

$$\mathcal{J}^{sig}(m|\mu,\sigma,\nu,\tau) = \frac{1}{\mathcal{N}_J}\frac{e^{-\frac{1}{2}r^2}}{c\cdot\sigma\cdot\tau\cdot\sqrt{z^2+1}},$$

with:

$$
\begin{aligned}
r &= -\nu + \frac{\operatorname{asinh}(z)}{\tau}, \\
z &= \frac{m - (\mu + c \cdot \sigma \cdot \sqrt{w}\sinh(\omega))}{c \cdot \sigma}, \\
c &= \frac{w - 1}{2\sqrt{w \cdot \cosh(2\omega) + 1}}, \\
w &= e^{\tau^2}, \\
\omega &= -\nu \cdot \tau.
\end{aligned}
$$

The parametrisation is chosen such that μ, σ, ν and τ correspond to the first, second, third and fourth statistical moments of the distribution. This means, the parameter μ describes the mean, σ is the standard deviation and ν and τ are the skewness and kurtosis, respectively, which allow to describe the asymmetric tails. $\mathcal{N}_J$ is just a proper normalisation factor. For each decay channel, the mass shapes are determined individually. In Figure 4.2, the fits to $m(D^0)$ spectra of the simulated $D^0 \to \pi^+\pi^-\mu^+\mu^-$ and $D^0 \to K^+K^-\mu^+\mu^-$ candidates are shown. The bottom panel shows the *pull distribution*, which is the difference between the data points and the fit function normalised by the data uncertainties. The pulls are a graphical illustration of the goodness of the fit. As the available statistics in simulations is exceeding the data statistics by at least two orders of magnitude, the discrepancies visible in the tails of the distributions in Figure 4.2 are not relevant when fitting the data. The effect of possible limitations of the simulations to describe the signal mass shapes are discussed later and dedicated systematic uncertainties are assigned.

The D^0-mass shape for misidentified hadronic decays is determined by using data samples of $D^{*+} \to D^0(\to h^+h^-\pi^+\pi^-)\pi_s^+$ candidates, where two oppositely charged pions are assigned muon mass to mimic the situation as present in the signal samples. While this choice is unambiguous for $D^0 \to K^-K^+\pi^+\pi^-$, in the case of $D^0 \to \pi^-\pi^+\pi^+\pi^-$ two pions are chosen at random. As visible in Figure 4.3, the characteristic peaking structure emerges, where the peak position is shifted by $\sim 20\,\mathrm{MeV}/c^2$ with respect to the nominal D^0 mass. As for the signal component, these shapes are parametrised by a Johnson's S_U distribution $\mathcal{J}^{misID}$. The long asymmetric tails of the distribution towards lower masses is caused by pions that decay into a $\mu\nu$ pair. As the undetected neutrino takes some fraction of the total momentum, the energy of the D^0 candidate is underestimated. The fraction of pion decaying in flight, and therefore also the shape of the distribution, depends on the selection requirements, in particular on muon particle identification criteria. As it

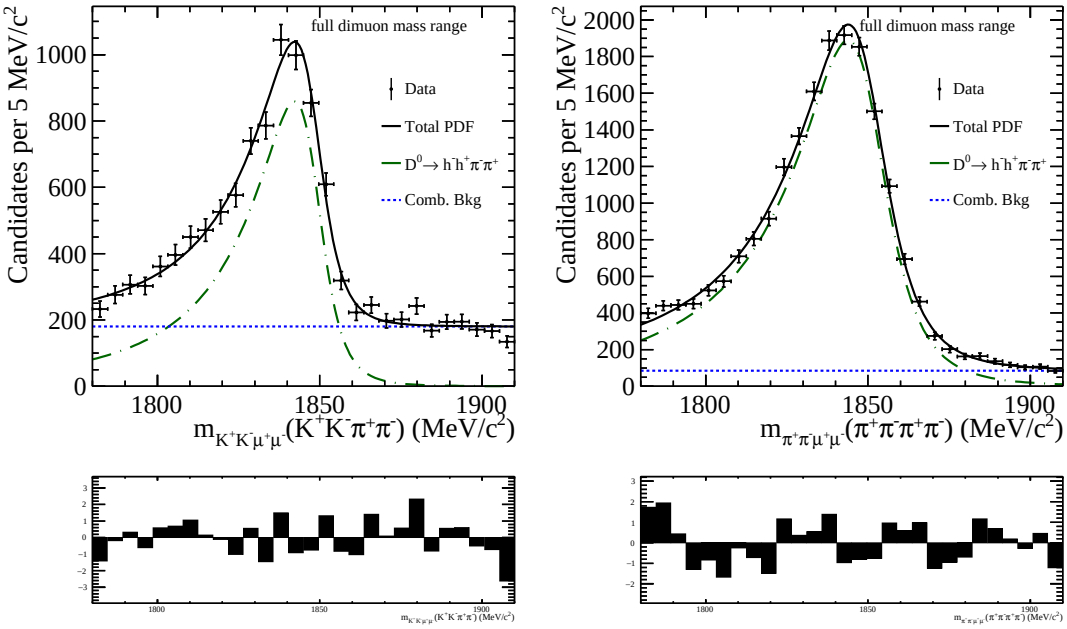

Figure 4.3: Fit to the D^0 mass distribution of data samples of hadronic (left) $D^0 \to K^+K^-\pi^+\pi^-$, and (right) $D^0 \to \pi^+\pi^-\pi^+\pi^-$ decays, where two oppositely charged pions have muon mass assigned (as indicated by the notation of the x-axis label) and one of those pions has also muon PID requirements (modified from [6]).

is not possible to apply the same selection to the control samples without revealing signal decays and ending up with unusable statistics, only looser requirements are imposed on muon particle identification. In particular, this means that only one of the pions is required to be identified as a muon. The consequence of the inability to select the control samples with exactly the same requirements used for the main sample is a source of systematic uncertainty that will be discussed later.

The D^0-mass shape of the combinatorial background is parametrised by an exponential function and determined directly on data.

$$\mathcal{E}^{comb}(m|\gamma) = \frac{1}{\mathcal{N}_{\mathcal{E}}} e^{\gamma \cdot m}$$

However, the very low statistics does not allow to leave the exponent γ free to float in the fits. Instead, a sideband in Δm is identified, which is used to fix the exponent of the PDFs before. To suppress signal-like random D^0 candidates, which are uniformly distributed in Δm, the BDT defined in chapter 3 is used in the sideband region by an inverted requirement. Potential effects of the sideband definition on the background shape will be treated as systematic uncertainties. Two example fits are shown in Figure 4.4 for $D^0 \to K^+K^-\mu^+\mu^-$ (left) and $D^0 \to \pi^+\pi^-\mu^+\mu^-$

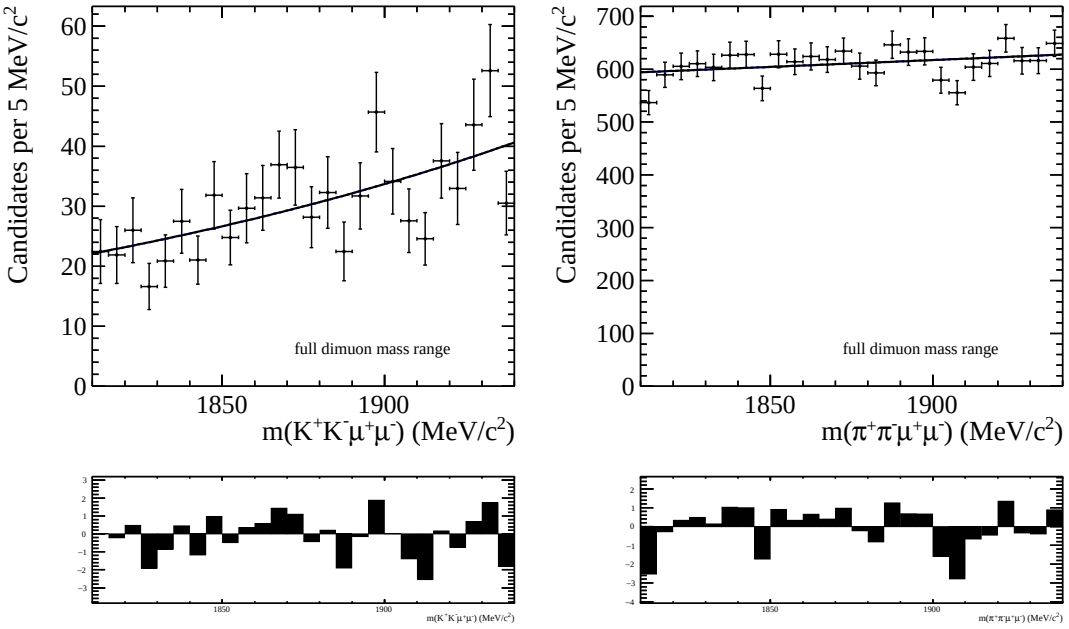

Figure 4.4: Fit to the D^0 mass distribution of data samples in the (Δm, BDT) sideband as defined in the text for (left) $D^0 \to K^+K^-\mu^+\mu^-$ and (right) $D^0 \to \pi^+\pi^-\mu^+\mu^-$ candidates (modified from [6]).

(right).

The total PDF to describe the measured mass distribution is the sum of the signal and the two background components with appropriate coefficients N_{sig}, N_{misID} and N_{comb} describing the yields of signal, misidentified and combinatorial backgrounds, respectively:

$$\mathcal{PDF}(m|N_{sig}, N_{misID}, N_{comb}) = N_{sig} \cdot \mathcal{J}^{sig} + N_{misID} \cdot \mathcal{J}^{misID} + N_{comb} \cdot \mathcal{E}^{comb}$$

As all shape parameters are fixed, the only free parameters of the fit are the yields. Example for a total PDFs used to fit the $m(D^0)$ distributions of $D^0 \to K^+K^-\mu^+\mu^-$ and $D^0 \to \pi^+\pi^-\mu^+\mu^-$ candidates is shown in Figure 4.5. Because of the smaller amount of energy released in the decay, the width of $D^0 \to K^+K^-\mu^+\mu^-$ signals is smaller compared to the $D^0 \to \pi^+\pi^-\mu^+\mu^-$ mode. Furthermore, as the effect of bremsstrahlung is more suppressed for kaons, the low-mass tail of the signal distribution of $D^0 \to K^+K^-\mu^+\mu^-$ decays is less pronounced.

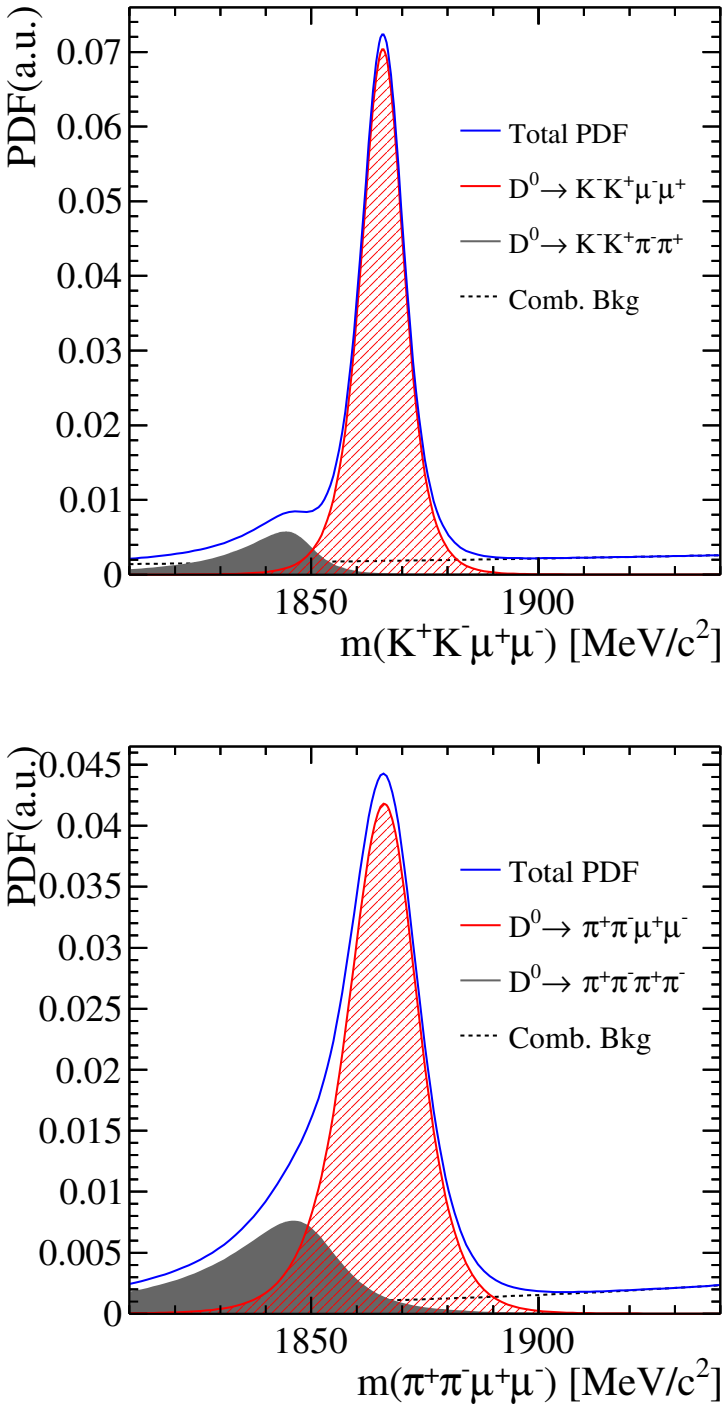

Figure 4.5: Examples of the total PDFs used to fit the $m(D^0)$ distributions of (top) $D^0 \to K^+K^-\mu^+\mu^-$ and (bottom) $D^0 \to \pi^+\pi^-\mu^+\mu^-$ candidates.

5 First observation and branching fraction measurement

This chapter describes the first observation and the determination of the branching fractions for $D^0 \to \pi^+\pi^-\mu^+\mu^-$ and $D^0 \to K^+K^-\mu^+\mu^-$ decays.

5.1 Measurement strategy

Decays of D^0 mesons to $\pi^+\pi^-\mu^+\mu^-$ and $K^+K^-\mu^+\mu^-$ final states have never been observed before. The first goal is therefore to perform a *search* for these decays and measure or put limits on branching fractions, depending on whether a significant signal is found or not.

Experimentally, a determination of an absolute branching fraction of a decays $D^0 \to f$ can be done by measuring the yield of all produced D^0 mesons, as well as the amount of D^0 decays to final state f. This is challenging because it relies on a precise knowledge of the D^0 production rate (luminosity times cross-section) and on the determination of absolute reconstruction and selection efficiencies for the given final state f. A simpler approach which is subject to smaller uncertainties is to perform the branching fraction measurement relative to a *normalisation* decay mode having similar topology. In this analysis, the decay mode $D^0 \to K^-\pi^+[\mu^+\mu^-]_{\rho^0/\omega}$ is chosen, where the two muons are consistent with coming from a ρ^0/ω resonance (dimuon mass in the range $675 - 875\,\mathrm{MeV}/c^2$). The ratio between signal and normalisation branching fractions can be computed as follows:

$$\frac{\mathcal{B}(D^0 \to h^+h^-\mu^+\mu^-)}{\mathcal{B}(D^0 \to K^-\pi^+\mu^+\mu^-)} = \frac{N(D^0 \to h^+h^-\mu^+\mu^-)}{N(D^0 \to K^-\pi^+\mu^+\mu^-)} \, \frac{\epsilon(D^0 \to K^-\pi^+\mu^+\mu^-)}{\epsilon(D^0 \to h^+h^-\mu^+\mu^-)}, \quad (5.1)$$

where N are the observed yields and ϵ the total reconstruction and selection efficiencies[1]. Only the ratio of yields and ratio of efficiencies for signal and normal-

[1]For better readability, $D^0 \to K^-\pi^+[\mu^+\mu^-]_{\rho^0/\omega}$ is abbreviated as $D^0 \to K^-\pi^+\mu^+\mu^-$ if it is used as an argument in the following.

	$m(\mu^+\mu^-)$ [MeV/c^2]				
Decay mode	low mass	η	ρ^0/ω	ϕ	high mass
$D^0 \to K^+K^-\mu^+\mu^-$	< 525	$525 - 565$	> 565	NA	NA
$D^0 \to \pi^+\pi^-\mu^+\mu^-$	< 525	$525 - 565$	$565 - 950$	$950 - 1100$	> 1100

Table 5.1: Definition of the dimuon-mass bins used in the analysis. The bins that are not kinematically allowed are indicated with the acronym NA (modified from [5]).

isation mode need to be determined. It is very convenient to determine relative quantities instead of absolute ones, as many systematic effects are cancelled in the ratio if the two final states are similar. The $D^0 \to K^-\pi^+[\mu^+\mu^-]_{\rho^0/\omega}$ candidates are built and preselected in full analogy to the $D^0 \to h^+h^-\mu^+\mu^-$ signal candidates as described in chapter 3. The signal branching fraction can be determined from Equation 5.1, using as external input the branching fraction of the normalisation mode measured by LHCb [119]:

$$\mathcal{B}(D^0 \to K^-\pi^+[\mu^+\mu^-]_{\rho^0/\omega}) = (4.17 \pm 0.12\,_{\text{(stat)}} \pm 0.40\,_{\text{(syst)}}) \cdot 10^{-6}.$$

To gain discrimination between the short-distance (SD) and long-distance (LD) contributions to the branching fraction, the analysis is performed in different bins of the dimuon mass as defined in Table 5.1. Three of these cover the regions which are expected to be dominated by intermediate resonances (η, ρ^0/ω and ϕ), while the high and low dimuon-mass regions are defined such that the influence of the resonances is minimal. If a significant signal is observed in a dimuon-mass region, the branching fraction is measured. Otherwise, an upper limit is set. No further attempt to separate the SD and LD contributions within a dimuon-mass region is done. Note that the reduced energy released in the $D^0 \to K^+K^-\mu^+\mu^-$ decay restricts the measurement to the first three dimuon-mass regions; the ϕ and high dimoun-mass regions are kinematically not accessible. Furthermore, the total dimoun-mass integrated branching fraction for the two signal decays will be computed at the end.

The measurement uses about $2\,\text{fb}^{-1}$ of integrated luminosity collected by LHCb during 2012 and has been performed as *blind* analysis in the regions of the dimuon-mass spectrum where no signal is expected. This means, the measured quantities as well as the mass projections remained unknown and were examined only after the analysis procedure had been finalised. Blinding is a common procedure in experimental high-energy physics to avoid potential experimenter's bias on the measurement. The ϕ and ρ^0/ω regions of the dimuon mass in the $D^0 \to \pi^+\pi^-\mu^+\mu^-$ case were not blinded and used to validate the quality of the fits and evaluate

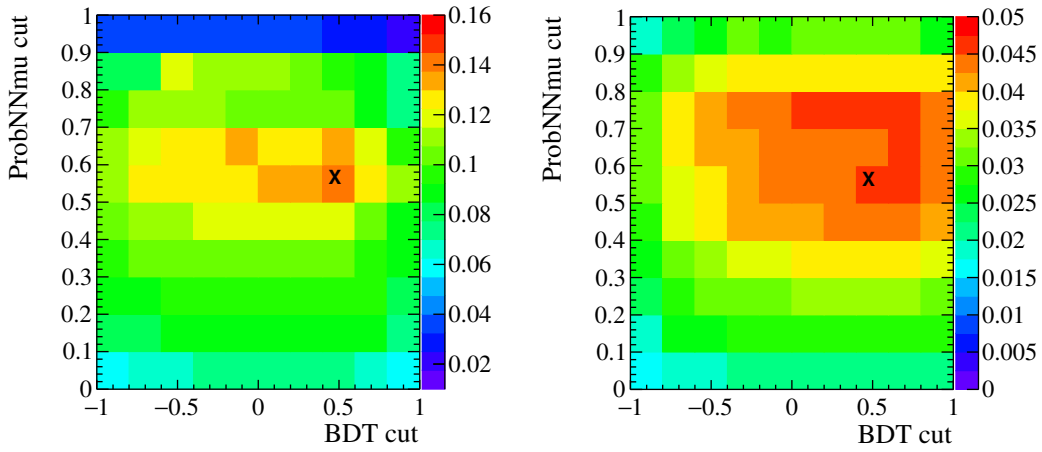

Figure 5.1: Figure-of-merit scan in the two dimensional space of minimum BDT and ProbNNmu requirements for (left) $D^0 \to K^+K^-\mu^+\mu^-$ and (right) $D^0 \to \pi^+\pi^-\mu^+\mu^-$ decays. Only the subsets with positive polarity are shown. The black crosses represent the chosen/optimal selection requirements [5].

systematic uncertainties.

5.2 Selection optimisation

The measurement of the branching fractions aims at a first discovery of the signal channels $D^0 \to \pi^+\pi^-\mu^+\mu^-$ and $D^0 \to K^+K^-\mu^+\mu^-$. The BDT and ProbNNmu selection criteria are optimised to maximise the chances of discovery by maximising the value of the figure of merit [184]

$$\text{FOM} = \frac{\epsilon_{\text{sig}}}{a/2 + \sqrt{N_{\text{bkg}}}},$$

where ϵ_{sig} is the signal efficiency and N_{bkg} is the total background yield, *i.e.* the sum of the combinatorial and the misidentified background yields in the signal range. The parameter a is set to be $a = 5$ to optimise the selection for a statistical signal significance of 5σ. The background yields N_{bkg} are determined from blind fits to the data (following the model introduced in chapter 4), while the signal efficiency ϵ_{sig} is estimated using simulated samples. The optimal selection configuration is found in a scan of the two-dimensional space of the minimal ProbNNmu and BDT requirements, where the requirement on ProbNNmu is applied to both muons. To avoid unwanted biases, the data is split into two disjoint sub-samples (selected according to the magnet polarity[2]) and the scan in performed independently in

[2] As explained in chapter 2, the polarity of the LHCb dipole magnet is periodically switched, leading to two disjoint sub-samples with similar statistics.

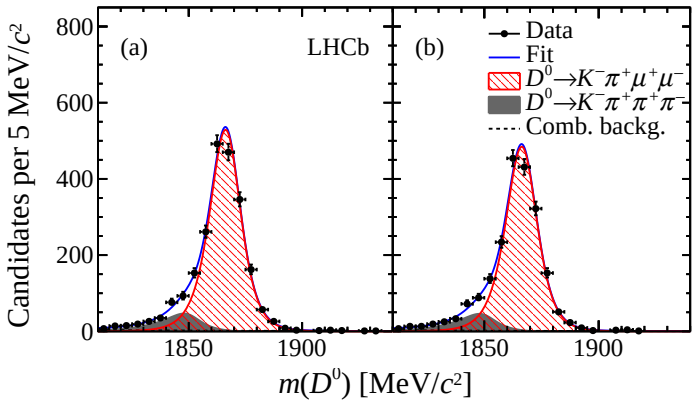

Figure 5.2: D^0 mass distributions for the $D^0 \to K^-\pi^+[\mu^+\mu^-]_{\rho^0/\omega}$ decays resulting from the selection optimised for (left) $D^0 \to \pi^+\pi^-\mu^+\mu^-$ and (right) $D^0 \to K^+K^-\mu^+\mu^-$ signals (and fit projections overlaid) [3].

each of these, where compatible results are observed. Figure 5.1 shows the results of the scan for both signal channels, on the samples with positive polarity. The maximum of the figure of merit is found to be at the requirements `ProbNNmu`> 0.5 and `BDT`> 0.4 for both decays.

To minimize the uncertainty on the efficiency ratio, the normalisation mode is filtered with exactly the same requirements as the signal modes. As the BDT was trained separately for both signal decay modes, the normalisation mode is classified with both BDTs. When used to normalise $D^0 \to \pi^+\pi^-\mu^+\mu^-$ decays, the corresponding selection was applied, and accordingly when normalising $D^0 \to K^+K^-\mu^+\mu^-$ decays.

5.3 Yields determination

In each dimuon-mass region, the yields are obtained by using one dimensional extended maximum likelihood fits to the D^0 mass of fully selected signal candidates as explained in chapter 4. An analogous model for $D^0 \to K^-\pi^+[\mu^+\mu^-]_{\rho^0/\omega}$ decays is defined. To account for a mismodelling of the signal shape in the simulated samples, two scale factors allowing for an adjustment of the width (s_1) and peak position (s_2) are introduced. These factors are left free to float in the fit to the normalisation mode. Due to the low statistics, the scale factors cannot be left free to float in the fits to the signal modes. Instead, they are fixed to the numerical values $s_1 = 1.10 \pm 0.03$ and $s_2 = 1.00003 \pm 0.0001$ obtained from the $D^0 \to K^-\pi^+[\mu^+\mu^-]_{\rho^0/\omega}$ fits. The D^0 mass spectra of the normalisation mode for the $D^0 \to \pi^+\pi^-\mu^+\mu^-$ and $D^0 \to K^+K^-\mu^+\mu^-$ selections are shown in Figure 5.2 with fit projections overlaid. The D^0 mass spectra and fit projections of the signal

Channel	$m(\mu^+\mu^-)$ [MeV/c^2]	N_{sig}	N_{misID}	N_{comb}	significance	
					p-Value	Gaussian σ
$D^0 \to K^-\pi^+[\mu^+\mu^-]_{\rho^0/\omega}$						
selection $\pi^-\pi^-\mu^+\mu^-$	$675-875$	1971.2±50.5	258.1±37.6	42.5±20.9		
selection $K^-K^-\mu^+\mu^-$	$675-875$	1805.9±48.3	254.0±34.5	35.1±18.4		
$D^0 \to \pi^+\pi^-\mu^+\mu^-$	< 525	26.6±6.4	24.7±6.8	19.7±6.5	$5 \cdot 10^{-8}$	5.4
	$525-565$	4.9±2.6	8.1±3.1	0.0±0.8	$7 \cdot 10^{-3}$	2.5
	$565-950$	208.3±16.7	64.3±13.1	49.4±11.9	$7 \cdot 10^{-73}$	18.0
	$950-1100$	311.9±19.7	29.3±12.3	40.8±10.9	$5 \cdot 10^{-120}$	23.3
	> 1100	9.4±5.7	7.2±6.4	43.3±8.7	$6 \cdot 10^{-2}$	1.6
$D^0 \to K^+K^-\mu^+\mu^-$	< 525	5.4±2.6	0.0±1.4	6.5±2.8	$9 \cdot 10^{-4}$	3.1
	$525-565$	–	–	–		
	> 565	28.6±5.4	3.4±2.1	0.0±24.3	$2 \cdot 10^{-16}$	8.1

Table 5.2: The yields extracted by the one dimensional fit for all channels and dimuon-mass bins with their uncertainties. For the signal modes, the scale factors for width and mean of the distribution are fixed to the values as obtained by the fit to the normalisation mode (modified from [5]).

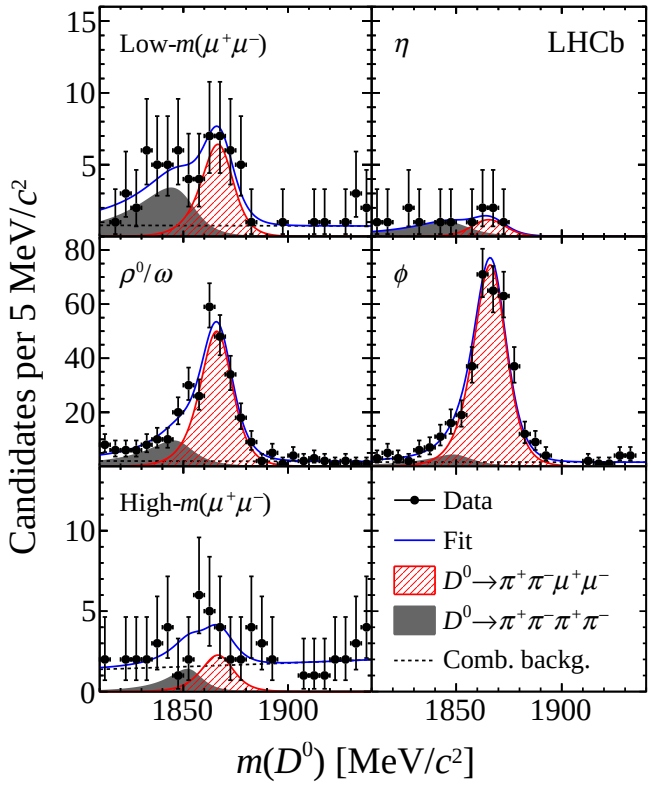

Figure 5.3: D^0 mass distributions for selected $D^0 \to \pi^+\pi^-\mu^+\mu^-$ candidates in the low-$m(\mu^+\mu^-)$, η, ρ^0/ω, ϕ and high-$m(\mu^+\mu^-)$ regions (with fit projections) [1].

$D^0 \to \pi^+\pi^-\mu^+\mu^-$ and $D^0 \to K^+K^-\mu^+\mu^-$ decays are shown in Figure 5.3 and Figure 5.4, separately for the 5(3) dimuon-mass regions. No fit can be performed in the η dimuon-mass region of $D^0 \to K^+K^-\mu^+\mu^-$, where only two candidates are observed. In all other dimuon-mass bins a fit is performed. The determined signal and background yields are reported in Table 5.2.

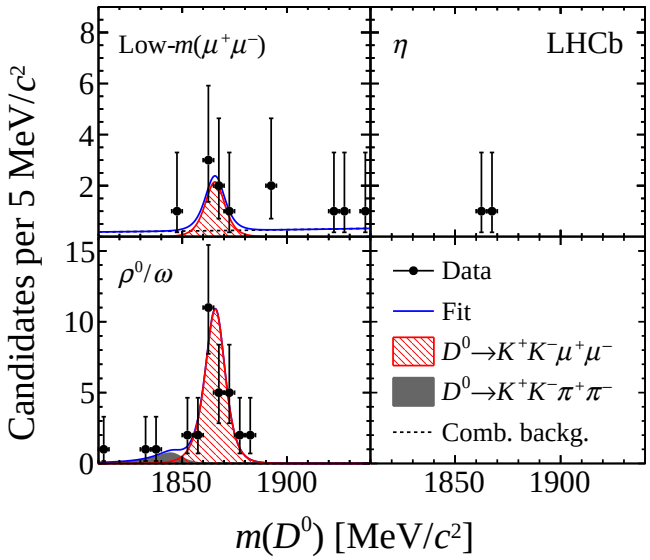

Figure 5.4: D^0 mass distributions for selected $D^0 \to K^+K^-\mu^+\mu^-$ candidates in the low-$m(\mu^+\mu^-)$, η and ρ^0/ω regions (with fit projections). No fit can be performed in the η region, where only two candidates are found [1].

The fitter has been validated using a large number of pseudo-experiments. The fit procedure is stable and returns unbiased estimates of the yields and the uncertainties in the range of interest for the signal branching fraction ($\geq 10^{-8}$) as shown in Appendix C.

The *statistical significance* of the signal in each dimuon-mass region is estimated from the likelihood ratio between the signal-plus-background hypothesis and the background-only hypothesis, using Wilks' theorem [185]. From these ratios, p-values are computed for the background-only hypothesis as reported in Table 5.2. Furthermore, the p-values are translated into equivalents of Gaussian standard deviations σ, such that $\int_\sigma^\infty \frac{1}{\sqrt{2\pi}} \exp(-x^2/2)dx = p$. The branching fraction is computed only for regions where the statistical significance exceeds 3σ, and upper limits are set for the others.

5.4 Efficiency ratio determination

This section describes the determination of the ratio of the total reconstruction and selection efficiencies for signal and normalisation modes, $\epsilon(h^+h^-\mu^+\mu^-)/\epsilon(K^-\pi^+\mu^+\mu^-)$, which is the second essential component of the analysis. The total efficiency ϵ for each decay mode can be written as product of

the following partial efficiencies:

$$\epsilon = \epsilon_{\text{acc}} \cdot \epsilon_{\text{presel}} \cdot \epsilon_{\text{PID}} \cdot \epsilon_{\text{trig}} \cdot \epsilon_{\text{BDT}},$$

Here, the individual components are detector acceptance, preselection efficiency, PID efficiency, trigger efficiency and defined as follows:

$$\begin{aligned}
\epsilon_{\text{acc}} &= N_{\text{in acceptance}}/N_{\text{produced}}, \\
\epsilon_{\text{presel}} &= N_{\text{reconstructed and preselected}}/N_{\text{in acceptance}}, \\
\epsilon_{\text{PID}} &= N_{\text{passing PID selection}}/N_{\text{reconstructed and preselected}}, \\
\epsilon_{\text{trig}} &= N_{\text{passing trigger requirements}}/N_{\text{passing PID selection}}, \\
\epsilon_{\text{BDT}} &= N_{\text{passing BDT selection}}/N_{\text{passing trigger requirements}},
\end{aligned}$$

where N are the yields before and after the selection steps as indicated by the subscripts. Note that the partial efficiencies are defined as conditional efficiencies, *i.e.* under the condition of having past all previous selection steps, such as the partial efficiencies can be determined from distinct samples while the remaining parts are estimated from simulations. Only the ratios between the efficiencies of the signal and normalisation decays are reported. Figure 5.5 shows the ratios of the partial efficiencies as function of dimuon mass. The PID and trigger efficiencies are further split into hadron and muon PID efficiency and L0 and Hlt trigger efficiencies, respectively. A more detailed description is given in the following sections.

LHCb acceptance, reconstruction and preselection efficiency

Due to the LHCb detector geometry, which is only covering a limited region of the solid angle in the forward region, only a fraction of the produced signal decays falls within the acceptance. Large simulated samples of signal and normalisation decays are generated and the fraction of candidates where the final state particles are found within the detector acceptance ϵ_{acc} is computed in all dimuon-mass regions. The ratio of acceptances for signal and normalisation modes are shown in the top row of Figure 5.5. Simulated candidates passing the acceptance requirement are further processed and the combined efficiency ϵ_{presel} for the reconstruction and preselection criteria as described in chapter 3 is computed. After the offline reconstruction, also simulated samples contain a small contamination of incorrectly reconstructed backgrounds in the order of a few percent. These backgrounds can be removed by *truth matching*, an algorithm that tries to associate the reconstructed particles with

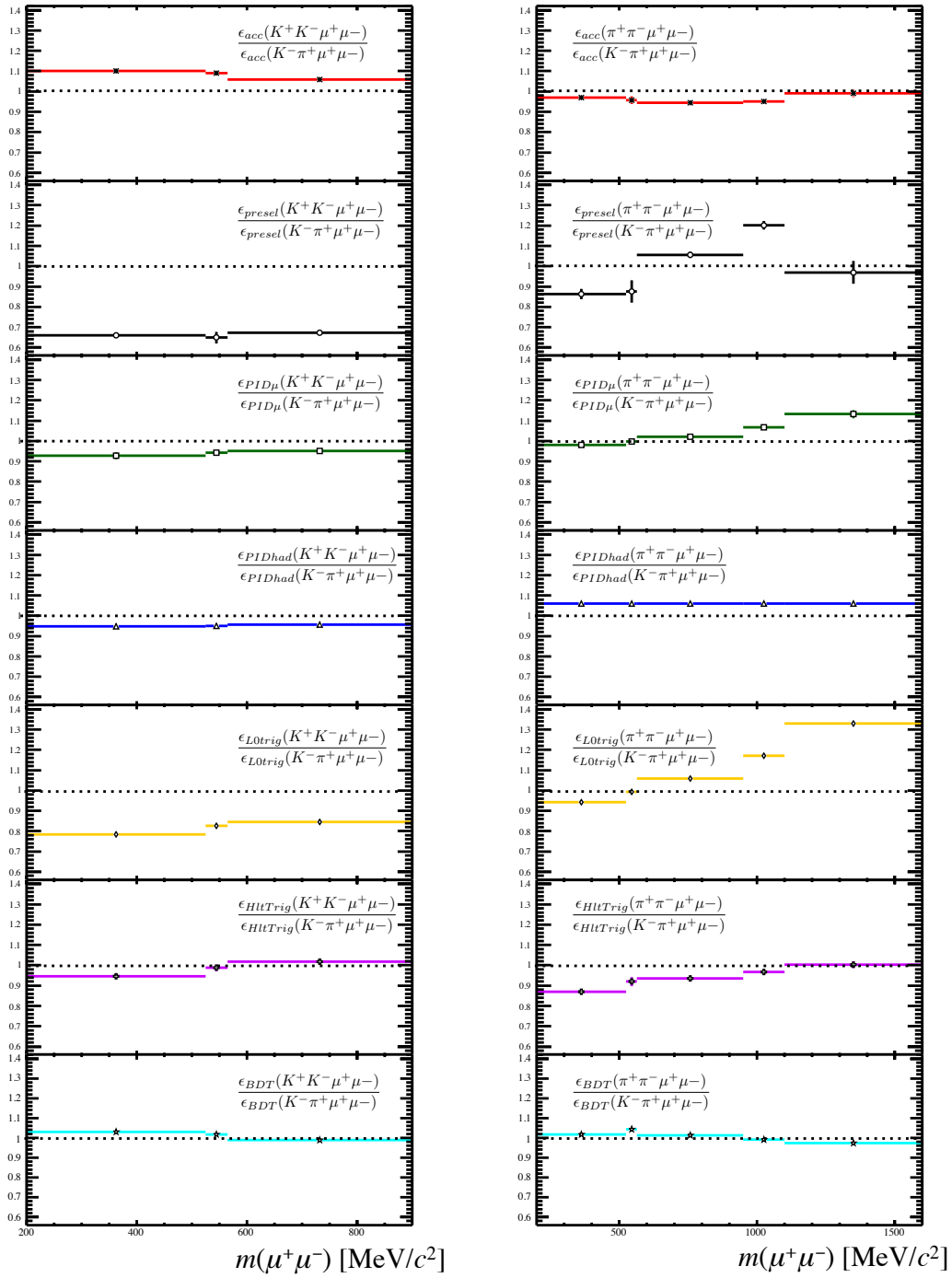

Figure 5.5: Summary of the individual components of the relative signal to normalisation mode efficiency, to be explained in more detail in the text. From top to bottom: Detector acceptance (ϵ_{acc}), combined resconstruction and preselection efficiency (ϵ_{presel}), muon and hadron PID efficiencies (ϵ_{PID}), trigger selection efficiency ϵ_{trig} and BDT selection efficiency (ϵ_{BDT}). Left is for $D^0 \to K^-K^+\mu^+\mu^-$ and right for $D^0 \to \pi^-\pi^+\mu^+\mu^-$ (modified from [5]).

the generated ones. The matching criteria is a somewhat arbitrary requirement that by itself has a certain efficiency. For this reason, the yields are determined using fits to the D^0 mass distributions of the simulated candidates that do not have any truth-matching requirement. In these fits, the background component is described by a simple exponential function, while the signal is described by the nominal model (a Johnson's S_U distribution) as explained in chapter 4. A systematic uncertainty is assigned due to these assumptions in section 5.5. The results of the combined relative reconstruction and preselection efficiency is shown in Figure 5.5. Due to differences between the kinematical distributions of the final state particles (*e.g.* momenta, opening angles), in $D^0 \to K^+K^-\mu^+\mu^-$ decays a significantly lower reconstruction efficiency is measured compared to $D^0 \to \pi^+\pi^-\mu^+\mu^-$. Note that in the definition of the combined reconstruction and preselection efficiency, resolution effects of the dimuon mass are also taken into account. In particular, the probability of a D^0 candidate to be reconstructed in a dimuon-mass region that is different than the region in which the true (*i.e.* generated) dimuon mass falls, is included in the efficiency.

Particle identification efficiency

The PID efficiency is split into two terms, $\epsilon_{PID\mu}$ and ϵ_{PIDh}, corresponding to the efficiencies of the PID requirements on the final state muons and hadrons, respectively. Each of these terms is evaluated using a data-driven approach as implemented in the `PIDCalib` software package [186] of LHCb. The package allows to determine the efficiency for a given PID selection requirement using a *tag and probe* method, where a *tag* particle is tightly selected to clean the high statistic calibration samples from unwanted backgrounds and the *probe* particle is used to determine the efficiency. Samples of $J/\psi \to \mu^+\mu^-$ decays are used to determine the muon PID efficiency and $D^{*+} \to D^0(\to K^-\pi^+)\pi^+$ decays are used for kaon and pion PID efficiencies. As the PID information is mainly based on information of the RICH detectors, the performance (and consequently the efficiency for a PID requirement) is highly depended on the kinematics of a particle. To cope with the different kinematics of the particles in the calibration and signal samples, the efficiency is evaluated in a user defined multidimensional phase-space binning. In this analysis, a two dimensional binning in $(p;\eta)$ is chosen. Details on the binning scheme for each particle species can be found in Appendix B. In each bin i, the efficiency ϵ_i is measured in the calibration sample. As proxy for the kinematics of the signal decays, simulated candidates are used as reference samples. The average efficiency $\bar{\epsilon}$ in the signal samples can then be simply calculated by computing the

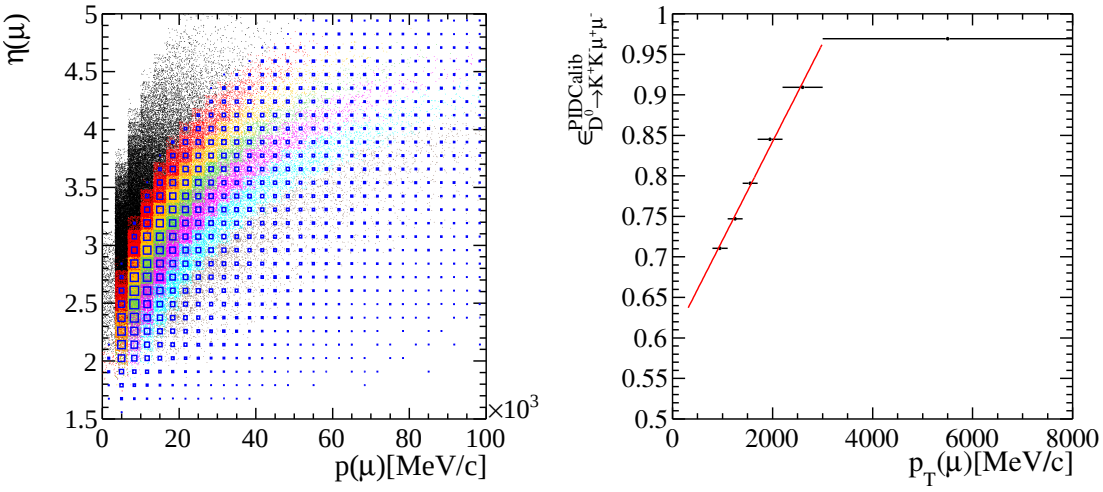

Figure 5.6: (Left) p-η space for muons coming from simulated $D^0 \to K^+K^-\mu^+\mu^-$ decays. Each color corresponds to a certain $p_T(\mu)$ range, which appears as bands in this space. Overlaid in blue boxes is the PID calibration sample, not covering the black low $p_T < 800\,\text{MeV}$ band of the signal sample. (Right) The single muon PID efficiency in $p_T(\mu)$ bins (*i.e.* evaluated in each coloured band) and the extrapolation to the regime not covered by the calibration sample (modified from [5]).

weighted average over all bins:

$$\bar{\epsilon} = \frac{\sum_{i \in bins} N_i \epsilon_i}{\sum_{i \in bins} N_i} \tag{5.2}$$

with N_i being the number of simulated candidates in the reference sample in bin i. The statistical uncertainty caused by the limited size of the control samples is negligibly small. The uncertainty on the PID efficiency will be dominated by systematic effects as discussed in section 5.5.

To estimate the PID efficiency from data calibration samples, a full coverage of the phase-space distributions of the signal final state particles by the calibration samples must be assured. This is not the case for the muons selected in this analysis as shown in Figure 5.6, where the two dimensional $(p;\eta)$ distributions of muons in the signal and calibration data samples are compared. The uncovered (black coloured) region is the effect of a $p_T > 800\,\text{MeV}/c$ requirement present in the selection of the calibration samples, which appears as a band in the $(p;\eta)$ space. Depending on the considered dimuon-mass region of the signal decays, the $p_T(\mu) < 800\,\text{MeV}/c$ region contains $\sim 20\%$ of the signal candidates. Removing these signal candidates is therefore not desirable. To overcome this problem, the reference sample is split in regions of muon p_T and the single muon PID efficiency is determined using Equation 5.2 in each of these. The efficiency evaluated for

$p_T > 800\,\text{MeV}/c$ is extrapolated with a linear fit into the region below $800\,\text{MeV}/c$ (down to the minimum threshold of $300\,\text{MeV}/c$) as shown in the right panel of Figure 5.6. A conservative uncertainty, corresponding to the full variation of the fit function within the low p_T region, is assigned. As the extrapolated low p_T efficiencies for muons in all signal decays (and also evaluated individually in each dimuon-mass region) turn out to be compatible, a single averaged value is used in all cases. In particular, the same value for signal and normalisation mode is assumed, leading to a large cancellation in the ratio of efficiencies. The total single muon PID efficiency is then the average of the efficiencies $\epsilon_{\text{PID}\mu}(p_T > 800\,\text{MeV}/c)$ as evaluated from the control sample and $\epsilon_{\text{PID}\mu}(300\,\text{MeV}/c < p_T < 800\,\text{MeV}/c)$ obtained from the extrapolation, weighted by their fractions as taken from simulations.

The final muon PID efficiency, is calculated as the product of the two single muon PID efficiencies. Apart from kinematical correlations, which are taken care of by the binning in $(p;\eta)$, the two efficiencies are assumed to be independent, since only D^0 candidates are selected where the two muon do not share any hits in the muon stations. However, the assumption has also been validated in simulations.

The determination of the hadron PID efficiency is straightforward as the control samples fully cover the kinematical distributions of all final state hadrons of the signal decays. The total hadron PID efficiency ϵ_{PIDhad} is again the product of the individual contributions of each final state hadron.

The results of the relative signal to normalisation mode muon and hadron PID efficiencies are shown in Figure 5.5.

Trigger selection efficiency

The trigger efficiency ϵ_{trig} is split into two parts, the efficiency of the lowest level hardware trigger selection ϵ_{L0Muon} and the software high level trigger ϵ_{Hlt}.

The branching fraction measurement uses only D^0 candidates with at least one of the two muons associated to the trigger signal responsible for a positive decision of `L0Muon`. Generally, the efficiency of `L0Muon` is very high ($> 90\%$) as long as the offline reconstructed p_T of the muon is well above the trigger threshold of $\gtrsim 1.7\,\text{GeV}/c$, which is not true for muons coming from $D^0 \to h^+h^-\mu^+\mu^-$ decays. Since it is not clear if the hardware trigger efficiency at the threshold is reliably modelled in simulations, ϵ_{L0Muon} is also determined directly on data using a calibration sample of $D_s^+ \to \pi^+[\mu^+\mu^-]_\phi$ decays recorded under the same conditions as the signal decays. Analogous to the signal selection, the two muons in the calibration sample must not share any hits in the muon stations. As done for the PID efficiency, ϵ_{L0Muon} for a single muon is evaluated using a *tag and probe*

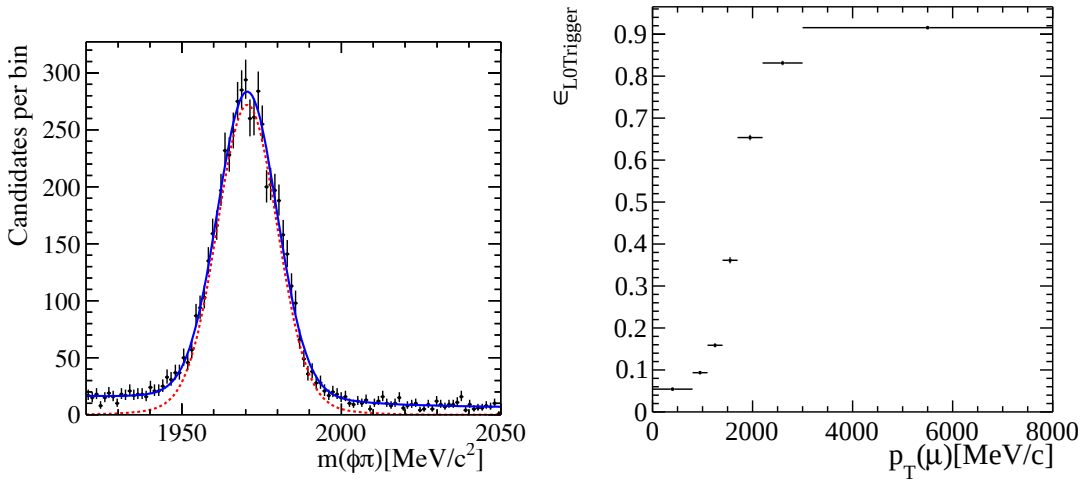

Figure 5.7: Example mass fit (left) to the D_s^+ mass of $D_s^+ \to \pi^+[\mu^+\mu^-]_\phi$ decays, corresponding to the range $3 < p_T < 8\,\text{GeV}/c$ of the probe muon. Single-muon `L0Muon` trigger efficiency (right) as function of the probe muon p_T [5].

method. The efficiency on the trigger selection requirement is then just obtained by dividing the yield of D_s^+ candidates where the *probe* fulfils the trigger selection requirement by:

$$\epsilon_{\texttt{L0Muon}} = \frac{N(\mu_{\text{probe}}^{\text{firedTrigger}} | \mu_{\text{tag}}^{\text{tightly selected}})}{N(\mu_{\text{tag}}^{\text{tightly selected}})}.$$

The yields are obtained through fits to the D_s^+ mass distribution as shown in the left panel of Figure 5.7.

Similar to the PID efficiency, the $L0$ efficiency for a single muon is measured in bins of the muon transverse momentum (right panel of Figure 5.7) to account for the different kinematic distributions of the signal and calibration samples. As the binning is based on the offline-reconstructed momenta, the trigger threshold $p_T \gtrsim 1.7\,\text{GeV}/c$ is smeared by the limited resolutions at hardware trigger level. The efficiency of the logical OR requirement is calculated from the single-muon efficiency as

$$\epsilon_{\texttt{L0Muon}}(\mu_0\,\text{OR}\,\mu_1) = \epsilon_{\texttt{L0Muon}}(\mu_0) + \epsilon_{\texttt{L0Muon}}(\mu_1) - \epsilon_{\texttt{L0Muon}}(\mu_0) \cdot \epsilon_{\texttt{L0Muon}}\ (\mu_1). \quad (5.3)$$

Equation 5.3 is evaluated on a candidate-by-candidate basis using simulated candidates as proxies for the signal muon kinematics. The final efficiency $\epsilon_{\texttt{L0Muon}}$ is then the averaged value over all candidates.

The effect of limited statistics of the control sample is evaluated by performing pseudo-experiments. As the efficiencies of two tracks are correlated if they fall into

the same p_T bin, in each pseudo-experiment all bins are fluctuated according to a normal distribution with the bin content as mean and the bin uncertainty as width. The whole efficiency determination is repeated with the fluctuated histogram resulting in a new efficiency $\epsilon'_{\texttt{LOMuon}}$ for each pseudo-experiment. The uncertainty $\Delta\epsilon_{\texttt{LOMuon}}$ is then defined as the standard deviation of the resulting distribution of $\epsilon'_{\texttt{LOMuon}}$.

Apart from kinematics, no additional relevant correlations between the two final state muons are expected as the muons do not share any hits in the muon system, which is the subdetector mainly responsible for the trigger decision. The validity of the *tag and probe* method is checked and systematic uncertainties due to its potential limitations are studied in section 5.5.

The efficiency of the Hlt selection ϵ_{Hlt}, which is purely based on software, is determined using simulated samples and results are shown in Figure 5.5. The quoted Hlt selection efficiency is the combined Hlt1 and Hlt2 selection requirements.

MVA selection efficiency

The last remaining part of the total efficiency is related to the BDT requirement. As the BDT was trained separately for both signal channels, the relative BDT selection efficiencies shown in Figure 5.5 are normalised by different BDT selection efficiencies for the normalisation mode. When normalising $\epsilon(\pi^+\pi^-\mu^+\mu^-)$, the efficiency of the BDT trained with $D^0 \to \pi^+\pi^-\mu^+\mu^-$ candidates on $D^0 \to K^-\pi^+[\mu^+\mu^-]_{\rho^0/\omega}$ candidates is used, and accordingly the BDT trained on $D^0 \to K^+K^-\mu^+\mu^-$ is applied to the normalisation mode in the ratio $\epsilon(K^+K^-\mu^+\mu^-)/\epsilon(K^-\pi^+\mu^+\mu^-)$.

Total efficiency ratio

As anticipated in the beginning of this section, the total relative efficiency is the product of the individual partial efficiencies. The results which will enter the branching fraction computation are shown in Figure 5.8. As parts of the efficiency (*e.g.* reconstruction and preselection, L0 muon trigger, muon PID) strongly depend on the momenta of the muons, which on average increase as a function of dimuon mass, the total efficiency ratio increases as function thereof. This is also the reason why the ratio of efficiencies is larger than unity for $D^0 \to \pi^+\pi^-\mu^+\mu^-$ decays in dimuon-mass regions which are significantly higher compared to the normalisation mode. For $D^0 \to K^+K^-\mu^+\mu^-$ decays, the reduced decay phase space leads to lower momenta of the D^0 daughter muons and thus to a reduced efficiency in general.

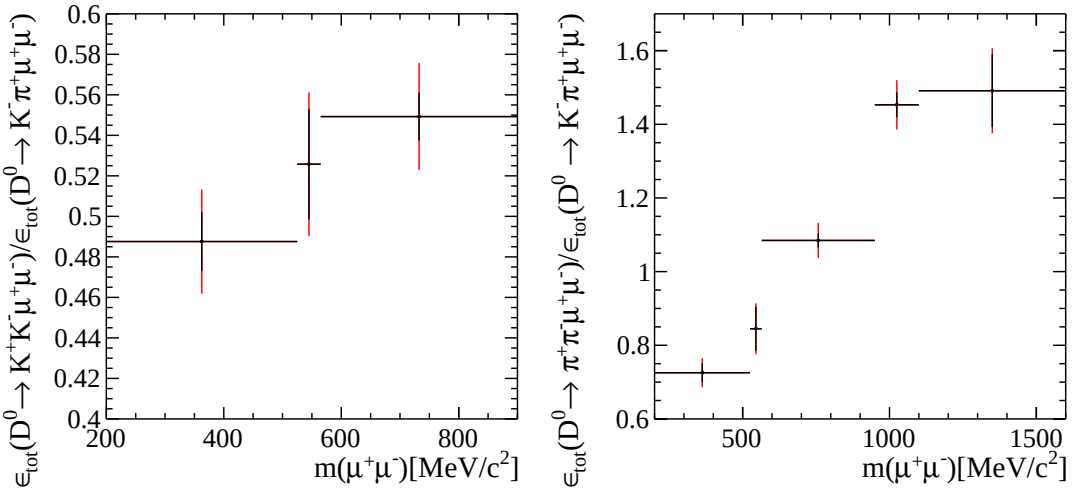

Figure 5.8: The total relative efficiency as a function of the dimuon mass for (left) $D^0 \to K^-K^+\mu^+\mu^-$ and (right) $D^0 \to \pi^-\pi^+\mu^+\mu^-$ decays. The black error bars report only statistical uncertainties, the red error bars include also the systematic uncertainties discussed in section 5.5 [5].

5.5 Systematic uncertainties

Sources of systematic uncertainties affecting the measurements of the branching fractions can be grouped into three main categories:

- uncertainties due to the limited knowledge of the branching fraction of the normalisation decay;
- uncertainties in the determination of the ratio of yields;
- uncertainties in the determination of the ratio of efficiencies.

Small fractions of background from random soft pions ($\sim 1.4\%$) and secondary D^{*+} mesons ($\sim 1.3\%$) have been neglected. These backgrounds can bias the determination of the measured branching fractions if their fractions in the signal and normalisation mode deviate from each other. As compatible (and very small) fractions of these backgrounds in $D^0 \to h^+h^-\mu^+\mu^-$ and $D^0 \to K^-\pi^+[\mu^+\mu^-]_{\rho^0/\omega}$ decays are estimated from a Δm sideband and simulations, respectively, any bias is below the percent level and negligible compared to other systematic uncertainties. No additional systematic uncertainty due to neglected backgrounds is assigned.

Uncertainty on the normalisation mode branching fraction

The branching fraction of the normalisation mode is measured with a 10% relative uncertainty [119], which is propagated to the signal branching fractions. Being

completely independent of the presented analysis, this uncertainty is quoted as a separate contribution to the total uncertainty and not combined with other systematic uncertainties to allow for an update in case a more precise measurement becomes available.

In the following, the uncertainties related to the determination of the yields and ratio of efficiencies are discussed in detail.

Uncertainties on the ratio of yields

When the ratio of yields $R_{\text{yields}} = \frac{N(D^0 \to h^+h^-\mu^+\mu^-)}{N(D^0 \to K^-\pi^+\mu^+\mu^-)}$ are determined, several arbitrary choices in the description of the PDFs are made, whose impact is now evaluated. In particular, this concerns:

- the effect of residual differences of the signal shape due to differences in simulations and data;
- the inability to select the $D^0 \to h^+h^{(\prime)-}\mu^+\mu^-$ samples used to determine the shape of misidentified hadronic four-body decays with the same requirements as the signal;
- the definition of the sideband region to constrain the shape of the combinatorial background.

Systematic variations of the yield ratio are studied using the ϕ resonance region of $D^0 \to \pi^+\pi^-\mu^+\mu^-$, where the signal was not blind. These uncertainties are directly evaluated on the ratio of yields, as systematic effects are expected to cancel partially.

The PDF used to describe the signal shape is determined from simulated samples. To account for possible simulation-data differences, two scale factors accounting for a possible shift of the maximum and an adjustment of the width are free to float when fitting the normalisation mode. As a systematic check, the scale factors are also left free to float when fitting $D^0 \to \pi^+\pi^-\mu^+\mu^-$ in the ϕ resonance region of the dimuon mass, where, in contrast to other dimuon-mass regions, sufficient statistics allows for a stable fit. A value of 1.01 ± 0.07 is found for the factor scaling the width of the distribution, compatible with what has been obtained in the normalisation mode (1.10 ± 0.03). The scale factor for the mean is compatible with unity at a level of 10^{-4} in both cases. The variation of R_{yield} is investigated using the different scale factors and only a negligible difference is observed. No additional systematic uncertainty is assigned.

As described in chapter 4, when the shape of peaking background from four-body hadronic decays is determined in data control samples, it is not possible to

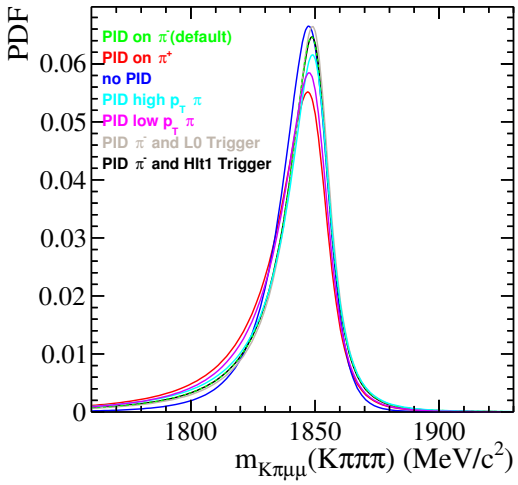

Figure 5.9: Different peaking background shapes we studied to investigate the effect of our inability to select the control samples with exactly the same PID and trigger requirements used for the main samples [5].

apply the same requirements on muon particle identification and trigger selection without revealing signal decays and ending up in unusable small statistics. Instead, only one pion should pass the muon PID criterium, where always the pion with charge opposite to the charge of the tag pion π_s is chosen. In total four alternative requirements are tested.

- muon PID for the pion with the same charge as the π_s;
- muon PID for the pion having larger transverse momentum;
- muon PID for the pion having smaller transverse momentum;
- no muon PID at all.

As the shape depends on the kinematics of the final-state particles and the fraction of pion decays in flight $\pi \to \mu\nu$, which are depending on muon kinematics and muon PID requirements, these alternative requirements are chosen such that large variations on the shape are expected. The resulting PDFs of misidentified $D^0 \to K^-\pi^+\pi^+\pi^-$ can be seen on Figure 5.9. The ratio of yields as obtained by using the alternative background PDFs are reported in Table 5.3. The maximum deviation, which corresponds to a relative change of 1.4% on the ratio, is taken as systematic uncertainty and propagated to all dimuon-mass regions and signal channels. Variations on the assumed background shape in the fits to the hadronic modes produce negligible ($< 0.1\%$) changes on the ratio of yields.

As a reminder, the sideband used to constrain the shape of the combinatorial background is defined by an inverted `BDT` < 0.4 requirement and

Muon PID requirement	Yield of $D^0 \to \pi^+\pi^-[\mu^+\mu^-]_\phi$	Yield of $D^0 \to K^-\pi^+[\mu^+\mu^-]_{\rho^0/\omega}$	Their ratio R_{yields}
Pion with opposite charge as π_s (default)	312 ± 20	1971 ± 51	0.158 ± 0.011
Pion with same charge as π_s	311 ± 20	1992 ± 49	0.156 ± 0.011
Pion with larger p_T	312 ± 20	1986 ± 50	0.157 ± 0.011
Pion with smaller p_T	311 ± 20	1969 ± 51	0.158 ± 0.011
None	311 ± 20	1985 ± 51	0.157 ± 0.011

Table 5.3: Systematic study on the impact of the muon PID requirement for the determination of the peaking-background shapes [5].

$\Delta m > 150\,\text{MeV}/c^2$. The effect of this particular choice on the shape of the combinatorial background is evaluated by the comparison of the results obtained in eight alternative sideband definitions, varying both the requirement on Δm ($> 150\,\text{MeV}/c^2, 150 - 160\,\text{MeV}/c^2, > 165\,\text{MeV}/c^2$) and `BDT` ($< 0.4, < 0$, no BDT requirement). In each of these regions, the coefficient of the exponential background is determined. The variations of the resulting ratio of yields obtained using the alternative PDFs are far below the percent level and negligible compared to the uncertainty on the peaking background PDF.

Finally, the statistical uncertainty on the normalisation mode yield is propagated as systematic uncertainty to the final measurement. After the $D^0 \to \pi^+\pi^-\mu^+\mu^-$ ($D^0 \to K^+K^-\mu^+\mu^-$) selection, normalisation mode yields of 1971.2 ± 50.5 (1805 ± 48.3) are measured, leading to relative statistical uncertainties of $\Delta N_{norm}/N_{norm} = 2.6\%(2.7\%)$.

In summary, the following two relative uncertainties on the ratio of yields are considered:

- 1.4% caused by the limited knowledge of the shape of the peaking background component;
- 2.6% (2.7%) due to the statistical uncertainty of the normalisation mode yields for $D^0 \to \pi^+\pi^-\mu^+\mu^-$ ($D^0 \to K^+K^-\mu^+\mu^-$)

These uncertainties are summed in quadrature and assigned as systematic uncertainty on ratio of yields of each dimuon-mass bin.

Uncertainties on the ratio of efficiencies

The uncertainty on the ratio of efficiencies ΔR_ϵ will be treated as systematic uncertainty on the branching fraction measurement. Foremost, R_ϵ has a statistical component on its own $\Delta R_{\epsilon,stat}$, which results from the limited size of the simulated or data control samples. In addition, the determination of the individual partial

efficiencies as explained in section 5.4 is done with help of several methods that have limitations. In particular, these limitations are caused by

- the fit model used to determine simulation yields;
- the methods used in the determination of the PID and trigger efficiency;
- the inaccuracy of the simulations to describe the data;
- the effect of the assumed intermediate resonances in the simulations.

In the following, more details on these sources of uncertainties are given.

When determining the combined reconstruction and preselection efficiency, the candidate yields after applying the selection criteria are obtained through simple fits to the D^0 mass distribution of simulated data to statistically subtract the small fraction of background present. In this fit, the signal component is described by a Johnson's S_U distribution and the background by an exponential function. All shape parameters are left free to float in the fit. As systematic study, the reconstruction and preselection efficiency is evaluated using an alternative fit model, which is the sum of two Gaussians with shared mean for the signal and a constant for the background. The study is done for each signal channel and dimuon-mass region separately. For each region, the difference between the efficiencies ΔR_ϵ obtained by the two alternative models is computed. The studies are combined into a common single value by computing the *root mean square* (RMS) of the variations. The RMS of the resulting ΔR_ϵ distribution of 1.0% is assigned as absolute systematic uncertainty for all dimuon-mass regions and signal channels.

The evaluated efficiency is depending on the kinematics of the signal decays, which in turn depend on the assumed decay model in the simulated samples. The evaluation of the efficiency is done separately in regions of dimuon mass, so that the dependency on resonances in dimuon mass is accounted for, since only small variations within a restricted dimuon-mass region can occur. However, no binning in dihadron mass is done, so that a wrong modelling of the hadronic spectrum can bias the efficiency. The potential bias caused by the decay model is evaluated as follows: With respect to the default model (*cf.* Table 2.1), the relative contributions of the dihadron resonances are increased and decreased by 50% and the efficiency is recomputed for each region of dimuon mass. Accordingly, alternative compositions of dimuon-mass resonances are tested. Instead of a mixture of several components, each dimuon-mass region is assumed to contain only the dominant resonance. To translate the efficiency variations into a systematic uncertainty, the resulting signal

efficiencies are compared to the default model. The RMS of their relative deviations as obtained in each dimuon-mass region and for each signal decay mode, is taken as common systematic. For the alternative hadronic models, a RMS of 1.7% is found, while the spread of the efficiency variations caused by the alternative dimuon models is determined to be 2.9%. Adding these two contributions in quadrature results in a total systematic relative uncertainty of 3.4% due to the limited knowledge of the decay model.

The hadron and muon PID efficiencies are evaluated using control samples of $J/\psi \to \mu^+\mu^-$ and $D^{*+} \to D^0(\to K^-\pi^+)\pi^+$ decays. A two dimensional binning scheme is defined in $(p;\eta)$ to account for the different kinematics of the probe particles in the calibration samples and the signal decays, such that sufficient statistics are available in each of the two dimensional regions. The effect of the specific choice for the definition of the bins is tested using two alternative binning schemes. A coarser and finer scheme is defined (details in Appendix B) and the signal PID efficiencies are evaluated using each of them. Again, the study is performed for each dimuon-mass region and signal decays and the RMS of the observed variations of 0.6% and 0.5% for the muon and hadron efficiencies, respectively, is determined. This leads to a total systematic of 0.8% caused by the method to determine PID efficiencies, taken as absolute uncertainty on ΔR_ϵ. This uncertainty is much larger than the uncertainty caused by the limited statistics of the control samples.

To determine the L0 trigger efficiency, a *tag and probe* method is developed to estimate the efficiency from a calibration sample of $D_s^+ \to \pi^+[\mu^+\mu^-]_\phi$ decays. Two main assumptions need to be validated. First, the method assumes that the tight selection requirements on the *tag* muon do not bias the efficiency of the *probe* muon. Second, it is assumed that the single muon trigger efficiency as obtained from a control sample can be transported to any other dimuon final state, where the efficiency of the "or" requirement can be calculated using Equation 5.3. This implies that, apart from kinematical correlations, the trigger efficiencies of the two muons are independent, and furthermore that the kinematical correlations are sufficiently described by the one dimensional binning in p_T. A closure test of the method is done as follows: Simulated $D^0 \to K^-\pi^+[\mu^+\mu^-]_{\rho^0/\omega}$ candidates are used to test the tag and probe method by creating a reference histogram with the single muon trigger efficiency as function of p_T (similar to what is done in data in Figure 5.7). In a second step, the ratio of L0 trigger efficiencies is determined from this histogram by using Equation 5.3. The difference of the relative efficiencies obtained by the tag and probe method is compared with the fully simulated trigger output (a.k.a. *truth-level information*) for each dimuon-mass region and

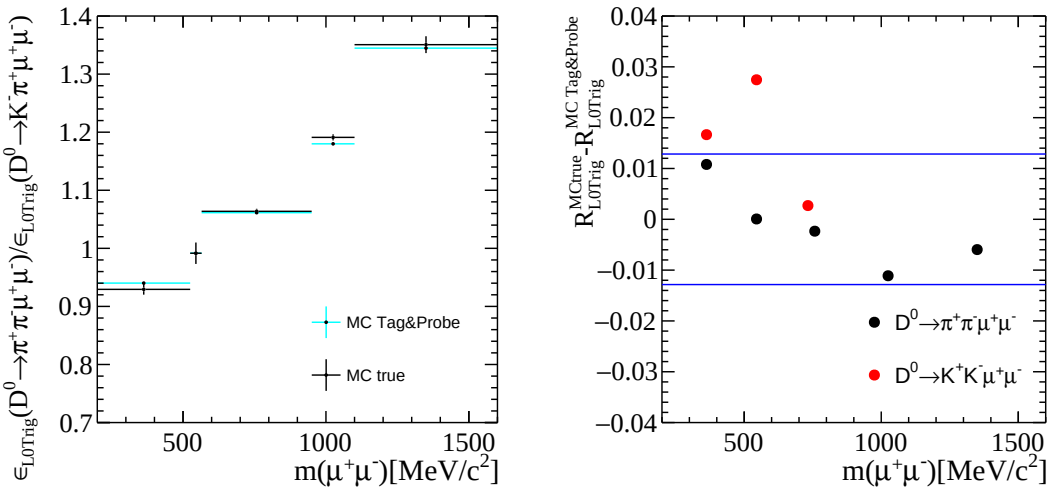

Figure 5.10: (Left) Ratio of `L0Muon` efficiencies for $D^0 \to \pi^+\pi^-\mu^+\mu^-$ over $D^0 \to K^-\pi^+\mu^+\mu^-$ decays as a function of the numerator dimuon mass, as determined on simulation using (black) truth-level information and (cyan) the *tag and probe* method calibrated on simulated $D^0 \to K^-\pi^+\mu^+\mu^-$ decays. (Right) Differences observed for the two methods for the two signal channels and in each dimuon-mass bin. The blue lines represent the assigned systematic uncertainty (modified from [5]).

both signal decays as shown in Figure 5.10. The RMS of the observed differences of 1.3% is propagated as common systematic uncertainty for all.

Finally, the level of agreement between simulated and data distributions are tested by comparing the normalised and background subtracted[3] data BDT responses of $D^0 \to \pi^+\pi^-[\mu^+\mu^-]_\phi$ and $D^0 \to K^-\pi^+[\mu^+\mu^-]_{\rho^0/\omega}$ decays with the distributions as obtained in simulations (Figure 5.11). As the BDT is trained using several kinematical and topological variables (*cf.* section 3.4), the BDT selection efficiency is expected to be a good proxy for the general agreement of data and simulated distributions. Small deviations can be seen especially in the region of high-BDT values, so that the absolute efficiency for the cut of $\texttt{BDT} > 0.4$ determined in data and simulations differs by $\sim 4.4\%$. However, comparing the ratio of efficiencies $\epsilon_{BDT}(D^0 \to \pi^+\pi^-[\mu^+\mu^-]_\phi)/\epsilon_{BDT}(D^0 \to K^-\pi^+[\mu^+\mu^-]_{\rho^0/\omega})$ only a difference of 1.3% is observed. This value is cross-checked using high-yield samples of $D^0 \to \pi^+\pi^-[\pi^+\pi^-]_\phi$ and $D^0 \to K^-\pi^+[\pi^+\pi^-]_{\rho^0/\omega}$. A similar level of disagreement of 1.4% is found. The difference of 1.3% is taken as absolute uncertainty on the ratio of efficiencies due to potential simulation-data differences,

[3]Throughout this thesis, *background subtracted* refers to the *sPlot* technique [187]. The *sPlot* technique allows to subtract background contributions on a statistical basis using candidate weights which are computed on an event-by-event basis from the PDF and covariance matrix of a fit to a *discriminating variable*, in which the signal and backgrounds can be distinguished (the D^0 meson mass distribution in this thesis).

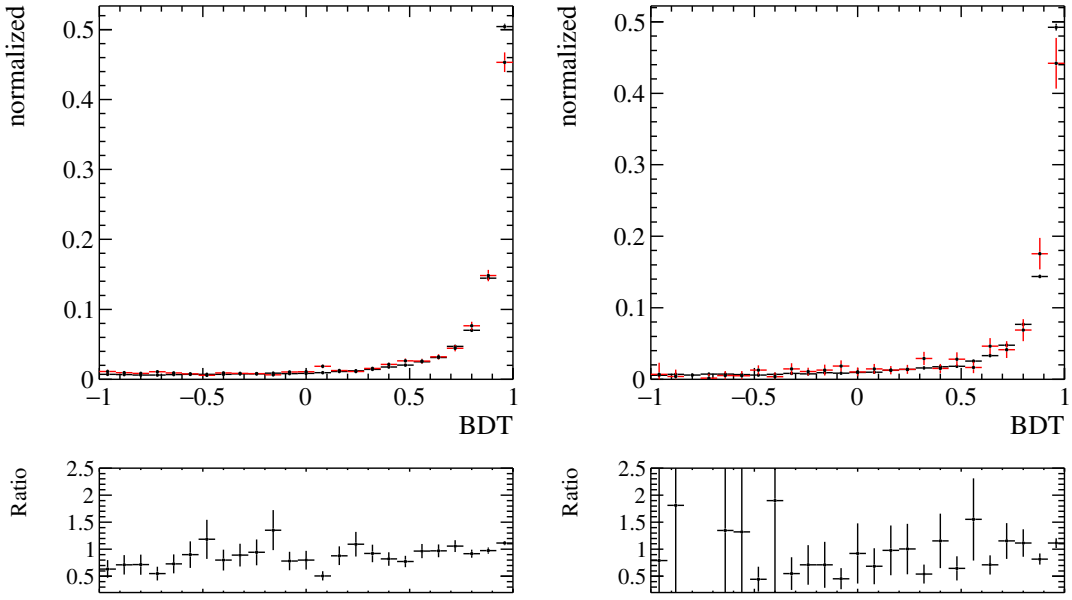

Figure 5.11: Distribution of the BDT output for (black) simulated and (red) background-subtracted $D^0 \to K^-\pi^+[\mu^+\mu^-]_{\rho^0/\omega}$ (left) and $D^0 \to \pi^+\pi^-[\mu^+\mu^-]_{\phi}$ (right) data [5].

propagated to all dimuon-mass regions and both signal decay channels.

In conclusion, the following systematic uncertainties on the ratio of signal-to-normalisation efficiencies are considered:

- 1.0% due to the fit model used to determine the simulation yields;
- 3.4% relative uncertainty due to the assumed dimuon- and dihadron-mass models;
- 0.8% for the PID efficiency, as resulting from the variation of the defined binning schemes;
- 1.3% on the L0 trigger efficiency, as resulting from the consistency check of the *tag and probe* method on simulated candidates;
- 1.3% on the BDT efficiency for the observed data-simulation differences.

The total systematic uncertainty is the sum in quadrature of the individual contributions, which is assigned to both signal decays and for each dimuon-mass region. The final ratio of efficiencies, with total statistical and systematic relative uncertainties, are summarised in Table 5.4. The statistical and systematic uncertainties on the ratio of efficiencies are added in quadrature and are entirely propagated to the systematic uncertainty of the branching fraction measurement.

Channel	$m(\mu^+\mu^-)$ [MeV/c^2]	R_ϵ	$\frac{\Delta R_\epsilon}{R_\epsilon}$ stat [%]	$\frac{\Delta R_\epsilon}{R_\epsilon}$ syst [%]	$\frac{\Delta R_\epsilon}{R_\epsilon}$ tot [%]
$D^0 \to \pi^+\pi^-\mu^+\mu^-$	< 525	0.73	3.6	4.1	5.5
	$525 - 565$	0.84	7.1	4.1	8.2
	$565 - 950$	1.08	1.8	4.0	4.4
	$950 - 1100$	1.45	2.3	4.0	4.6
	> 1100	1.53	6.6	4.0	7.7
$D^0 \to K^+K^-\mu^+\mu^-$	< 525	0.49	3.0	4.4	5.3
	$525 - 565$	0.53	5.2	4.3	6.8
	> 565	0.55	2.2	4.3	4.8

Table 5.4: The total relative efficiencies of the signal decays with respect to the normalisation channel in all dimuon-mass bins and their relative statistical, systematic and total uncertainties [5].

Summary systematic uncertainties

All non-negligible systematic uncertainties are summarised in Table 5.5. The dominant systematic for both signal decays and all dimuon-mass regions is the uncertainty resulting from the limited knowledge of the normalisation mode branching fraction, which is, as already said, quoted as a separate contribution. Uncertainties related to the determination of the yields marginally contribute to the total, while the uncertainty inherited from the determination of the ratio of efficiencies only plays a role in regions where no significant signal is observed. The relative uncertainties on the ratio of efficiencies and yields are quadratically added to $\frac{\Delta\mathcal{B}_{syst}}{\mathcal{B}}$ as shown in Table 5.5.

Channel	$m(\mu^+\mu^-)$ [MeV/c^2]	$\frac{\Delta R_{yield}}{R_{yield}}$ [%]	$\frac{\Delta R_\epsilon}{R_\epsilon}$ [%]	$\frac{\Delta\mathcal{B}_{syst}}{\mathcal{B}}$ [%]	$\frac{\Delta\mathcal{B}_{norm}}{\mathcal{B}_{norm}}$ [%]
$D^0 \to \pi^+\pi^-\mu^+\mu^-$	< 525	2.9	5.5	6.2	10.0
	$525 - 565$	2.9	8.2	8.7	10.0
	$565 - 950$	2.9	4.4	5.3	10.0
	$950 - 1100$	2.9	4.6	5.5	10.0
	> 1100	2.9	7.7	8.3	10.0
$D^0 \to K^+K^-\mu^+\mu^-$	< 525	3.0	5.3	6.1	10.0
	$525 - 565$	3.0	6.8	7.4	10.0
	> 565	3.0	4.8	5.7	10.0

Table 5.5: Summary of the systematic uncertainties on the branching fraction for both signal decay channels and in each dimuon-mass region. The uncertainties on the ratio of efficiencies and ratio of yields are quadratically added to $\frac{\Delta\mathcal{B}_{syst}}{\mathcal{B}}$, while the uncertainty on the normalisation mode branching fraction is kept separate (modified from [5]).

5.6 Determination of the (partial) branching fractions and limit setting

The measured yields of signal and normalisation mode as determined in section 5.3 and the ratio of efficiencies R_{ϵ_i} as described in section 5.4, are translated into partial branching fractions in each dimuon-mass region i according to the following equation:

$$\mathcal{B}_i = \frac{N_i(D^0 \to h^+h^-\mu^+\mu^-)}{N(D^0 \to K^-\pi^+\mu^+\mu^-)} \frac{\mathcal{B}(D^0 \to K^-\pi^+[\mu^+\mu^-]_{\rho^0/\omega})}{R_{\epsilon_i}(D^0 \to h^+h^-\mu^+\mu^-)},$$

where the normalisation mode branching fraction is taken from the Ref. [119]. The measured branching fractions are summarised in Table 5.6. Note that Table 5.6 reports measured branching fractions for all dimuon-mass regions, *i.e.* also the regions with no significant signals, as they are needed to compute the total branching fractions, which is the sum of the partial ones. As a reminder, no significant signals are observed in the region of dimuon mass containing the η resonance ($525 - 565\,\mathrm{MeV}/c^2$) of both signal decays, as well as the high dimuon-mass region for $D^0 \to \pi^+\pi^-\mu^+\mu^-$. For $D^0 \to K^+K^-\mu^+\mu^-$, the two observed candidates in the η region of dimuon mass are treated as signal with a relative statistical uncertainty of 100% as no fit can be performed. Upper limits on the branching fractions are determined in these regions with a frequentist approach.

More specifically, the CL_s method [188] as implemented in the `RooStats` Project [189] is used. As test statistic, the negative logarithm of the likelihood ratio is chosen, defined as

$$q = -2\ln\frac{L_{s+b}}{L_b}, \tag{5.4}$$

Channel	$m(\mu^+\mu^-)$ $[\mathrm{MeV}/c^2]$	$\mathcal{B}$ $[10^{-8}]$	Δ_{stat} $[10^{-8}]$	Δ_{sys} $[10^{-8}]$	Δ_{norm} $[10^{-8}]$
$D^0 \to \pi^+\pi^-\mu^+\mu^-$	< 525	7.8	1.9	0.5	0.8
	$525 - 565$	1.2	0.7	0.1	0.1
	$565 - 950$	40.6	3.3	2.1	4.1
	$950 - 1100$	45.4	2.9	2.5	4.5
	> 1100	1.3	0.8	0.1	0.1
$D^0 \to K^+K^-\mu^+\mu^-$	< 525	2.6	1.2	0.2	0.3
	$525 - 565$	0.8	0.8	0.1	0.1
	> 565	12.0	2.3	0.7	1.2

Table 5.6: Measured branching fractions and their uncertainties (modified from [5]).

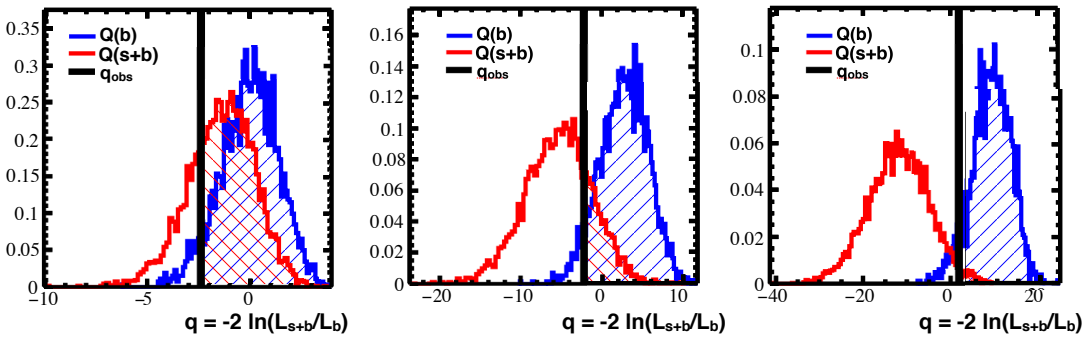

Figure 5.12: Example distributions for $Q(s+b)$ and $Q(b)$ under assumption of three different (increasing from left to right) signal branching fractions. The black bar shows q_{obs} as obtained from the fit to the data. The red (blue) hatched areas correspond to the CL_{s+b} (1-CL_b) as defined in the main text.

where L_{s+b} and L_b are the likelihood functions of the fit under the signal plus background ($s+b$) and background-only (b) hypotheses, respectively. Qualitatively, if the data are better described by the $s+b$ hypothesis, the observed q_{obs} tends to "smaller" values, but is by itself subject to statistical fluctuations. To get the distributions of Q under the $s+b$ and b hypotheses, denoted as $Q(s+b)$ and $Q(b)$ in the following, pseudo-experiments are performed. For a given hypothesis, many pseudo-data sets are generated and refitted to evaluate Equation 5.4. Examples corresponding to three hypothesised signal branching fractions are shown in Figure 5.12. Together with q_{obs} (black line), the red and blue curves show the resulting $Q(s+b)$ and $Q(b)$ distributions, respectively. From this, one defines the $CL_{s+b} = \mathcal{P}(q > q_{obs}|s+b)$ as probability to measure a q value larger or equal to q_{obs} (red hatched area in Figure 5.12). One rejects a signal hypothesis, if CL_{s+b} is smaller than a predefined value of for example 5%. To avoid the exclusion of branching fraction values for which the data has no sensitivity (*i.e.* when $Q(s+b)$ and $Q(b)$ are very similar) one defines:

$$CL_s = \frac{CL_{s+b}}{1 - CL_b}$$

with $(1 - CL_b) = \mathcal{P}(q > q_{obs}|b)$. A signal hypothesis is then rejected at (90%)95% confidence level (CL), if $CL_s < 0.1(0.05)$. While there is no sensitivity to distinguish the two hypotheses in the distributions of the test statistics, the CL_s remains one and no exclusion is made. In the limiting case in which $Q(s+b)$ and $Q(b)$ are completely separated, CL_s equals CL_{s+b}. The likelihood functions are derived from the fit model introduced in chapter 4. Rewriting the signal yield as

Channel	$m(\mu^+\mu^-)$ $[\mathrm{MeV}/c^2]$	Expected upper limit $[10^{-8}]$ 90% (95%) CL			Observed upper limit $[10^{-8}]$
		median	-1σ	$+1\sigma$	90% (95%) CL
$D^0 \to \pi^+\pi^-\mu^+\mu^-$	$525-565$	1.3(1.5)	1.0(1.2)	1.6(2.0)	2.4 (2.8)
	>1100	1.6(2.0)	1.1(1.5)	2.3(2.7)	2.8 (3.3)
$D^0 \to K^+K^-\mu^+\mu^-$	$525-565$	–	–	–	0.7 (0.8)

Table 5.7: Expected and observed upper limits (assuming no signal) and their uncertainties for the regions where no significant signal is observed. All systematic uncertainties are included in the determination [5].

$N_{sig} = \mathcal{B}_{sig} \cdot N_{norm} \cdot R_\epsilon/\mathcal{B}_{norm}$ allows to write the likelihood as a function of the data for a given signal branching fraction $\mathcal{B}_{sig}$, where the normalisation mode yield, branching fraction as well as the ratio of efficiencies appear as nuisance parameters, *i.e.* parameters of the likelihood of no interest for the measurement. In the computation of q_{obs}, they are fixed to their values as determined in section 5.3 and section 5.4. Their uncertainties are propagated to the limits by considering them in the computation of the CL_s. The nuisance parameters are fluctuated within their uncertainties in the generation of the pseudo-experiments when determining $Q(s{+}b)$ and $Q(b)$, which are then used to perform the integration.

The CL_s is computed as a function of the hypothesised signal branching fraction as shown in Figure 5.13 for the η (left) and high (right) dimuon-mass regions of $D^0 \to \pi^+\pi^-\mu^+\mu^-$. All signal branching fractions, where a $CL_s < 5\%(10\%)$ is observed, are excluded at a 95%(90%) confidence level. The upper limit is the smallest branching fraction fulfilling this relation. In addition to the observed CL_s (solid black curve), the expected CL_s with its one (dark red) and two (light red) sigma confidence intervals is shown. These are obtained with the help of pseudo-experiments under the hypothesis that the data are composed of only background. For each pseudo-experiment, q_{obs}^{pseudo} is calculated as done in data. The mean and percentiles of the resulting distribution for q_{obs}^{pseudo} are interpreted as the expected CL_s with its uncertainty bands. The expected and observed upper limits are summarised in Table 5.7. As small (but statistically insignificant) signal contributions with significances of $2.5\sigma(1.6\sigma)$ are measured in the η (high) dimuon-mass regions of $D^0 \to \pi^+\pi^-\mu^+\mu^-$ (*cf.* section 5.3), the observed CL_s shown in Figure 5.13 is slightly above the expected CL_s which is computed under the assumption of no signal.

In the η region of $D^0 \to K^+K^-\mu^+\mu^-$, where only two candidates are observed in the signal window, no attempt to fit the data is done. A simple conservative estimation of the upper limits assuming Poisson statistics and that the two

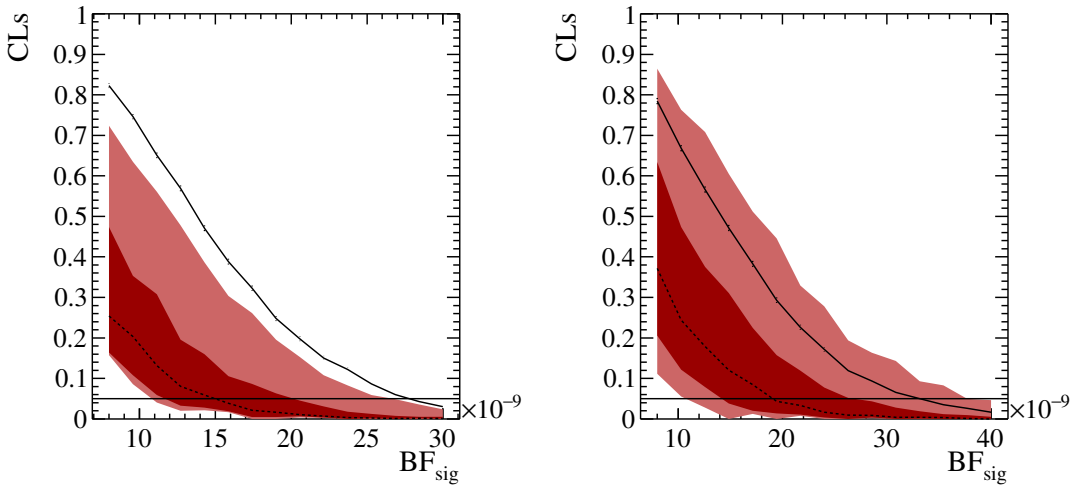

Figure 5.13: (Dashed) Expected and (solid) observed upper limits as a function of the hypothesised signal branching fraction under assumption of no signal for the η (left) and high (right) dimuon-mass of $D^0 \to \pi^+\pi^-\mu^+\mu^-$ regions where no significant signals are observed. The dark (light) red band shows the $1(2)\sigma$ range of the expected CLs [5].

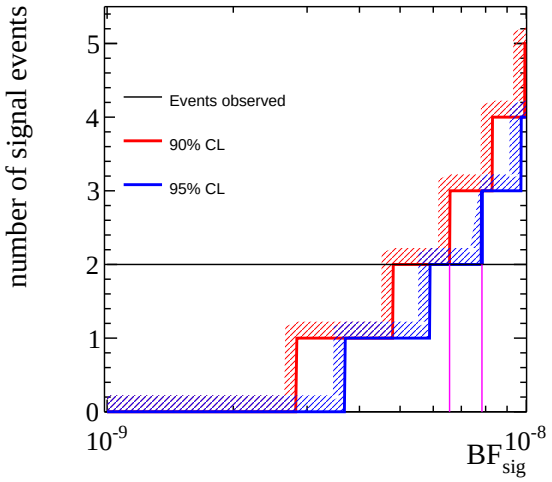

Figure 5.14: Neyman confidence belt showing the upper limit for the η bin of the $D^0 \to K^+K^-\mu^+\mu^-$ sample as a function of the observed number of events (modified from [5]).

observed candidates are signal finds limits of $6.6(7.8)\cdot10^{-9}$ at 90%(95%) CL.

The total branching fractions are computed as the sum of the individual partial branching fractions (which are reported in Table 5.6) to be $\mathcal{B}(D^0 \to \pi^+\pi^-\mu^+\mu^-) = (9.64 \pm 0.48 \pm 0.51 \pm 0.97) \cdot 10^{-7}$ and, analogously, $\mathcal{B}(D^0 \to K^+K^-\mu^+\mu^-) = (1.54 \pm 0.27 \pm 0.09 \pm 0.16) \cdot 10^{-7}$, where the three listed uncertainties are statistical, systematic and due to the limited knowledge of the

normalisation mode branching fraction.

To estimate the correlation between the two integrated branching fractions, the covariance matrix is computed assuming the commonly estimated systematic uncertainties on the ratio of efficiencies and yields, as well as the uncertainty on the normalisation mode branching fraction to be fully correlated. The statistical uncertainties on the simulated samples and data samples are independent. The correlation between the two integrated branching fractions is estimated to be 0.497. The correlation between the partial branching fraction can be found in Appendix D.

5.7 Summary

Using a sample of proton-proton collision data corresponding to $2\,\text{fb}^{-1}$ recorded by the LHCb experiment in 2012, the following branching fractions of rare four-body $D^0 \to h^+h^-\mu^+\mu^-$ decays are measured:

$$\mathcal{B}(D^0 \to \pi^+\pi^-\mu^+\mu^-) = (9.64 \pm 0.48 \pm 0.51 \pm 0.97) \cdot 10^{-7},$$
$$\mathcal{B}(D^0 \to K^+K^-\mu^+\mu^-) = (1.54 \pm 0.27 \pm 0.09 \pm 0.16) \cdot 10^{-7},$$

where the uncertainties are statistical, systematic and due to the limited knowledge of the normalisation mode branching fraction. The results correspond to the first observation of these decays and represent the rarest decays of a charm meson measured to date. The total branching fractions are in good agreement with the SM expectation [95] of

$$\mathcal{B}(D^0 \to \pi^+\pi^-\mu^+\mu^-)^{theo} \sim 1.3 \cdot 10^{-6},$$
$$\mathcal{B}(D^0 \to K^+K^-\mu^+\mu^-)^{theo} \sim 1.1 \cdot 10^{-7}.$$

The branching fractions are also measured as a function of dimuon mass and summarised in Table 5.8. For $D^0 \to \pi^+\pi^-\mu^+\mu^-$, signals with statistical significances exceeding 3σ are observed in the low, ρ^0/ω and ϕ regions of dimuon mass and the branching fraction is measured in each of these. Upper limits on the signal branching fraction are set in the η and high dimuon-mass regions. Analogously, for $D^0 \to K^+K^-\mu^+\mu^-$ branching fractions in the low and ρ^0/ω regions of dimuon mass are provided, while an upper limit is set in the η region. The differential branching fractions as function of the dimuon mass are shown in Figure 5.15, which are obtained from the partial branching fractions by dividing by the width of the

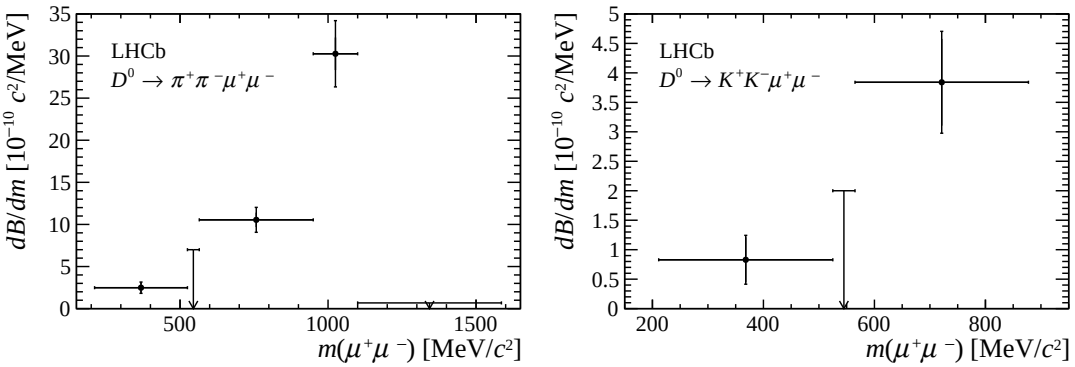

Figure 5.15: Differential branching fraction as a function of the dimuon mass for (left) $D^0 \to \pi^+\pi^-\mu^+\mu^-$ and (right) $D^0 \to K^+K^-\mu^+\mu^-$ decays. The arrows represent the upper limits at 95% confidence level [3].

corresponding dimuon-mass bin. They confirm the domination of long-distance contributions in $D^0 \to h^+h^-\mu^+\mu^-$ decays. The results have been published in Physical Review Letters [1] and triggered further theoretical interest in these decays [120, 190]. Based on the presented measurements, Ref. [120] concludes that no room to probe beyond SM in the non-resonant regions of $D^0 \to h^+h^-\mu^+\mu^-$ decays is left. This can also be seen in Figure 5.16, where potential new physics effects are compared to the long-distance contributions amended by the presented experimental results. The long-living tails of the resonances are expected to shade the short-distance physics in the entire dimuon-mass range and the observed signal yields in the low dimuon-mass regions are estimated to be consistent with coming from intermediate resonant states.

The promising measured yields in Run 1 data motivate a further investigation of asymmetries in these decays including data taken during Run 2 as presented in detail in the next chapter. As already explained in chapter 1, asymmetries are caused by the interference between beyond SM and SM dynamics and therefore expected to be the maximally pronounced in the vicinity of resonances, making them an ideal tool to search for new physics in rare charm decays which are indeed dominated by long-distance contributions.

$m(\mu^+\mu^-)$ [MeV/c^2]	$\mathcal{B} \pm \Delta_{\text{stat}} \pm \Delta_{\text{syst}} \pm \Delta_{\text{norm}}$ [10^{-8}]
$D^0 \to \pi^+\pi^-\mu^+\mu^-$	
< 525	$7.8 \pm 1.9 \pm 0.5 \pm 0.8$
$525 - 565$	$< 2.4\,(2.8)$ at 90% (95%) CL
$565 - 950$	$40.6 \pm 3.3 \pm 2.1 \pm 4.1$
$950 - 1100$	$45.4 \pm 2.9 \pm 2.5 \pm 4.5$
> 1100	$< 2.8\,(3.3)$ at 90% (95%) CL
$D^0 \to K^+K^-\mu^+\mu^-$	
< 525	$2.6 \pm 1.2 \pm 0.2 \pm 0.3$
$525 - 565$	$< 0.7\,(0.8)$ at 90% (95%) CL
> 565	$12.0 \pm 2.3 \pm 0.7 \pm 1.2$

Table 5.8: Measured partial branching fractions and their uncertainties in the dimuon-mass regions as defined in the main text for (top) $D^0 \to \pi^+\pi^-\mu^+\mu^-$ and (bottom) $D^0 \to K^+K^-\mu^+\mu^-$ decays (modified from [5]).

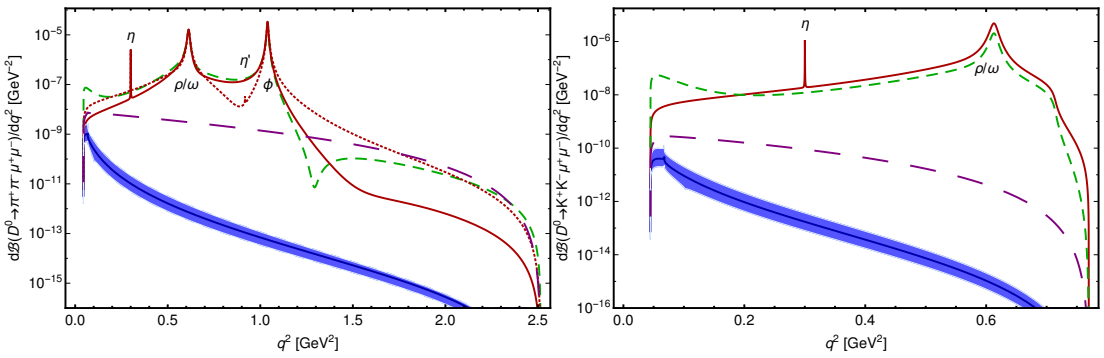

Figure 5.16: Differential branching fraction of (left) $D^0 \to \pi^+\pi^-\mu^+\mu^-$ and (right) $D^0 \to K^+K^-\mu^+\mu^-$ decays, taken from Ref [120]. The blue curve shows the SM short-distance contributions with uncertainty, while the long-dashed purple line indicates potential new physics contributions (assuming $C_9^{NP} = 1$). The red solid (dashed) red line are show the resonant contributions assuming a strong phase difference between the intermediate ρ and ϕ resonances of $\delta_\rho - \delta_\phi = \pi$ ($\delta_\rho - \delta_\phi = 0$). As comparison, also the model developed in [95] is indicated in green.

6 Measurement of CP and angular asymmetries

This chapter describes the measurement of the CP asymmetry A_{CP}, the muon forward-backward asymmetry A_{FB}, as well as the angular asymmetry between the dihadron and dimuon decay planes $A_{2\phi}$ in $D^0 \to \pi^+\pi^-\mu^+\mu^-$ and $D^0 \to K^+K^-\mu^+\mu^-$ decays.

6.1 Measurement strategy

In addition to the branching fraction measurements, a very sensitive tool to probe the SM with rare four-body decays is to perform null tests of the SM via the measurement of asymmetries. This thesis presents the first measurement of the CP asymmetry A_{CP} and the angular asymmetries A_{FB} and $A_{2\phi}$ defined as :

$$
\begin{aligned}
A_{CP} &= \frac{\Gamma(D^0 \to h^+h^-\mu^+\mu^-) - \Gamma(\overline{D}^0 \to h^+h^-\mu^+\mu^-)}{\Gamma(D^0 \to h^+h^-\mu^+\mu^-) + \Gamma(\overline{D}^0 \to h^+h^-\mu^+\mu^-)}, \\
A_{FB} &= \frac{\Gamma(D \to h^+h^-\mu^+\mu^-; \cos\theta_\mu > 0) - \Gamma(D \to h^+h^-\mu^+\mu^-; \cos\theta_\mu < 0)}{\Gamma(D \to h^+h^-\mu^+\mu^-; \cos\theta_\mu > 0) + \Gamma(D \to h^+h^-\mu^+\mu^-; \cos\theta_\mu < 0)}, \\
A_{2\phi} &= \frac{\Gamma(D \to h^+h^-\mu^+\mu^-; \sin 2\phi > 0) - \Gamma(D \to h^+h^-\mu^+\mu^-; \sin 2\phi < 0)}{\Gamma(D \to h^+h^-\mu^+\mu^-; \sin 2\phi > 0) + \Gamma(D \to h^+h^-\mu^+\mu^-; \sin 2\phi < 0)}.
\end{aligned}
\tag{6.1}
$$

As the flavour of the D^0 meson is inferred from the charge of the π_s^+ in the decay chain $D^{*+} \to D^0\pi_s^+$, two additional *nuisance asymmetries* could be present and need to be considered when CP asymmetries are measured. Even though $c\bar{c}$ are produced in pairs in pp collisions, due to the valence quark content of protons (only quarks and no anti quarks), the production cross sections σ for D^{*+} and D^{*-} mesons might not be equal. This leads to a production asymmetry denoted as $A_P(D^{*+}) = [\sigma(D^{*+}) - \sigma(D^{*-})]/[\sigma(D^{*+}) + \sigma(D^{*-})]$ in the following. Furthermore, the efficiencies to detect positively or negatively charged pions, $\epsilon(\pi^+)$ and $\epsilon(\pi^-)$, are different. This is mainly caused by the asymmetric material interaction of positive and negative particles with the detector material, as well as

	$m(\mu^+\mu^-)$ [MeV/c^2]				
Decay mode	low mass	η	ρ^0/ω	ϕ	high mass
$D^0 \to K^+K^-\mu^+\mu^-$	< 525	525-565	> 565	NA	NA
$D^0 \to \pi^+\pi^-\mu^+\mu^-$	< 525	525-565	565-780 780-950	950-1020 1020-1100	> 1100

Table 6.1: Definition of the dimuon-mass regions used in the analysis. The regions that are not kinematically allowed are indicated with the acronym NA; those where no significant signal has been previously observed with NS [6].

tracking asymmetries, in the following together referred to as detection asymmetry $A_d(\pi^+) = [\epsilon(\pi^+) - \epsilon(\pi^-)]/[\epsilon(\pi^+) + \epsilon(\pi^-)]$. Instead of measuring decays rates as indicated in Equation 6.1, experimentally, it is more convenient to determine the asymmetries in the measured yields N. While for A_{FB} and $A_{2\phi}$ it is sufficient to measure the yields split by $\cos\theta_\mu$ and $\sin 2\phi$ (see chapter 1 for the definition of the angles) greater or less than zero, respectively, A_P and A_d lead to the presence of artificial asymmetries when measuring A_{CP}. The measured, uncorrected "raw" asymmetry can be expanded as linear sum of the involved asymmetries as long as the individual asymmetries are small [129] :

$$\begin{aligned} A_{CP}^{\text{raw}}(f) &= \frac{N[D^{*+} \to D^0(\to f)\pi^+] - N[D^{*-} \to \overline{D}^0(\to f)\pi^-]}{N[D^{*+} \to D^0(\to f)\pi^+] + N[D^{*-} \to \overline{D}^0(\to f)\pi^-]} \\ &\approx A_{CP}(f) + A_d(\pi^+) + A_P(D^{*+}), \end{aligned}$$

As the final states $f = \pi^+\pi^-\mu^+\mu^-, K^+K^-\mu^+\mu^-$ are symmetric under CP transformations, no further detection asymmtries are expected. To get access to the underlying CP asymmetry, a suitable control channel which is subject to the same production and detection asymmetry can be used. In this analysis, the nuisance asymmetries are constrained using high-statistics samples of $D^{*+} \to D^0(\to K^+K^-)\pi_s^+$ decays. Knowing the CP asymmetry of the control channel from an independent measurement of Ref. [191], the CP asymmetry is obtained by subtraction[1]:

$$A_{CP}(h^+h^-\mu^+\mu^-) = A_{CP}^{\text{raw}}(h^+h^-\mu^+\mu^-) - A_{CP}^{\text{raw}}(K^+K^-) + A_{CP}(K^+K^-)$$

As the nuisance asymmetries depend on the kinematics of the D^{*+} meson and the tagging pion, a kinematic equalisation of signal and calibration channels needs to be performed to assure a precise cancellation.

All asymmetries are measured on the full dimuon-mass integrated sample of $D^0 \to \pi^+\pi^-\mu^+\mu^-$ and $D^0 \to K^+K^-\mu^+\mu^-$ decays, but also in regions of dimuon mass. As explained in chapter 1, some of the asymmetries may be greatly enhanced

[1]The same detection and production asymmetries are assumed in the control channel, *i.e.* $A_{CP}^{\text{raw}}(K^+K^-) = A_{CP}(K^+K^-) + A_d(\pi^+) + A_P(D^{*+})$.

by the interference between the short-distance and long-distance amplitudes. The definition of these regions can be found in Table 6.1 and is guided by the scheme introduced for the branching fraction measurement, with the difference that the regions around the ϕ and ρ^0/ω regions are split in two at the resonance pole mass. As the strong phase of a resonance varies across the pole, this choice may enhance the sensitivity to CP asymmetries that might change sign at the pole position, and would then average to zero when integrated in a region symmetric about the resonance peak. Besides, the asymmetries are only measured in the regions of dimuon mass, where a significant signal has been observed in the branching fraction measurement.

As many different resonant and potentially non-resonant processes contribute to the decay process, the asymmetries might change as a function of the five-dimensional phase space. If the total reconstruction and detection efficiency is not constant across these variables, the asymmetries might be artificially biased. To allow for a meaningful theoretical interpretation of the results, a correction for phase-space depended efficiency variations is therefore a crucial part of this analysis.

The analysis uses approximately $5\,\text{fb}^{-1}$ of integrated luminosity collected by LHCb during the years 2011-2016. As done for the branching fraction measurement, the measurement of asymmetries has also been performed as a blind analysis. The blinding strategy was to shift the measured asymmetries by an offset chosen randomly between $[-0.1, 0.1]$, whose value was never shown to the experimentalists before the analysis strategy, including the evaluation of the systematic uncertainties, was fixed.

6.2 Selection optimisation

In addition to the preselection described in chapter 3, the requirement on the track ghost probability of the slow pion is tightened (`TrackGhostProb` < 0.05) to suppress ghost slow pion background to a negligible level following an optimisation study in Ref. [192]. Furthermore, as shown in Figure 6.1, regions in the phase space of the tagging pion with very large instrumental asymmetries are identified, where low momentum pions of one charge are bent out of the detector acceptance or into the LHC beampipe. Following Ref. [193], the π_s is required to satisfy: $|p_x| \geq a(p_z - p_0)$, with $a = 0.317$ and $p_0 = 2400\,\text{MeV}/c$. If $|p_y/p_z| < 0.02$, also $p_1 - b_1 p_z < |p_x| < p_2 + b_2 p_z$, with $p_1 = 418\,\text{MeV}/c$, $p_2 = 497\,\text{MeV}/c$, $b_1 = 0.01397$ and $b_2 = 0.016015$. The effects of these requirements is to get rid of these regions as shown in Figure 6.1 (represented by the solid black lines).

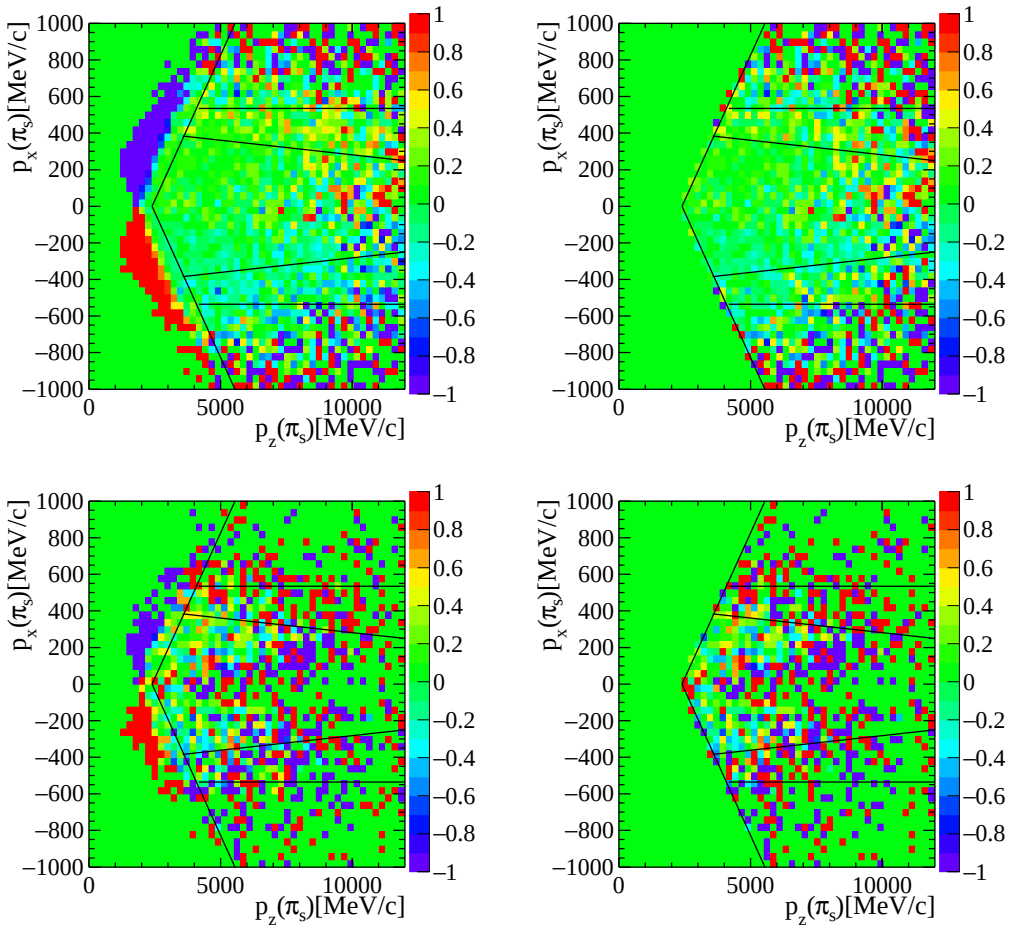

Figure 6.1: Raw asymmetry for (top) $D^0 \to \pi^+\pi^-\mu^+\mu^-$ and (bottom) $D^0 \to K^+K^-\mu^+\mu^-$ candidates as a function of the soft pion (p_x, p_z), (left) before and (right) after the fiducial cuts (represented by the solid black lines) have been applied [6].

The `BDT` and `ProbNNmu` selection criteria are optimised to minimise the statistical uncertainty on the measured asymmetries. The optimisation procedure is carried out directly on data by performing the asymmetry measurement on candidate decays that have been assigned a random tag to mimic a null asymmetry (as expected in the SM). In Figure 6.2, the statistical uncertainties on the fitted asymmetries are shown. The set of cuts for which this uncertainty is minimal is chosen. Small differences in the MVA and PID performance between Run 1 and Run 2 are observed. For this reason, the optimisation is done separately for both data taking periods and signal decay modes. For $D^0 \to \pi^+\pi^-\mu^+\mu^-$ decays, optimal (`ProbNNmu`;`BDT`) requirements of (0.3;-0.2) and (0.5;-0.2) for data taken during Run 1 and Run 2, respectively, is found. Accordingly, the requirements (0.2;-0.6) is found to be optimal for $D^0 \to K^+K^-\mu^+\mu^-$ decays (both data taking periods).

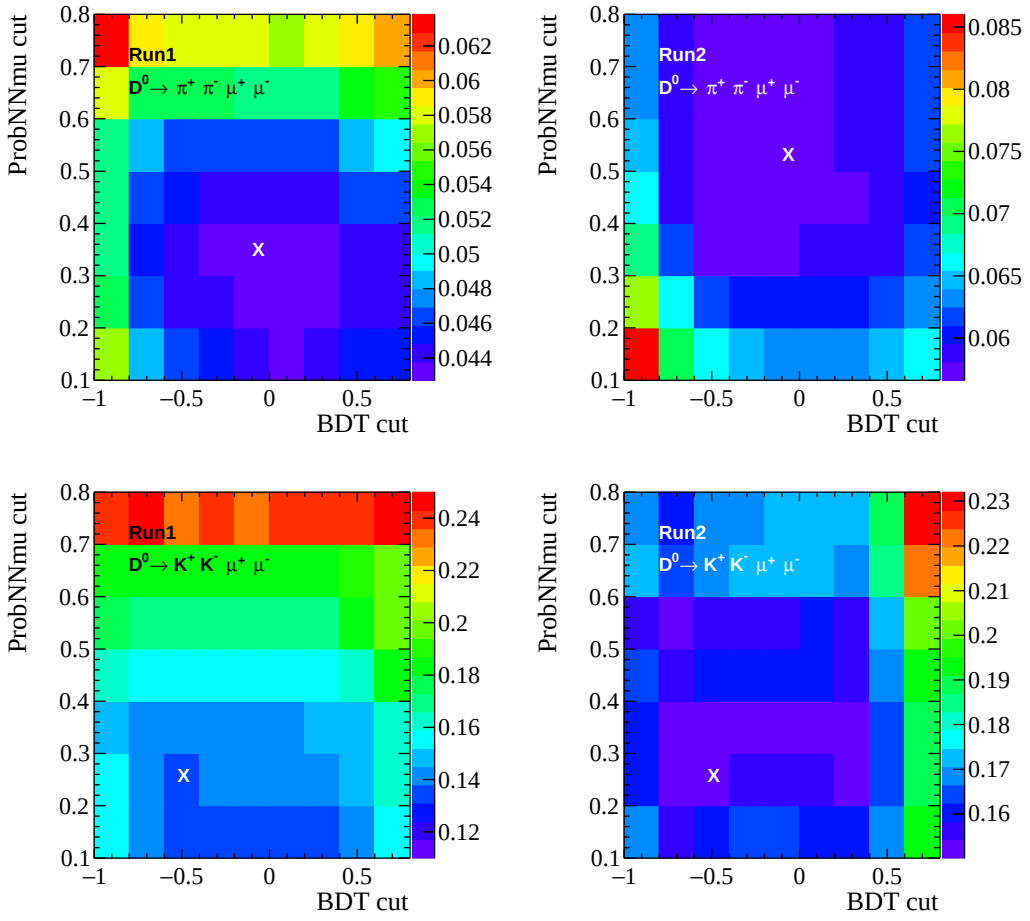

Figure 6.2: Scan of the uncertainty on the measured asymmetry on a randomly tagged sample in the two dimensional space of minimum BDT and `ProbNNmu` requirements for (top) $D^0 \to K^+K^-\mu^+\mu^-$ and (bottom) $D^0 \to \pi^+\pi^-\mu^+\mu^-$ decays and for (left) Run 1 and (right) Run 2 data. The white crosses represent the chosen/optimal selection requirements [6].

6.3 Correction for phase-space dependent efficiencies

Different physical processes contribute to $D^0 \to h^+h^-\mu^+\mu^-$ decays, which populate distinct regions in phase space. If the reconstruction and selection efficiency is not constant across the phase space, their relative contributions will be artificially changed. If, furthermore, the physical asymmetry is depending on the position in phase space, a bias on the measured asymmetries can be introduced. To allow for a clear interpretation of the measured quantities, a correction for these effects is needed. The phase space of a four body final state requires a five-dimensional description. Together with the dihadron ($m(h^+h^-)$) and dimuon

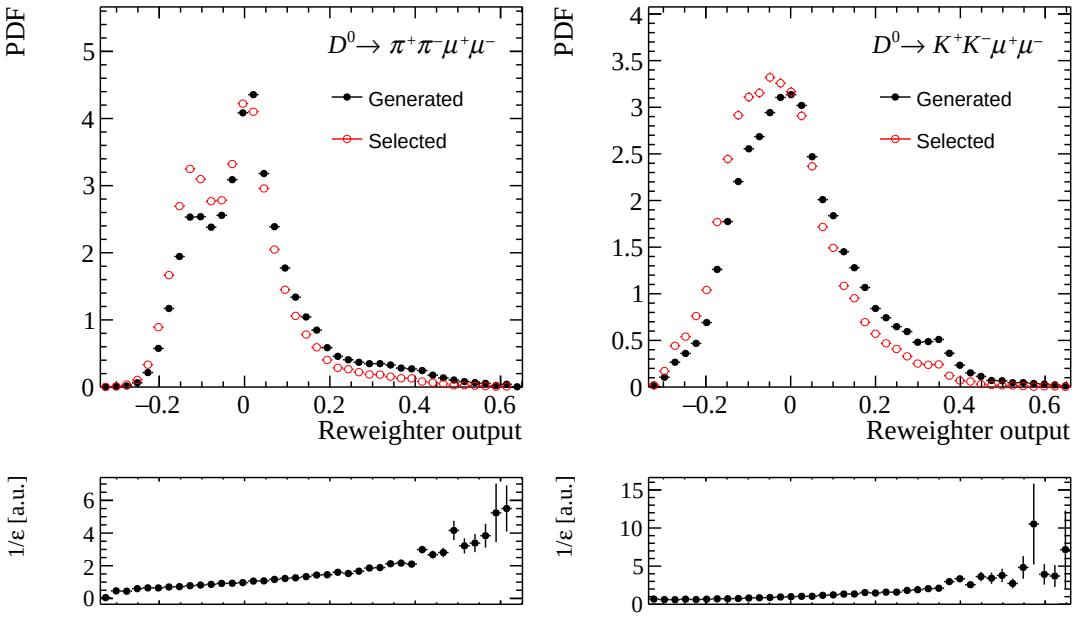

Figure 6.3: Output distributions of the BDT reweighter for simulated samples of (left) $D^0 \to \pi^+\pi^-\mu^+\mu^-$ and (right) $D^0 \to K^+K^-\mu^+\mu^-$ decays at (closed black) generator level and (open red) after selection. The bottom panels show the ratio between generated and selected decays (*i.e.* the inverse of the efficiency) as a function the reweighter output [2].

$(m(\mu^+\mu^-))$ masses, the following three angular variables (as defined in chapter 1) are used to model the efficiency across the phase space: $\sin 2\phi$, $\cos\theta_\mu$ and $\cos\theta_h$.

The multidimensional efficiency correction [194] is done using MVA techniques. More specifically, a BDT with gradient boosting [179–181] is trained on two simulated samples of the same decay, one containing generator-level and the other fully reconstructed/selected quantities, where any observed difference is caused by distortions due to selection requirements. The BDT combines the multidimensional differences of the input variables of the training samples into a single value, the classifier output, hereafter denoted as *reweighter output*. However, instead of discriminating signal and background, the reweighter output is used to correct for the differences, taking also the correlations of the input variables into account. The assumption is that an equalisation of the reweighter output distributions for generator-level simulations ($\texttt{BDT}^{\text{gen}}$) and fully selected simulated candidates ($\texttt{BDT}^{\text{sel}}$) simultaneously leads to an equalisation of the input variables. Therefore, from the ratio of the reweighter output distributions $\texttt{BDT}^{\text{gen}}$ and $\texttt{BDT}^{\text{sel}}$, per-candidate weights w, corresponding to the inverse of the per-candidate efficiency (in arbitrary

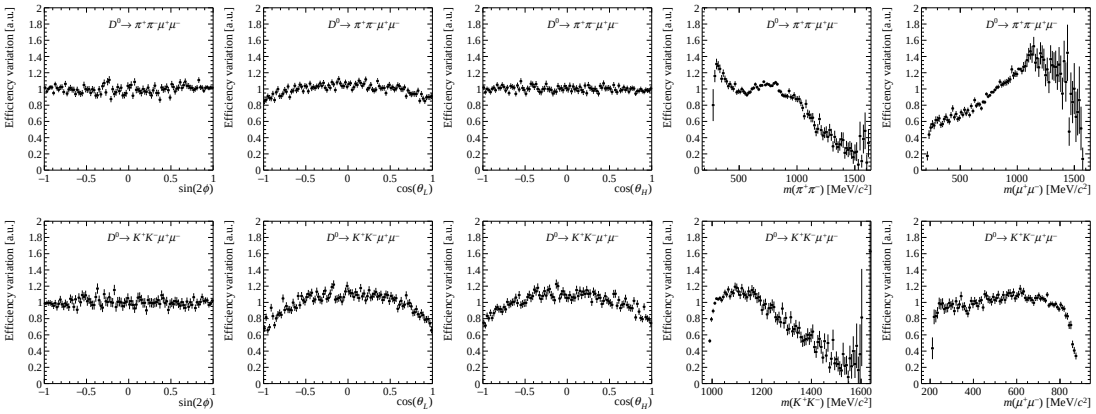

Figure 6.4: Efficiency variation as a function of the phase-space variables, separately for simulated (top) $D^0 \to \pi^+\pi^-\mu^+\mu^-$ and (bottom) $D^0 \to K^+K^-\mu^+\mu^-$ decays [6].

units) are derived:

$$w(\text{output}) = \frac{1}{\epsilon(\text{output})} = \left(\frac{\texttt{BDT}^{\text{sel}}(\text{output})}{\texttt{BDT}^{\text{gen}}(\text{output})}\right)^{-1},$$

such that the weighted $\texttt{BDT}^{\text{sel}}$ distribution matches $\texttt{BDT}^{\text{gen}}$. Hence, also the weighted input variables of the fully reconstructed samples are expected to match their generator level counterparts, which is equivalent to an efficiency correction. Note that in contrast to the branching fraction measurement, the absolute efficiency does not play any role. Only the variation of the efficiency across the phase space has to be corrected for.

The reweighter BDT is trained using $m(h^+h^-)$, $m(\mu^+\mu^-)$, $|\cos\theta_\mu|$ and $|\cos\theta_h|$ as input variables because the efficiency variations observed in $\cos\theta_\mu$ and $\cos\theta_h$ are found to be symmetric around zero, while the efficiency in $\sin 2\phi$ appears to be constant (and independent of the other variables). The reweighter output distributions for generator-level and fully reconstructed/selected simulated samples are shown in Figure 6.3, together with the weights as functions of the output value for both channels. The efficiency variation of the input variables can be found in Figure 6.4. The method is validated in an independent sample of simulated, reconstructed and selected decays. The reweighter BDT is applied to the sample and its candidate-by-candidate output value is used to determine the weights. These in turn are used to reweight the input variables and compare them to generator level quantities. A decent agreement can be seen in Figure 6.5. The small deviations at high dimuon and dihadron masses are expected to be caused by limited statistics of the training samples. However, the available statistics

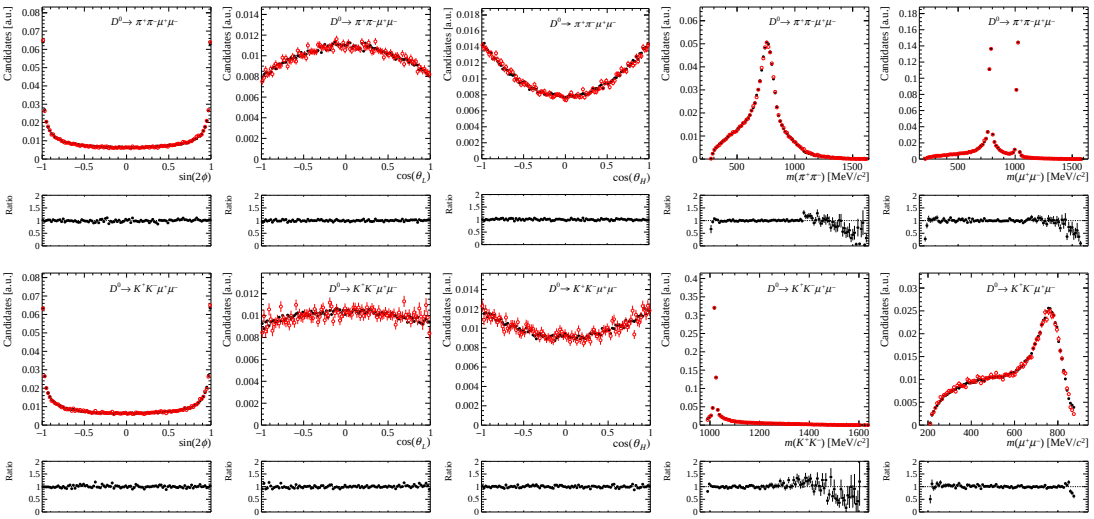

Figure 6.5: Phase-space distribution of simulated $D^0 \to K^+K^-\mu^+\mu^-$ decays at (closed black) generator level and (open red) after selection and efficiency correction. The bottom panel of each plot shows the ratio between the two distributions [6].

in simulations is still exceeding the data statistics by at least two orders of magnitude and the effect of limited training statistics has been found to be negligible compared to systematic uncertainties caused by potential simulation-data differences (details in section 6.6). Not only the one dimensional projections are tested, also all possible two-dimensional representations have been checked in Appendix F. Indeed, it can be concluded that the weighting *is* equivalent to an efficiency corrections. Similarly, the reweighter BDT is applied to the signal data and weights are computed accordingly. In the following, the data are weighted (*i.e.* efficiency-corrected), unless stated otherwise.

For a weighted data set containing N candidates, the yield after weighting is computed as $N_w = \sum_i w_i$, with w_i the candidate weights. The uncertainty ΔN_w is given by $\Delta N_w = \sqrt{\sum_i w_i^2}$. It can be shown that weighting data distributions with non-uniform weights effectively leads to a loss of statistical power. Therefore, it is convenient to rescale the weighted yield N_w of a data set by the factor $w_{eff} = \sum_{i=1}^{N} w_i / \sum_{i=1}^{N} w_i^2$, such that the effective statistics N_{eff}, computed as [195] :

$$N_{eff} = \frac{(\sum_{i=1}^{N} w_i)^2}{\sum_{i=1}^{N} w_i^2}$$

with $N_{eff} \leq N$, corresponds to the statistical power of an unweighed sample containing N_{eff} candidates. In the limit of equally distributed weights, $N_{eff} = N$. The comparison of the original and effective yields of the data sets used in

Channel	N_{original}	$\sum w_i$	$\sum w_i^2$	$N_{\text{effective}}$	$\frac{N_{\text{effective}}}{N_{\text{original}}}$
$D^0 \to \pi^+\pi^-\mu^+\mu^-$	2858	2921	3446	2476	0.87
$D^0 \to K^+K^-\mu^+\mu^-$	400	411	491	344	0.86

Table 6.2: Weighting statistics computed on the data samples after correcting for the efficiency variation across phase space [6].

this analysis are listed in Table 6.2. To summarise, due to the weighting, the statistical power of the $D^0 \to \pi^+\pi^-\mu^+\mu^-$ ($D^0 \to K^+K^-\mu^+\mu^-$) sample is reduced by approximately 13%(14%).

6.4 Correction for nuisance charge asymmetries

Production and detection asymmetries are determined using high-yield samples of $D^{*+} \to D^0(\to K^+K^-)\pi^+$ decays for which the CP asymmetry has been precisely measured at LHCb to be $A_{CP}(K^+K^-) = (-0.06 \pm 0.18)\%$ [191], such that the combined detection and production asymmetry can be determined as:

$$A_d(\pi_s^+) + A_P(D^{*+}) = A_{CP}^{\text{raw}}(K^+K^-) - A_{CP}(K^+K^-),$$

As the production and detection asymmetries depend on the kinematics of the D^{*+} and ${\pi^+}_s$ candidates, the control sample is selected with the same requirements as the signal samples whenever possible. However, the different particle contents of the final states do not allow for exactly the same selection, which is reflected in residual differences in the D^{*+} and π_s^+ kinematics. A kinematic equalisation is done as follows: The raw asymmetry of the control channel $A_{CP}^{\text{raw}}(K^+K^-)$ is evaluated in regions of transverse and longitudinal momenta of the D^{*+} meson through unbinned maximum likelihood fits to the D^0 mass distribution of candidates split by the charge of the tagging pion. As detector effects might have been altered depending on the run conditions, a correction is calculated individually for each data taking period and later combined into a single value according to their relative fractions. Subsets of $\sim 3M$ $D^0 \to K^+K^-$ decays have been randomly selected from the total available samples for each period. The two dimensional asymmetry distributions, separately for data taken during Run 1 and Run 2, are shown in Figure 6.6. Using simulated signal candidates as proxy for the D^{*+} kinematics, the correction is obtained by integrating the D^{*+} kinematics of the signal decays over the two dimensional asymmetry distributions. Due to the high kinematical correlation between the D^{*+} and the π_s^+ mesons, a kinematical equalisation in the D^{*+} kinematics sufficiently accounts also for the differences in the π_s^+ kinematics.

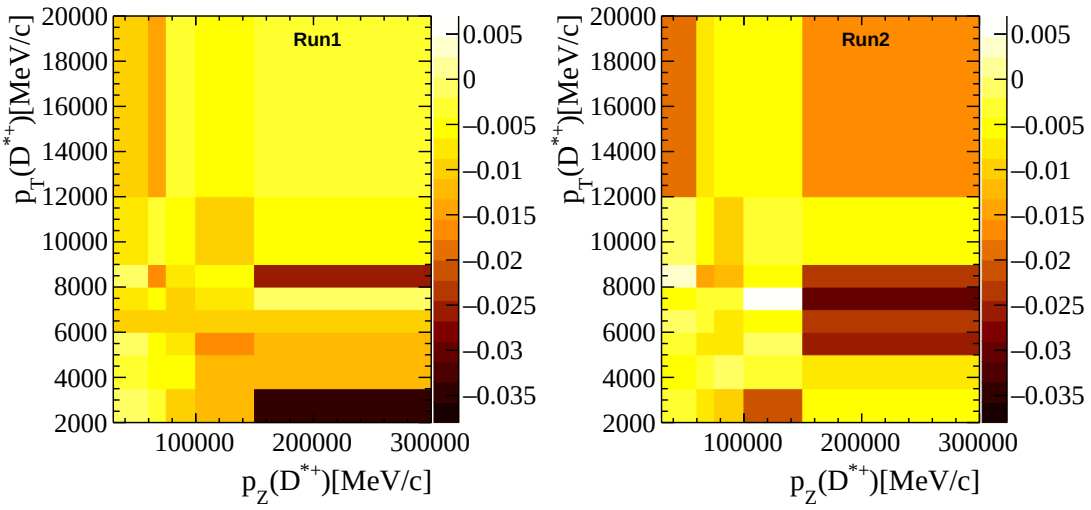

Figure 6.6: Raw asymmetry of the $D^0 \to K^+K^-$ decays in bins of $p_T(D^*)$ and $p_Z(D^*)$ for Run1 (left) and Run 2 (right) data (modified from [6]).

This can be seen in Figure 6.7, where the transverse and longitudinal momenta of the π_s^+ of simulated candidates are compared to the distributions as obtained from the background subtracted control sample, after reweighting the $(p_T; p_Z)$ of the D^{*+} candidates to match the simulated spectra, using the binning scheme defined for the integration. The effect of an imperfect matching of the kinematic distributions is discussed in section 6.6. However, as shown in Table 6.3, the difference of the raw asymmetries of the control channel considering or neglecting the kinematical matching is very small anyhow. Furthermore, due to the very similar kinematics of the $D^0 \to \pi^+\pi^-\mu^+\mu^-$ and $D^0 \to K^+K^-\mu^+\mu^-$ signal decays, a common correction to $A_{CP}(D^0 \to h^+h^-\mu^+\mu^-)$ of

$$A_d({\pi^+}_s) + A_P(D^{*+}) = (-0.66 \pm 0.19)\%$$

is found, averaged on both data taking periods by the observed proportions of $D^0 \to h^+h^-\mu^+\mu^-$ signal yields. The uncertainty on the correction is completely dominated by the uncertainty on $A_{CP}(K^+K^-)$ and is negligible with respect to the precision of a few percent expected on the A_{CP} $(D^0 \to h^+h^-\mu^+\mu^-)$ measurement.

Data	$A_{CP}^{\text{raw}}(K^+K^-)$ [%]		
	unweighted value	kinematics matched to $D^0 \to \pi^+\pi^-\mu^+\mu^-$	kinematics matched to $D^0 \to K^+K^-\mu^+\mu^-$
Run 1	-0.67 ± 0.06	-0.75 ± 0.07	-0.75 ± 0.07
Run 2	-0.51 ± 0.06	-0.68 ± 0.11	-0.68 ± 0.11
Combined	–	-0.72 ± 0.06	-0.72 ± 0.06

Table 6.3: The raw asymmetries measured in the control channel $D^0 \to K^+K^-$ with and without considering the differences in D^{*+} kinematics with respect to the signal decays [6]. To compute the correction for the production and detection asymmetries, these values have to be corrected by $A_{CP}(K^+K^-)$.

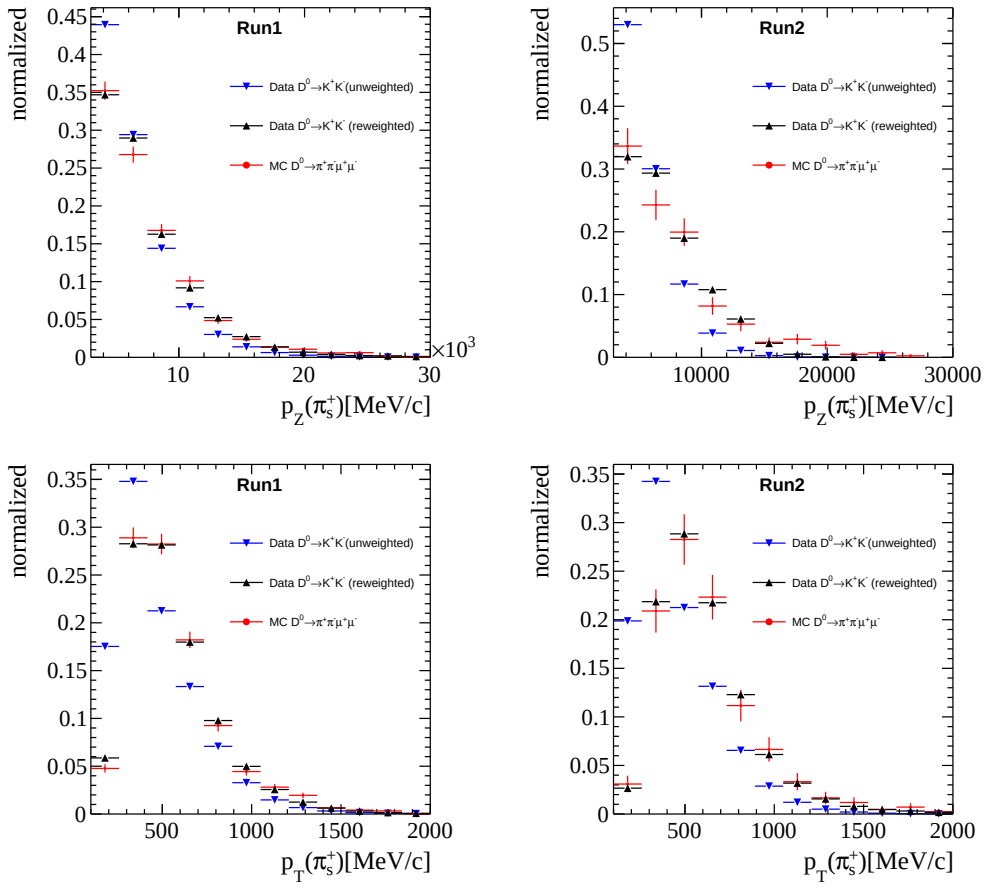

Figure 6.7: Distributions of the π_s^+ longitudinal and transverse momenta for simulated signal $D^0 \to \pi^+\pi^-\mu^+\mu^-$ decays, weighted and unweigthed $D^0 \to K^+K^-$ decays. Run 1 and Run 2 samples are shown separately. Effects of residual differences are considered as sources of systematic uncertainties in section 6.6 (modified from [6]).

6.5 Determination of the signal asymmetries

The asymmetries are obtained through unbinned maximum likelihood fits to the efficiency-corrected D^0 mass of the finally selected candidates. The fit model explained in detail in chapter 4 is used. In contrast to the branching fraction measurement, an additional splitting of the data according to a *tag* depending on the asymmetry is needed. For the measurement of A_{CP}, this tag is defined by the charge of the tag pion, $Q(\pi_s^+)$, while for A_{FB} and $A_{2\phi}$ it given by $\cos\theta_\mu$ or $\sin 2\phi$ larger or smaller than zero, respectively. The same mass shapes are assumed for all tag categories and determined independently for each signal decay and dimuon-mass region. The asymmetry is fitted by means of a simultaneous fit to both tag categories, where the asymmetries and total yields are treated as shared parameters. Therefore, for each fit component i (signal, misidentified hadronic decays and combinatorial background), the yield of the two tag categories (N_i^+ and N_i^-) is expressed in terms of the total yield of that component ($N_i = N_i^+ + N_i^-$) and the associated asymmetries as: $N_i^\pm = N_i(1 \pm A_i)/2$.

As examples, the fits on the dimuon-mass integrated samples are shown for $D^0 \to \pi^+\pi^-\mu^+\mu^-$ and $D^0 \to K^+K^-\mu^+\mu^-$ in Figure 6.8 and Figure 6.9. The fits in regions of dimuon mass can be found in Appendix E. The measured yields are reported in Table 6.4 for both signal channels and all considered dimuon-mass regions. On the dimuon-mass integrated samples, total signal yields of 1083 ± 41

$D^0 \to \pi^+\pi^-\mu^+\mu^-$ yields			
$m(\mu^+\mu^-)$ [MeV/c^2]	N_{sig}	N_{misID}	N_{comb}
525	90 ± 17	233 ± 25	108 ± 22
$< 565 - 780$	326 ± 23	253 ± 24	145 ± 21
$780 - 950$	141 ± 14	159 ± 15	89 ± 14
$950 - 1020$	244 ± 16	63 ± 13	43 ± 9
$1020 - 1100$	258 ± 14	33 ± 9	44 ± 9
full range	1083 ± 41	827 ± 42	579 ± 39
$D^0 \to K^+K^-\mu^+\mu^-$ yields			
$m(\mu^+\mu^-)$ [MeV/c^2]	N_{sig}	N_{misID}	N_{comb}
< 525	32 ± 8	5 ± 13	124 ± 20
> 565	74 ± 9	39 ± 7	48 ± 8
full range	110 ± 13	49 ± 12	181 ± 19

Table 6.4: Efficiency-weighted signal and background yields for (top) $D^0 \to \pi^+\pi^-\mu^+\mu^-$ and (bottom) $D^0 \to K^+K^-\mu^+\mu^-$ decays in the dimuon-mass ranges. Notice that the full range includes the dimuon-mass regions that are not considered in the analysis, therefore the sum of yields in the dimuon-mass regions are not expected to match the yields of the full range [6].

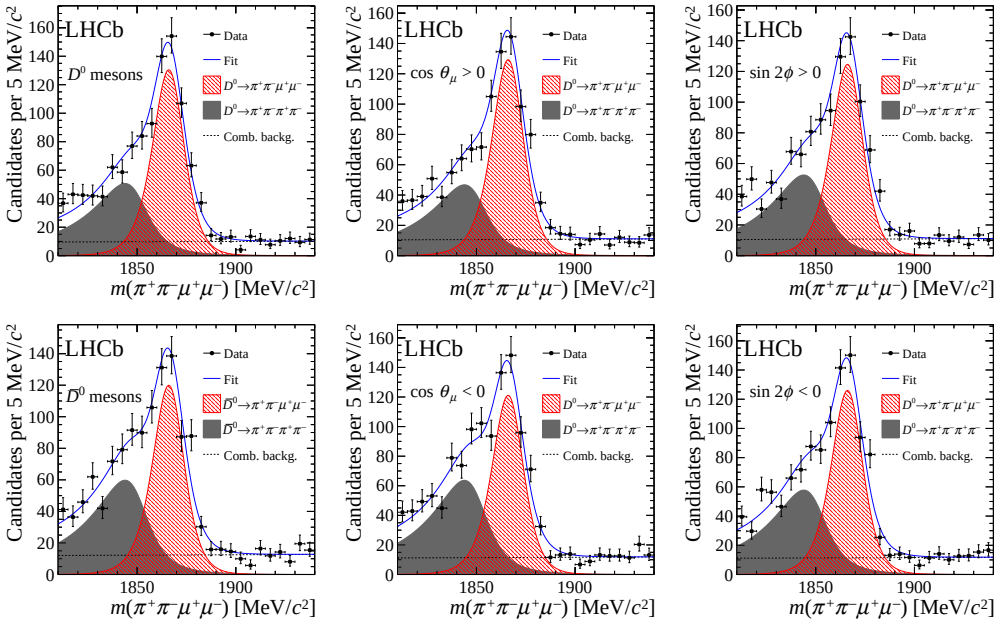

Figure 6.8: Efficiency-corrected distribution of the D^0 meson mass $m(D^0)$ for the full dimuon-mass range, separately (from left to right) for D^0 and $\overline{D}^0$ mesons, for $\cos\theta_\mu > 0$ and $\cos\theta_\mu < 0$, for $\sin 2\phi > 0$ and $\sin 2\phi < 0$, for $D^0 \to \pi^-\pi^+\mu^+\mu^-$ with fit projections overlaid [4].

(110 ± 13) for $D^0 \to \pi^+\pi^-\mu^+\mu^-$ ($D^0 \to K^+K^-\mu^+\mu^-$) are measured. All signal (and background) asymmetries can be found in Table 6.5. On the dimuon-mass integrated samples, the following signal asymmetries are found:

$$
\begin{aligned}
A_{CP}(D^0 \to \pi^+\pi^-\mu^+\mu^-) &= (\ \ 4.9 \pm 3.8)\%, \\
A_{FB}(D^0 \to \pi^+\pi^-\mu^+\mu^-) &= (\ \ 3.3 \pm 3.7)\%, \\
A_{2\phi}(D^0 \to \pi^+\pi^-\mu^+\mu^-) &= (-0.6 \pm 3.7)\%, \\
A_{CP}(D^0 \to K^+K^-\mu^+\mu^-) &= (0 \pm 11)\%, \\
A_{FB}(D^0 \to K^+K^-\mu^+\mu^-) &= (0 \pm 11)\%, \\
A_{2\phi}(D^0 \to K^+K^-\mu^+\mu^-) &= (9 \pm 11)\%,
\end{aligned}
$$

where the uncertainties are purely based on statistics. All measured asymmetries are compatible with zero within their statistical uncertainties. Systematic uncertainties are discussed in the following section.

Using pseudo-experiments, the fitter has been validated and does not introduce any bias and correctly estimates the uncertainties on the asymmetries as shown in Appendix C. Signal and background asymmetries in the range of $[-0.2, 0.2]$ are tested. The efficiency correction is mimicked by sampling weights from the

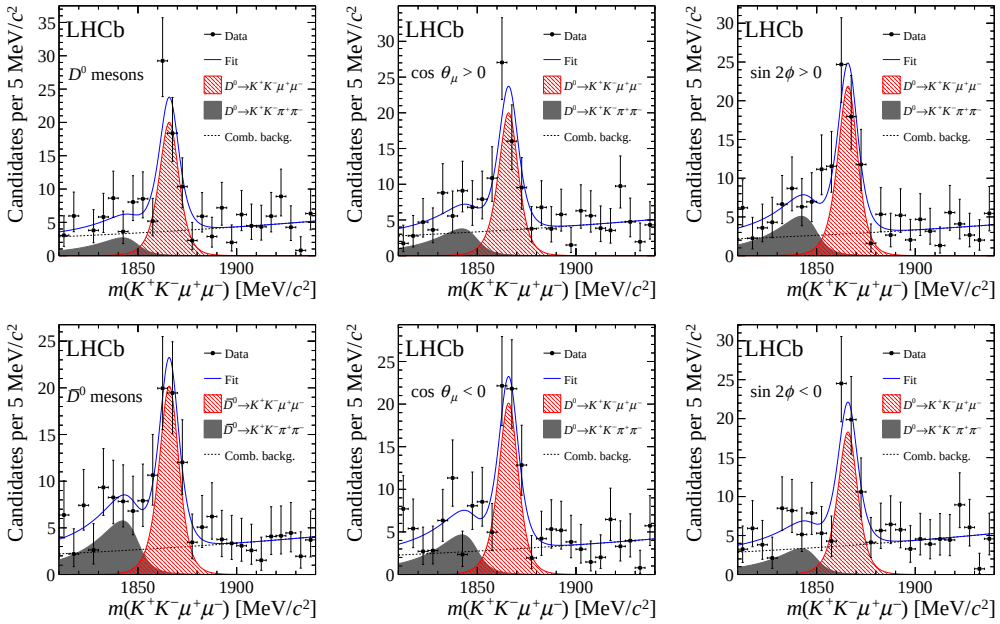

Figure 6.9: Efficiency-corrected distribution of the D^0 meson mass $m(D^0)$ for the full dimuon-mass range, separately (from left to right) for D^0 and $\overline{D}^0$ mesons, for $\cos\theta_\mu > 0$ and $\cos\theta_\mu < 0$, for $\sin 2\phi > 0$ and $\sin 2\phi < 0$, for $D^0 \to K^-K^+\mu^+\mu^-$ with fit projections overlaid [4].

signal weight distributions as obtained from data.

6.6 Systematic uncertainties

The following sources of systematic uncertainties affecting the measurements of the asymmetries are investigated:

- uncertainties related to the fit procedure, *i.e.* assumed mass shapes;
- uncertainties due to detection and production effects;
- uncertainties caused by neglected background.

Not all the measured asymmetries are subject to the same sources of systematic uncertainties. For instance, A_{CP} and A_{FB} require the knowledge of the D^0 flavour, hence are sensitive to possible flavour mistags. However, this has no effect on $A_{2\phi}$. In the following, a detailed discussion of all systematic uncertainties is given, specifying also explicitly which asymmetries are affected or not.

$D^0 \to \pi^+\pi^-\mu^+\mu^-$				
Asymmetry	$m(\mu^+\mu^-)$ $[\,\mathrm{MeV}/c^2]$	A_{sig}	A_{misID}	A_{comb}
A_{CP}^{raw}	< 525	0.158 ± 0.200	-0.027 ± 0.105	-0.356 ± 0.192
	$565 - 780$	-0.135 ± 0.071	-0.092 ± 0.094	-0.042 ± 0.146
	$780 - 950$	0.161 ± 0.100	-0.089 ± 0.095	-0.087 ± 0.164
	$950 - 1020$	0.068 ± 0.065	-0.281 ± 0.206	-0.227 ± 0.202
	$1020 - 1100$	0.092 ± 0.055	-0.319 ± 0.288	0.087 ± 0.218
	full range	0.042 ± 0.038	-0.083 ± 0.052	-0.113 ± 0.068
A_{CP}	< 525	0.165 ± 0.200		
	$565 - 780$	-0.129 ± 0.071		
	$780 - 950$	0.167 ± 0.100		
	$950 - 1020$	0.075 ± 0.065		
	$1020 - 1100$	0.099 ± 0.055		
	full range	0.049 ± 0.038		
A_{FB}	< 525	0.016 ± 0.197	-0.006 ± 0.106	0.077 ± 0.209
	$565 - 780$	0.081 ± 0.071	-0.231 ± 0.092	-0.221 ± 0.144
	$780 - 950$	0.072 ± 0.100	-0.270 ± 0.097	0.167 ± 0.161
	$950 - 1020$	0.031 ± 0.065	-0.381 ± 0.209	-0.062 ± 0.211
	$1020 - 1100$	0.009 ± 0.056	-0.125 ± 0.268	0.012 ± 0.219
	full range	0.033 ± 0.037	-0.153 ± 0.052	-0.035 ± 0.069
$A_{2\phi}$	< 525	-0.282 ± 0.200	-0.051 ± 0.107	0.055 ± 0.208
	$565 - 780$	0.074 ± 0.071	0.016 ± 0.094	-0.232 ± 0.143
	$780 - 950$	-0.139 ± 0.100	0.001 ± 0.096	-0.090 ± 0.163
	$950 - 1020$	0.012 ± 0.064	-0.411 ± 0.224	0.244 ± 0.202
	$1020 - 1100$	0.014 ± 0.055	-0.003 ± 0.267	0.102 ± 0.218
	full range	-0.006 ± 0.037	-0.048 ± 0.052	-0.031 ± 0.069
$D^0 \to K^+K^-\mu^+\mu^-$				
Asymmetry	$m(\mu^+\mu^-)$ $[\,\mathrm{MeV}/c^2]$	A_{sig}	A_{misID}	A_{comb}
A_{CP}^{raw}	< 525	-0.155 ± 0.259	0.000 ± 0.000	0.128 ± 0.115
	> 565	0.111 ± 0.116	-0.066 ± 0.174	-0.093 ± 0.172
	full range	-0.004 ± 0.113	-0.364 ± 0.239	0.123 ± 0.103
A_{CP}	< 525	-0.148 ± 0.259		
	> 565	0.118 ± 0.116		
	full range	0.003 ± 0.113		
A_{FB}	< 525	0.006 ± 0.259	0.000 ± 0.000	0.042 ± 0.111
	> 565	-0.059 ± 0.117	0.003 ± 0.175	0.298 ± 0.167
	full range	-0.003 ± 0.113	-0.107 ± 0.224	0.096 ± 0.105
$A_{2\phi}$	< 525	0.172 ± 0.259	0.000 ± 0.000	-0.046 ± 0.112
	> 565	0.038 ± 0.116	0.095 ± 0.175	-0.341 ± 0.173
	full range	0.089 ± 0.113	0.210 ± 0.223	-0.137 ± 0.106

Table 6.5: Signal and background asymmetries for (top) $D^0 \to \pi^+\pi^-\mu^+\mu^-$ and (bottom) $D^0 \to K^+K^-\mu^+\mu^-$ decays in the dimuon-mass ranges. Notice that the full range includes the dimuon-mass regions that are not considered in the analysis. As the fitter is not sensitive to the misID yield in the low dimuon-mass region for $D^0 \to K^+K^-\mu^+\mu^-$ due to the very low statistics, A_{misID} is fixed to zero [6].

Mass model used in the fit

The asymmetries are measured through fits to the D^0 mass distributions. The fit model used in chapter 4 is used, where the shape parameters are fixed in simulated and data control/sideband samples. All asymmetries are affected by the uncertainty related to the fit model. As done for the branching fraction measurement, the effect of the particular choice of the mass shapes is evaluated by identifying a set of alternative shapes (*cf.* section 5.5). Pseudo-experiments are used to quantify the effects as follows: The alternative models (and the default one as reference) are used to generate pseudo-data, which are then fitted by the default model, assuming vanishing as well as non-zero asymmetries in the range $[-0.2, 0.2]$. In all cases, no dependency on the generated asymmetries is observed. The RMS of the distributions of the differences of the asymmetry measured by the default and the alternative models (assuming zero asymmetries) is then taken as systematic uncertainty. The study is done for each dimuon mass to account for the observed signal over background levels by generating the yields for each component as obtained in section 6.5 (*cf.* Table 6.4).

To test the uncertainty related to the signal mass shape, in total 10 alternative signal shapes are tested. To get a decent variation, the signal mass shape is determined in five different regions of dimuon mass, while the default model is determined on the total sample. As the resolution varies across the dimuon-mass range, alternatives with respect to the default are tested. In addition, the study is repeated by allowing for a multiplicative scale factor that can adjust the width of the distribution. As example, the alternative signal shapes for $D^0 \to \pi^+\pi^-\mu^+\mu^-$ can be found in Figure 6.10 (left), together with the distribution of the differences of the fitted asymmetries. A RMS of 0.2% for the dimuon-mass integrated $D^0 \to \pi^+\pi^-\mu^+\mu^-$ samples is found and taken as systematic uncertainty. Analogously, a value of 0.4% is found for $D^0 \to K^+K^-\mu^+\mu^-$ candidates. The separate results as found in all dimuon-mass regions can be found in Table 6.6. As the effect of the signal mass shape on the measured asymmetry is negligible compared to the statistical precision of the measurement, no scale factors have been allowed for in the signal mass fits.

The uncertainty coming from the determination of the misidentified $D^0 \to h^+h^-\pi^+\pi^-$ shape is evaluated by varying the muon PID requirements and the assumed combinatorial background shape as described in more detail for the branching fraction measurement in section 5.5. In addition, an alternative control sample with different preselection requirements (but lower statistics) has been identified and used to determine the mass shapes. A total of 18 alternative

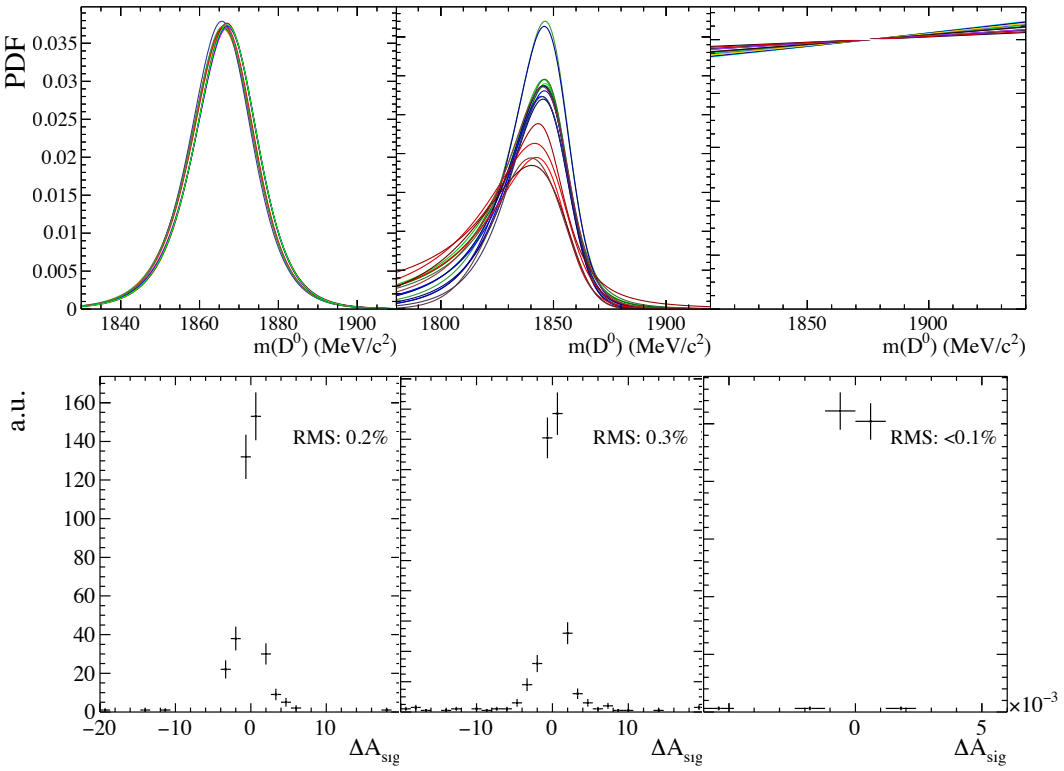

Figure 6.10: (Top) Tested D^0-mass shapes for $D^0 \to \pi^+\pi^-\mu^+\mu^-$ (left) signal, (center) misidentified hadronic decays and (right) combinatorial background. (Bottom) Distribution of the difference between the asymmetry measured by the default model and the asymmetry measured by the alternative models in a set pseudo-experiments with zero generated asymmetry. Shown is the study for the dimuon-mass integrated sample (modified from [6]).

models are tested, whose graphical illustration are shown in Figure 6.10 (middle). The observed RMS for each dimuon-mass region can be found in Table 6.6 for both signal decay modes. On the integrated samples, variations of 0.3% (0.4%) are determined for $D^0 \to \pi^+\pi^-\mu^+\mu^-$ ($D^0 \to K^+K^-\mu^+\mu^-$).

Similar as it has been done for the branching fraction measurement, the effect of the requirement of the BDT and Δm sideband on the description of the combinatorial background mass shape is determined by varying the Δm requirement, the BDT and muon PID thresholds. In total, 20 different sideband definitions have been tested. The different PDFs as obtained in the various sidebands are shown in Figure 6.10 (right) for $D^0 \to \pi^+\pi^-\mu^+\mu^-$. The uncertainties for all dimuon-mass regions are listed individually in Table 6.6, but are negligible with respect to the uncertainties caused by the other two components.

The total uncertainty assigned due to the fit model is the sum in quadrature of the three contributions from signal, misidentified and combinatorial background and found to be 0.4% (0.5%) on the dimoun mass integrated samples

$m(\mu^+\mu^-)$	$D^0 \to \pi^+\pi^-\mu^+\mu^-$			
$[\,\mathrm{MeV}/c^2]$	signal Shape $\Delta A_{\mathrm{sig}}[\%]$	misID shape ΔA_{sig} [%]	combinatorial shape $\Delta A_{\mathrm{sig}}[\%]$	total $\Delta A_{\mathrm{sig}}[\%]$
< 525	0.5	0.8	< 0.1	1.0
$565 - 780$	0.3	0.3	< 0.1	0.4
$780 - 950$	0.4	0.5	< 0.1	0.6
$950 - 1020$	0.2	0.3	0.1	0.4
$1020 - 1100$	0.3	0.4	0.1	0.5
full range	0.2	0.3	< 0.1	0.4

$m(\mu^+\mu^-)$	$D^0 \to K^+K^-\mu^+\mu^-$			
$[\,\mathrm{MeV}/c^2]$	signal Shape ΔA_{sig} [%]	misID shape ΔA_{sig} [%]	combinatorial shape ΔA_{sig} [%]	total ΔA_{sig} [%]
< 525	0.7	0.6	0.2	0.9
> 565	0.3	0.4	< 0.1	0.5
full range	0.4	0.4	0.1	0.5

Table 6.6: Systematic uncertainties due to the assumed mass shapes for all dimuon-mass bins of (top) $D^0 \to \pi^+\pi^-\mu^+\mu^-$ and (bottom) $D^0 \to K^+K^-\mu^+\mu^-$ [6].

(dimuon-mass binned values are to be found in Figure 6.10) of $D^0 \to \pi^+\pi^-\mu^+\mu^-$ ($D^0 \to K^+K^-\mu^+\mu^-$) decays. These systematic uncertainties correspond to $\lesssim 10\%$ of the statistical precision of the measurement.

Detector induced effects

Uncertainties due to detection and production effects include limitations of the method used to correct for phase-space dependent efficiencies, the finite resolution on the angular variables and possibly uncertainties coming from an imperfect cancellation of nuisance asymmetries (affecting only A_{CP}).

Phase-space dependent efficiencies

Per-candidate weights are defined as the inverse efficiencies, as functions of a reweighter BDT output. The weighting corrects for efficiency variations across the five dimensional phase space. As the reweighter is trained on simulated samples, this section investigates the effect of limitations of the simulation to accurately describe the data. In total, 15 alternative reweighter BDTs have been trained, neglecting or tightening requirements on quantities that are expected to be *not* well described by the simulation, such as PID, trigger efficiencies and particle multiplicities. In more detail, these alternative requirements are:

- no requirement on the hardware and/or software trigger;

$m(\mu^+\mu^-)$ [MeV/c^2]	$D^0 \to \pi^+\pi^-\mu^+\mu^-$		
	ΔA_{CP} [%]	ΔA_{FB} [%]	$\Delta A_{2\phi}$ [%]
< 525	1.8	1.6	1.9
$565 - 780$	0.3	0.3	0.4
$780 - 950$	0.8	0.9	0.4
$950 - 1020$	0.4	0.2	0.1
$1020 - 1100$	0.3	0.3	0.2
full range	0.4	0.2	0.3

$m(\mu^+\mu^-)$ [MeV/c^2]	$D^0 \to K^+K^-\mu^+\mu^-$		
	ΔA_{CP} [%]	ΔA_{FB} [%]	$\Delta A_{2\phi}$ [%]
< 525	3.5	4.3	3.2
> 565	0.5	3.7	0.6
full range	1.3	1.5	0.9

Table 6.7: Systematic uncertainties caused by potential data-simulation differences impacting the phase-space efficiency correction for all dimuon-mass bins of (top) $D^0 \to \pi^+\pi^-\mu^+\mu^-$ and (bottom) $D^0 \to K^+K^-\mu^+\mu^-$ (modified from [6]).

- no or tighter `BDT` requirement;
- no/tighter `PID` requirement on the muons and/or on the hadrons;
- various combinations of the above, including no trigger, `BDT` and PID requirements at all.

The bias caused by an inaccurate efficiency correction depends on the measured asymmetries and also on their variations across the phase space. For example, if one assumes a vanishing or constant asymmetry across all phase-space variables, no bias can be caused at all. Thus, the data are refitted using the 15 alternative reweighter BDTs and the measured asymmetries are compared to the default configuration and the standard deviation of the observed differences is taken as systematic uncertainty. The study is done individually for all dimuon-mass regions and on the total sample. To give an example, on the total sample, a systematic uncertainty of 0.4% (1.3%) is assigned on A_{CP} for $D^0 \to \pi^+\pi^-\mu^+\mu^-$ ($D^0 \to K^+K^-\mu^+\mu^-$) decays. Results for all asymmetries and dimuon-mass regions can be found in Table 6.7. Evaluating the systematic uncertainty by refitting the data has the risk to include also a statistical component in the observed variations. However, given the small variations found compared to the statistical precision of

the measurement ($\lesssim 14\%$ of the statistical uncertainty), the method is considered to be sufficiently accurate for the presented analysis.

Asymmetric angular efficiencies and experimental resolution

The reweighter BDT is trained assuming that the efficiency variation as a function of the angular variable is symmetric with respect to zero, and the absolute values of $\cos\theta_\mu$ and $\cos\theta_h$ are used. Effectively, this assumption leads to higher statistics in the training (by a factor of four). The assumption is validated using simulations where no angular asymmetries are generated. Any measured angular asymmetry in the simulated candidates is therefore caused by detector effects. The angular asymmetries are measured to be $A_{FB} = (0.3 \pm 0.4)\%$ ($(0.7 \pm 0.6)\%$) and $A_{2\phi} = (0.1 \pm 0.4)\%$ ($(-0.1 \pm 0.6)\%$) for $D^0 \to \pi^-\pi^+\mu^+\mu^-$ ($D^0 \to K^-K^+\mu^+\mu^-$) decays. All asymmetries are consistent with zero, but conservatively their uncertainties are taken as systematic uncertainties on the measured asymmetries A_{FB} and $A_{2\phi}$.

Experimental resolution on the angular variables can also lead to a bias. To measure A_{FB} ($A_{2\phi}$), the signal data samples are split according to $\cos\theta_\mu$ ($\sin 2\phi$) greater or smaller than zero. Candidates that migrate from positive to negative values (and vice versa) because of resolution effects are *mistagged*. The mistag rate f_w translates into a bias on the angular asymmetries of:

$$\Delta_A = \frac{2f_w}{1-2f_w} A_{\text{meas}},$$

where A_{meas} is the measured asymmetry. The mistag rate in $\cos\theta_\mu$ is determined in simulation to be $0.4\%(0.5\%)$ for $D^0 \to \pi^-\pi^+\mu^+\mu^-$ ($D^0 \to K^-K^+\mu^+\mu^-$) decays, leading to a bias on A_{FB} of $< 0.1\%$ ($< 0.1\%$). Similarly, a mistag rate of $0.8\%(1.4\%)$ is found in $\sin 2\phi$, which translates into a bias of $< 0.1\%$ (0.2%) on $A_{2\phi}$. These biases are assigned as systematic uncertainties on the corresponding angular asymmetries. The same uncertainties are propagated to each dimuon-mass region.

Nuisance charge asymmetries

As explained in section 6.4, the measured raw asymmetries A_{CP}^{raw} are corrected by production and detection asymmetries using high statistic samples of $D^{*+} \to D^0(\to K^+K^-)\pi_s^+$ decays. The correction is done in regions of transverse and longitudinal momenta of the D^{*+} candidate to cover the different kinematics of the control and signal samples.

Simulated samples have been used as proxies for the signal channel kinematics.

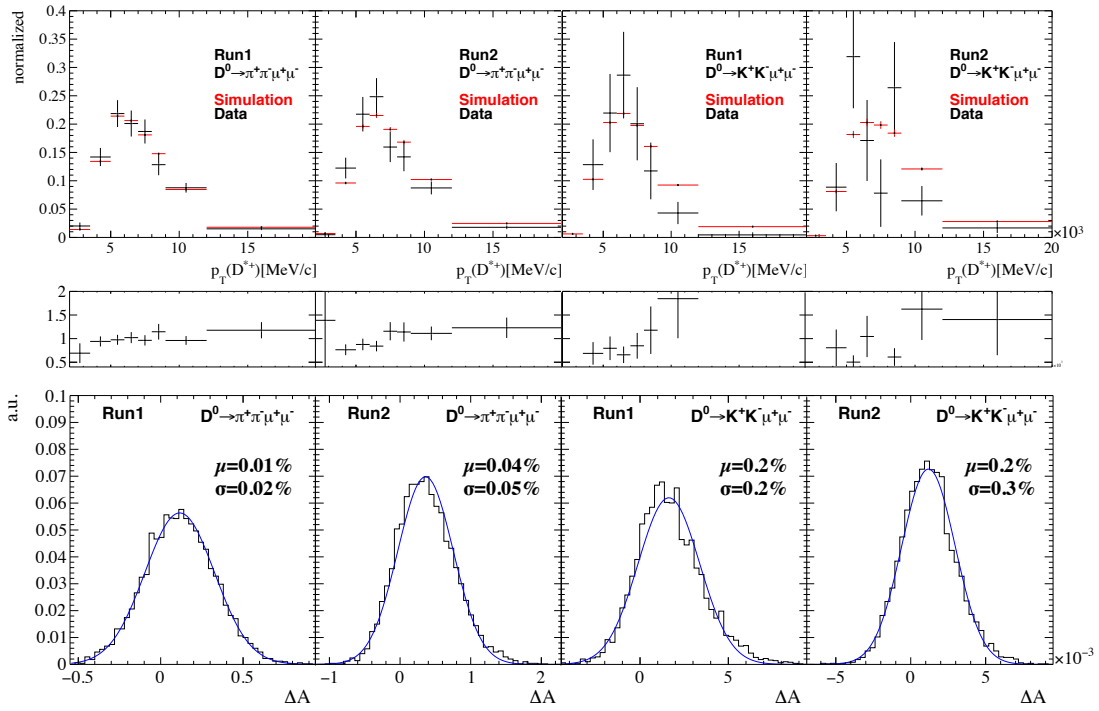

Figure 6.11: (Top) Comparison between $p_T(D^*)$ distributions of background-subtracted (left) $D^0 \to \pi^+\pi^-\mu^+\mu^-$ and (right) $D^0 \to K^+K^-\mu^+\mu^-$ candidates with corresponding simulated candidates and (middle) their ratio. (Bottom) Distributions of the deviation from the default value of the correction for the nuisance charge asymmetries when several alternative $p_T(D^*)$ distributions are used to reweight the control sample kinematics (modified from [6]).

To check effect of potential differences of simulations and data, the background subtracted $p_T(D^{*+})$ spectra from data are compared to the simulated ones in Figure 6.11, separately for data taken in Run 1 and Run 2 and $D^0 \to \pi^+\pi^-\mu^+\mu^-$ (left) and $D^0 \to K^+K^-\mu^+\mu^-$ (right) signal decays. Their ratios are also shown in the bottom panels. The agreement is fairly good. However, the effect of small deviation is evaluated as follows. The correction procedure is re-evaluated 5000 times. In each iteration, an alternative $p_T(D^{*+})$ distribution is chosen by weighting the $p_T(D^{*+})$ spectrum with weights as obtained from the ratio of simulated and background subtracted data spectra (by random sampling from the ratio). In this way, the alternative, reweighted $p_T(D^{*+})$ spectra on average account for the observed simulation-data differences. The bottom row in Figure 6.11 shows the resulting distribution of the differences of the default and alternative corrections. The largest variations are observed for $D^0 \to K^+K^-\mu^+\mu^-$ (Run 2), where relatively large uncertainties on the ratio are driven by the limited statistics of the data sample. Nevertheless, the sum of mean and width of the distribution is never larger than 0.4%. Conservatively, this value is combined quadratically

with the uncertainty on the combined correction for the production and detection asymmetry of 0.2%. In total, this results in systematic uncertainty of 0.5% which is assigned to the A_{CP} measurement of both signal decays and each dimuon-mass region.

As additional cross check, a possible dependency of the correction on the considered dimuon-mass range is investigated. At first order, the kinematics of the D^{*+} and π_s^+ do not depend on the kinematics of the D^0 decay products. However, some selection requirements might indirectly also change the kinematics of the parent particles. The combined correction for the production and detection asymmetry is determined for signal candidates in the low and high dimuon-mass regions independently. In these two regions, the largest (relative) difference in kinematics of the dimoun pair is expected. Compatible values of $(-0.67 \pm 0.19)\%$ and $(-0.65 \pm 0.19)\%$ are found. No additional systematic uncertainty is assigned.

Residual background contaminations

A small fraction of backgrounds from random soft pions and secondary D^{*+} mesons from decays of b-flavoured hadrons has been neglected. The impact of their presence is evaluated in the following, where effects caused by random soft pions are affecting the determination of A_{CP} and A_{FB} (which need flavour tagging)[2], while secondary D^{*+} decays play only a role for A_{CP}.

Generally, also the effect of $D^0 - \overline{D}^0$ mixing needs to be accounted for as all asymmetries are meausured integrated over the D^0 decay time. This means that A_{FB} is diluted by D^0 candidates that have oscillated before they decay. Given the small charm mixing parameters [12], this effects is completely negligible compared to other systematic uncertainties.

Random soft pions

The signal yields are determined through fits to the $m(D^0)$ distributions, so random pions are considered as signals in the fit. Their fraction, however, is greatly suppressed by a very tight requirement on Δm ($144.5 < \Delta m < 146.5\,\mathrm{MeV}/c^2$). Candidate decays consisting of a real D^0 and a random soft pion have a random flavour tag. To evaluate the bias on measured asymmetries A_{signal} ($= A_{FB}, A_{CP}$) that need flavour tagging, the totally measured asymmetry $A^{\mathrm{raw}}_{\mathrm{signal}}$ is written as:

$$A^{\mathrm{raw}}_{\mathrm{signal}} = (1 - f_{\mathrm{random}})A_{\mathrm{signal}} + f_{\mathrm{random}}A_{\mathrm{random}}, \tag{6.2}$$

[2]Due to the definition of the angles (*cf.* section 1.5), $\cos\theta_\mu$ changes sign when transforming from D^0 to $\overline{D}^0$ (while $\sin 2\phi$ stays unchanged), making A_{FB} sensitive to wrong flavour tags.

The fraction f_{random} is estimated by extrapolating (assuming a flat distribution in Δm) the D^0 candidates observed in the Δm sideband defined as $148 < \Delta m < 158\,\text{MeV}/c^2$ into the signal region. To profit from higher statistics, the fraction is evaluated on a sample of kinematically very similar $D^0 \to K^-\pi^+[\mu^+\mu^-]_{\rho^0/\omega}$ decays subject to the signal selection and determined to be $f_{\text{random}}^{K\pi\mu\mu} = (1.4 \pm 0.1)\%$. Compatible, but less precise values are determined on the signal samples. Using the same sideband definition, the fraction of random pion background in the $D^0 \to K^+K^-$ control sample is determined to be $f_{\text{random}}^{KK} = (5.3 \pm 0.1)\%$. The same sideband candidates are furthermore used to estimate the asymmetry A_{random} to be $(0.6 \pm 0.1)\%$, which is assumed to be independent of the final state. Terms in Equation 6.2 proportional to $f_{\text{random}} A_{\text{random}} \sim \mathcal{O}(10^{-4})$ can therefore safely be neglected. Given the uncertainty of 0.18% on $A_{CP}(K^+K^-)$ [191], any bias on $A_{CP}^{\text{raw}}(K^+K^-) \sim \mathcal{O}(10^{-4})$ is also negligible. For the signal asymmetries, the remaining bias of $\Delta_A = f_{\text{random}} A_{\text{signal}} \sim 1.4\% \cdot A_{\text{signal}}^{\text{raw}}$ is assigned as systematic uncertainty for both signal decays and all dimuon-mass regions.

Secondary D^{*+} decays

The analysis does also not distinguish D^0 mesons coming from secondary D^{*+} decays, which arise from decays of intermediate B-hadrons. As secondary mesons exhibit a different production mechanism, they are also subject to a different production asymmetry inherited from the production of the parent b-flavoured hadron. So, the total production asymmetry is a sum:

$$A_P(D^{*+}) = (1 - f_{\text{sec}}) A_{\text{prim}} + f_{\text{sec}} A_{\text{sec}},$$

with f_{sec} being the fraction of secondary decays, and A_{prim} and A_{sec} the production asymmetries of primary and secondary D^{*+} decays, respectively. The production asymmetry is only relevant for the measurement of A_{CP}, which is corrected by the value as measured in a control sample of $D^0 \to K^+K^-$ decays. The difference of the production asymmetries in terms of the secondary fractions in signal ($f_{\text{sec}}^{hh\mu\mu}$) and control mode ($f_{\text{sec}}^{KK}$) reads as follows:

$$\begin{aligned} \Delta_{A_{CP}} &= A_P(h^+h^-\mu^+\mu^-) - A_P(K^+K^-) \\ &= [f_{\text{sec}}^{hh\mu\mu} - f_{\text{sec}}^{KK}](A_{\text{sec}} - A_{\text{prim}}). \end{aligned}$$

A residual bias $\Delta_{A_{CP}}$ remains if the secondary fractions in signal and control samples are not equal, which is proportional to their difference and $(A_{\text{sec}} - A_{\text{prim}})$.

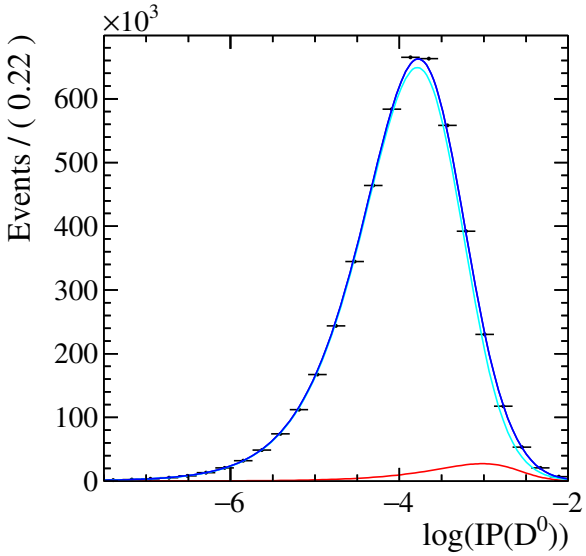

Figure 6.12: Distribution of the logarithm of the IP of D^0 mesons for background-subtracted $D^0 \to K^+K^-$ candidates (black data points), with fit projection overlaid [6]. The PDF describing primary decays is shown in cyan, the one for secondaries in red. The total PDF is coloured in dark blue.

As explained in chapter 4, secondary decays can be distinguished from the primary decays by comparing the IP distributions of the D^0 mesons, which are on average larger for secondary decays due to the finite distance the intermediate B-hadron flies before it decays. The difference of the production asymmetries is estimated by comparing the measured raw asymmetries in two primary-dominated and secondary-dominated regions, defined by $\mathrm{IP}_{\chi^2}(D^0) < 25$ and $\mathrm{IP}_{\chi^2}(D^0) > 25$ to be $(A_{\mathrm{sec}} - A_{\mathrm{prim}}) = (-0.2 \pm 0.2)\%$. The fraction of secondary decays in the control sample f_{sec}^{KK} is determined by a fit to the logarithm of the background subtracted IP distribution of the D^0 mesons as shown in Figure 6.12 to be 3.7%. The PDFs to describe the distributions are determined using simulated samples. The low statistics in the signal modes do not allow for a stable fit, so their secondary fractions are estimated from simulations to be 1.6%(2.5%) for $D^0 \to \pi^+\pi^-\mu^+\mu^-$ ($D^0 \to K^+K^-\mu^+\mu^-$). Given the marginal resulting bias of 0.1% (< 0.1%) for $D^0 \to \pi^+\pi^-\mu^+\mu^-$ ($D^0 \to K^+K^-\mu^+\mu^-$) decays, the level of accuracy is considered sufficient and the estimated bias is taken as systematic uncertainty, which is also propagated to each dimuon-mass region.

Consistency checks

To identify sources of systematic uncertainties that have not been considered so far and check internal consistency of the results, several *sanity checks* have been

Source	$D^0 \to \pi^+\pi^-\mu^+\mu^-$			$D^0 \to K^+K^-\mu^+\mu^-$		
	ΔA_{CP} [%]	ΔA_{FB} [%]	$\Delta A_{2\phi}$ [%]	ΔA_{CP} [%]	ΔA_{FB} [%]	$\Delta A_{2\phi}$ [%]
Mass model	0.4	0.4	0.4	0.5	0.5	0.5
Efficiency correction	0.4	0.2	0.3	1.3	1.5	0.9
Angular asymmetries	–	0.4	0.4	–	0.6	0.6
Angular resolution	–	< 0.1	< 0.1	–	< 0.1	0.3
Nuisance asymmetries	0.5	–	–	0.5	–	–
Secondary D^{*+} decays	0.1	–	–	< 0.1	–	–
Random pions background	0.1	0.1	–	< 0.1	< 0.1	–
Total systematic unc.	0.7	0.6	0.6	1.4	1.7	1.3

Table 6.8: Summary of the systematic uncertainties on the dimuon-mass integrated samples (modified from [6]).

performed by splitting the total data set in disjoint subsamples and measuring the asymmetries in those. In particular, splittings according to global event variables are carried out such as number of tracks, number of PVs and event number even or odd. Furthermore, splittings of detector configurations such as year of data taking, magnet polarity, and hardware trigger category are considered. Finally, also dependencies on transverse momentum of the D^{*+} and the IP_{χ^2} of the D^0 candidates are investigated. In all cases the measured asymmetries are consistent with being uniformly distributed across these splittings.

Summary systematic uncertainties

A summary of all systematic uncertainties is given in Table 6.8 (for the dimuon-mass integrated sample). The total systematic uncertainty of each asymmetry does not exceed 0.7%(1.4%) for $D^0 \to \pi^+\pi^-\mu^+\mu^-$ ($D^0 \to K^+K^-\mu^+\mu^-$) decays. These values only play a very minor role compared to the statistical precision of 3.7%(11%) on the measured asymmetries.

6.7 Summary

Using a sample of $5\,\text{fb}^{-1}$ of proton-proton collision data recorded by LHCb during 2011-2016, the CP asymmetry A_{CP} and angular asymmetries A_{FB} and $A_{2\phi}$ are measured in rare $D^0 \to \pi^+\pi^-\mu^+\mu^-$ and $D^0 \to K^+K^-\mu^+\mu^-$ decays. On the dimuon integrated samples, the following asymmetries are measured:

$$
\begin{aligned}
A_{CP}(D^0 \to \pi^+\pi^-\mu^+\mu^-) &= (\ \ 4.9 \pm 3.8 \pm 0.7)\%, \\
A_{FB}(D^0 \to \pi^+\pi^-\mu^+\mu^-) &= (\ \ 3.3 \pm 3.7 \pm 0.6)\%, \\
A_{2\phi}(D^0 \to \pi^+\pi^-\mu^+\mu^-) &= (-0.6 \pm 3.7 \pm 0.6)\%, \\
A_{CP}(D^0 \to K^+K^-\mu^+\mu^-) &= (0 \pm 11 \pm 1)\%, \\
A_{FB}(D^0 \to K^+K^-\mu^+\mu^-) &= (0 \pm 11 \pm 2)\%, \\
A_{2\phi}(D^0 \to K^+K^-\mu^+\mu^-) &= (9 \pm 11 \pm 1)\%
\end{aligned}
$$

where the first uncertainty is statistical and the second systematic. The precision of the results is completely dominated by the statistical uncertainty. The asymmetries measured as a function of dimuon mass are shown in Table 6.9 and Figure 6.13. All measured asymmetries are consistent with zero and therefore compatible with SM predictions. No dependency of the asymmetries on the dimuon mass is observed. These are the first measurements of asymmetries in rare charm hadron decays. The results [2] have been published in Physical Review Letters and help to constrain models of physics beyond the SM, which often predict asymmetries at the percent level (*cf.* chapter 1). At the same time as the results have been shown to a public

$m(\mu^+\mu^-)$ [MeV/c^2]	A_{CP}	A_{FB}	$A_{2\phi}$
	$D^0 \to \pi^+\pi^-\mu^+\mu^-$		
< 525	$17 \pm 20 \pm 2$	$2 \pm 20 \pm 2$	$-28 \pm 20 \pm 2$
$565 - 780$	$-12.9 \pm 7.1 \pm 0.7$	$8.1 \pm 7.1 \pm 0.7$	$7.4 \pm 7.1 \pm 0.7$
$780 - 950$	$17 \pm 10 \pm 1$	$7 \pm 10 \pm 2$	$-14 \pm 10 \pm 2$
$950 - 1020$	$7.5 \pm 6.4 \pm 2$	$3.1 \pm 6.5 \pm 2$	$1.2 \pm 6.4 \pm 2$
$1020 - 1100$	$9.9 \pm 5.5 \pm 0.7$	$0.9 \pm 5.6 \pm 0.7$	$1.4 \pm 5.5 \pm 0.6$
	$D^0 \to K^+K^-\mu^+\mu^-$		
< 525	$-33 \pm 26 \pm 4$	$23 \pm 26 \pm 4$	$9 \pm 26 \pm 3$
> 565	$13 \pm 12 \pm 1$	$1 \pm 12 \pm 1$	$22 \pm 12 \pm 1$

Table 6.9: Measured asymmetries for (top) $D^0 \to \pi^+\pi^-\mu^+\mu^-$ and (bottom) $D^0 \to K^+K^-\mu^+\mu^-$ decays in the dimuon-mass ranges. Notice that the full range includes the dimuon-mass regions that are not considered in the analysis. The first uncertainty is statistical, the second systematic [6].

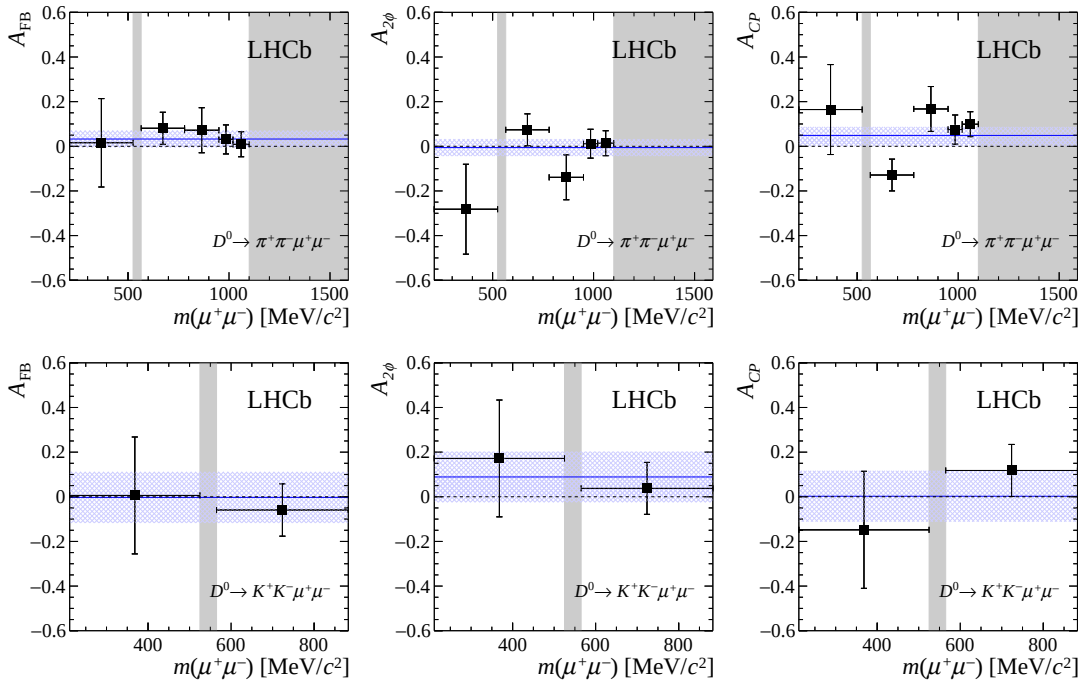

Figure 6.13: Measured values of (left) A_{CP}, (center) A_{FB} and (right) $A_{2\phi}$ for (top) $D^0 \to \pi^+\pi^-\mu^+\mu^-$ and (bottom) $D^0 \to K^+K^-\mu^+\mu^-$ decays in the dimuon-mass ranges. The hatched band corresponds to the integrated measurement. The uncertainties include both statistical and systematic sources [4].

audience for the first time, Ref. [96] has worked out a systematic analysis of the the full angular distribution of $D^0 \to h^+h^-\mu^+\mu^-$ decays as applied in B-decays [196]. In addition to the asymmetries measured in the scope of this thesis, additional clean SM null tests can be constructed and motivate further investigations of these decays, making use of the full statistics of future LHCb data sets to further constrain the SM.

Final concluding remarks

This dissertation presents a comprehensive study of rare $D^0 \to \pi^+\pi^-\mu^+\mu^-$ and $D^0 \to K^+K^-\mu^+\mu^-$ decays at LHCb. Rare charm decays are sensitive to contributions from FCNC $c \to u\ell^+\ell^-$ transitions and therefore ideal places to search for physics beyond the SM in processes involving quantum loops in the up-type quark sector. Due to their high suppression, the branching fractions of these decays had been below the sensitivity of any previous experiment in the pre-LHCb era.

A full selection sequence for $D^0 \to h^+h^-\mu^+\mu^-$ decays at LHCb is presented. Background contaminations from candidates made of randomly associated tracks are greatly suppressed by selecting D^0 mesons arising from the decay chain $D^{*+} \to D^0\pi^+$. Further suppression is achieved by using multivariate analysis techniques and tight requirements on muon particle identification to effectively reduce background candidates from misidentified hadronic four-body decays. A fit model is developed to separate the remaining backgrounds and the signal component on a statistical basis.

Using pp collision data corresponding to $2\,\text{fb}^{-1}$ of integrated luminosity recorded by the LHCb experiment during Run 1 at a center-of-mass energy of 8 TeV, the first observation of $D^0 \to K^+K^-\mu^+\mu^-$ and $D^0 \to \pi^+\pi^-\mu^+\mu^-$ decays is reported. To control systematic uncertainties, the branching fractions are measured relative to the decay mode $D^0 \to K^-\pi^+[\mu^+\mu^-]_{\rho^0/\omega}$ and determined to be:

$$\mathcal{B}(D^0 \to \pi^+\pi^-\mu^+\mu^-) = (9.64 \pm 0.48 \pm 0.51 \pm 0.97) \cdot 10^{-7},$$
$$\mathcal{B}(D^0 \to K^+K^-\mu^+\mu^-) = (1.54 \pm 0.27 \pm 0.09 \pm 0.16) \cdot 10^{-7}.$$

These are consistent with SM expectations of long-distance contributions. The results represent the rarest decays of a charm hadron measured to date.

The unique phenomenology of rare charm decays among the heavy flavoured systems leads to almost vanishing CP violating effects and the absence of axial vector couplings in electroweak decay processes. Asymmetries with vanishing SM expectations can be constructed which are sensitive to the interference of the SM dynamics with contributions from new physics. These might significantly modify

the angular distributions of the final state particles or introduce additional sources of CPV.

Using an enlarged data set corresponding to $5\,\text{fb}^{-1}$ of integrated luminosity, including pp collisions recently recorded during Run 2 at a center-of-mass energy of 13 TeV, the first measurement of the CP asymmetry A_{CP}, the forward-backward asymmetry A_{FB} in the lepton system and the triple-product asymmetry $A_{2\phi}$ is presented. The flavour of the D^0 meson is determined by the charge of the pion in the decay chain $D^{*+} \to D^0\pi^+$. Spurious instrumental asymmetries are cancelled with a data driven approach using high-statistics samples of $D^{*+} \to D^0(\to K^+K^-)\pi^+$ decays. Efficiency variations across the five-dimensional phase-space are corrected using machine learning algorithms to allow for a meaningful theoretical interpretation of the results. The asymmetries are measured to be

$$\begin{aligned}
A_{CP}(D^0 \to \pi^+\pi^-\mu^+\mu^-) &= (\ \ 4.9 \pm 3.8 \pm 0.7)\%, \\
A_{FB}(D^0 \to \pi^+\pi^-\mu^+\mu^-) &= (\ \ 3.3 \pm 3.7 \pm 0.6)\%, \\
A_{2\phi}(D^0 \to \pi^+\pi^-\mu^+\mu^-) &= (-0.6 \pm 3.7 \pm 0.6)\%, \\
A_{CP}(D^0 \to K^+K^-\mu^+\mu^-) &= (0 \pm 11 \pm 1)\%, \\
A_{FB}(D^0 \to K^+K^-\mu^+\mu^-) &= (0 \pm 11 \pm 2)\%, \\
A_{2\phi}(D^0 \to K^+K^-\mu^+\mu^-) &= (9 \pm 11 \pm 1)\%
\end{aligned}$$

and confirming SM predictions. The analysis represents the first measurement of this kind of asymmetries and therefore a novel approach to test the SM in rare charm decays. The systematic uncertainties on the measured asymmetries are negligible and also expected to be sub leading for future measurements with increased data sets.

All observables are also investigated as function of dimuon mass to gain sensitivity to non-SM contributions that might populate distinct regions in the decay phase space. Regions in dimuon mass are defined to cover intermediate resonances as well as a high and low dimuon-mass region where the influence of the resonances is minimal. The results presented in this thesis help to constrain models of physics beyond the SM which modify FCNC processes of charm hadrons.

In the past decades, most experimental effort was focussed on FCNC processes in the b-quark system involving $b \to s\ell^+\ell^-$ transitions, where a consistent pattern of hints of signs of physics beyond the SM has emerged in the angular distributions and differential branching fractions. If these effects are really caused by physics beyond the SM, studies of FCNC processes in the charm system will help to better understand the origin of the anomalies. Based on the results of this thesis, a full

angular analysis of rare four-body charm decays as routinely applied in B-decays appears feasible in the near future at the LHCb experiment.

Bibliography

[1] LHCb collaboration, R. Aaij *et al.*, *Observation of D^0 meson decays to $\pi^+\pi^-\mu^+\mu^-$ and $K^+K^-\mu^+\mu^-$ final states*, Phys. Rev. Lett. **119** (2017) 181805, arXiv:1707.08377.

[2] LHCb collaboration, R. Aaij *et al.*, *Measurement of angular and CP asymmetries in $D^0 \to \pi^+\pi^-\mu^+\mu^-$ and $D^0 \to K^+K^-\mu^+\mu^-$ decays*, Phys. Rev. Lett. **121** (2018) 091801, arXiv:1806.10793.

[3] *See supplemental material for LHCB-PAPER-2017-019 on the CERN document sever (CDS)*, https://cds.cern.ch/record/2276004?ln=en.

[4] *See supplemental material for LHCB-PAPER-2018-020 on the CERN document sever (CDS)*, https://cds.cern.ch/record/2627588?ln=en.

[5] D. S. Mitzel, A. Contu, A. Di Canto, and B. Viaud, *Search for $D^0 \to h^+h^-\mu^+\mu^-$ decays with 2fb^{-1} at LHCb*, LHCb-ANA-2017-013.

[6] D. S. Mitzel, A. Contu, and A. Di Canto, *Measurement of angular and CP asymmetries in $D^0 \to h^+h^-\mu^+\mu^-$ decays at LHCb*, LHCb-ANA-2018-007.

[7] S. L. Glashow, *Partial Symmetries of Weak Interactions*, Nucl. Phys. **22** (1961) 579.

[8] S. Weinberg, *A model of leptons*, Phys. Rev. Lett. **19** (1967) 1264.

[9] A. Salam, *Weak and Electromagnetic Interactions*, Conf. Proc. **C680519** (1968) 367.

[10] M. E. Peskin and D. V. Schroeder, *An Introduction to quantum field theory*, Addison-Wesley, Reading, USA, 1995.

[11] E. Noether, *Invariant Variation Problems*, Gott. Nachr. **1918** (1918) 235, arXiv:physics/0503066, [Transp. Theory Statist. Phys.1,186(1971)].

[12] Particle Data Group, C. Patrignani *et al.*, *Review of particle physics*, Chin. Phys. **C40** (2016) 100001, and 2017 update.

[13] P. W. Higgs, *Broken symmetries and the masses of gauge bosons*, Phys. Rev. Lett. **13** (1964) 508.

[14] F. Englert and R. Brout, *Broken Symmetry and the Mass of Gauge Vector Mesons*, Phys. Rev. Lett. **13** (1964) 321, [,157(1964)].

[15] G. S. Guralnik, C. R. Hagen, and T. W. B. Kibble, *Global Conservation Laws and Massless Particles*, Phys. Rev. Lett. **13** (1964) 585, [,162(1964)].

[16] M. Kobayashi and T. Maskawa, *CP violation in the renormalizable theory of weak interaction*, Prog. Theor. Phys. **49** (1973) 652.

[17] N. Cabibbo, *Unitary symmetry and leptonic decays*, Phys. Rev. Lett. **10** (1963) 531.

[18] CKMfitter group, J. Charles *et al.*, *CP violation and the CKM matrix: Assessing the impact of the asymmetric B factories*, Eur. Phys. J. **C41** (2005) 1, `arXiv:hep-ph/0406184`, updated results and plots available at `http://ckmfitter.in2p3.fr/`.

[19] L. Wolfenstein, *Parametrization of the Kobayashi-Maskawa matrix*, Phys. Rev. Lett. **51** (1983) 1945.

[20] I. I. Y. Bigi, *CP violation: An Essential mystery in nature's grand design*, Surveys High Energ. Phys. **12** (1998) 269, `arXiv:hep-ph/9712475`, [Proc. Int. Sch. Phys. Fermi137,451(1998)].

[21] G. Luders, *On the Equivalence of Invariance under Time Reversal and under Particle-Antiparticle Conjugation for Relativistic Field Theories*, Kong. Dan. Vid. Sel. Mat. Fys. Med. **28N5** (1954) 1.

[22] Belle collaboration, S. K. Choi *et al.*, *Observation of a resonance-like structure in the $\pi^+\psi'$ mass distribution in exclusive $B \to K\pi^+\psi'$ decays*, Phys. Rev. Lett. **100** (2008) 142001, `arXiv:0708.1790`.

[23] LHCb collaboration, R. Aaij *et al.*, *Observation of the resonant character of the $Z(4430)^-$ state*, Phys. Rev. Lett. **112** (2014) 222002, `arXiv:1404.1903`.

[24] LHCb collaboration, R. Aaij *et al.*, *Observation of $J/\psi p$ resonances consistent with pentaquark states in $\Lambda_b^0 \to J/\psi p K^-$ decays*, Phys. Rev. Lett. **115** (2015) 072001, `arXiv:1507.03414`.

[25] S. Martin, *A Supersymmetry primer*, Adv. Ser. Direct. High Energy Phys. **18** (1997) 1, `arXiv:hep-ph/9709356`.

[26] M. Schmaltz and D. Tucker-Smith, *Little Higgs review*, Ann. Rev. Nucl. Part. Sci. **55** (2005) 229, arXiv:hep-ph/0502182.

[27] L. Randall and R. Sundrum, *A Large mass hierarchy from a small extra dimension*, Phys. Rev. Lett. **83** (1999) 3370, arXiv:hep-ph/9905221.

[28] L. Randall and R. Sundrum, *An Alternative to compactification*, Phys. Rev. Lett. **83** (1999) 4690, arXiv:hep-th/9906064.

[29] I. Doršner *et al.*, *Physics of leptoquarks in precision experiments and at particle colliders*, Phys. Rept. **641** (2016) 1, arXiv:1603.04993.

[30] W. Buchmuller, R. Ruckl, and D. Wyler, *Leptoquarks in Lepton - Quark Collisions*, Phys. Lett. **B191** (1987) 442, [Erratum: Phys. Lett.B448,320(1999)].

[31] Blake, T. *et al.*, *Round table: Flavour anomalies in $b \to s\ell^+\ell^-$ processes*, EPJ Web Conf. **137** (2017) 01001.

[32] V. C. Rubin, W. K. Ford, Jr. and N. Thonnard, *Rotational properties of 21 SC galaxies with a large range of luminosities and radii, from NGC 4605 /R = 4kpc/ to UGC 2885 /R = 122 kpc/*, Astrophys. J. **238** (1980) 471.

[33] K. G. Begeman, A. H. Broeils, and R. H. Sanders, *Extended rotation curves of spiral galaxies - Dark haloes and modified dynamics*, Mon. Not. Roy. Astron. Soc. **249** (1991) 523.

[34] M. Bartelmann and P. Schneider, *Weak gravitational lensing*, Phys. Rept. **340** (2001) 291, arXiv:astro-ph/9912508.

[35] J. R. Ellis *et al.*, *Supersymmetric Relics from the Big Bang*, Nucl. Phys. **B238** (1984) 453, [,223(1983)].

[36] Super-Kamiokande, Y. Fukuda *et al.*, *Evidence for oscillation of atmospheric neutrinos*, Phys. Rev. Lett. **81** (1998) 1562, arXiv:hep-ex/9807003.

[37] SNO collaboration, Q. R. Ahmad *et al.*, *Measurement of the rate of $\nu_e + d \to p + p + e^-$ interactions produced by ^8b solar neutrinos at the sudbury neutrino observatory*, Phys. Rev. Lett. **87** (2001) 071301.

[38] Z. Maki, M. Nakagawa, and S. Sakata, *Remarks on the Unified Model of Elementary Particles*, Progress of Theoretical Physics **28** (1962) 870.

[39] B. Pontecorvo, *Inverse beta processes and nonconservation of lepton charge*, Sov. Phys. JETP **7** (1958) 172, [Zh. Eksp. Teor. Fiz.34,247(1957)].

[40] A. Kusenko, *Sterile neutrinos: The Dark side of the light fermions*, Phys. Rept. **481** (2009) 1, arXiv:0906.2968.

[41] G. Steigman, *Observational tests of antimatter cosmologies*, Annual Review of Astronomy and Astrophysics **14** (1976) 339.

[42] A. D. Sakharov, *Violation of CP Invariance, C asymmetry, and baryon asymmetry of the universe*, Pisma Zh. Eksp. Teor. Fiz. **5** (1967) 32, [Usp. Fiz. Nauk161,no.5,61(1991)].

[43] G. R. Farrar and M. E. Shaposhnikov, *Baryon asymmetry of the universe in the standard electroweak theory*, Phys. Rev. **D50** (1994) 774, arXiv:hep-ph/9305275.

[44] P. Huet and E. Sather, *Electroweak baryogenesis and standard model CP violation*, Phys. Rev. **D51** (1995) 379, arXiv:hep-ph/9404302.

[45] M. B. Gavela, M. Lozano, J. Orloff, and O. Pene, *Standard model CP violation and baryon asymmetry. Part 1: Zero temperature*, Nucl. Phys. **B430** (1994) 345, arXiv:hep-ph/9406288.

[46] XENON1T collaboration, E. Aprile, *The XENON1T Dark Matter Search Experiment*, Springer Proc. Phys. **148** (2013) 93, arXiv:1206.6288.

[47] XENON collaboration, E. Aprile *et al.*, *Physics reach of the XENON1T dark matter experiment*, JCAP **1604** (2016) 027, arXiv:1512.07501.

[48] O. S. Brüning *et al.*, *LHC Design Report*, CERN Yellow Reports: Monographs, CERN, Geneva, 2004.

[49] ATLAS collaboration, A. Airapetian *et al.*, *ATLAS detector and physics performance: Technical Design Report, 2*, Technical Design Report ATLAS, CERN, Geneva, 1999.

[50] CMS Collaboration, *The CMS experiment at the CERN LHC*, Journal of Instrumentation **3** (2008) S08004.

[51] ATLAS collaboration, G. Aad *et al.*, *Observation of a new particle in the search for the Standard Model Higgs boson with the ATLAS detector at the LHC*, Phys. Lett. **B716** (2012) 1, arXiv:1207.7214.

[52] CMS collaboration, S. Chatrchyan *et al.*, *Observation of a new boson at a mass of 125 GeV with the CMS experiment at the LHC*, Phys. Lett. **B716** (2012) 30, arXiv:1207.7235.

[53] M. Bott-Bodenhausen *et al.*, *Search for decay of neutral kaons into charged lepton pairs*, Physics Letters B **24** (1967) 194 .

[54] H. Foeth *et al.*, *Search for $K_L \to \mu^+\mu^-$ and $K_L \to e^+e^-$*, Physics Letters B **30** (1969) 282 .

[55] S. L. Glashow, J. Iliopoulos, and L. Maiani, *Weak interactions with lepton-hadron symmetry*, Phys. Rev. D **2** (1970) 1285.

[56] J. J. Aubert *et al.*, *Experimental observation of a heavy particle j*, Phys. Rev. Lett. **33** (1974) 1404.

[57] J.-E. Augustin *et al.*, *Discovery of a narrow resonance in e^+e^- annihilation*, Phys. Rev. Lett. **33** (1974) 1406.

[58] S. Bianco, F. L. Fabbri, D. Benson, and I. Bigi, *A Cicerone for the physics of charm*, Riv. Nuovo Cim. **26N7** (2003) 1, `arXiv:hep-ex/0309021`.

[59] A. Di Canto, *Measurement of CP-Violating Asymmetries in $D^0 \to \pi^+\pi^-$ and $D^0 \to K^+K^-$ Decays at CDF*, PhD thesis, Pisa U., 2012-04, doi: 10.2172/1248346.

[60] H. Georgi, *D^0-$\overline{D}^0$ mixing in heavy quark effective field theory*, Physics Letters B **297** (1992) 353 .

[61] T. Ohl, G. Ricciardi, and E. H. Simmons, *D^0-$\overline{D}^0$ mixing in heavy quark effective field theory: The Sequel*, Nucl. Phys. **B403** (1993) 605.

[62] I. I. Y. Bigi and N. G. Uraltsev, *D^0-$\overline{D}^0$ oscillations as a probe of quark hadron duality*, Nucl. Phys. **B592** (2001) 92.

[63] A. F. Falk *et al.*, *The D^0-$\overline{D}^0$ mass difference from a dispersion relation*, Phys. Rev. **D69** (2004) 114021.

[64] A. F. Falk, Y. Grossman, Z. Ligeti, and A. A. Petrov, *SU(3) breaking and D^0-$\overline{D}^0$ mixing*, Phys. Rev. **D65** (2002) 054034.

[65] K. Lande *et al.*, *Observation of long-lived neutral v particles*, Phys. Rev. **103** (1956) 1901.

[66] ARGUS collaboration, H. A. et al. *Observation of B^0-$\overline{B}^0$ mixing*, Physics Letters B **192** (1987) 245 .

[67] CDF collaboration, A. A. et al. *Observation of B_s^0 - $\overline{B}_s^0$ Oscillations*, Phys. Rev. Lett. **97** (2006) 242003.

[68] Heavy Flavor Averaging Group, Y. Amhis *et al.*, *Averages of b-hadron, c-hadron, and τ-lepton properties as of summer 2016*, Eur. Phys. J. **C77** (2017) 895, arXiv:1612.07233, updated results and plots available at https://hflav.web.cern.ch.

[69] LHCb collaboration, R. Aaij *et al.*, *Observation of D^0–$\overline{D}^0$ oscillations*, Phys. Rev. Lett. **110** (2013) 101802, arXiv:1211.1230.

[70] Y. Grossman, A. L. Kagan, and Y. Nir, *New physics and CP violation in singly Cabibbo suppressed D decays*, Phys. Rev. D **75** (2007) 036008.

[71] J. H. Christenson, J. W. Cronin, V. L. Fitch, and R. Turlay, *Evidence for the 2π decay of the k_2^0 meson*, Phys. Rev. Lett. **13** (1964) 138.

[72] BaBar collaboration, B. Aubert *et al.*, *Observation of CP violation in the B^0 meson system*, Phys. Rev. Lett. **87** (2001) 091801, arXiv:hep-ex/0107013.

[73] Belle collaboration, K. Abe *et al.*, *Observation of large CP violation in the neutral B meson system*, Phys. Rev. Lett. **87** (2001) 091802, arXiv:hep-ex/0107061.

[74] BarBar collaboration, B. Aubert *et al.*, *Direct CP Violating Asymmetry in $B^0 \to K^+\pi^-$ Decays*, Phys. Rev. Lett. **93** (2004) 131801.

[75] Belle collaboration, Y. Chao *et al.*, *Evidence for direct CP violation in $B^0 \to K^+\pi^-$ decays*, Phys. Rev. Lett. **93** (2004) 191802, arXiv:hep-ex/0408100.

[76] Belle collaboration, A. Poluektov *et al.*, *Evidence for direct CP violation in the decay $B \to D^*K_s$, $D \to K_s\pi^+\pi^-$ and measurement of the CKM phase ϕ_3*, Phys. Rev. **D81** (2010) 112002, arXiv:1003.3360.

[77] BaBar collaboration, P. del Amo Sanchez *et al.*, *Measurement of CP observables in $B^{+-} \to D_{CP}K^{+-}$ decays and constraints on the CKM angle γ*, Phys. Rev. **D82** (2010) 072004, arXiv:1007.0504.

[78] LHCb collaboration, R. Aaij *et al.*, *Observation of CP violation in $B^\pm \to DK^\pm$ decays*, Phys. Lett. **B712** (2012) 203, Erratum ibid. **B713** (2012) 351, arXiv:1203.3662.

[79] LHCb collaboration, R. Aaij *et al.*, *First observation of CP violation in the decays of B_s^0 mesons*, Phys. Rev. Lett. **110** (2013) 221601, arXiv:1304.6173.

[80] S. de Boer, *Probing the standard model with rare charm decays*, PhD thesis, Technische Universität Dortmund, 2017-08.

[81] A. Paul, I. I. Bigi, and S. Recksiegel, *On $D \to X_u \ell^+ \ell^-$ within the Standard Model and frameworks like the littlest Higgs model with T parity*, Phys. Rev. **D83** (2011) 114006, arXiv:1101.6053.

[82] BaBar collaboration, P. F. Harrison and H. R. Quinn, *The BaBar physics book: Physics at an asymmetric B factory*, .

[83] M. Neubert, *Effective field theory and heavy quark physics*, in *Physics in $D \geq 4$. Proceedings, Theoretical Advanced Study Institute in elementary particle physics, TASI 2004, Boulder, USA, June 6-July 2, 2004*, pp. 149–194, 2005, arXiv:hep-ph/0512222.

[84] K. G. Wilson, *Non-lagrangian models of current algebra*, Phys. Rev. **179** (1969) 1499.

[85] J. C. Collins, *The Problem of scales: Renormalization and all that*, in *QCD and beyond. Proceedings, Theoretical Advanced Study Institute in Elementary Particle Physics, TASI-95, Boulder, USA, June 4-30, 1995*, pp. 269–326, 1995, arXiv:hep-ph/9510276.

[86] K. G. Chetyrkin, M. Misiak, and M. Munz, *Weak radiative B meson decay beyond leading logarithms*, Phys. Lett. **B400** (1997) 206, arXiv:hep-ph/9612313, [Erratum: Phys. Lett.B425,414(1998)].

[87] C. Bobeth, M. Misiak, and J. Urban, *Photonic penguins at two loops and m_t dependence of $BR[B \to X_s \ell^+ \ell^-]$*, Nucl. Phys. **B574** (2000) 291, arXiv:hep-ph/9910220.

[88] P. Gambino, M. Gorbahn, and U. Haisch, *Anomalous dimension matrix for radiative and rare semileptonic B decays up to three loops*, Nucl. Phys. **B673** (2003) 238, arXiv:hep-ph/0306079.

[89] de Boer, Stefan and Müller, Bastian and Seidel, Dirk, *Higher-order Wilson coefficients for $c \to u$ transitions in the standard model*, JHEP **08** (2016) 091, arXiv:1606.05521.

[90] S. Fajfer, P. Singer, and J. Zupan, *The Radiative Leptonic Decays $D^0 \to e^+e^-\gamma, \mu^+\mu^-\gamma$ in the Standard Model and Beyond*, Eur. Phys. J. C **27** (2002) 201.

[91] G. Burdman, E. Golowich, J. Hewett, and S. Pakvasa, *Rare charm decays in the standard model and beyond*, Phys. Rev. D **66** (2002) 014009.

[92] R.-M. Wang *et al.*, *Decays $D^+_{(s)} \to \pi(K)^+\ell^+\ell^-$ and $D^0 \to \ell^+\ell^-$ in the MSSM with and without R-parity*, Int. J. Mod. Phys. **A30** (2015) 1550063, arXiv:1409.0181.

[93] S. Fajfer, S. Prelošek, and P. Singer, *Rare charm meson decays $D \to P\ell^+\ell^-$ and $c \to u\ell^+\ell^-$ in the standard model and the minimal supersymmetric standard model*, Phys. Rev. D **64** (2001) 114009.

[94] S. Fajfer, N. Košnik, and S. c. v. Prelovšek, *Updated constraints on new physics in rare charm decays*, Phys. Rev. D **76** (2007) 074010.

[95] L. Cappiello, O. Catà, and G. D'Ambrosio, *Standard model prediction and new physics tests for $D^0 \to h_1^+ h_2^- \ell^+\ell^-$ ($h = \pi, K$; $\ell = e, \mu$)*, JHEP **04** (2013) 135, arXiv:1209.4235.

[96] S. de Boer and G. Hiller, *Flavor and new physics opportunities with rare charm decays into leptons*, Phys. Rev. **D93** (2016) 074001, arXiv:1510.00311.

[97] S. Fajfer and N. Košnik, *Prospects of discovering new physics in rare charm decays*, Eur. Phys. J. **C75** (2015) 567, arXiv:1510.00965.

[98] S. Fajfer and N. Košnik, *Leptoquarks in flavor changing neutral current charmFCNC charm decays*, Phys. Rev. **D79** (2009) 017502, arXiv:0810.4858.

[99] S. Sahoo and R. Mohanta, *New physics effects in charm meson decays involving $c \to u\ell^+\ell^-(\ell_i^\mp \ell_j^\pm)$ transitions*, Eur. Phys. J. **C77** (2017) 344, arXiv:1705.02251.

[100] A. Paul, I. I. Bigi, and S. Recksiegel, *On $D \to X_u l^+ l^-$ within the Standard Model and Frameworks like the Littlest Higgs Model with T Parity*, Phys. Rev. **D83** (2011) 114006, arXiv:1101.6053.

[101] S. Fajfer and S. Prelovšek, *Effects of littlest Higgs model in rare D meson decays*, Phys. Rev. **D73** (2006) 054026, arXiv:hep-ph/0511048.

[102] S. Fajfer and S. Prelošek, *Search for new physics in rare D decays*, Conf. Proc. **C060726** (2006) 811, arXiv:hep-ph/0610032, [,811(2006)].

[103] I. I. Bigi and A. Paul, *On CP asymmetries in two-, three- and four-body D decays*, JHEP **03** (2012) 021, arXiv:1110.2862.

[104] C. Delaunay, J. F. Kamenik, G. Perez, and L. Randall, *Charming CP Violation and Dipole Operators from RS Flavor Anarchy*, JHEP **01** (2013) 027, arXiv:1207.0474.

[105] A. Paul, A. de la Puente, and I. I. Bigi, *Manifestations of warped extra dimension in rare charm decays and asymmetries*, Phys. Rev. **D90** (2014) 014035, arXiv:1212.4849.

[106] S. Fajfer, S. Prelovšek, and P. Singer, *Rare charm meson decays $D \to P\ell^+\ell^-$ and $c \to u\ell^+\ell^-$ in SM and MSSM*, Phys. Rev. **D64** (2001) 114009, arXiv:hep-ph/0106333.

[107] X.-D. Guo *et al.*, *Looking for New Physics via Semi-leptonic and Leptonic rare decays of D and D_s*, Chin. Phys. **C41** (2017) 093107, arXiv:1703.08799.

[108] E. Golowich, J. Hewett, S. Pakvasa, and A. A. Petrov, *Relating D^0–$\overline{D}^0$ mixing and $D^0 \to \ell^+\ell^-$ with new physics*, Phys. Rev. D **79** (2009) 114030.

[109] A. Paul, I. I. Bigi, and S. Recksiegel, *$D^0 \to \gamma\gamma$ and $D^0 \to \mu^+\mu^-$ rates on an unlikely impact of the littlest higgs model with t parity*, Phys. Rev. D **82** (2010) 094006.

[110] LHCb collaboration, R. Aaij *et al.*, *Search for the rare decay $D^0 \to \mu^+\mu^-$*, Phys. Lett. **B725** (2013) 15, arXiv:1305.5059.

[111] S. Fajfer, S. Prelošek, and P. Singer, *Resonant and nonresonant contributions to the weak $D \to V\ell^+\ell^-$ decays*, Phys. Rev. **D58** (1998) 094038, arXiv:hep-ph/9805461.

[112] S. Fajfer and N. Košnik, *Resonance catalyzed CP asymmetries in $D \to P\ell^+\ell^-$*, Phys. Rev. **D87** (2013) 054026, arXiv:1208.0759.

[113] S. De Boer, *Charm decays*, in *17th International Conference on B-Physics at Frontier Machines (Beauty 2018) La Biodola, Elba island, Italy, May 7-11, 2018*, 2018, arXiv:1807.05845.

[114] S. Fajfer, N. Kosnik, and S. Prelovsek, *Updated constraints on new physics in rare charm decays*, Phys. Rev. **D76** (2007) 074010, arXiv:0706.1133.

[115] LHCb collaboration, R. Aaij *et al.*, *Search for $D^+_{(s)} \to \pi^+\mu^+\mu^-$ and $D^+_{(s)} \to \pi^-\mu^+\mu^+$ decays*, Phys. Lett. **B724** (2013) 203, arXiv:1304.6365.

[116] E791 collaboration, L. M. Cremaldi *et al.*, *Fermilab E791*, AIP Conf. Proc. **272** (1992) 1058, arXiv:hep-ex/0010027.

[117] E791 collaboration, E. M. Aitala *et al.*, *Search for rare and forbidden charm meson decays $D^0 \to V\ell^+\ell^-$ and $hh\ell\ell$*, Phys. Rev. Lett. **86** (2001) 3969, arXiv:hep-ex/0011077.

[118] LHCb collaboration, R. Aaij *et al.*, *Search for the decay $D^0 \to \pi^+\pi^-\mu^+\mu^-$*, Phys. Lett. **B728** (2014) 234, arXiv:1310.2535.

[119] LHCb collaboration, R. Aaij *et al.*, *First observation of the decay $D^0 \to K^-\pi^+\mu^+\mu^-$ in the $\rho^0 - \omega$ region of the dimuon mass spectrum*, Phys. Lett. **B757** (2016) 558, arXiv:1510.08367.

[120] S. de Boer and G. Hiller, *Null tests from angular distributions in $D \to P_1P_2\ell^+\ell^-$, $l = e, \mu$ decays on and off peak*, Phys. Rev. **D98** (2018) 035041, arXiv:1805.08516.

[121] KTeV collaboration, E. Abouzaid *et al.*, *A Measurement of the K0 charge radius and a CP violating asymmetry together with a search for CP violating e1 direct photon emission in the rare decay K(L) $\to \pi^+\pi^-e^+e^-$*, Phys. Rev. Lett. **96** (2006) 101801, arXiv:hep-ex/0508010.

[122] C. Lazzeroni, *New NA48 results on CP violation*, Eur. Phys. J. **C33** (2004) S330.

[123] LHCb collaboration, R. Aaij *et al.*, *Measurement of the polarization amplitudes and triple product asymmetries in the $B_s^0 \to \phi\phi$ decay*, Phys. Lett. **B713** (2012) 369, arXiv:1204.2813.

[124] LHCb collaboration, R. Aaij *et al.*, *Search for CP violation using triple product asymmetries in $\Lambda_b^0 \to pK^-\pi^+\pi^-$, $\Lambda_b^0 \to pK^-K^+K^-$, and $\Xi_b^0 \to pK^-K^-\pi^+$ decays*, JHEP **08** (2018) 039, arXiv:1805.03941.

[125] FOCUS collaboration, J. M. Link *et al.*, *Search for T violation in charm meson decays*, Phys. Lett. **B622** (2005) 239, arXiv:hep-ex/0506012.

[126] BaBar collaboration, P. del Amo Sanchez *et al.*, *Search for CP violation using T-odd correlations in $D^0 \to K^+K^-\pi^+\pi^-$ decays*, Phys. Rev. **D81** (2010) 111103, arXiv:1003.3397.

[127] BaBar collaboration, J. P. Lees *et al.*, *Search for CP violation using T-odd correlations in $D^+ \to K^+K_S^0\pi^+\pi^-$ and $D_s^+ \to K^+K_S^0\pi^+\pi^-$ decays*, Phys. Rev. **D84** (2011) 031103, arXiv:1105.4410.

[128] LHCb collaboration, R. Aaij *et al.*, *Search for CP violation using T-odd correlations in $D^0 \to K^+K^-\pi^+\pi^-$ decays*, JHEP **10** (2014) 005, arXiv:1408.1299.

[129] LHCb collaboration, R. Aaij *et al.*, *Measurement of CP asymmetry in $D^0 \to K^+K^-$ decays*, Phys. Lett. **B767** (2017) 177, arXiv:1610.09476.

[130] LHCb collaboration, R. Aaij *et al.*, *Measurement of the difference of time-integrated CP asymmetries in $D^0 \to K^-K^+$ and $D^0 \to \pi^-\pi^+$ decays*, Phys. Rev. Lett. **116** (2016) 191601, arXiv:1602.03160.

[131] LHCb collaboration, A. A. Alves Jr. *et al.*, *The LHCb detector at the LHC*, JINST **3** (2008) S08005.

[132] LHCb collaboration, R. Aaij *et al.*, *LHCb detector performance*, Int. J. Mod. Phys. **A30** (2015) 1530022, arXiv:1412.6352.

[133] LHCb collaboration, R. Aaij *et al.*, *First observation of forward $Z \to b\bar{b}$ production in pp collisions at $\sqrt{s} = 8$ TeV*, Phys. Lett. **B776** (2017) 430, arXiv:1709.03458.

[134] LHCb collaboration, R. Aaij *et al.*, *Measurement of forward $W \to e\nu$ production in pp collisions at $\sqrt{s} = 8$ TeV*, JHEP **10** (2016) 030, arXiv:1608.01484.

[135] LHCb collaboration, R. Aaij *et al.*, *Measurement of forward W and Z boson production in association with jets in proton-proton collisions at $\sqrt{s} = 8$ TeV*, JHEP **05** (2016) 131, arXiv:1605.00951.

[136] LHCb collaboration, R. Aaij *et al.*, *Study of prompt D^0 meson production in pPb collisions at $\sqrt{s_{NN}} = 5$ TeV*, JHEP **10** (2017) 090, arXiv:1707.02750.

[137] LHCb collaboration, R. Aaij *et al.*, *Prompt and nonprompt J/ψ production and nuclear modification in pPb collisions at $\sqrt{s_{NN}} = 8.16$ TeV*, Phys. Lett. **B774** (2017) 159, arXiv:1706.07122.

[138] LHCb collaboration, R. Aaij *et al.*, *Study of $\psi(2S)$ production cross-sections and cold nuclear matter effects in pPb collisions at $\sqrt{s_{NN}} = 5$ TeV*, JHEP **03** (2016) 133, arXiv:1601.07878.

[139] LHCb collaboration, R. Aaij *et al.*, *Study of Υ production and cold nuclear matter effects in pPb collisions at $\sqrt{s_{NN}} = 5$ TeV*, JHEP **07** (2014) 094, arXiv:1405.5152.

[140] LHCb collaboration, R. Aaij *et al.*, *Study of J/ψ production and cold nuclear matter effects in pPb collisions at $\sqrt{s_{NN}} = 5$ TeV*, JHEP **02** (2014) 072, arXiv:1308.6729.

[141] LHCb collaboration, *Measurement of J/ψ and D^0 production in pAr collisions at $\sqrt{s_{NN}} = 110$ GeV*, LHCb-CONF-2017-001.

[142] LHCb collaboration, *Measurement of antiproton production in pHe collisions at $\sqrt{s_{NN}} = 110$ GeV*, LHCb-CONF-2017-002.

[143] LHCb collaboration, R. Aaij *et al.*, *Measurement of the $B_s^0 \to \mu^+\mu^-$ branching fraction and effective lifetime and search for $B^0 \to \mu^+\mu^-$ decays*, Phys. Rev. Lett. **118** (2017) 191801, arXiv:1703.05747.

[144] LHCb collaboration, *LHCb VELO (VErtex LOcator): Technical Design Report*, CERN-LHCC-2001-011.

[145] R. Aaij *et al.*, *Performance of the LHCb Vertex Locator*, JINST **9** (2014) P09007, arXiv:1405.7808.

[146] LHCb collaboration, *LHCb magnet: Technical Design Report*, CERN-LHCC-2000-007.

[147] P. d'Argent *et al.*, *Improved performance of the LHCb Outer Tracker in LHC Run 2*, JINST **9** (2017) P11016, arXiv:1708.00819.

[148] LHCb collaboration, *LHCb inner tracker: Technical Design Report*, CERN-LHCC-2002-029.

[149] LHCb collaboration, *LHCb outer tracker: Technical Design Report*, CERN-LHCC-2001-024.

[150] R. Arink *et al.*, *Performance of the LHCb Outer Tracker*, JINST **9** (2014) P01002, arXiv:1311.3893.

[151] B. Storaci, *Optimization of the LHCb track reconstruction*, J. Phys. Conf. Ser. **664** (2015) 072047.

[152] M. Adinolfi *et al.*, *Performance of the LHCb RICH detector at the LHC*, Eur. Phys. J. **C73** (2013) 2431, arXiv:1211.6759.

[153] LHCb collaboration, *LHCb RICH: Technical Design Report*, CERN-LHCC-2000-037.

[154] LHCb collaboration, *LHCb muon system: Technical Design Report*, CERN-LHCC-2001-010.

[155] A. A. Alves Jr. *et al.*, *Performance of the LHCb muon system*, JINST **8** (2013) P02022, arXiv:1211.1346.

[156] J. R. Harrison, *Radiation damage studies in the LHCb VELO detector and searches for lepton flavour and baryon number violating tau decays*, PhD thesis, Manchester U., 2014.

[157] LHCb collaboration, *LHCb calorimeters: Technical Design Report*, CERN-LHCC-2000-036.

[158] R. Aaij *et al.*, *Performance of the LHCb calorimeters*, LHCb-DP-2013-004, in preparation.

[159] R. Aaij *et al.*, *Selection and processing of calibration samples to measure the particle identification performance of the LHCb experiment in Run 2*, arXiv:1803.00824.

[160] M. De Cian, S. Farry, P. Seyfert, and S. Stahl, *Fast neural-net based fake track rejection in the LHCb reconstruction*, Tech. Rep. LHCb-PUB-2017-011. CERN-LHCb-PUB-2017-011, CERN, Geneva, Mar, 2017.

[161] F. Archilli *et al.*, *Performance of the muon identification at LHCb*, JINST **8** (2013) P10020, arXiv:1306.0249.

[162] LHCb collaboration, *LHCb trigger system: Technical Design Report*, CERN-LHCC-2003-031.

[163] LHCb collaboration, *LHCb Trigger and Online Technical Design Report*, CERN-LHCC-2014-016.

[164] R. Aaij *et al.*, *The LHCb trigger and its performance in 2011*, JINST **8** (2013) P04022, arXiv:1211.3055.

[165] A. Puig, *The LHCb trigger in 2011 and 2012*, LHCb-PUB-2014-046.

[166] G. Dujany and B. Storaci, *Real-time alignment and calibration of the LHCb Detector in Run II*, No. LHCb-PROC-2015-011, Apr, 2015.

[167] LHCb collaboration, *The Brunel project*, http://lhcb-release-area.web.cern.ch/LHCb-release-area/DOC/brunel/.

[168] LHCb collaboration, *The daVinci project*, http://lhcb-release-area.web.cern.ch/LHCb-release-area/DOC/davinci/.

[169] S. Benson, V. Gligorov, M. A. Vesterinen, and J. M. Williams, *The lhcb turbo stream*, Journal of Physics: Conference Series **664** (2015) 082004.

[170] T. Sjöstrand, S. Mrenna, and P. Skands, *PYTHIA 6.4 physics and manual*, JHEP **05** (2006) 026, arXiv:hep-ph/0603175.

[171] T. Sjöstrand, S. Mrenna, and P. Skands, *A brief introduction to PYTHIA 8.1*, Comput. Phys. Commun. **178** (2008) 852, arXiv:0710.3820.

[172] I. Belyaev *et al.*, *Handling of the generation of primary events in Gauss, the LHCb simulation framework*, J. Phys. Conf. Ser. **331** (2011) 032047.

[173] D. J. Lange, *The EvtGen particle decay simulation package*, Nucl. Instrum. Meth. **A462** (2001) 152.

[174] Geant4 collaboration, S. Agostinelli *et al.*, *Geant4: A simulation toolkit*, Nucl. Instrum. Meth. **A506** (2003) 250.

[175] Geant4 collaboration, J. Allison *et al.*, *Geant4 developments and applications*, IEEE Trans. Nucl. Sci. **53** (2006) 270.

[176] LHCb collaboration, *The Boole project*, http://lhcb-release-area.web.cern.ch/LHCb-release-area/DOC/boole/.

[177] LHCb collaboration, *The Moore project*, http://lhcb-release-area.web.cern.ch/LHCb-release-area/DOC/moore/.

[178] W. D. Hulsbergen, *Decay chain fitting with a Kalman filter*, Nucl. Instrum. Meth. **A552** (2005) 566, arXiv:physics/0503191.

[179] L. Breiman, J. H. Friedman, R. A. Olshen, and C. J. Stone, *Classification and regression trees*, Wadsworth international group, Belmont, California, USA, 1984.

[180] B. P. Roe *et al.*, *Boosted decision trees as an alternative to artificial neural networks for particle identification*, Nucl. Instrum. Meth. **A543** (2005) 577, arXiv:physics/0408124.

[181] A. Hoecker *et al.*, *TMVA - Toolkit for Multivariate Data Analysis*, PoS **ACAT** (2007) 040, arXiv:physics/0703039.

[182] G. Cowan, *Statistical data analysis*, Oxford science publications, Clarendon Press, Oxford, 1998.

[183] N. L. Johnson, *Systems of frequency curves generated by methods of translation*, Biometrika **36** (1949) 149.

[184] G. Punzi, *Sensitivity of searches for new signals and its optimization*, eConf **C030908** (2003) MODT002, arXiv:physics/0308063.

[185] S. S. Wilks, *The large-sample distribution of the likelihood ratio for testing composite hypotheses*, Ann. Math. Stat. **9** (1938) 60.

[186] L. Anderlini *et al.*, *The PIDCalib package*, LHCb-PUB-2016-021.

[187] M. Pivk and F. R. Le Diberder, *sPlot: A statistical tool to unfold data distributions*, Nucl. Instrum. Meth. **A555** (2005) 356, arXiv:physics/0402083.

[188] A. L. Read, *Presentation of search results: The CL_s technique*, J. Phys. **G28** (2002) 2693.

[189] L. Moneta *et al.*, *The RooStats Project*, PoS **ACAT2010** (2010) 057, arXiv:1009.1003.

[190] O. Catàr, *Studies on $D^0 \to P_1^+ P_2^- \ell^+ \ell^-$: SM prediction and windows on NP*, Presented at the 10th International Workshop on the CKM Unitarity Triangle, Heidelberg, 2018.

[191] LHCb collaboration, R. Aaij *et al.*, *Measurement of CP asymmetry in $D^0 \to K^-K^+$ and $D^0 \to \pi^-\pi^+$ decays*, JHEP **07** (2014) 041, arXiv:1405.2797.

[192] LHCb collaboration, R. Aaij *et al.*, *First observation of $D^0 - \overline{D}^0$ oscillations in $D^0 \to K^+\pi^+\pi^-\pi^-$ decays and a measurement of the associated coherence parameters*, Phys. Rev. Lett. **116** (2016) 241801, arXiv:1602.07224.

[193] LHCb collaboration, R. Aaij *et al.*, *Measurement of CP asymmetry in $D^0 \to K^-K^+$ decays*, Phys. Lett. **B767** (2017) 177, arXiv:1610.09476.

[194] B. Viaud, *On the potential of multivariate techniques for the determination of multidimensional efficiencies*, Eur. Phys. J. Plus **131** (2016) 191.

[195] L. Kish, *Survey sampling*, Wiley, New York [u.a.], 1965.

[196] D. Das, G. Hiller, M. Jung, and A. Shires, *The $\overline{B} \to \overline{K}\pi\ell\ell$ and $\overline{B}_s \to \overline{K}K\ell\ell$ distributions at low hadronic recoil*, JHEP **09** (2014) 109, arXiv:1406.6681.

A Additional material on the sample selection

This chapter shows additional material concerning the sample selection. Figure A.1 and Figure A.2 show the selection variables used in the training of the BDT for $D^0 \to K^+K^-\mu^+\mu^-$ signal decays as explained in detail in section 3.4.

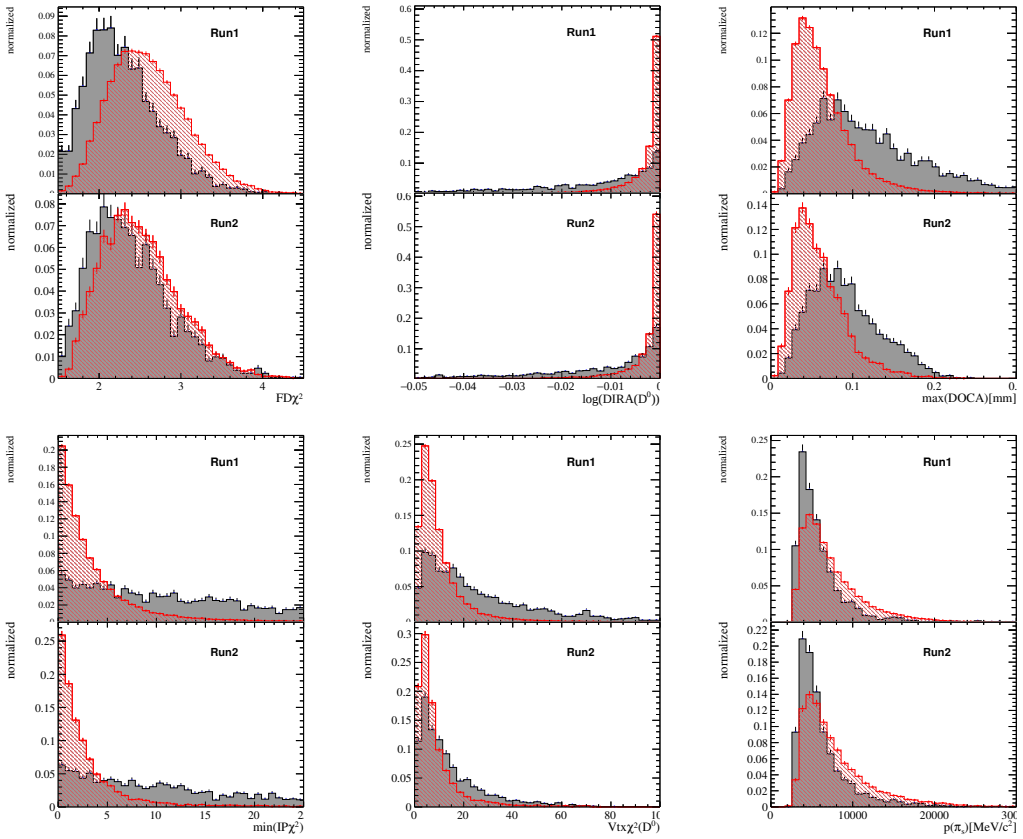

Figure A.1: Distributions of the BDT input variables for (red) $D^0 \to K^+K^-\mu^+\mu^-$ signal and (grey) background events, and separately for (top) Run 1 and Run 2 (bottom) data. From top-left to bottom-right: log(FDχ^2), log(DIRA), max(DOCA), min(IPχ^2), D^0 vertex χ^2, log(IPχ^2) of the soft pion, momentum of the soft pion [6].

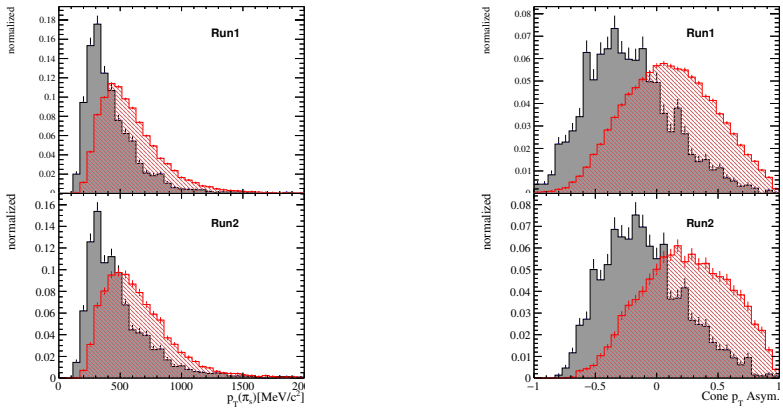

Figure A.2: Distributions of the BDT input variables for (red) $D^0 \to K^+K^-\mu^+\mu^-$ signal and (grey) background events, and separately for (top) Run 1 and Run 2 (bottom) data. (Left) Transverse momentum of the soft pion and (right) D^*-cone p_T asymmetry [6].

B Definition of the binning schemes for PID calibration

This chapter gives details on the binning schemes used for the PID calibration. Table B.1 shows the default, finer and coarser binning schemes used to evaluate the PID efficiency in section 5.4 and its associated systematic in section 5.5. See chapter 5 for details.

track type	scheme	p[GeV/c^2]	η
K, π	default	3.0 : 9.3 : 15.6 : 19.0 : 24.4: 29.8 : 35.2 : 40.6 : 46.0 : 51.4: 56.8 : 62.2 : 67.7 : 73.0 : 78.4 : 83.8 : 89.2 : 94.6 : 100 .0	1.5:2.375:3.25:5.125:5.0
	fine	3.0 : 4.5 : 6.0 : 7.5 : 9.0 : 10.5 : 12.0 : 13.0 : 14.0 : 15.0 16.0 : 17.0 : 18.0 : 19.0 : 20 : 21.5 : 23.0 : 24.5: 26.0 : 27.5 : 29.0 : 30.5 : 32.0 : 33.5 : 35.0 : 37.5 : 40.5 : 42.5 : 44.0 : 50.0: 60.0 : 70.0 : 100 .0	1.5 : 2.6: 2.9: 3.2: 3.5: 3.8: 4.2 : 5.0
	coarse	3.0 : 8.0 : 12.0 : 18.0 : 24.0 : 30.0 : 60.0 : 100.0	1.5 : 3.25 : 5
μ	default	3.0: 6.0: 10.0 : 12.0 : 14.5 : 14.5 : 17.5 : 21.5 : 27.0 : 32.0 : 40.0 : 60.0 : 70.0 : 100.0	1.5 : 2.375 : 3.25 : 4.125 : 5.0
	fine	3.0 : 4.5 : 6.0 : 7.5 : 9.0 : 10.5 : 12.0 : 13.0 : 14.0 : 15.0 16.0 : 17.0 : 18.0 : 19.0 : 20 : 21.5 : 23.0 : 24.5: 26.0 : 27.5 : 29.0 : 30.5 : 32.0 : 40.0 : 60.0 : 70.0 : 100.0	1.5 : 2.6: 2.9: 3.2: 3.5: 3.8: 4.2 : 5.0
	coarse	3.0 : 8.0 : 12.0 : 18.0 : 24.0 : 30.0 : 60.0 : 100.0	1.5 : 3.25 : 5

Table B.1: Binning schemes used in `PIDCalib [5]`.

C Validation of the fitting procedure

The fitting procedure has been validated using a large number of pseudo-experiments to check that the fits do not introduce any bias and correctly estimate the uncertainties on the measured signal yields and asymmetries. The pull distributions are defined as $pull = (N_{sig}^{fit} - N_{sig}^{gen})/\sigma^{fit}$ when measuring the branching fraction and $pull = (A_{sig}^{fit} - A_{sig}^{gen})/\sigma^{fit}$ for the asymmetry measurement. N_{sig}^{fit} (A_{sig}^{gen}) is the signal yield (asymmetry) as determined from the fit and σ^{fit} the corresponding fit parameter uncertainty, while N_{sig}^{gen} (A_{sig}^{gen}) is the value used in the generation of the pseudo-data.

Measurement of the branching fraction

For each dimuon-mass region and signal channel, 500 pseudo-data sets are generated reflecting the data statistics as reported in Table 5.2 by sampling from the signal and background PDFs. The yields for each component are assumed to follow Poisson distributions. The pull distributions for $D^0 \to \pi^+\pi^-\mu^+\mu^-$ and $D^0 \to K^+K^-\mu^+\mu^-$ decays are shown in Figure C.1 and Figure C.2, respectively. Results are summarised in Table C.1. Unbiased estimates of the signal yields and their uncertainties are observed.

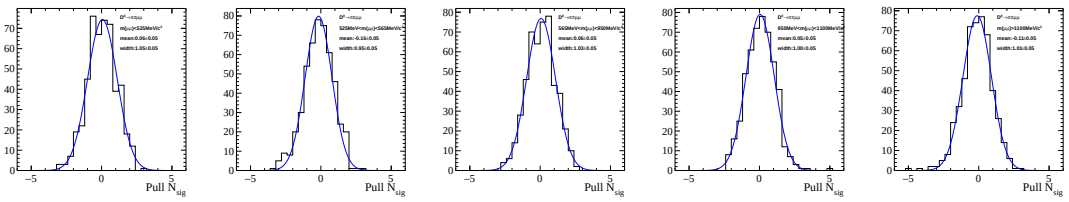

Figure C.1: Pull distributions for $D^0 \to \pi^+\pi^-\mu^+\mu^-$ pseudo-experiments generated according to the signal and background yields as observed in each dimuon-mass bin.

Figure C.2: Pull distributions for $D^0 \to K^+K^-\mu^+\mu^-$ pseudoe-xperiments generated according to the signal and background yields as observed in each dimuon-mass bin.

Measurement of the asymmetries

According to the yields reported in Table 6.4, 700 pseudo-data sets are generated for each dimuon-mass range and signal channel by sampling from the signal and background PDFs. A weight which is sampled from the distribution of weights as observed in data is assigned to mimic the effect of the correction of the efficiency variation. Furthermore, three (independent) tags are assigned to define the three measured asymmetries. Figure C.3 (Figure C.4) shows the pull distributions for the $D^0 \to \pi^+\pi^-\mu^+\mu^-$ ($D^0 \to K^+K^-\mu^+\mu^-$) toys generated with null asymmetries, while Figure C.5 shows the average of the pull distribution as a function of the generated signal or background asymmetries, with uncertainty corresponding to the width of the pull distribution. Results are also summarised in Table C.2. The fit procedure is found to be stable and unbiased estimates of the asymmetries and their uncertainties are expected.

$D^0 \to \pi^+\pi^-\mu^+\mu^-$			
N_{sig}	$m(\mu^+\mu^-)$ $[\text{MeV}/c^2]$	Pull mean	Pull width
	< 525	0.06 ± 0.05	1.05 ± 0.05
	$565 - 780$	-0.16 ± 0.05	0.95 ± 0.05
	$780 - 950$	0.06 ± 0.05	1.03 ± 0.05
	$950 - 1020$	0.05 ± 0.05	1.00 ± 0.05
	$1020 - 1100$	-0.11 ± 0.05	1.01 ± 0.05
$D^0 \to K^+K^-\mu^+\mu^-$			
N_{sig}	$m(\mu^+\mu^-)$ $[\text{MeV}/c^2]$	Pull mean	Pull width
	< 525	-0.14 ± 0.05	1.03 ± 0.05
	> 565	-0.08 ± 0.05	1.04 ± 0.05

Table C.1: Summary of the results reported in Figure C.1 and Figure C.2.

$D^0 \to \pi^+\pi^-\mu^+\mu^-$			
Asymmetry	$m(\mu^+\mu^-)$ $[\,\mathrm{MeV}/c^2]$	Pull mean	Pull width
A_{CP}	< 525	-0.08 ± 0.04	0.94 ± 0.02
	$565 - 780$	0.01 ± 0.04	0.94 ± 0.03
	$780 - 950$	0.01 ± 0.04	0.92 ± 0.03
	$950 - 1020$	0.03 ± 0.03	0.99 ± 0.02
	$1020 - 1100$	-0.05 ± 0.04	1.02 ± 0.03
	full range	0.03 ± 0.04	1.02 ± 0.03
A_{FB}	< 525	-0.02 ± 0.04	1.02 ± 0.03
	$565 - 780$	0.04 ± 0.04	1.01 ± 0.03
	$780 - 950$	-0.04 ± 0.04	1.04 ± 0.03
	$950 - 1020$	-0.05 ± 0.04	0.98 ± 0.03
	$1020 - 1100$	-0.02 ± 0.04	1.04 ± 0.03
	full range	0.02 ± 0.04	1.00 ± 0.03
$A_{2\phi}$	< 525	0.01 ± 0.04	1.00 ± 0.04
	$565 - 780$	-0.05 ± 0.04	0.99 ± 0.04
	$780 - 950$	0.01 ± 0.04	0.99 ± 0.04
	$950 - 1020$	-0.04 ± 0.04	1.00 ± 0.04
	$1020 - 1100$	-0.01 ± 0.04	1.02 ± 0.04
	full range	-0.02 ± 0.04	1.00 ± 0.04
$D^0 \to K^+K^-\mu^+\mu^-$			
Asymmetry	$m(\mu^+\mu^-)$ $[\,\mathrm{MeV}/c^2]$	Pull mean	Pull width
A_{CP}	< 525	0.00 ± 0.04	1.02 ± 0.03
	> 565	-0.02 ± 0.04	1.06 ± 0.03
	full range	-0.01 ± 0.04	1.02 ± 0.03
A_{FB}	< 525	0.07 ± 0.04	0.97 ± 0.03
	> 565	-0.05 ± 0.04	1.05 ± 0.03
	full range	-0.06 ± 0.04	1.08 ± 0.03
$A_{2\phi}$	< 525	-0.04 ± 0.04	1.02 ± 0.04
	> 565	-0.01 ± 0.04	1.00 ± 0.04
	full range	-0.02 ± 0.04	0.97 ± 0.04

Table C.2: Summary of the results reported in Figure C.3 and Figure C.4 [6].

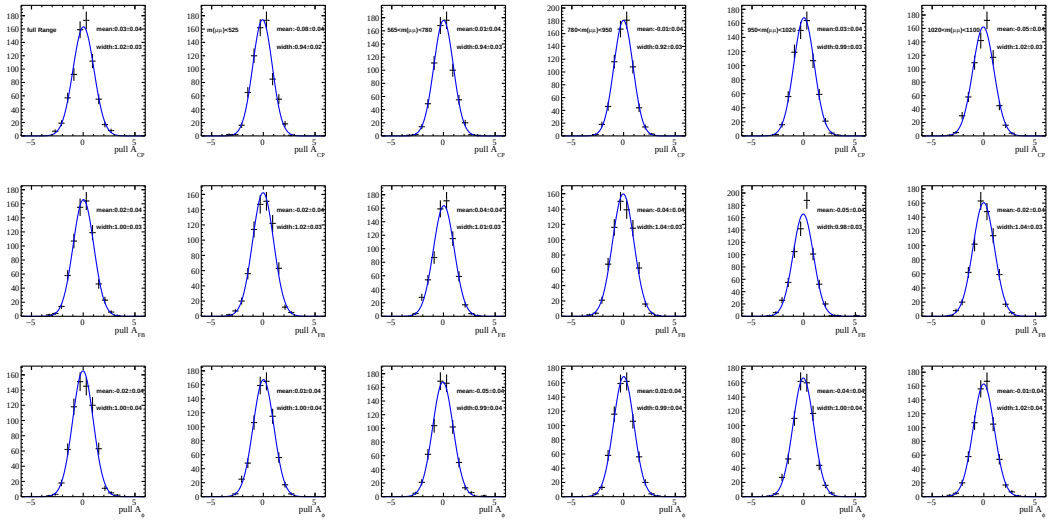

Figure C.3: Pull distributions for $D^0 \to \pi^+\pi^-\mu^+\mu^-$ pseudo-experiments generated with null asymmetries and for different dimuon-mass bins [6].

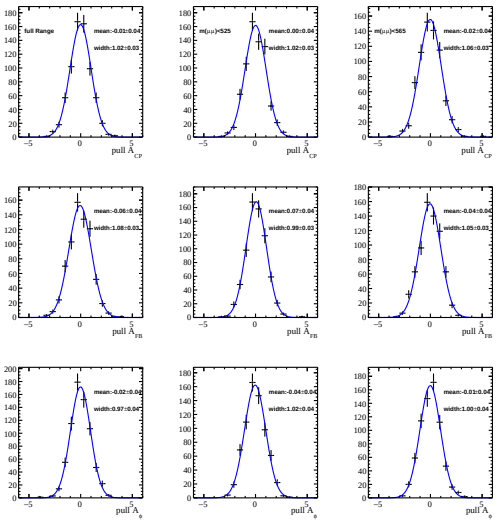

Figure C.4: Pull distributions for $D^0 \to K^+K^-\mu^+\mu^-$ pseudo-experiments generated with null asymmetries and for different dimuon-mass bins [6].

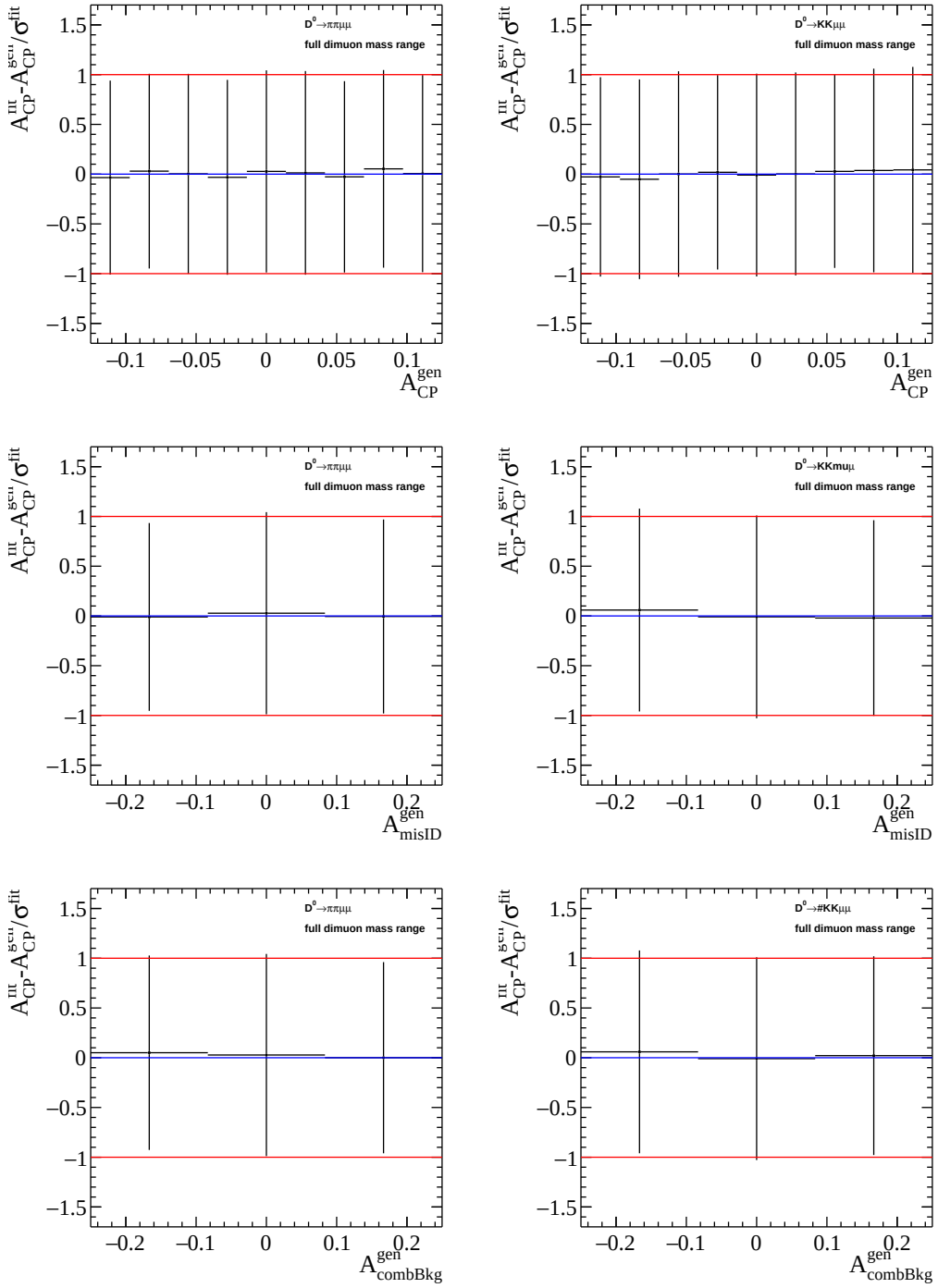

Figure C.5: Average of the pull distributions for (left) $D^0 \to \pi^+\pi^-\mu^+\mu^-$ and (right) $D^0 \to K^+K^-\mu^+\mu^-$ pseudo-experiments as a function of the generated (top) signal, (middle) misidentified $D^0 \to h^+h^-\mu^+\mu^-$ background and (bottom) combinatorial background asymmetries. The uncertainty corresponds to the width of the pull distribution [6].

D Correlations between the branching fractions

This chapter reports the correlations coefficients between the measured branching fractions. Table D.1 and Table D.2 report the correlation coefficients between the various bins for $\pi^+\pi^-\mu^+\mu^-$ and $K^+K^-\mu^+\mu^-$ final states, respectively, which are used when computing the total (integrated) branching fractions. See section 5.6 for details.

$\mathcal{B}(D^0 \to \pi^+\pi^-\mu^+\mu^-)$					
$[\,\mathrm{MeV}/c^2\,]$	< 525	525–565	565–950	950–1100	> 1100
< 525	1.000	0.512	0.832	0.818	0.558
525–565		1.000	0.587	0.577	0.393
565–950			1.000	0.937	0.639
950–1100				1.000	0.628
> 1100					1.000
< 525	1.000	0.088	0.343	0.366	0.078
525–565		1.000	0.170	0.181	0.039
565–950			1.000	0.706	0.151
950–1100				1.000	0.161
> 1100					1.000

Table D.1: Correlation coefficients between the $D^0 \to \pi^+\pi^-\mu^+\mu^-$ branching fractions in the different dimuon-mass ranges considered for the (top) systematic-only and (bottom) total uncertainties. The statistical uncertainties are uncorrelated [1].

$\mathcal{B}(D^0 \to K^+K^-\mu^+\mu^-)$			
$[\,\mathrm{MeV}/c^2\,]$	< 525	525–565	> 565
< 525	1.000	0.724	0.916
525–565		1.000	0.740
> 565			1.000
< 525	1.000	0.027	0.123
525–565		1.000	0.059
> 565			1.000

Table D.2: Correlation coefficients between the $D^0 \to K^+K^-\mu^+\mu^-$ branching fractions in the different dimuon-mass ranges considered for the (top) systematic-only and (bottom) total uncertainties. The statistical uncertainties are uncorrelated [1].

E Additional fits to determine the signal asymmetries

All fits to the D^0 mass distributions of $D^0 \to K^+K^-\mu^+\mu^-$ and $D^0 \to \pi^+\pi^-\mu^+\mu^-$ candidates to determine the asymmetries in bins of dimuon mass are shown in this chapter. Figure E.1, Figure E.2 and Figure E.3 show the D^0 mass distributions of $D^0 \to K^+K^-\mu^+\mu^-$ candidates split by the π_s^+ charge, $\cos\theta_L$ and $\sin 2\phi$ greater or less than zero, respectively, with fit projection overlaid. Corresponding distributions for $D^0 \to \pi^+\pi^-\mu^+\mu^-$ candidates can be found in Figure E.4, Figure E.5 and Figure E.6. See section 6.5 for details.

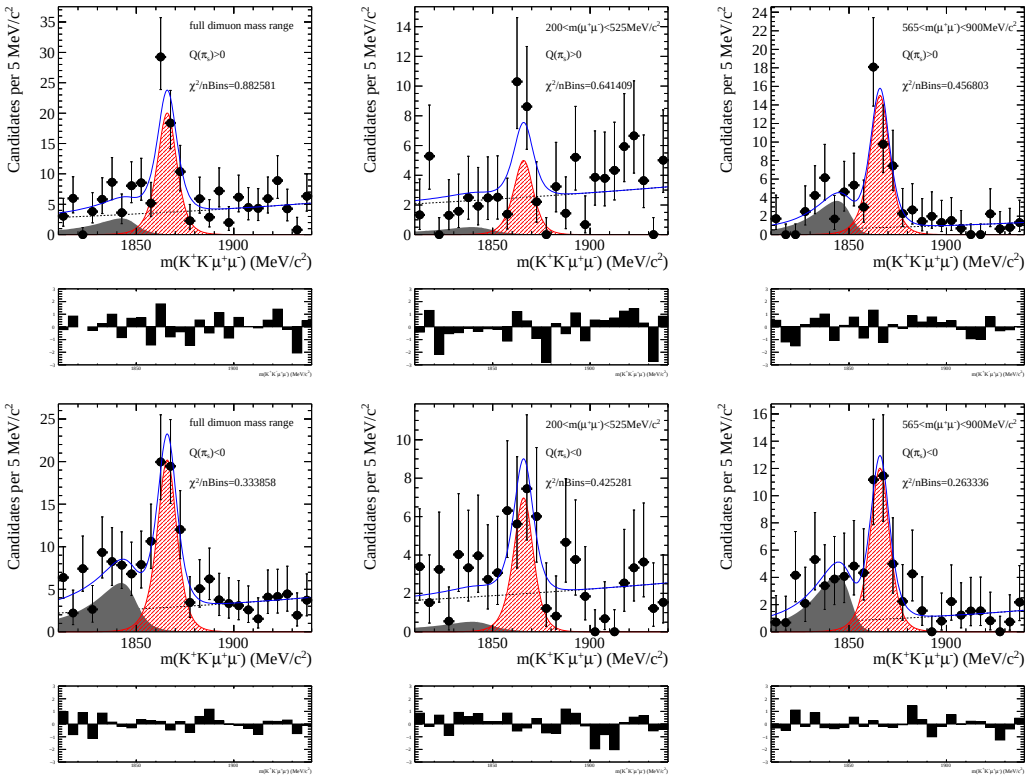

Figure E.1: Distribution of the D^0 mass for $D^0 \to K^-K^+\mu^+\mu^-$ decays, separately for D^0 and $\overline{D}^0$ and for different dimuon-mass bins, with fit projections overlaid [6].

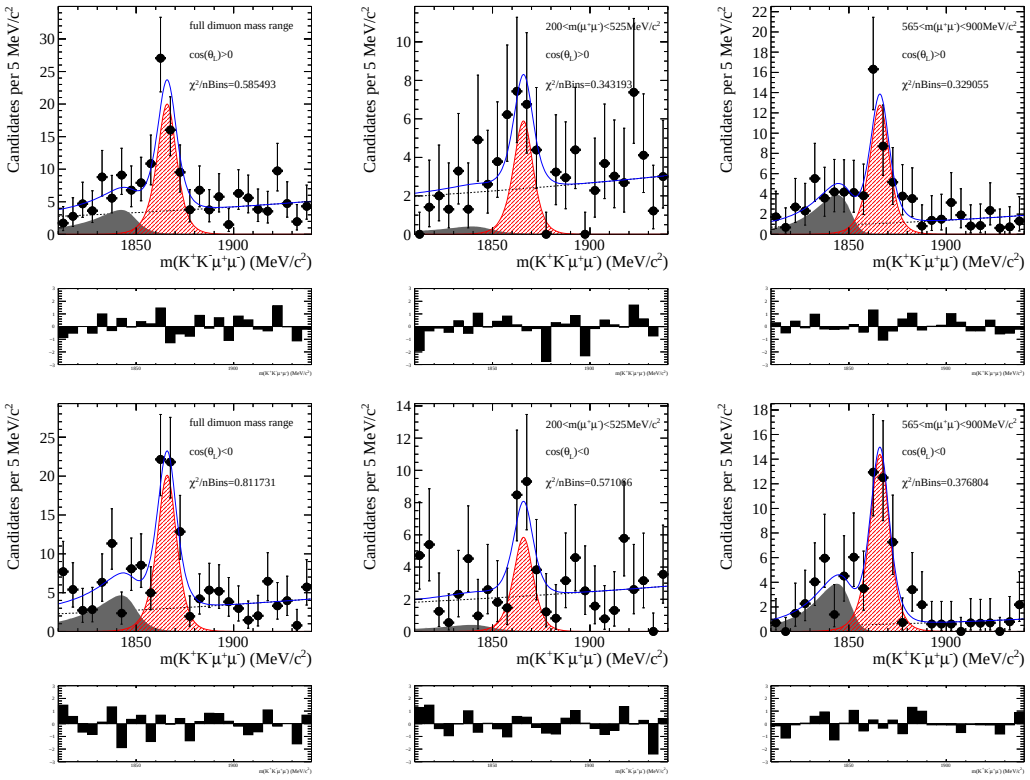

Figure E.2: Distribution of the D^0 mass for $D^0 \to K^-K^+\mu^+\mu^-$ decays, separately for $\cos\theta_L > 0$ and $\cos\theta_L < 0$ and for different dimuon-mass bins, with fit projections overlaid [6].

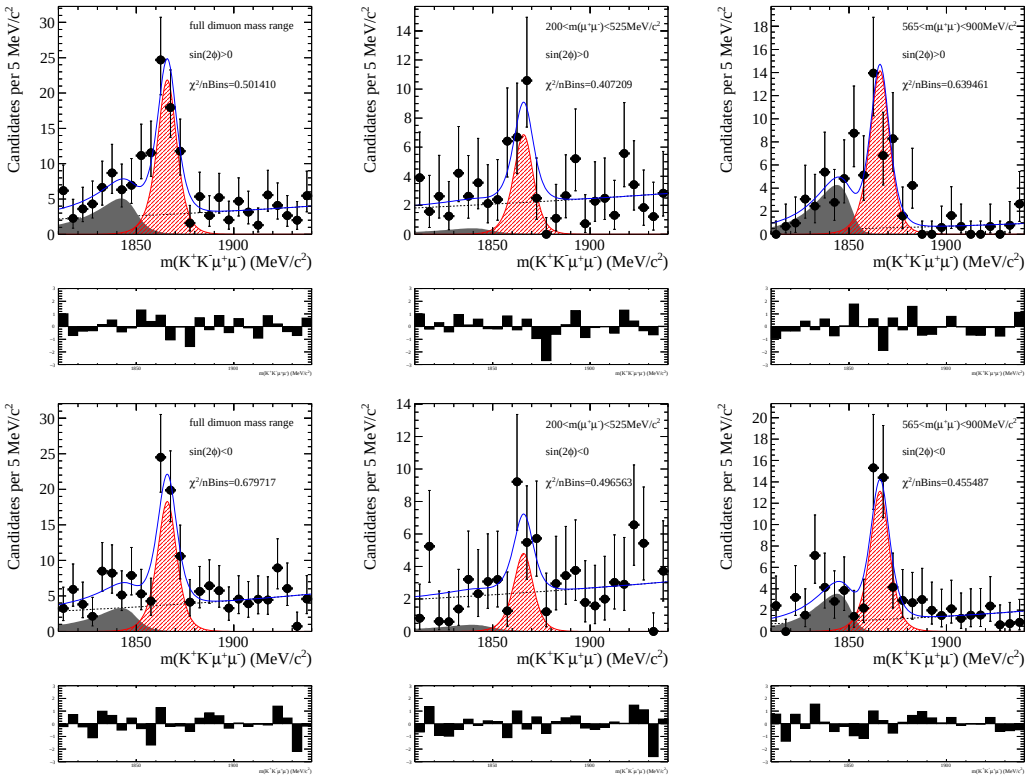

Figure E.3: Distribution of the D^0 mass for $D^0 \to K^-K^+\mu^+\mu^-$ decays, separately for $\sin 2\phi > 0$ and $\sin 2\phi < 0$ and for different dimuon-mass bins, with fit projections overlaid [6].

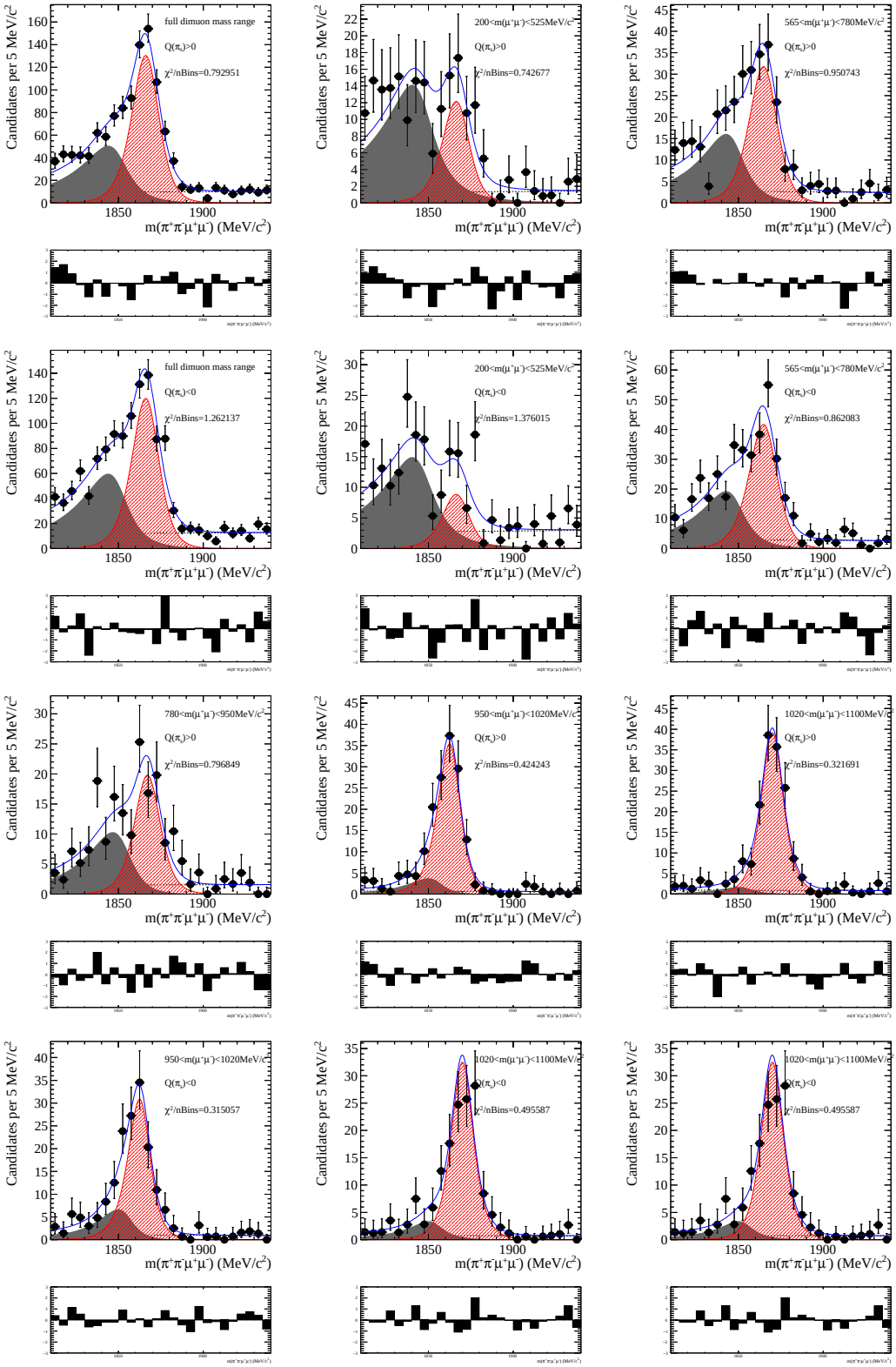

Figure E.4: Distribution of the D^0 mass for $D^0 \to \pi^-\pi^+\mu^+\mu^-$ decays, separately for D^0 and $\overline{D}^0$ and for different dimuon-mass bins, with fit projections overlaid [6].

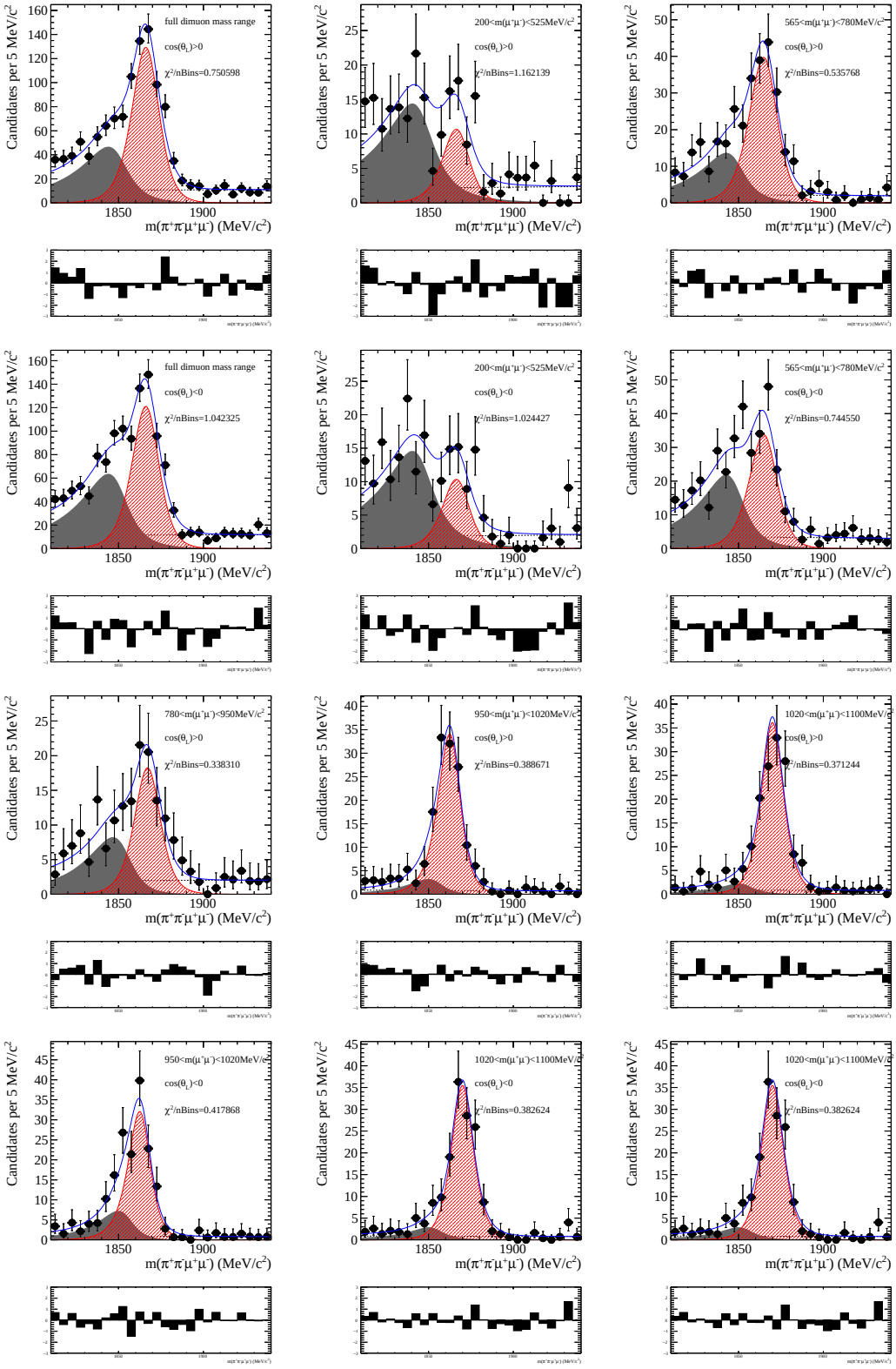

Figure E.5: Distribution of the D^0 mass for $D^0 \to \pi^-\pi^+\mu^+\mu^-$ decays, separately for $\cos\theta_L > 0$ and $\cos\theta_L < 0$ and for different dimuon-mass bins, with fit projections overlaid.

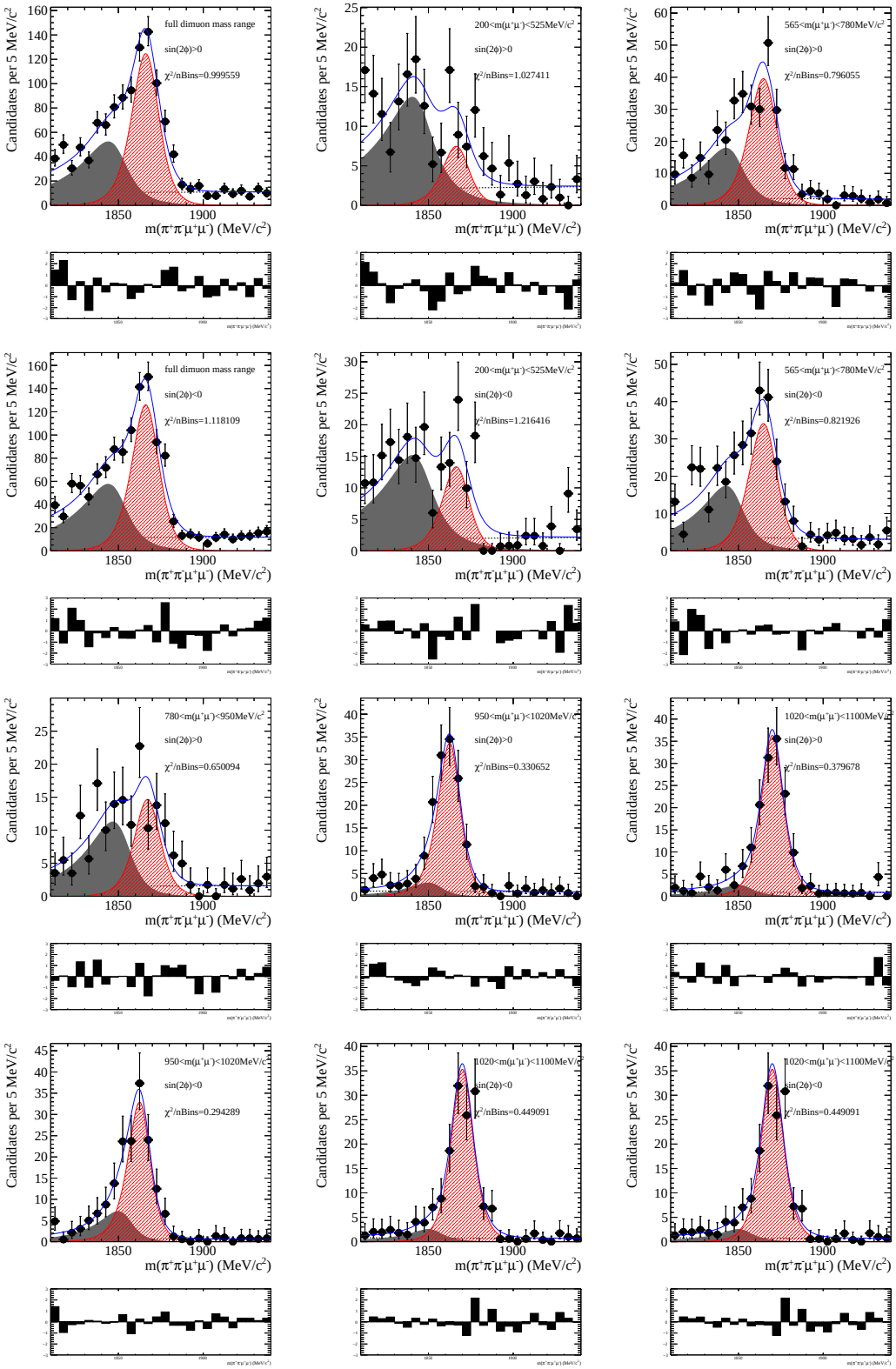

Figure E.6: Distribution of the D^0 mass for $D^0 \to \pi^-\pi^+\mu^+\mu^-$ decays, separately for $\sin 2\phi > 0$ and $\sin 2\phi < 0$ and for different dimuon-mass bins, with fit projections overlaid [6].

F

Additional material on the efficiency correction

This chapter shows additional material on the phase-space dependent efficiency correction, whose details are outline in section 6.3. Figure F.1 and Figure F.2 show the efficiency variation as function of two pairs of phase-space variables for simulated $D^0 \to \pi^+\pi^-\mu^+\mu^-$ and $D^0 \to K^+K^-\mu^+\mu^-$ candidates, respectively. Figure F.3 and Figure F.4 show the phase-space distribution of simulated signal candidates at generator level (top) and the ratio between the candidates after selection and efficiency correction and those at genenrator level (bottom), also separately for $D^0 \to \pi^+\pi^-\mu^+\mu^-$ and $D^0 \to K^+K^-\mu^+\mu^-$ candidates.

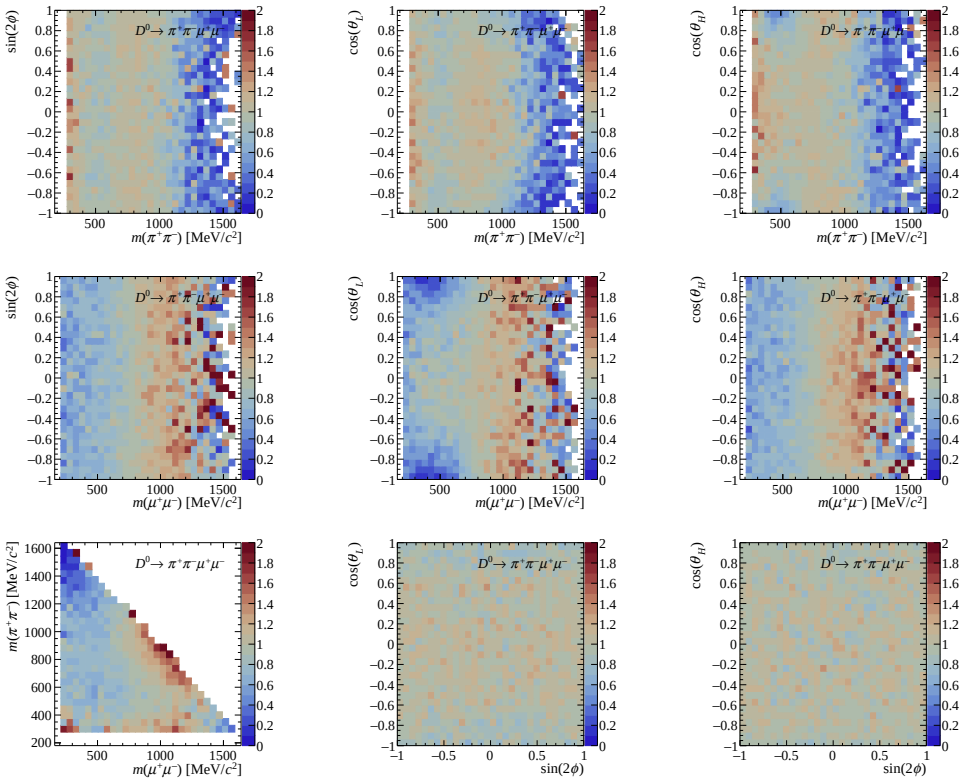

Figure F.1: Efficiency variation as a function of pairs of phase-space variables for simulated $D^0 \to \pi^+\pi^-\mu^+\mu^-$ decays [6].

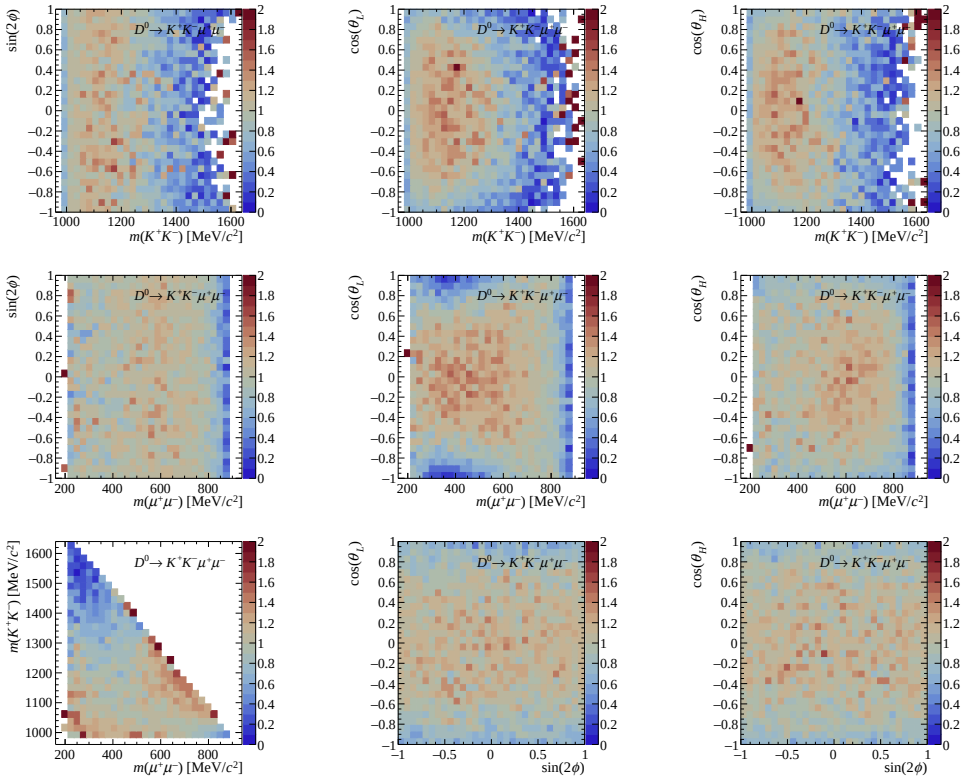

Figure F.2: Efficiency variation as a function of pairs of phase-space variables for simulated $D^0 \to K^+K^-\mu^+\mu^-$ decays [6].

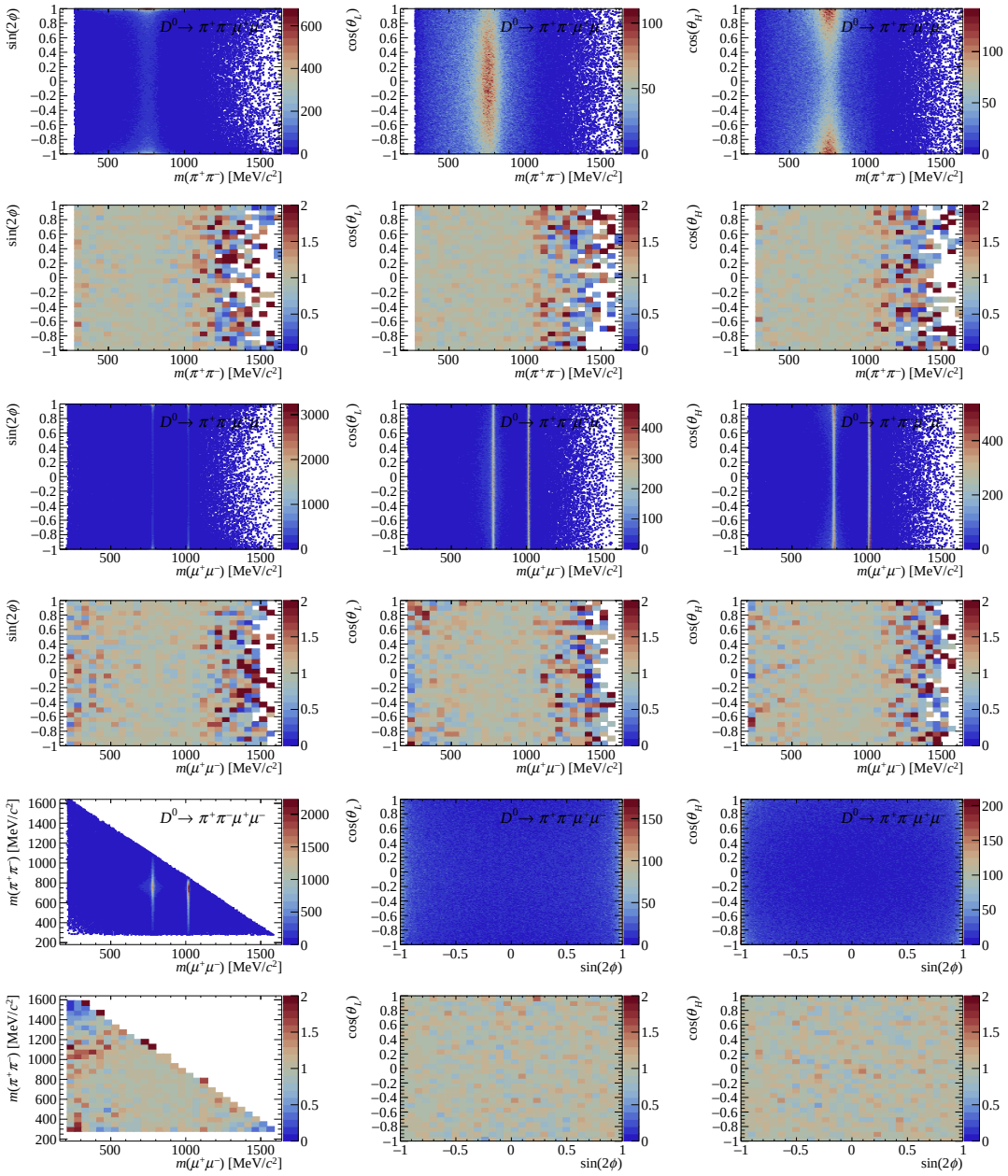

Figure F.3: The top panel of each plot shows the phase-space distribution of simulated $D^0 \to \pi^+\pi^-\mu^+\mu^-$ decays at generator level. The bottom panel of each plot shows the ratio between the candidates after selection and efficiency correction and those at genenrator level [6].

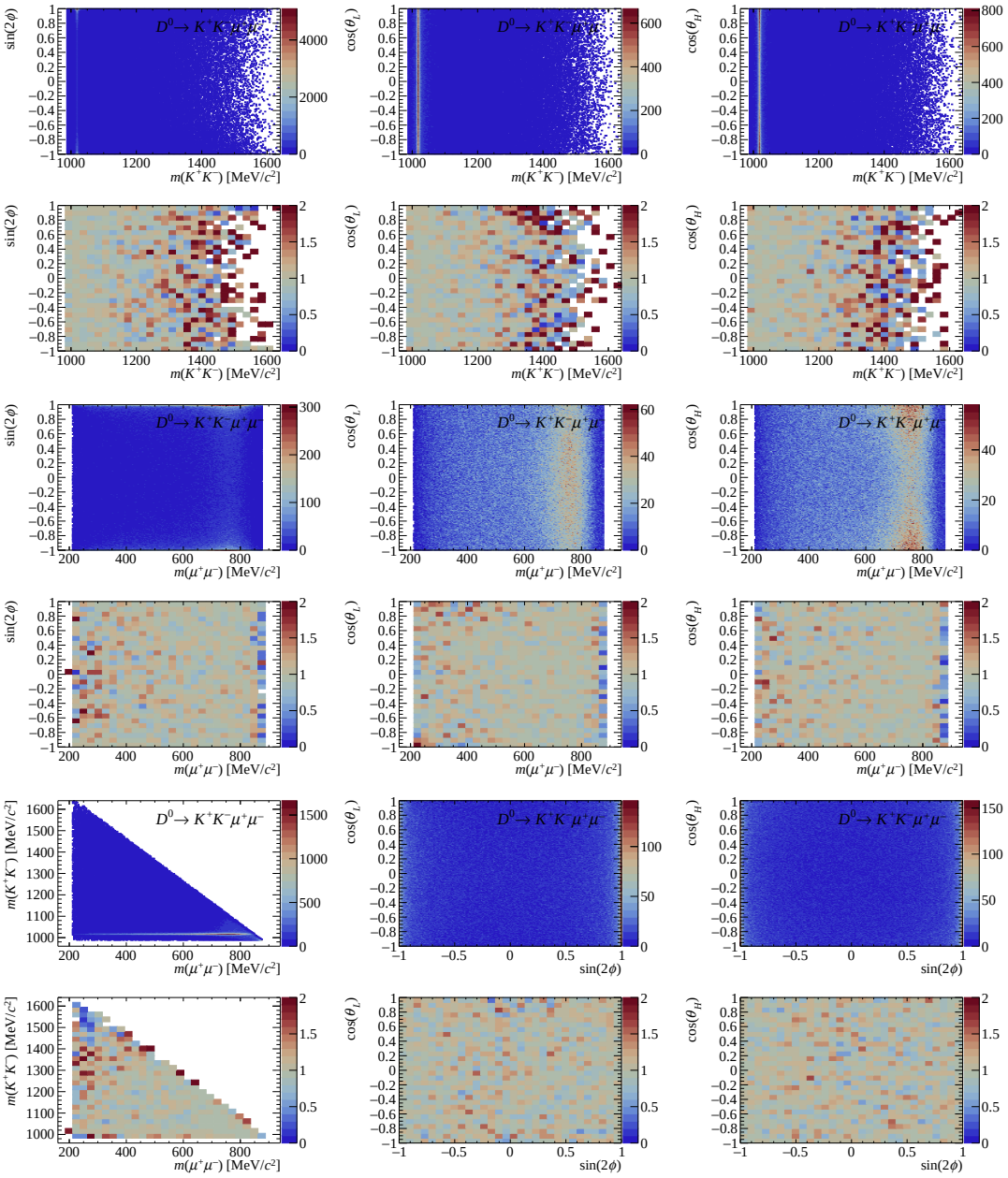

Figure F.4: The top panel of each plot shows the phase-space distribution of simulated $D^0 \to K^+K^-\mu^+\mu^-$ decays at generator level. The bottom panel of each plot shows the ratio between the candidates after selection and efficiency correction and those at genenrator level [6].

Acknowledgements

This work would not have been possible without the help of many people. At this point, I would like to thank everybody who has supported me during the last nine years since I started studying physics in Heidelberg. Unfortunately, I cannot list every single name as this chapter would become the largest one of the thesis; however, I still would like to mention some persons explicitly, already saying sorry to anybody I might have forgotten.

First, I would like to thank my supervisor Professor Ulrich Uwer for giving me the chance to work on my PhD thesis in the Heidelberg LHCb group and giving me the freedom to work on whatever topic I was interested in. I would also like to express my gratitude for the chance to spend a lot of time at CERN, summer schools, conferences and workshops all around the world.

Second, I would like to thank Professor Klaus Reygers who agreed to be the second referee of this thesis, as well as Professor Tilman Plehn and Professor Ulrich Glasmacher who agreed to complete the examination committee.

I would like to thank all members and former members of the Heidelberg LHCb group, in particular Professor Stephanie Hansmann-Menzemer and Dr. Sebastian Neubert, for creating an enjoyable working atmosphere, providing a countless number of cakes and helping with any physics and/or technical question I had. And of course, Dr. Alexey Zhelezov, who is able to help with any (seriously) computing problem one could think of. Furthermore, I would like to thank the members of the LHCb collaboration (especially the Charm WG) that continuously helped to improve the quality of my scientific output.

It is certainly true when I say that I learned the most (by far) about particle physics and data analysis when I was working on the analyses described in this thesis in the team of Dr. Andrea Contu, Dr. Benoit Viaud and my co-supervisor Dr. Angelo di Canto. In particular, I would like to thank Angelo, who always provided feedback, suggestions and corrections to any question I could think of (at any time of a day and seven days a week), not only for my PhD studies, but already for my master thesis. And for the support and advise concerning my career as a physicist. I know that this assistance cannot be taken for granted and I could

not have succeeded without his support.

At this point, I would also like to thank my high school physics teacher Herbert Hahn, who put the idea into my head to start studying physics in the first place. I am quite sure, this thesis would have never come into existence without his suggestion.

Next, I would like to say thanks to a bunch of guys who were by my side since the very first days I arrived in Heidelberg and always made the time as a PhD (and as an undergraduate student) more bearable. David, Matthieu, Philippe and Sebastian, who would have thought that we all would write a PhD thesis when we complained about the difficulties of theoretical physics and maths during the first semesters (except for Sebi who bravely was able to solve any exercise sheet)? The same thanks goes to the non- and ex-physicist friends Timo, Lars, Andi, Felix, Steffi and Marc who I met during my time in Heidelberg.

I am grateful for my friends Marco, Philipp, David, Kevin, Janosch, Lukas and Benedikt from my home town Iffezheim, to whom contacts have always remained in place, even though I did manage to came back too often recently.

Finally, I would like to express my particular gratitude to my family, especially my parents who have always accepted and supported my plans and Christine for the continuous support and understanding during the last years.

Sorry to everybody who had to suffer from my fluctuations in mood, especially if things did not work out the way I wanted. If I look at this long list, I can definitely consider myself lucky.